Université Catholique de Louvain
Secteur des sciences et technologies
Institut de Recherche en Mathématique et Physique
Centre for Cosmology, Particle Physics and Phenomenology

# *Precision top-quark physics at the LHC*

Doctoral dissertation presented by

Ioannis Tsinikos

in fulfilment of the requirements for the degree of Doctor in Sciences

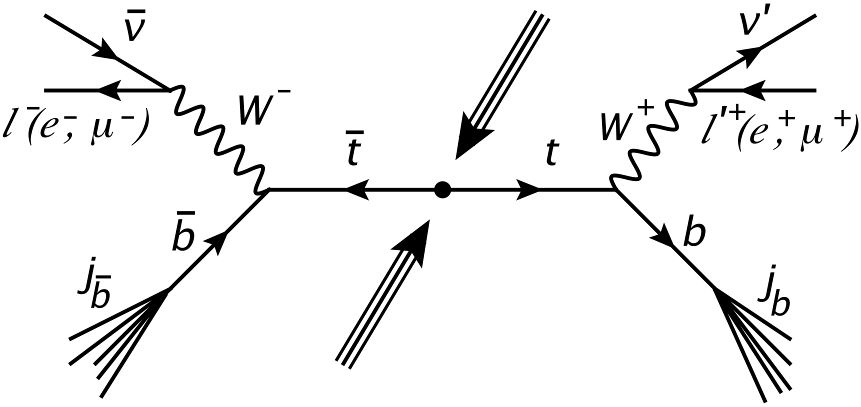

**Jury de thèse**

| | |
|---|---|
| Prof. Jean-Marc Gérard (presidént) | UCL, Belgium |
| Prof. Fabio Maltoni (promoteur) | UCL, Belgium |
| Dr. Andrea Giammanco | UCL, Belgium |
| Prof. Eric Laenen | UvA, Netherlands |
| Prof. Matteo Cacciari | UPMC, France |

July 3, 2017

# Acknowledgments

This work is a result of very strong collaborations and help as well as guidance that I received during these four years. In the following I would like to express my sincere gratitude to people without whom, it would not be possible to complete this research. I will restrict myself to people who contributed to the academic part of my life during these four years.

I would like to start with the jury of my PhD defence. Jean-Marc, Andrea, Eric, Matteo and Fabio, thank you for the very interesting discussion during my private defence and for the corrections on my Thesis. Your questions on the private defence and your feedback on the Thesis, improved my knowledge on the topic.

The person who made this whole project possible is my advisor Fabio Maltoni. Fabio, from the moment I came to CP3, your guidance was priceless. Your continuous flow of ideas for new projects and your constant excitement about physics are transmitted to anyone who works with you. I remember you telling me in the first day: "Ioannis, we decide what to work on and once we start we go as far as it goes until we understand everything". I later understood what it meant exactly. I enjoyed to the last bit working on every project and looking into all the details, digging more and more whenever there was an unclear point. I was so happy to realise that my projects were not only about producing results, but also about learning physics, explaining every behaviour, every deviation from what we expected and performing all possible cross checks. Thank you very much also for encouraging me to attend and give talks to workshops and conferences and participating to the PhD schools. It was a journey of knowledge for me and I hope that our collaboration will continue also in the future.

The projects I worked on, would have been much more difficult to manage, without my close collaborators. Marco, Davide and Eleni, thank you very much for the continuous constant support at both the technical and the physics level. Marco and Davide, thank you for introducing me to the EW corrections and having the patience to get me through step by step. Thank you for the numerous discussions we had and for all the explanations on every possible question I could thing of. Eleni, thank you for introducing me to the EFT framework. Understanding EFT is a challenge for me and without you it would have been impossible to proceed to the point I stand today. Thank you for your patience on giving to me many examples and even repeating explanations in order to make sure I understand.

Even without being directly involved to my projects, there are people who ended up being close collaborators for me. Manoj and Ambresh, thank you very much for introducing to me the ideas of 2-loop calculations. Thank you for our physics-Saturdays, where I have realised many concepts on higher order corrections. Ambresh, thank you for having the patience to discuss and give me feedback on my Thesis introduction, while I was writing it. Manoj, thank you for our discussions on the multiplicative approach, helping me understand in depth these ideas. Thank you both very much for having the patience to discuss with me in detail all the topics of my private defence.

Apart from my close collaborators, there are other people within the institute, with whom I had very interesting physics discussions. I would like to thank Ken for many clarifications on the EFT framework and our discussions on the 'nasty' $O_G$. I would like to thank David for all the discussions we had during the informal pheno meetings. I would like also to thank Federico, for our discussions on PYTHIA8, for helping me on the bureaucracy concerning the Thesis and for sharing with me his Thesis template.

Slightly deviating from the academic part, I would like to thank Ambresh, Manoj, Alessia and Claudio for making me realise in which city I was leaving for the last four years. Thank you for our dinners and the funny moments we shared.

Finally I would like to thank Ginette and Carinne for providing the best possible support on every aspect concerning CP3, Jerome and Pavel for constantly supporting the computing part and the whole institute for providing an ideal environment for scientific research.

This work has been supported by the Fonds de la Recherche Scientique (FNRS) through an Aspirant Research Fellowship, in part by the Belgian Federal Science Policy Office through the Inter-university Attraction Pole P7/37 and in part by the ERC grant 291377 "LHCtheory: Theoretical predictions and analyses of LHC physics: advancing the precision frontier".

# Abstract

My research focuses on top-quark physics. The top quark is the heaviest elementary particle known to date. The top-quark mass is at the same order with the vacuum expectation value of the Higgs boson. Furthermore, despite the fact that it is a quark, it can be studied as a freely propagating particle. These properties have remarkable consequences, which provide enough motivation for detailed studies. The aim of my work is to perform such studies, as briefly described below, at the highest possible level of accuracy and precision in order to fully exploit the experimental information.

The first part of this study is concentrated on the $t\bar{t}$ production at the LHC. On the QCD part, inclusive and differential cross sections are already calculated up to NNLO accuracy. At this level of accuracy effects due to Electro-Weak (EW) corrections cannot be neglected, especially for differential distributions, where the physical hierarchy between the strong and electroweak interactions may not be respected. On the one hand, when large scales are probed ($Q \gg m_W$), the so-called Sudakov logarithms render EW corrections large and negative. On the other hand, EW corrections receive also contributions from channels that feature photons in the initial state, thus they depend on the PDF of the photon. In order to examine these effects, a study at NLO QCD+EW accuracy is performed for both 8 and 13 TeV. Furthermore I proceed to the combination of NNLO QCD + NLO EW results in order to provide the best predictions for $t\bar{t}$ distributions at 13 TeV. Different combination approaches are compared to each other and in all cases the latest available PDF sets, which include the photon PDF, are used. The effect of the Heavy Boson Radiation (HBR) is studied, but is not included in the prediction for the $t\bar{t}$ distributions, since these emissions are resolved and considered to be different processes. The second part of this study is focused on these processes.

By studying the top quark pair production in association with a vector or a Higgs boson, one is naturally probing important features related to the top quark. The different effect of the $t\bar{t}V(V = W^{\pm}, Z, \gamma)$ processes on the $t\bar{t}$ asymmetry, which is a NLO QCD effect, is studied. The $t\bar{t}H$ production is analysed as a tree level probe of the top Yukawa, the value of which is a still untested prediction of Standard Model Higgs boson sector. The $t\bar{t}V$ processes have been seen already at 8 TeV by the CMS, ATLAS collaborations. The current 13 TeV Run of the CERN collider will improve the statistics and will allow for detailed comparisons between experiment and theoretical predictions. Furthermore, the particle multiplicity is increased by considering $t\bar{t}VV$ and $t\bar{t}t\bar{t}$ production. These rare Standard Model processes in addition with the

$t\bar{t}V$ constitute the full irreducible background of $t\bar{t}H$. They are all studied in a realistic 13 TeV analysis, including detector limitations and experimental selection cuts, providing results in different final state signal regions.

The third part of this research is focused on Beyond the Standard Model (BSM) scenarios using the Effective Field Theory (EFT) approach. On the BSM part the Standard Model Effective Field Theory (SMEFT) approach has been adopted and calculations are performed at NLO in QCD. The EW top quark couplings, appearing in $t\bar{t}V$ processes, and possible deviations from the Standard Model are explored via the EFT approach. The global and differential effects of the CP-even EFT operators, entering the top-quark couplings, in the processes $t\bar{t}Z$, $t\bar{t}\gamma$ are studied and the results are available to be compared with the 8 TeV available experimental data.

# Contents

# 1 Introduction

During the last century, the level of understanding of the basic structure of nature has increased significantly. The community of high energy physics has been trying to identify the elementary constituents of matter as well as the forces responsible for their interactions. The rapid technological advancement of the last 40 years provided the opportunity to experimental collaborations to develop accelerators and detectors, in order to study the behaviour of nature at high energies. This advancement created the groundwork for testing many theories and revealing many pieces of the puzzle of the behaviour of elementary particles.

The current understanding of high energy physics indicates that there are four fundamental forces acting on matter. Their relative strength differs by many orders of magnitude and they do not all act upon all the matter. In table 1.1 one can see the details of the properties of the known forces. Moving from left to right in table 1.1 the interactions become weaker ending up to Gravity, which is normally ignored in short distance high energy physics. On the other hand, in large scale distances Gravity is the dominant force. The theory of General Relativity (GR) provides the mathematical framework describing Gravity as a result of the curvature of spacetime. The latter is encapsulated in the metric tensor. Contrary to the frameworks describing the other three forces, GR is not directly connected or based to an internal symmetry, rather than to the concept of invariance of the properties of spacetime, which dictates the invariance of the form of the laws of physics under coordinate transformations. In a case by case basis one has to look for symmetries which depend on the given metric tensor. However the absence of curvature, described by a flat (Minkowski) metric tensor, leads to a very well studied symmetry of spacetime: the symmetry of the Poincaré group. This includes the Lorentz transformations and the translations, and is described in section 1.2. Moreover the GR

| | Strong | Electromagnetic | Weak | Gravity |
|---|---|---|---|---|
| Current theory | QCD | QED (part of EW) | Weak (part of EW) | GR |
| Charge | color | electric charge | flavor | Energy |
| Acts on | quarks, gluons | charged particles | quarks, leptons | all |
| Strength | 1 | $10^{-2}$ | $10^{-5}$ | $10^{-39}$ |
| Mediators | Gluons | photon | $W^{\pm}$, $Z$ bosons | Graviton (?) |
| Mediator mass | 0 | 0 | $\sim 80$, $\sim 91$ GeV | 0 |
| Mediator spin | 1 | 1 | 1 | 2 |
| Range (fm) | 1 | $\infty$ | $10^{-3}$ | $\infty$ |

Table 1.1: Properties of fundamental forces.

framework is a classical field theory, i.e. fully deterministic if having the initial conditions. This is not the case for the other three frameworks shown in table 1.1. They are based on quantum field theory, i.e. they provide probabilistic predictions. Furthermore as mathematical descriptions, they are direct consequences of internal symmetries. These differences already reveal one of the open questions in high energy physics, which is the fact that there is no common ground for a unique description of small and large distance scale physics. In this work, the focus is laid in the short distance scale physics.

Experimentally the short distance scale physics is studied at the particle colliders. During the last 30 years the particle accelerator history started with the Large Electron-Positron (LEP) collider, which was an electron-positron circular collider operating at CERN during 1989-2000 at 91 and 209 GeV. At LEP the masses of the $Z, W$ bosons were precisely determined and a lower limit on the mass of the Higgs boson at 115 GeV [1]. At DESY the Hadron-Electron Ring Accelerator (HERA), which was running during 1992-2007 at 318 GeV, provided crucial information on the structure of the proton, which was probed by high energy electrons. During 1987-2011 at Fermilab, the Tevatron was a fully hadronic accelerator, colliding protons with antiprotons at 1.8 and 1.96 TeV. The Tevatron was hosting two large experimental collaborations, CDF and D0. The major discovery of the Tevatron is that of the top quark (details in section 1.4). Furthermore it constrained the mass of the Higgs boson in the region $115 \leq m_H \leq 135$ GeV [2,3]. The most recent one, which is also currently

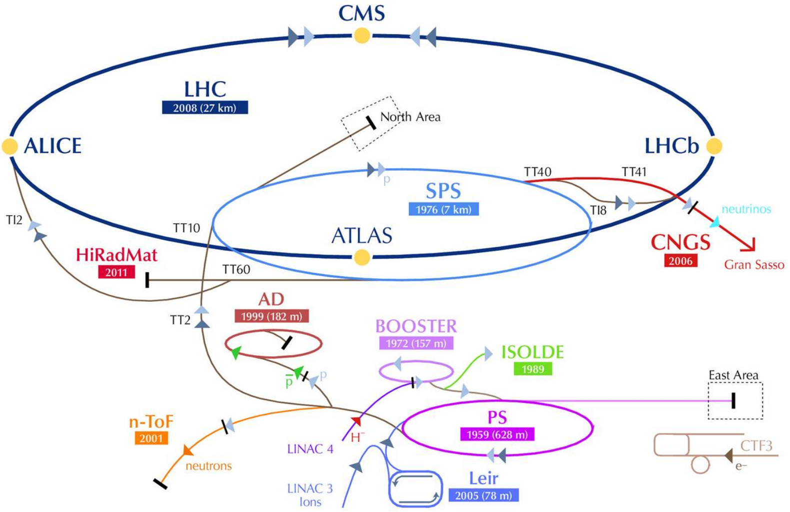

Figure 1.1: The Large Hadron Collider

operating is the Large Hadron Collider (LHC) at CERN (fig. 1.1). The LHC is a proton-proton collider mostly operated at 7,8 and now 13 TeV. The LHC collider consists of 4 main detectors, the ATLAS, the CMS, the LHCb and the ALICE. At the LHC, precision physics takes place systematically for numerous processes and the major discovery so far is the Higgs boson at $\sim 125$ GeV [4,5]. All the aforementioned experiments are being developed, in order to test the theoretical model describing the elementary particles and their interactions, i.e. the first three frameworks listed in table 1.1. This thesis focuses on specific parts of this theoretical description and searches for possible windows, where new physics may appear. The mathematical model, which describes the Strong, Electromagnetic and Weak interactions is the Standard Model of physics (SM) and is described in section 1.2. More specifically this project discusses the physics around the top quark, which is introduced in section 1.4. Before this, we will start by explaining the structure of this thesis in the following section 1.1.

## 1.1 Structure of this thesis

Chapter 1 is dedicated to introducing the reader to, and motivate, the main subject. Before entering the projects in detail, which constitute this thesis, an introduction to the Standard Model is provided. Section 1.2 addresses the questions on the general structure of the Standard Model, the mathematical constructive part as well as the physical implications. In section 1.3 we move from the Lagrangian level to the actual calculational framework at the level of the observables. Section 1.4 focuses on the features of the top quark, which have a special importance in the physics related to it. The introduction is concluded with section 1.5, where Effective Field Theory (EFT) is presented and motivated as a model independent approach to physics beyond the SM.

Chapters 2, 3 and 4, present and discuss the results of this research. Since in each chapter there is a detailed introduction and in order to avoid repetition, this paragraph provides a brief sketch of the main part of the thesis in order to guide the reader to what to expect. Chapter 2 focuses on the SM, looking at high precision the $t\bar{t}$ production. It is divided in two parts. The first part focuses on differential distributions at NLO QCD+EW accuracy. The phase space regions, where the EW corrections and especially the effect of the photon-induced contributions become important are identified. Different PDF sets (NNPDF2.3QED, CT14QED) including the photon PDF are compared in detail at 13 TeV. Furthermore, using the available 8 TeV data, a comparison between theory and experiment is performed at differential level and part of the results is extrapolated for a future 100 TeV collider. The presence of NNLO

QCD results for $t\bar{t}$ distributions reduces significantly the scale uncertainties on these observables. The second part is motivated by the latter and aims to provide predictions at NNLO QCD + NLO EW accuracy, for $t\bar{t}$ distributions at 13 TeV. The latest available PDF sets (NNPDF3.0QED, LUXQED) are compared and different approaches for the combination of the QCD and EW corrections are studied. Chapter 3 focuses on the top pair production in association with one, two vector bosons or another top pair. The study is realised at NLO in QCD for all these processes. These processes are irreducible backgrounds for the $t\bar{t}H$ production. The latter is included in the study as a direct probe of the top Yukawa coupling. In the first part of this work a Fixed NLO calculation provides predictions at the cross section and differential level, comparing different definitions of the renormalisation and factorisation scales. Part of these results are extrapolated to a future collider of 100 TeV. In the second part a realistic analysis takes place at NLO in QCD including the decays and matching to parton shower. Considering the $t\bar{t}H$ as the signal and the other processes as backgrounds, predictions at cross section level are given for different signal regions according to lepton multiplicity. In chapter 4 the focus is on $t\bar{t}Z, t\bar{t}\gamma$. Within the EFT framework this BSM study includes the full set of dimension-six operators that enter the interactions between the top quark and the neutral SM gauge bosons. Cross section and differential level predictions are provided for each operator for the interference ($1/\Lambda^2$) and the squared ($1/\Lambda^4$) terms, as being different perturbative orders in the EFT expansion. We have also considered the effects of a subset of these operators, which affects the loop-induced process $gg \to HZ$. Furthermore we have studied the $t\bar{t}$ production at the ILC as being sensitive to the weak dipole operators and therefore complementary to the LHC. Finally, expecting the new LHC measurements, the sensitivity of these processes to this set of operators is studied.

All the results presented in this thesis are public and produced in collaboration with groups who will be mentioned explicitly in each chapter. What follows is a list of the publications emerged by this 4-year research.

Published papers:

- F. Maltoni, M. L. Mangano, I. Tsinikos and M. Zaro, *Top-quark charge asymmetry and polarization in $t\bar{t}W$ production at the LHC*, Phys. Lett. B **736**, 252 (2014), `arXiv:1406.3262 [hep-ph]` [6]

- F. Maltoni, D. Pagani and I. Tsinikos, *Associated production of a top-quark pair with vector bosons at NLO in QCD: impact on* $\mathrm{t\bar{t}H}$ *searches at the LHC*, JHEP **1602**, 113 (2016), `arXiv:1507.05640 [hep-ph]` [7]

- O. Bessidskaia Bylund, F. Maltoni, I. Tsinikos, E. Vryonidou and C. Zhang, *Probing top quark neutral couplings in the Standard Model Effective Field Theory at NLO in QCD*, JHEP **1605**, 052 (2016), `arXiv:1601.08193 [hep-ph]` [8]
- D. Pagani, I. Tsinikos and M. Zaro, *The impact of the photon PDF and electroweak corrections on $t\bar{t}$ distributions*, Eur. Phys. J. C **76**, no. 9, 479 (2016), `arXiv:1606.01915 [hep-ph]` [9]
- M. Czakon, D. Heymes, A. Mitov, D. Pagani, I. Tsinikos and M. Zaro, *Top-pair production at the LHC through NNLO QCD and NLO EW*, submitted to JHEP, `arXiv:1705.04105 [hep-ph]` [10]

Contributions on specific sections in reports:

- M. L. Mangano *et al.*, *Physics at a 100 TeV pp collider: Standard Model processes (chapter 13)* , `arXiv:1607.01831 [hep-ph]` [11, ch. 13]
- D. de Florian *et al.*, *Handbook of LHC Higgs Cross Sections: 4. Deciphering the Nature of the Higgs Sector (section I.6.7)*, `arXiv:1610.07922 [hep-ph]` [12, sec. I.6.7]

Contributions to conference proceedings:

- I. Tsinikos, *EW corrections to $t\bar{t}$ distributions: the photon PDF effect*, Top2016 conference, `arXiv:1611.08234 [hep-ph]` [13]

## 1.2 The Standard Model

The interactions between the fundamental particles, ignoring the curvature of space-time, are described by the Standard Model (SM). The aim of this section is a brief sketch of the structure of the SM. There are numerous textbooks and papers introducing the Quantum Field Theory (QFT) approach and the SM. The books used for this section are [14] and [15]. This mathematical model uses the Lagrangian formalism and is based on the concept of symmetry. The symmetries of the Standard Model are described within the framework of group theory. As mentioned in the beginning of chapter 1 the absence of gravity introduces the Poincaré symmetry. On top of that, using the $SU(2)_L$, $U(1)_Q$ and $SU(3)_C$ symmetries, one can describe the weak, electromagnetic and strong forces respectively. Before going through the details on these symmetries and their effects, we will proceed with a general presentation of the particles entering the SM. The fundamental fields, appearing in the model, can have bosonic or fermionic nature. All the particles of the Standard model (fig.

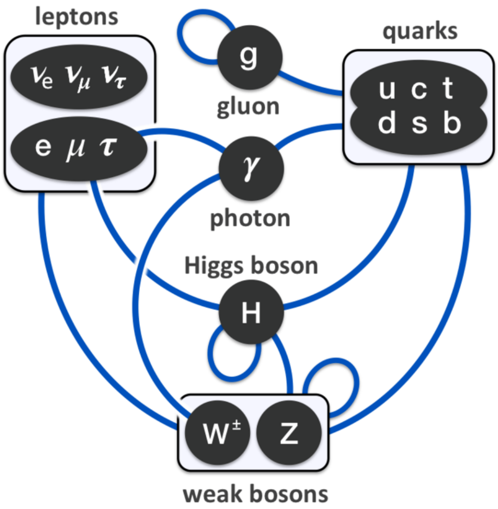

Figure 1.2: The Standard model of physics. Image taken from [16].

1.2) are excited forms (quanta) of the fields. The fermionic particles form the matter and have spin $\frac{1}{2}$. They are divided into two types: leptons and quarks. The charged leptons $(e^-, \mu^-, \tau^-)$ interact with the electromagnetic and weak forces. The neutral leptons $(\nu_e, \nu_\mu, \nu_\tau)$ interact only weakly. The quarks, on the other hand, are charged and interact with all three forces. The force carriers are bosonic particles (gauge bosons) with spin 1. The photon $(\gamma)$ is responsible for the electromagnetic interaction, the $W^+$, $W^-$, $Z^0$ are the carriers of the weak force and the gluons $(g)$ of the strong force (table 1.1). Both leptons and quarks form (right handed singlets, left handed isospin doublets) the three generations of matter (table 1.2). The Weak force acts only on the left handed

| | 1st Generation | 2nd Generation | 3rd Generation |
|---|---|---|---|
| Quarks | $\begin{pmatrix} u \\ d \end{pmatrix}_L, u_R, d_R$ | $\begin{pmatrix} c \\ s \end{pmatrix}_L, c_R, s_R$ | $\begin{pmatrix} t \\ b \end{pmatrix}_L, t_R, b_R$ |
| Leptons | $\begin{pmatrix} \nu_e \\ e^- \end{pmatrix}_L, e^-_R$ | $\begin{pmatrix} \nu_\mu \\ \mu^- \end{pmatrix}_L, \mu^-_R$ | $\begin{pmatrix} \nu_\tau \\ \tau^- \end{pmatrix}_L, \tau^-_R$ |

Table 1.2: Generations of fermions.

isospin doublets. The puzzle is complete with the Higgs boson ($H$), a spin 0 particle. The weak and electromagnetic interactions are described in a unified way by the electroweak (EW) theory and the strong interactions are described by quantum chromodynamics (QCD). The Higgs boson results from the EW symmetry breaking mechanism, which provides masses to itself, weak vector bosons and the fermions. In the following we shall see how the concept of symmetry gives rise to the gauge bosons and describes their interactions.

### 1.2.1 Fields and spacetime

The spacetime in which the Standard Model 'lives' is flat and described by the Minkowski metric $\eta_{\mu\nu} \equiv diag(1,-1,-1,-1)$. The isotropy of the Minkowski spacetime gives rise to invariance under boosts and rotations, which are the six generators of the Lorentz group. The homogeneity of this metric is connected to the translational invariance described by the four spacetime translation generators. These two subgroups form the Poincaré group. A spacetime point $x$ transforms under this group as $x' = \Lambda x + a$ or in detail as

$$x'^{\mu} = \Lambda^{\mu}{}_{\nu} x^{\nu} + a^{\mu} \ . \tag{1.1}$$

A rotation of an infinitesimal angle $\phi$ around an $i$-axis is given by $\Lambda_R = e^{-i\phi J^i} \overset{\text{inf.}}{\approx} \mathbb{1} - i\phi J^i$. Similarly a boost of infinitesimal rapidity $\zeta$ along an $i$-axis is given by $\Lambda_B = e^{-i\zeta K^i} \overset{\text{inf.}}{\approx} \mathbb{1} - i\zeta K^i$. In both cases $i = 1,2,3$ and the $J^i$'s, $K^i$'s are defined as the six generators of the Lorentz subgroup. Translations are described by the term $a^{\mu}$ in equation 1.1. A translation of infinitesimal length $\epsilon$ in spacetime is given by $T = e^{-i\epsilon_{\nu}P^{\nu}} \overset{\text{inf.}}{\approx} \mathbb{1} - i\epsilon_{\nu}P^{\nu}$, where now $\nu = 0,1,2,3$. The four $P^{\nu}$'s are the generators of translations. A general Poincaré transformation is given by

$$(\Lambda\{\phi_{\hat{\mathbf{n}}}, \zeta_{\hat{\mathbf{m}}}\}|a) = e^{-i\phi\hat{\mathbf{n}}\cdot\mathbf{J}} e^{-i\zeta\hat{\mathbf{m}}\cdot\mathbf{K}} e^{-ia_{\nu}P^{\nu}} \ . \tag{1.2}$$

The generator $P^0$ corresponds to time translation and therefore has a special meaning. It is usually denoted as the Hamiltonian $H$ and is separated from the other spatial translation generators $P^i$. The commutation relations between these ten generators form the Lie algebra of the group, which is shown in the following equation

$$\begin{aligned}
&[P^i, P^j] = [P^i, H] = [J^i, H] = 0 \ , \\
&[J^i, J^j] = i\epsilon^{ijk} J^k \ , \ [J^i, P^j] = i\epsilon^{ijk} P^k \ , \ [J^i, K^j] = i\epsilon^{ijk} K^k \ , \\
&[K^i, H] = iP^i \ , \ [K^i, K^j] = -i\epsilon^{ijk} J^k \ , \ [K^i, P^j] = i\delta^{ij} H \ .
\end{aligned} \tag{1.3}$$

Since the Poincaré group is related to spacetime, its generators can be visualised and therefore the physical meaning is understood. The concept of rotation, boost and translation of a vector $\delta x^\mu \equiv x'^\mu - x^\mu$ is self explanatory for what stands behind these objects. The corresponding Lie algebra has also a physical meaning, which is not as obvious as its constituents. Mathematically it shows whether the order upon which the operators act on an object matters or not. Quantum mechanically the commutator is interpreted as quantifying the (in-) compatibility of (non-)commuting operators, i.e. the potentiality of knowing simultaneously the corresponding physical values. It further expresses how the change of the system by one operator is affected by the others. This is why the $P^0 \equiv H$ has a special significance. Since it expresses the time evolution, if an operator commutes with the $H$, it means that, being time independent, it is connected to a conserved physical quantity. The first line of equation 1.3 shows the momentum and angular momentum conservation. The commutative part of the Lie algebra is called Abelian. If the whole Lie algebra is commutative then the symmetry is Abelian. This property has important consequences for internal symmetries as we will see in sections 1.2.2 and 1.2.3.

But what does one mean exactly by saying 'transformation' or 'invariance' under the Poincaré group? If we assume a scalar field $\phi(x)$ and perform a transformation of our coordinates to $x' = (\Lambda|a)x = \Lambda x + a$, a new $\phi'(x')$ will emerge. Being invariant under this transformation implies that $\phi'(x') = \phi(x)$. However if we consider a vector field $V^\mu(x)$ and perform the same transformation $x \to x'$ the new $V'^\mu(x')$ will be $V'^\mu(x') \neq V^\mu(x)$. This seems inconsistent if one conceives the vector as a collection of four scalars. How is it possible that a scalar is invariant under a transformation but a collection of scalars is not? The reason is that the vector field includes also the notion of direction and length which are the ones that change. Therefore in order to retain the initial vector, $V^\mu(x)$ has to transform on top of $x$ and we get $V^\mu(x) = \Lambda^\mu{}_\nu V'^\nu(x')$. In this sense, vectors, tensors and spinors are considered Poincaré covariants whereas scalars are Poincaré invariants. The Lagrangian itself is a scalar as a functional of the fields and their first order derivatives. Therefore every term in $\mathcal{L}[\phi(x), \partial^\mu\phi(x), V_\mu(x), \partial^\mu V_\mu(x), \psi(x), \partial^\mu\psi(x)]$ is also Poincaré invariant.

### 1.2.2 The Abelian QED

The more symmetries we impose to a Lagrangian the more restricted it becomes. In section 1.2.1 we have embedded the fields in a Minkowski spacetime, but we did not study their interactions. They are described by imposing further internal symmetries to the Lagrangian. In this section we start with the QED description. Let us consider the Lagrangian which describes a free spin 1/2 dirac particle of mass $m$. It is

$$\mathcal{L}^{free}_{\mathrm{D}irac} = \bar{\psi}(x)[i\gamma_\mu\partial^\mu - m]\psi(x)\ . \qquad (1.4)$$

This Lagrangian is invariant under global $U(1)$ transformations, i.e. under $\psi' \to e^{iqa}\psi, \bar{\psi}' \to e^{-iqa}\bar{\psi}$. However if we make the phase local ($a \to a(x)$) this is no longer true. By applying this transformation we get

$$\mathcal{L}^{free}_{\mathrm{D}irac}{}' = L^{\mathrm{free}}_{\mathrm{D}irac} + q\bar{\psi}(x)\gamma_\mu\partial^\mu a(x)\psi(x)\ . \tag{1.5}$$

At first sight this extra term looks like an interaction term between the spinors $\bar{\psi}(x), \psi(x)$ and the vectorial object $\partial^\mu a(x)$. As long as the internal $U(1)$ symmetry is global, it is disconnected from the Poincaré symmetry ($\partial^\mu a = 0$). Once we force the $U(1)$ to be local it picks up the spacetime information, but the derivative $\partial^\mu$ still does not include the infinitesimal displacement of $\psi(x)$ in the internal $U(1)$ space. This is what this term stands for. $U(1)$ is an 1-dimensional internal space, therefore has one generator. If we want to be consistent, this generator needs also to be included in this local transformation, being an indirect part of this same Lagrangian. Had we included this transformation from the beginning, we would have got an invariant Lagrangian. Keeping the vectorial form of $\partial^\mu a(x)$, let us express this term as exactly this difference that we seem to miss in the following

$$\partial^\mu a(x) = A^\mu{}'(x) - A^\mu(x)\ , \tag{1.6}$$

where $A^\mu$ is an arbitrary vector field and substitute this expression to equation 1.5. We get

$$\begin{aligned}\mathcal{L}^{free}_{\mathrm{D}irac}{}' &= L^{\mathrm{free}}_{\mathrm{D}irac} + q\bar{\psi}(x)\gamma_\mu[A^\mu{}'(x) - A^\mu(x)]\psi(x) \Rightarrow \\ \Rightarrow \mathcal{L}^{\mathrm{free}}_{\mathrm{D}irac}{}' - q\bar{\psi}(x)\gamma_\mu A^\mu{}'(x)\psi(x) &= \mathcal{L}^{free}_{\mathrm{D}irac} - q\bar{\psi}(x)\gamma_\mu A^\mu(x)\psi(x)\ .\end{aligned} \tag{1.7}$$

However,

$$\begin{aligned}q\bar{\psi}(x)\gamma_\mu A^\mu{}'(x)\psi(x) &= q\bar{\psi}(x)e^{-iqa(x)}\gamma_\mu A^\mu{}'(x)e^{iqa(x)}\psi(x) = \\ =&q\bar{\psi}'(x)\gamma_\mu A^\mu{}'(x)\psi'(x) = [q\bar{\psi}(x)\gamma_\mu A^\mu(x)\psi(x)]'\ .\end{aligned} \tag{1.8}$$

Therefore the $U(1)$ locally invariant Lagrangian becomes

$$\begin{aligned}\mathcal{L}_{\mathrm{D}irac} &= \bar{\psi}(x)[i\gamma_\mu\partial^\mu - m]\psi(x) - q\bar{\psi}(x)\gamma_\mu A^\mu(x)\psi(x) = \\ &= \bar{\psi}(x)i\gamma_\mu\partial^\mu\psi(x) - q\bar{\psi}(x)\gamma_\mu A^\mu(x)\psi(x) - m\bar{\psi}(x)\psi(x) = \\ &= \bar{\psi}(x)[i\gamma_\mu\partial^\mu - q\gamma_\mu A^\mu(x)]\psi(x) - m\bar{\psi}(x)\psi(x) \Rightarrow \\ \Rightarrow \mathcal{L}_{\mathrm{D}irac} &= \bar{\psi}(x)i\gamma_\mu D^\mu\psi(x) - m\bar{\psi}(x)\psi(x)\ , D^\mu \equiv \partial^\mu - iqA^\mu(x)\ .\end{aligned} \tag{1.9}$$

Looking at what is done from equation 1.4 to equation 1.9 we had to introduce the vector field $A^\mu$, which is called gauge field, in order to correctly describe an invariant spin-1/2 Lagrangian under Poincaré and local $U(1)$ symmetries.

We resulted with a new interaction term between $\bar{\psi}(x), \psi(x), A^\mu$ and furthermore we already now that $A^\mu$ transforms according to equation 1.6. One could directly go from equation 1.4 to 1.9 by substituting $\partial^\mu$ with $D^\mu$. The latter is defined as the covariant derivative. The covariant derivative describes the full infinitesimal translation of the spinor field $\psi(x)$ in both the actual spacetime and the internal 1-dimensional $U(1)$ space. This second part of the covariant derivative together with the equation 1.6 are defined as the gauge transformation. The new vector field is the photon and the parameter $q$ is the charge of the fermion. Since the field $A^\mu$ is introduced, any related term allowed by the symmetries needs to be added to the Lagrangian. The same way that there is an $\mathcal{L}^{free}_{\mathrm{D}irac}$ there should be an $\mathcal{L}^{free}_{\mathrm{p}hoton}$ describing the kinetic and possible self energy photon terms. This can be constructed by the electromagnetic field strength tensor, which can be expressed by the aforementioned covariant derivative. The full $U(1)$ locally invariant Lagrangian, which describes QED is

$$\mathcal{L}_{QED} = -\frac{1}{4}F^{\mu\nu}F_{\mu\nu}+\bar{\psi}(x)[i\gamma_\mu D^\mu - m]\psi(x)\ , F_{\mu\nu} = \frac{i}{q}[D_\mu, D_\nu] = \partial_\mu A_\nu - \partial_\nu A_\mu \ . \tag{1.10}$$

The symmetry $U(1)$ having only one generator is trivially Abelian. This is depicted to the Lagrangian of equation 1.10 to the fact that there are no self interaction terms for the photons, but only kinetic terms. Any self interaction term would come from the $\mathcal{L}^{free}_{\mathrm{p}hoton}$ part of the Lagrangian. In order to see this one can expand the $F_{\mu\nu}$ in equation 1.10 acting on a $\psi(x)$ field. It is

$$\begin{aligned}
[D_\mu, D_\nu]\psi(x) &= [\partial^\mu - iqA^\mu(x), \partial^\nu - iqA^\nu(x)]\psi(x) = \\
&= \{[\partial^\mu, \partial^\nu] - iq[\partial^\mu, A^\nu(x)] - iq[\partial^\nu, A^\mu(x)] - q^2[A^\mu(x), A^\nu(x)]\}\psi(x) = \\
&= \{-iq[\partial^\mu A^\nu(x) - \partial^\nu A^\mu(x)] - q^2\cancelto{0}{[A^\mu(x), A^\nu(x)]}\}\psi(x)
\end{aligned} \tag{1.11}$$

This last term being zero in equation 1.11 is a consequence of the fact that the symmetry is Abelian. As we will see in the following section, if this is not the case, this term gives rise to self interaction terms for the gauge bosons. It is interesting also to notice that a mass term of the form $\frac{1}{2}m_A^2 A^\mu A_\mu$ would not be gauge invariant, but for now this is not an issue since photons are massless. On the other hand a fermion mass term is allowed. Furthermore the fermion mass term mixes the right and left handed part of the spinor. It is

$$\begin{aligned}
\bar{\psi}[i\gamma_\mu D^\mu - m]\psi &= (\bar{\psi}_L + \bar{\psi}_R)i\gamma_\mu D^\mu(\psi_L + \psi_R) - (\bar{\psi}_L + \bar{\psi}_R)m(\psi_L + \psi_R) \\
&= \bar{\psi}_L i\gamma_\mu D^\mu \psi_L + \bar{\psi}_R i\gamma_\mu D^\mu \psi_R - m(\bar{\psi}_L\psi_R + \bar{\psi}_R\psi_L)
\end{aligned} \tag{1.12}$$

The $U(1)$ symmetry acts the same way on the left and right handed spinors, therefore the mass term is allowed. Each time a symmetry is imposed in a

Lagrangian, every term must be invariant (singlet) under this symmetry and also has to be chargeless under the corresponding charge.

### 1.2.3 The non Abelian QCD

The interactions due to the QCD are described by requiring an $SU(3)$ invariant Lagrangian. Starting again from the free Dirac Lagrangian of equation 1.4 one can now ask for a local $SU(3)$ symmetry. This symmetry has 8 generators and as a result the transformation of the fermion field will now be $\psi'(x) \to e^{ig_s a^b(x)\tau^b}\psi(x), \bar{\psi}'(x) \to e^{-ig_s a^b(x)\tau^b}\bar{\psi}(x), b = 1, ..., 8$. The $\tau^b$ 's are hermitian $3 \times 3$ matrices and they are the generators of the symmetry. Furthermore it is non Abelian. The Lie algebra of $SU(3)$ reads

$$[\tau^a, \tau^b] = if^{abc}\tau^c \ , \tag{1.13}$$

where the $f^{abc}$ are the fully antisymmetric structure constants and the $\lambda^a = \tau^a/2$ are the Gell-Mann matrices. Following the same procedure as in the previous section we can now define the covariant derivative as

$$D^\mu = \partial^\mu - ig_s\tau^b G^{b\mu}, \tag{1.14}$$

where the $G^\mu$'s play the role of the previous $A^\mu$ and they are as much as the generators of the $SU(3)$ internal space, in order to describe a full infinitesimal translation in this space. Defining the $G^{\mu\nu}$ as the gluon field strength and writing down the QCD equivalent of equation 1.10, we get

$$\mathcal{L}_{QCD} = -\frac{1}{4}G^{a\mu\nu}G^a_{\mu\nu} + \bar{\psi}(x)[i\gamma_\mu D^\mu - m]\psi(x) \ , \tau^a G^a_{\mu\nu} = \frac{i}{g_s}[D_\mu, D_\nu] \ . \tag{1.15}$$

At the first sight this looks the same like equation 1.10, but the main difference lies into the new field strength. Evaluating it we get

$$\begin{aligned}
[D_\mu,&D_\nu]\psi(x) = [\partial^\mu - ig_s\tau^b G^{b\mu}, \partial^\nu - ig_s\tau^b G^{b\nu}]\psi(x) = \\
&= \{[\partial^\mu, \partial^\nu] - ig_s[\partial^\mu, \tau^b G^{b\nu}] - ig_s[\partial^\nu, \tau^b G^{b\mu}] - g_s^2[\tau^b G^{b\mu}, \tau^b G^{b\nu}]\}\psi(x) = \\
&= \{-ig_s\tau^b[\partial^\mu G^{b\nu} - \partial^\nu G^{b\mu}] - g_s^2[\tau^a G^{a\mu}, \tau^b G^{b\nu}]\}\psi(x) = \\
&= \{-ig_s\tau^b[\partial^\mu G^{b\nu} - \partial^\nu G^{b\mu}] - g_s^2[\tau^a, \tau^b]G^{a\mu}G^{b\nu}\}\psi(x) \overset{1.13}{=} \\
&= \{-ig_s\tau^b[\partial^\mu G^{b\nu} - \partial^\nu G^{b\mu}] - ig_s^2 f^{abc}\tau^c G^{a\mu}G^{b\nu}\}\psi(x) \ .
\end{aligned} \tag{1.16}$$

The last term in equation 1.16, which is non zero due to the non Abelian nature of $SU(3)$, is the one that, through the first term of equation 1.15, gives rise to 3- and 4-point gluon interaction vertices. The charge of the symmetry is defined as colour and it takes three values: red, green, blue. Therefore every $\psi(x)$

is a triplet of colour charged Dirac spinors $\psi(x) = (\psi_r(x), \psi_g(x), \psi_b(x))$. The self interaction gluon terms are in agreement with the fact that the gluons are also coloured, in contrast to the chargeless photons of QED. Furthermore, similarly to the QED case, a fermion mass term is allowed since the $\psi_L(x), \psi_R(x)$ transform the same way under $SU(3)$.

### 1.2.4 The EW theory

In sections 1.2.2, 1.2.3 we pointed out the differences between an Abelian and a non Abelian symmetry and their implications to the corresponding theories. The Weak interactions could be partially described like the QCD ones by asking a Lagrangian with the $SU(2)$ symmetry. The $SU(2)$ symmetry has 3 generators and the Lie Algebra is

$$[\tau^a, \tau^b] = i\varepsilon^{abc}\tau^c \ , \tag{1.17}$$

where $\varepsilon^{abc}$ is the fully antisymmetric Levi-Civita and $\sigma^i = \tau^i/2$ are the $2 \times 2$ Pauli matrices. Defining the $W^{\mu\nu}$, $W^\mu$ as the Weak field strength and the gauge bosons respectively one can write down the following $SU(2)$ invariant Lagrangian

$$\mathcal{L}_{\mathrm{W}eak} = -\frac{1}{4}W^{a\mu\nu}W^a_{\mu\nu}+\bar{\psi}(x)[i\gamma_\mu D^\mu - m]\psi(x) \ , \tau^a W^a_{\mu\nu} = \frac{i}{g_w}[D_\mu, D_\nu] \ , \tag{1.18}$$

where $D^\mu$ is defined in an analogous way with the equation 1.14 as $D^\mu = \partial^\mu - ig_w\tau^b W^{b\mu}, b = 1, 2, 3$. This Lagrangian predicts the existence of three electrically neutral gauge bosons $(W^\mu_1, W^\mu_2, W^\mu_3)$. One can use the non diagonal pauli matrices $\tau_1, \tau_2$ in order to define the electrically charged ones $W^\pm = (W_1 \mp iW_2)\sqrt{2}$. This way one reproduces what the experiments suggest but with the abstraction of the mass for the gauge bosons. As stated in section 1.2.2, this formulation, Abelian or not, does not allow a gauge boson mass term since the Lagrangian would no longer be gauge invariant. A mass term would explicitly brake the symmetry. This is in contrast to what the experiments have shown, since the Weak vector bosons are all massive (table 1.1). This problem was addressed in 1964, by Peter Higgs, and independently by Robert Brout and Francois Englert by proposing the Spontaneous symmetry breaking process [17], known as BEH mechanism. It suggests that the existence of a massless theory based on a symmetry group can still allow massive terms if it acquires a non invariant ground state. We will see in the following how this mechanism is related to the unification of the Weak and Electromagnetic theories under the EW framework.

One can start with an $SU(2)_L \times U(1)_Y$ symmetry, where the $U(1)_Y$ is a $U(1)$ symmetry related to a new charge $Y$, which is defined as hypercharge and the $SU(2)_L$ symmetry acts only on doublets of left handed spinors. The charge corresponding to the $SU(2)_L$ is the Weak isospin. The $SU(2)_L \times U(1)_Y$ symmetric Lagrangian includes also a complex scalar doublet field (to which we will refer as the Higgs doublet) and is broken when the latter acquires a vacuum expectation value (vev). This doublet is defined as $\Phi = (\Phi^+, \Phi^0)$. This theory has three gauge bosons from the $SU(2)_L$ (the $W$'s) and one from the $U(1)_Y$ (the $B$) with couplings $g, g'$ respectively. The Higgs and gauge part of the Lagrangian before the symmetry breaking reads

$$\begin{aligned} \mathcal{L}^{\mathrm{H}iggs}_{Gauge,EW} &= -\frac{1}{4}(W^a_{\mu\nu})^2 - \frac{1}{4}B^{\mu\nu}B_{\mu\nu} + (D_\mu\Phi)^\dagger(D^\mu\Phi) + \mu^2\Phi^\dagger\Phi - \lambda(\Phi^\dagger\Phi)^2 \ , \\ D_\mu &= \partial_\mu - igW^a_\mu\tau^a - iYg'B_\mu \ . \end{aligned} \tag{1.19}$$

The vev should be electrically neutral and, including the fluctuations around it ($H(x)$), can be conveniently chosen as

$$\Phi = \frac{1}{\sqrt{2}}\begin{pmatrix} 0 \\ v + H(x) \end{pmatrix} . \tag{1.20}$$

This particular choice is defined as the unitary gauge and is the most convenient in order to give the physical interpretation. The new introduced real scalar field $H(x)$, is defined as the Higgs field and describes the perturbation around the value $v$ of the Higgs doublet vev. By substituting equation 1.20 to equation 1.19, we are entering the broken phase of the Lagrangian. The term $(D_\mu\Phi)^\dagger(D^\mu\Phi)$ will give interaction terms between the Higgs field and the gauge bosons, but also terms proportional to $v^2$, which will be mass terms for the gauge bosons. In particular it is

$$\mathcal{L}^{\mathrm{Gauge}}_{\mathrm{mass}} = \left[D_\mu \begin{pmatrix} 0 \\ v \end{pmatrix}\right]^2 = \frac{v^2}{8}[g^2(W^+_\mu)^2 + g^2(W^-_\mu)^2 + (g^2 + g'^2)Z^2_\mu]. \tag{1.21}$$

The $W^\pm$ mass terms appear after the substitution $W^\pm = (W^1 \mp iW^2)\sqrt{2}$ and the $Z$ mass term appears after the rotation/diagonalization of the fields $W^3, B$ to the fields $Z, A$ through the angle $\tan\theta_w = \dfrac{g'}{g}$. The masses of $W^\pm, Z$ are deduced from equation 1.21 as

$$m_W = \frac{1}{2}vg \ , \ m_Z = \frac{1}{2}v\sqrt{g^2 + g'^2} \ . \tag{1.22}$$

There is no corresponding mass term for the field $A$, which represents the residual $U(1)$ symmetry from this procedure. With this procedure we end up with three gauge bosons that break the symmetry via their mass terms ($W^\pm, Z$) and one massless gauge boson ($A$), which describes the new $U(1)_Q$, unbroken by the vacuum state.

It is interesting to notice that even the fermion mass term is forbidden from the symmetry in the unbroken phasse. The reason is that now the left and right handed spinors transform differently under the $SU(2)_L$. Therefore a mass term of the form of equation 1.12 explicitly breaks the $SU(2)_L$ symmetry. However, since $\Phi$ is also a Weak isospin doublet the left handed doublets and the right handed singlets are connected via interaction terms with the Higgs doublet. The fermionic part of the Lagrangian before the symmetry breaking is as follows

$$\begin{aligned}\mathcal{L}_{\mathrm{EW}}^{fermion} =& \bar{\psi}_L(x)[i\gamma_\mu D^\mu]\psi_L(x) + \bar{\psi}_R(x)[i\gamma_\mu D^\mu]\psi_R(x) - [Y_d\bar{\psi}_L(x)\Phi\psi_R(x)+ \\ &+ Y_u\bar{\psi}_L(x)\Phi_c\psi_R(x) + h.c.] \ ,\end{aligned} \tag{1.23}$$

where we have introduced the charge conjugate $\Phi_c$ of the $\Phi$ field and the Yukawa parameters of the down type quarks or leptons, and the up type quarks. In accordance to equation 1.20, the $\Phi_c$ acquires the corresponding vev+fluctuations

$$\Phi_c = \frac{1}{\sqrt{2}}\begin{pmatrix} v + H(x) \\ 0 \end{pmatrix} . \tag{1.24}$$

Another important remark on the fermionic Lagrangian is that, since the right handed fermions are $SU(2)_L$ singlets, they are not affected by the corresponding part of the covariant derivative. The covariant derivative is defined for the left and right handed fermions as follows

$$D_\mu\psi_L = (\partial_\mu - igW_\mu^a\tau^a - iYg'B_\mu)\psi_L \ , \ D_\mu\psi_R = (\partial_\mu - iYg'B_\mu)\psi_R \ . \tag{1.25}$$

Similarly to the bosonic case, in the broken phase, the Yukawa part of the fermionic Lagrangian will give rise the fermion mass terms and the interaction terms between fermions and the Higgs field. We illustrate this for the $\tau$ lepton in the following equation

$$\begin{aligned}\mathcal{L}_Y^\tau &= -\frac{Y_\tau}{\sqrt{2}}\left[(\bar{\nu}_\tau, \bar{\tau})_L\begin{pmatrix} 0 \\ v + H\end{pmatrix}\tau_R + \bar{\tau}_R(0, v + H)\begin{pmatrix}\nu_\tau \\ \tau\end{pmatrix}_L\right] = \\ &= -\frac{Y_\tau[v + H]}{\sqrt{2}}(\bar{\tau}_L\tau_R + \bar{\tau}_R\tau_L) = -\frac{Y_\tau[v + H]}{\sqrt{2}}\bar{\tau}\tau = -\frac{Y_\tau v}{\sqrt{2}}\bar{\tau}\tau - \frac{Y_\tau}{\sqrt{2}}H\bar{\tau}\tau \ .\end{aligned} \tag{1.26}$$

The Yukawa parameter is fixed by the mass term as $m_\tau = \frac{Y_\tau v}{\sqrt{2}}$, therefore the Yukawa coupling to the Higgs ($Y_\tau = \frac{\sqrt{2}m_\tau}{v}$) is proportional to this mass. This is true for all the massive fermions. For the leptons one can generalise this part of the Lagrangian including all the massive leptons. In that case it is

$$\mathcal{L}_Y^\ell = -\frac{Y_\ell^{ij}}{\sqrt{2}}\left[(\bar{\nu}_\ell, \bar{\ell})_L^i\begin{pmatrix} 0 \\ v + H\end{pmatrix}\ell_R^j + h.c.\right] \ , \ i, j = 1, 2, 3 \ . \tag{1.27}$$

The $Y_\ell^{ij}$ is a 3×3 matrix and since it connects the flavour eigenstates $\ell$, in principle it can be any complex matrix. For the leptons it is $Y_\ell^{ij} = diag(m_e, m_\mu, m_\tau)$. However the situation is more complicated for the quarks. The corresponding $Y_d^{ij}$ is not diagonal i.e. the mass eigenstates of quarks are not also flavour eigenstates. The diagonalisation procedure introduces the $V_{CKM}$ matrix, which appears in the weak couplings of the quarks if one wants to express them, more naturally, with the mass eigenstates. The charged ($W$'s) $SU(2)_L$ gauge bosons can connect different families of quarks. The strength of these connections are quantified by the entries of the $V_{CKM}$ matrix. The latter can be visualised in figure 1.3. The spontaneous symmetry breaking mechanism completes the picture of the SM Lagrangian at the classical level, which is summarised in the next section.

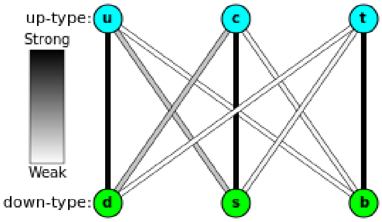

Figure 1.3: The quark Weak decay modes. Image taken from [18].

### 1.2.5 Summary of the SM and open issues

The Standard Model describes the fundamental elementary fields propagating in flat spacetime and their interactions. The corresponding Lagrangian is invariant under the Poincaré group. The internal symmetry of the SM is

$$SU(3)_C \times SU(2)_L \times U(1)_Y \xrightarrow[\text{breaking}]{\text{symmetry}} SU(3)_C \times U(1)_Q \,. \tag{1.28}$$

The Standard model Lagrangian can be divided in four parts [19], as shown in equation 1.29.

$$\mathcal{L} = \mathcal{L}_{\text{Gauge}} + \mathcal{L}_{\text{Matter}} + \mathcal{L}_{\text{Higgs}} + \mathcal{L}_{\text{Yukawa}} \,. \tag{1.29}$$

The $\mathcal{L}_{Gauge}$ term in equation (1.29) refers to the kinetic terms and interactions among the gauge bosons. Depending on the symmetries which generate the bosons (Abelian or non Abelian), there may be self interaction terms. The $\mathcal{L}_{Matter}$ term includes the interactions of the fermionic particles with the gauge bosons. These interactions are generated via the covariant derivatives. The

$\mathcal{L}_{\mathrm{H}iggs}$ term is the Higgs boson Lagrangian part, which includes the Higgs self interaction terms, the interactions between the Higgs and the gauge bosons and the Weak gauge boson mass terms. Finally the $\mathcal{L}_{\mathrm{Y}ukawa}$ term describes the interactions between the Higgs field and the fermions as well as the fermion mass terms. In the following table we summarise the Standard Model Fields, their representations under the internal symmetries and their spin ($S$), weak isospin ($T^3$), hypercharge ($Y$), electric charge ($Q$), quantum numbers for all the three fermion families $f = 1, 2, 3$ and the bosons. The hypercharge $Y$ is chosen so that in combination with the Weak Isospin gives the charge of a field according to $Q = T^3 + Y$. As we can see in table 1.3, a field being a singlet under a symmetry group implies that the corresponding charge is zero.

| Field | $SU(3)_C$ | $SU(2)_L$ | Quantum numbers | | | |
|---|---|---|---|---|---|---|
| | | | $S$ | $T^3$ | $Y$ | $Q$ |
| $Q_L^f = \begin{pmatrix} u^f \\ d^f \end{pmatrix}_L$ | **3** | **2** | 1/2 | $\begin{pmatrix} 1/2 \\ -1/2 \end{pmatrix}$ | 1/6 | $\begin{pmatrix} 2/3 \\ -1/3 \end{pmatrix}$ |
| $u_R^f$ | **3** | **1** | 1/2 | 0 | 2/3 | 2/3 |
| $d_R^f$ | **3** | **1** | 1/2 | 0 | -1/3 | -1/3 |
| $L_L^f = \begin{pmatrix} \nu^f \\ \ell^f \end{pmatrix}_L$ | **1** | **2** | 1/2 | $\begin{pmatrix} 1/2 \\ -1/2 \end{pmatrix}$ | -1/2 | $\begin{pmatrix} 0 \\ -1 \end{pmatrix}$ |
| $\ell_R^f$ | **1** | **1** | 1/2 | 0 | -1 | -1 |
| G | **8** | **1** | 1 | 0 | 0 | 0 |
| $\mathbf{W} = \begin{pmatrix} W^+ \\ W^0/Z \\ W^- \end{pmatrix}$ | **1** | **3** | 1 | $\begin{pmatrix} +1 \\ 0 \\ -1 \end{pmatrix}$ | 0 | $\begin{pmatrix} +1 \\ 0 \\ -1 \end{pmatrix}$ |
| B/A | **1** | **1** | 1 | 0 | 0 | 0 |
| $\Phi = \begin{pmatrix} \Phi^+ \\ \Phi^0/H \end{pmatrix}$ | **1** | **2** | 0 | $\begin{pmatrix} 1/2 \\ -1/2 \end{pmatrix}$ | 1/2 | $\begin{pmatrix} 1 \\ 0 \end{pmatrix}$ |

Table 1.3: Quantum numbers and internal symmetry group representations of SM fields.

The Standard model up to now it is in full agreement with the experimental results involving particle accelerators. Before completing the discussion on the SM, we shall briefly mention some of the unresolved issues within this theoretical framework. There are indeed strong indications that point to the fact that the SM cannot be a complete theory.

- As a theory it has 18 independent parameters. There are 9 fermion masses[1], the mass of the Higgs and the vev $v$, three gauge couplings, three mixing angles and one CP-violating phase in the CKM matrix. The first thing one notices is that the model itself does not say anything about the possible origin of these parameters and cannot justify their specific values.
- As mentioned in the beginning of this chapter, the SM is disconnected from GR. It ignores gravity and therefore it is already limited in explaining the universe structure. The SM 'lives' at the energy scale of the EW symmetry breaking, which is the vev $v = 246$ GeV of the Higgs doublet $\Phi$. On the other hand gravity becomes important at the Planck energy scale $\Lambda_{\mathrm{P}lanck} = 10^{19}$ GeV. This huge energy gap between these two natural scales is referred to as the 'hierarchy problem'. Any attempt to describe the very early universe with only the SM is weak. As we will be reaching the Planck energy scale and we can no longer ignore gravity.
- The current cosmological model includes dark matter, dark energy and inflation. The existence of these phenomena cannot be incorporated within the SM. Furthermore one needs a Beyond the SM approach in order to explain the matter/antimatter asymmetry in the universe.
- The neutrino experiments have shown the oscillation between neutrino flavours, which proves that the neutrinos have masses. Within the SM the neutrinos are massless. In principle one could treat the neutrinos as Dirac fermions, extend the Yukawa sector and include also the right-handed neutrinos $\nu_R^f$. A right-handed neutrino in table 1.3 would be a singlet under both $SU(3)_C, SU(2)_L$. Apart from the spin (1/2), all the other quantum numbers shown it this table would be zero. This way the SM would include neutrino masses. The right-handed neutrinos would have to be very weakly interacting and indeed they are not (yet) observed. However this way we would have to increase the number of free parameters of the SM (3 new masses) and the Yukawa sector would include the Higgs couplings from the tops to the neutrinos, spanning many orders of magnitude. This would introduce a further 'hierarchy problem', since it would not be explained within the SM.

---

[1] There are 12 masses if we include also the neutrino ones. In this case the parameters become 21 + 3 mixing anlgles + 1 phase = 25. This is discussed as a BSM scenario at the end of the current page.

- Claiming the existence of a symmetry in the SM Lagrangian is equivalent to including all the allowed terms. The $SU(3)_C$ symmetry allows a term of the form $\propto \theta G^{\mu\nu}\tilde{G}^{\mu\nu}$, which is CP-violating. However there are very strong experimental limits on this new $\theta$ parameter ($\theta < 10^{-10}$). This is an issue of a fine tuning, since this parameter has to be put by hand to an extremely small value and it is known as the strong-CP problem.

- The 'hierarchy problem', mentioned in the first point, is mirrored also in the mass of the Higgs boson. The Higgs mass in the SM is a fixed by experiment parameter. But given all the aforementioned points and assuming new physics at the GUT or Planck scale, new heavy particles ($M \sim$ new scales) should be there, coupling to the Higgs and correcting its physical mass. These large correction terms should almost exactly cancel in a fine tuned way, so that we would end up to the measured low Higgs mass.

All these issues point to the conclusion that most probably there is physics beyond the SM. We will introduce the BSM approach used in this research in section 1.5, but before that, in the following section, we will describe the calculational framework and in section 1.4 we will focus on the top quark.

## 1.3 Calculational framework

In section 1.2, we have discussed the SM Lagrangian at the classical level. Quantising the Lagrangian mathematically consists of defining the propagators or 2-point correlation functions, which describe the probability amplitude for the particles to travel from a spacetime point to another. This is done by inverting the kinetic terms that appear in the Lagrangian for every particle separately. However, these terms do not need to be necessarily invertible and indeed they are not for the gauge bosons. This issue is cured by adding a gauge-fixing kinetic term which for QED has the form [14, sec. 21.1] [15, sec. 8.5]

$$\mathcal{L}_{\mathrm{g}-f}^{\mathrm{Q}ED} = -\frac{1}{2\xi}(\partial^{\mu} A_{\mu})^2 \ . \tag{1.30}$$

This allows the inversion of the kinetic terms so that the propagator can be defined. Since it depends on the $\xi$ parameter, one has to choose a specific value (gauge) in order to get results and the final answers should be independent on this choice. On top of that, specifically for the QCD case, insisting on Lorentz invariance of the probabilistic results (amplitude), forces us to introduce new unphysical states, which are called ghosts [15, sec. 25.4]. These ingredients upgrade the Lagrangian to the quantum level.

### 1.3.1 Dealing with the divergences

Even from this stage, moving to actual observables requires a huge calculational effort. Following standard procedures one can derive the Feynman rules for a given Lagrangian, which map the diagrammatic expressions of Feynman diagrams with the corresponding mathematical expressions [14, app. A.1] [20, sec. 1.4]. The whole Feynman diagram approach is based on the perturbation theory assuming that the coupling constants, which appear in the vertices, are parameters smaller than the unity. In this sense the diagram in figure 1.4a is of the lowest order in the coupling constants and they are called tree level diagrams. Adding more vertices and keeping the same external legs leads to the loop diagrams like the one shown in figure 1.4b [2]. The NLO picture is complete with the real emission diagrams shown in figures 1.4c and 1.4d, for which we will discuss at the end of the current section. The physical amplitude or any observable Σ for a scattering process can be written as an expansion on the relevant coupling constants. For the process in figure 1.4 it is

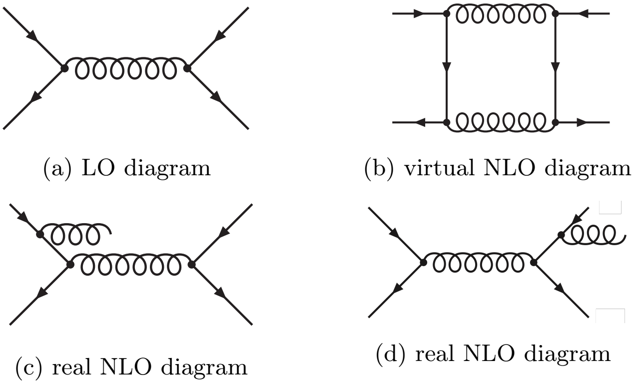

(a) LO diagram (b) virtual NLO diagram

(c) real NLO diagram (d) real NLO diagram

Figure 1.4: Representative leading (LO) and next to leading (NLO) order Feynman diagrams for $q\bar{q} \to q\bar{q}$ process. Figure taken from [21].

$$\Sigma(q\bar{q} \to q\bar{q}) = \Sigma^{\mathrm{LO}}\alpha_s^2 + \Sigma^{\mathrm{NLO}}\alpha_s^3 + \Sigma^{\mathrm{NNLO}}\alpha_s^4 + \dots \,. \tag{1.31}$$

At any given order there is a number of Feynman diagrams to be evaluated, which increases as the order increase. But with the couplings being small, the higher order diagrams should be corrections to the lower order ones, therefore one can truncate this infinite series according to the calculational and computational power.

---

[2] There are cases where the LO diagrams for a process is already at 1-loop level. These are called loop-induced processes. An example is the $gg \to HZ$ production, which is discussed in chapter 4.

This is the first calculational puzzle, because the calculation of the loop diagrams includes the full integration of the loop momentum, which usually leads to divergences at both the limits to infinity and zero. In the former case they are called ultra-violet (UV) divergences and in the latter infra-red (IR) divergences. The UV divergences are being tackled via the procedure of renormalisation. A gauge and Lorentz invariant regularisation scheme is the dimensional regularisation (DR) [14, app. A.4], in which one extends the theory to $d = 4 + \varepsilon$ dimensions. The divergences appear now as poles of $1/\varepsilon_{\mathrm{UV}}$, and they are absorbed in redefinitions of the fields and parameters (masses, couplings) of the theory. This redefinition is the renormalisation procedure and it is realised by substituting the (up to now) bare fields and parameters with the renormalised ones and at the same time add the so-called counter terms [14, ch. 10] [15, ch. 19]. The counter terms are defined in such a way that they compensate for the UV divergences from the loop diagrams. Therefore the divergent part of the counter terms is fixed in order to cancel the poles, but the finite part is ambiguously defined. This depends on the renormalisation (subtraction) scheme that one choses. The most widely used renormalisation schemes are the on-shell, the minimal subtraction (MS) and the modified minimal subtraction ($\overline{\mathrm{M}S}$). In the on-shell scheme the propagators, after the renormalisation, have the poles at their physical masses. In the MS scheme the counter terms are defined such that they cancel only the divergent part, whereas in the $\overline{\mathrm{M}S}$ scheme they include also the finite universal constant, which comes from the expansion around the pole. Moving from 1- to two 2- loop corrections new UV divergences will appear. However if the counter terms introduced to cure the 1-loop divergences are enough for all the higher orders, then the theory is called renormalisable [15, ch. 21]. The SM is such a theory.

During the DR procedure one has to introduce an arbitrary energy scale parameter $\mu^{-\varepsilon}$ as a regulator for dimensional consistency. This parameter will appear usually at the end in logarithms of the form of $\log(\mu/Q)$, where $Q$ is some characteristic scale of the process. It is internal, but when combined with the renormalisation procedure acquires also a physical meaning, since it is understood as the energy scale at which the subtraction of the divergences takes place and it is upgraded to the renormalisation scale $\mu_r$. After introducing the counter terms, the poles are removed and one can set $\varepsilon = 0$, returning to $d = 4$. However the $\mu$ dependence remains in the renormalised parameters because we have truncated the expansion series at the highest order we can calculate. At any fixed order in perturbation theory, the physical (renormalised) observables will appear to have a dependence on $\mu_r$.

This parameter is a mathematical artifact and not a genuine Lagrangian parameter, therefore the observables should be independent on it. Since the observables have direct and indirect dependence on $\mu_r$, e.g. via a coupling, it is

$$\frac{d}{d\log(\mu_r^2)}\Sigma_R\left(\frac{\mu}{Q},\alpha_s(\mu_r)\right)=\left(\frac{\partial}{\partial\log(\mu_r^2)}+\frac{\partial\alpha_s}{\partial\log(\mu_r^2)}\frac{\partial}{\partial\alpha_s}\right)\Sigma_R=0 \tag{1.32}$$

Differential equations of the form of 1.32, are called renormalisation group equations (RGEs) [14, ch. 12] [15, ch. 23] and solving them we get the dependence that the Lagrangian parameters ($\alpha_s$ in this case) should have on $\mu_r$ in order to cancel the direct dependence on $\log(\mu/Q)$ of the physical observable. The term $\frac{\partial}{\partial\log(\mu_r^2)}\alpha_s \equiv \beta(\alpha_s)$ is expanded in $\alpha_s$ and we get the $\beta_0$ (1-loop), $\beta_1$ (2-loop), ..., beta functions. Since this is dependent on $\mu_r$, it cannot correspond to any observable, but we can use it in order to predict the evolution (running) of the parameter given an initial condition. At 1-loop we get,

$$\alpha_s(Q)=\frac{\alpha_s(Q_0)}{1+\alpha_s(Q_0)\beta_0\log(Q^2/Q_0^2)}\,, \tag{1.33}$$

where $Q_0$ is a reference scale (usually $m_Z$), where the $\alpha_s$ is measured and from this the evolution is calculated. This evolution is verified by the experiments in high detail (figure 1.5). The evolution shown in figure 1.5 is strong test for the whole renormalisation procedure. Furthermore it shows an important property of QCD. At low energies $\alpha_s$ becomes large and the theory loses the property of being perturbative. Therefore the Feynman diagram technique cannot be used. Lattice techniques are used in order to describe this low energy region of QCD. An important characteristic of QCD is that quarks and gluons cannot be isolated in nature, but they appear only in colour neutral states

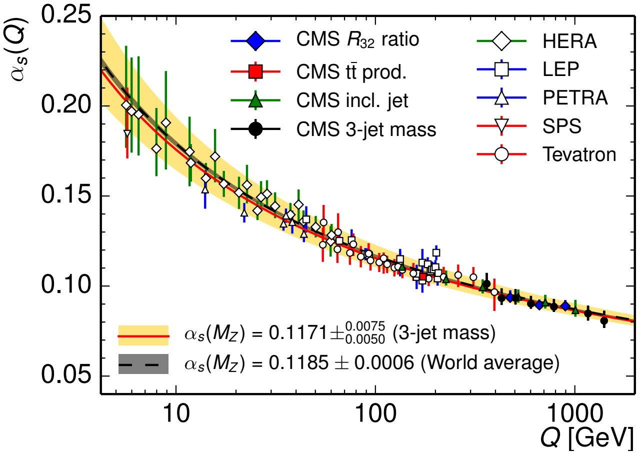

Figure 1.5: The running of the $\alpha_s$ as a function of the energy scale $Q$ [22].

(confinement). This explains the fact that although the gluons are massless like the photon, the strong force is a short-distance force. Furthermore, at high energies $\alpha_s$ becomes very small and this is translated to the gluons and quarks behaving as free particles at small distances. The latter is defined as asymptotic freedom [20, ch. 2].

The procedure of renormalisation tames the UV divergences. As we have mentioned in the beginning of this section, the loop integrals diverge also at the zero momentum limit. These divergences appear because if one increases the order via loop diagrams, he is not inclusive in this order in perturbation theory. In a QCD process like the $q\bar{q} \to q\bar{q}$ shown in figure 1.4, the tree level cross section is of order of $\alpha_s^2$. In the $\alpha_s^3$ order we have the interference of the 1-loop diagrams (fig. 1.4b) with the tree level ones (fig. 1.4a). These are the virtual corrections. However in the same order there are also the squares of the diagrams of the extra gluon emission i.e. $pp \to q\bar{q} + g$ shown in figures 1.4c, 1.4d. Once these are also included the IR divergences exactly cancel and we are finally remained with a finite NLO part, which is indeed a correction with respect to the LO one. This feature is summarised in the KLN theorem [23,24], which states that the IR divergences will cancel always in a unitary theory, if all the possible final and initial states are summed over for a given perturbative order. Since in scattering we are not inclusive in the initial states, there are uncanceled divergences [3] which are absorbed in the proton structure as we will see in the following section.

### 1.3.2 Collider physics

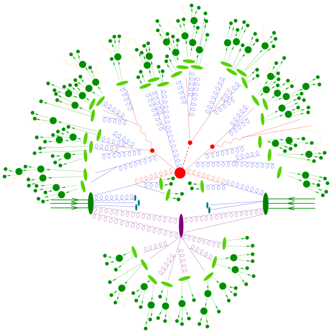

Figure 1.6: Pictorial representation of en event at the LHC [26].

In section 1.3.1, we have described the calculational steps at the Feynman diagram level. But a process like $t\bar{t}$ can be produced by different initial states

---

[3] These are the uncanceled mass singularities in the initial state [25, sec. 15.7.1].

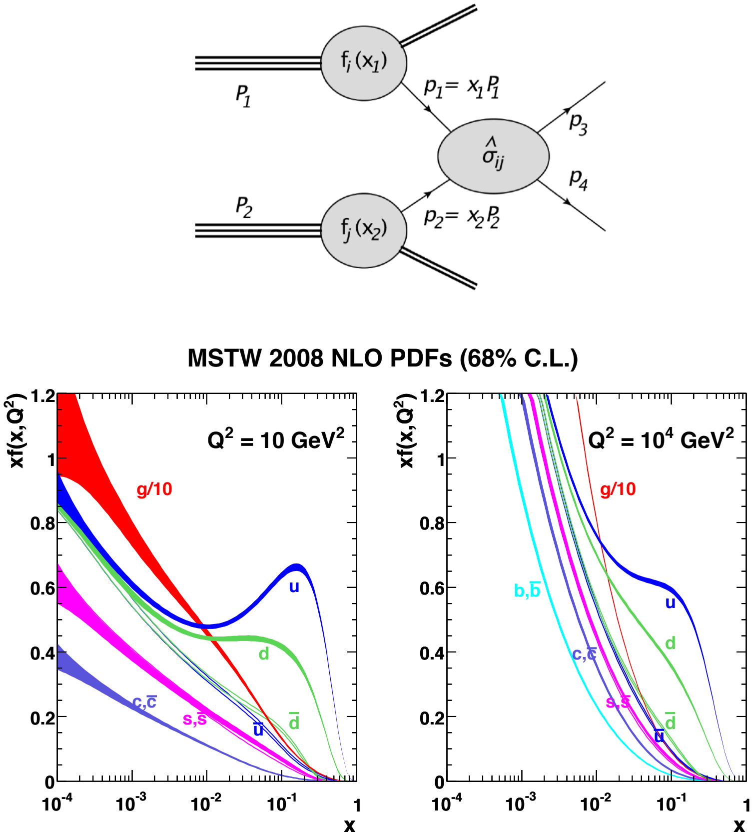

Figure 1.7: Top: pictorial representation of the factorisation theorem terms. Bottom: the MSTW2008 PDFs [27] at NLO accuracy at two different scales.

and there cannot be a $q\bar{q}$ or a $gg$ collider. Furthermore the top quarks, as we will see in section 1.4, are very short lived and QCD confined, so we could never see them at any kind of detector. We need to describe the structure of the proton as well as the further decays in order to reach the final objects that are actually detected. This is a complicated procedure as a whole and is depicted pictorially in figure 1.6. In this figure we see the two proton beams colliding from which two gluons are involved to the hard scattering (red). The final state particles are being decayed and any coloured state ends up creating a QCD shower(blue). From this shower, colour neutral states (mesons, baryons) are created (hadronisation) and they end up to the detector (green). On top of that there can be simultaneous other low energy collisions between other constituents of the initial protons as an underlying event (violet). What makes this whole procedure calculable is the fact that different stages are realised at different energies, therefore they can be treated separately from each other. The separation between the proton structure, the hard (parton level) event and the final shower/hadronisation ($F$ in eq. 1.34) is based on the mostly experience-based factorisation theorem. At hadron colliders the initial particles do not have a fixed longitudinal momentum. The proton (or antiproton at Tevatron) beam includes quarks and gluons, which are called partons. The longitudinal momentum of each one of them is not equal to the momentum of the proton beam, but it is a fraction $x$ of it, which is described by the parton model (fig. 1.7) [20, sec. 4.3] [15, ch. 32]. The cross section for a hard scattering process of two initial hadrons having momenta $P_1$, $P_2$ to a final state $X$ is

$$\begin{aligned}\sigma(P_1, P_2 \to X) = \sum_{i,j} \int dx_1 dx_2 f_i(x_1, \mu_f^2) f_j(x_2, \mu_f^2) \times \\ \times\, \hat{\sigma}_{ij}(x_1, x_2, \alpha_s(\mu_r), \mu_r^2, \mu_f^2, \hat{X}) \times F(\hat{X} \to X)\ ,\end{aligned} \tag{1.34}$$

where $f_i$, $f_j$ are the parton distribution functions (PDFs) corresponding to the $i, j$ partons and $\hat{\sigma}_{ij}$ is the perturbative cross section of the process. The PDFs as well as the cross section have a new dependency on the parameter $\mu_f$, which will be defined in the following paragraphs. The physical meaning of the PDFs is that the probability of a parton $i$ to have momentum fraction between $x$ and $x + dx$ is $f_i(x)dx$. As it is shown in figure 1.7, these functions differ from parton to parton and they depend on the energy scale. The partons that contribute to the proton with their quantum numbers are the valence quarks $(u, d)$. The sea quarks and the gluons appear via the interactions of the valence quarks. The relative momenta between the partons are small and they interact strongly, therefore the PDFs are not perturbative objects and they are fit by the experiment.

The whole discussion in section 1.3.1 was for the $\hat{\sigma}_{ij}$ part. Now we see that this has to be convoluted with the PDFs, and this convolution introduces a new dependence on the parameter $\mu_f$. The connection between the low energy PDF structure and the hard process is calculable, since we know that if we have an initial quark in the hard process, it originated either from a quark or from a gluon within the proton. This part is described by the spitting functions $P_{ij}(y)$, which are equal to the probability of a parton $i$ being emitted by another parton $j$ with a $y$ fraction of momentum. The evolution of the PDF of a quark can be written as

$$\frac{dq(x, \mu_f)}{d \log \mu_f^2} = \frac{a_s}{2\pi} \int_x^1 \frac{dy}{y} \left[ q(y, \mu_f) P_{qq}(\frac{x}{y}) + g(y, \mu_f) P_{qg}(\frac{x}{y}) \right]\ . \tag{1.35}$$

This is the DGLAP [28–30] equation for the quark PDF. As expected the PDFs depend on the energy scale and this is depicted in the parameter $\mu_f$. Similarly to what is done for the $\alpha_s$ running in equation 1.33, we can get the value of the PDFs at low energy scale from the experiment and then use the DGLAP equations in order to evolve them up to high energy scales. In figure 1.7 we see the PDFs at low $Q^2 = 10$ GeV$^2$, and then at high $Q^2 = 10^4$ GeV$^2$ as a result of the DGLAP evolution. In figure 1.8 we can see a pictorial representation of the splitting functions. These functions describe collinear emissions within the proton. This calculable part of the PDFs is naturally receiving corrections from higher order diagrams and so we can have LO, NLO and NNLO PDF sets available to convolute with the hard cross section $\hat{\sigma}$ of accuracy of the respective order. The parameter $\mu_f$ physically is the limit between the low energy of the non-perturbative proton structure and the energy scale of the hard process. The uncanceled IR divergences we had from the ISR need to be absorbed in this non-perturbative regime below the $\mu_f$.

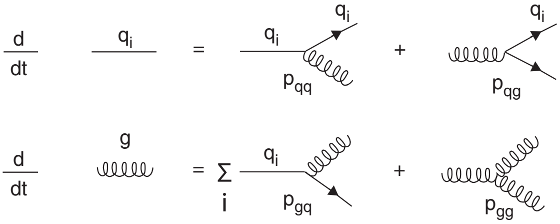

Figure 1.8: Pictorial representation of the quark and gluon splitting functions [31]. Here it is $t \equiv \log(\mu_f^2)$.

The last part of equation 1.34 is the $F(\hat{X} \to X)$, which describes the transition from the parton level final state $\hat{X}$ to the final collection $X$ of objects reaching the detector. A parton level coloured particle cannot be a final state. The process of shower describes the subsequent decays of these particles up to the point where they enter the hadronisation, forming colour neutral hadrons, which are the actual final states. Both these procedures take place at lower energy scales than the hard scattering and like the PDFs can be described in a universal and independent to the hard process way. Similarly to the PDF, the shower consists of collinear subsequent emissions of partons and they can be factorised from the hard matrix element. The probability of emission is described by the same splitting functions $P_{ij}$, which we introduced for the PDFs. Moving from LO to NLO in QCD introduces an ambiguity at this part, because extra parton emissions are included both at the hard process and the shower. The mechanism of avoiding this double counting is called matching and is necessary in order to combine higher order QCD calculations with parton shower. This connection between the hard event scale and the low hadronization scale is realised with several frameworks that will be discussed in the following section. At the final stage the partons end up to clusters of hadronic states, which are the jets. After all these steps we are finally left with the objects that will be actually detected in the experiment. Both the proton structure and the shower/hadronisation processes are considered to behave always under the SM and dominantly by QCD. Any BSM signature is expected to appear and therefore calculated for the hard parton level part of the process.

### 1.3.3 Automated calculations

The usual strategy in a calculation is to choose the two scales $\mu_f, \mu_r = \mu$ equal to a natural scale depending on the process and then vary them independently within the interval $\{\mu/2, 2\mu\}$, in order to estimate the uncertainties from higher missing orders. The higher the perturbative order we can include to the calculation, the smaller becomes the scale uncertainty. Another source for the theory uncertainties is coming from the PDFs and introduced via the fitting to the data. The scale and PDF uncertainties are the main theory uncertainties and they will be systematically considered in this research. The ratio of any observable between the NLO and LO QCD prediction is called $K$-factor and is studied in detail for associated $t\bar{t}$ production in chapter 3. NLO QCD corrections are also important at BSM studies, as shown in chapter 4. The perturbative expansion on the coupling constants is most important for the QCD one, since it is relatively larger than the coupling constants of the other forces (EW) (table 1.1). However there are phase space regions, where this natural hierarchy may be inverted. On top of that, once we reach the level, where the scale uncertainties from the QCD higher order corrections become very small, then deviations coming from the EW corrections can no longer be neglected. In this case PDFs which include the photon need to be used to include properly the photon initiated channels. This is discussed in detail for the $t\bar{t}$ production in the chapter 2. All these calculations involve numerous Feynman diagrams and therefore automation of all the steps described in the previous section is necessary.

The MADGRAPH5_AMC@NLO [32] is the fully automated framework, through which this research is realised. This code allows the automatic calculation of tree-level amplitudes, subtraction terms and their integration over phase space [33] as well as of loop-amplitudes [34–36] once the relevant Feynman rules and UV/$R_2$ counterterms for a given theory are provided [37–39]. A recent extension of the code allows to automatically calculate NLO QCD and EW corrections [40,41]. On top of that there are ongoing efforts of automating

NLO BSM simulations for colliders [42]. Event generation is obtained by matching short-distance events to the shower employing the MC@NLO method [43], which is implemented for PYTHIA6 [44], PYTHIA8 [45], HERWIG6 [46] and HERWIG++ [47]. MADGRAPH5_AMC@NLO is interfaced with these tools as well as with the PDF sets in an automated way. Throughout this work we adopt the 5 Flavor-scheme (5FS), i.e. we treat the $b$ quark as massless and we include it to the PDFs. Within the MADGRAPH5_AMC@NLO framework for the QCD and the EW corrections we use the $\overline{\text{M}S}$ subtraction scheme for all the relevant massless particles and the on-shell scheme for the massive ones.

Having described the SM at the Lagrangian and observable level we can now focus on the top quark physics.

## 1.4 The top quark

Having seen the SM Lagrangian and the calculational framework, we can now focus on the top quark. The top quark is a charge $Q = +\frac{2}{3}$, spin $S = \frac{1}{2}$ particle. It is the upper part of the 3rd generation left handed quark isospin doublet (tables 1.2, 1.3), therefore has isospin $T^3 = +\frac{1}{2}$. It is the most massive known fundamental particle. The mass of the top quark is around $m_t = 173.3$ GeV (fig. 1.9). Its existence (and that of the bottom quark) was predicted in 1973 by Makoto Kobayashi and Toshihide Maskawa [49] to explain the observed CP

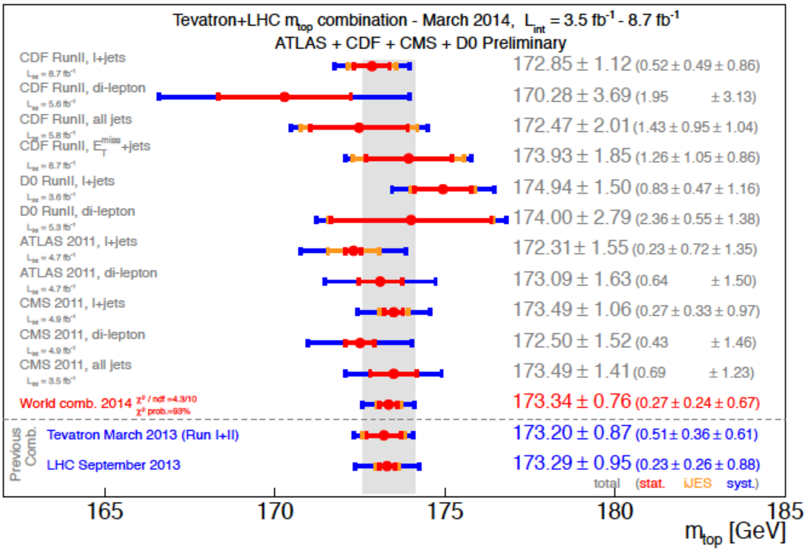

Figure 1.9: Measurements of the top quark mass in comparison with theory [48].

violations in kaon decay and it was discovered in 1995 at the Tevatron [50, 51]. Kobayashi and Maskawa won the 2008 Nobel Prize in Physics for the prediction of the top and bottom quark. Being by far the heaviest of the quarks, makes the physics around the top quark very interesting. It is an elementary particle as heavy as a gold atom. This property results the many peculiar features of the top quark. This section is based on the already extensive literature on the top quark. For a detailed description of the following paragraphs, we suggest to the reader the [19], [52] and [53] references.

- GENERAL FEATURES

It is $m_t > m_W + m_b$, therefore the top quark is the only quark that can decay in an on-shell $W$ and a $b$ quark. It 'feels' both the strong and the EW forces, but it decays only Weakly and almost at 100% to $t \to W^+ b$. This decay mode is proportional to the square of the corresponding $V_{CKM}$ element $|V_{tb}|^2$. Experimental results from single top quark production put constraints to $|V_{tb}| = 1.021 \pm 0.032$ [54]. Furthermore, assuming $|V_{tb}| = 1$, lattice QCD calculations indicate that $|V_{td}| = (8.4 \pm 0.6) \times 10^{-3}, |V_{ts}| = (40.0 \pm 2.7) \times 10^{-3}$ [54]. The unitarity relation $|V_{tb}|^2 + |V_{ts}|^2 + |V_{td}|^2 = 1$ shows that indeed the top quark decay is dominated by the $t \to W^+ b$ mode. The corresponding branching ratios are [52, 55]

$$BR(t \to W^+ b) \approx 0.998 \;,\; BR(t \to W^+ s) \approx 1.9{\times}10^{-3} \;,\; BR(t \to W^+ b) \approx 10^{-4} \;. \tag{1.36}$$

On top of that, the resulting $W^+$ boson is polarised in a sense that it can be only left-handed ($\sim$ 30%) or longitudinal ($\sim$ 70%) in the limit $m_b \to 0$. Keeping a non zero $m_b$ and performing EW and QCD corrections to the decay, the right-handed component appears at $\sim$ 0.1% [56].

Being able to treat the top quark as a free particle and studying the spin properties of the decay products is already a unique feature. The decay width at LO, neglecting $m_b$, is [52]

$$\Gamma(t \to Wb) = \frac{G_F m_t^3}{8\pi\sqrt{2}} |V_{tb}|^2 \left(1 - \frac{m_W^2}{m_t^2}\right)^2 \left(1 + 2\frac{m_W^2}{m_t^2}\right) . \tag{1.37}$$

Equation 1.37 results to a top decay width of $\Gamma_t \approx 1.5$ GeV, which corresponds to a very short lifetime $\tau_t = 1/\Gamma_t \approx 5 \times 10^{-25}$ seconds. This result is of crucial importance, since the top quark lifetime is shorter than the hadronization time ($\tau_{\mathrm{had}} \simeq 1/\Lambda_{QCD} \approx 3 \times 10^{-24}\ s$). The latter implies that the spin information of the top quark is kept and transmitted to the decay products. The quantum entanglement of the spin of the top quark with the momenta of the final state particles, which is called spin correlation, allows the study of the vertex structure of the EW processes in the top quark decays.

- Production and decay modes

The main production modes of the top quark is the single top production, the top pair production and the associated $W$ production. The single top production provides the top in association with a jet ( top of fig. 1.10). It is a Weak process, initiated by the $q\bar{q}'(qq')$ channel at LO, and it is realised via an s-(t-) channel $W$ boson exchange. In both these cases the $W$ boson provides a strong polarisation for the top quark. The top quark production in association with a $W$ boson (bottom of fig. 1.10) has a very small cross section at the Tevatron but not at the LHC. The cross section for these processes at the Tevatron and the LHC are shown in table 1.4. As mentioned in the general features of the top quark, all these production modes are ideal for studying the $|V_{tb}|$ element of the $V_{CKM}$ matrix [57]. Furthermore the top quark polarisation is depicted in the angular distributions of its leptonic decays, which makes these processes probes for spin correlation studies, since they are very sensitive to any BSM deviation of the EW SM couplings.

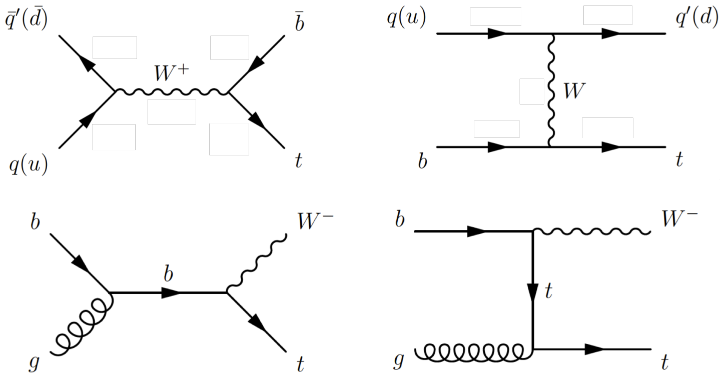

Figure 1.10: Single top quark production via an s- or t- channel $W$ boson exchange.

| cross section [pb] | $s$-channel | $t$-channel | $W$ associated |
|---|---|---|---|
| Tevatron | $\sim 1.08$ | $\sim 2.3$ | $\sim 0.28$ |
| LHC | $\sim 12.1$ | $\sim 242$ | $\sim 88$ |

Table 1.4: Cross sections for single top quark $(t+\bar{t})$ production at the Tevatron and the LHC14 [52].

The other main production mode of the top quark is in top $(t, \bar{t})$ pairs. This is the dominant production mode at both the Tevatron and the LHC. The large cross section of top pair production has characterised the LHC as a top factory. The cross section at the Tevatron is $\sigma^{t\bar{t}}_{p\bar{p}} = 7.35(\pm \sim 12\%)$ pb [52]. The cross section at the LHC8 is $\sigma^{t\bar{t}}_{pp} = (244.9 \pm 9.7)$ pb [58] and at the LHC14 is $\sigma^{t\bar{t}}_{pp} = 833(\pm \sim 15\%)$ pb [59]. The dominant production channel at the LHC is the $gg$ one, whereas at the Tevatron it is the $q\bar{q}$[4]. The LO Feynman diagrams are shown in figure 1.11. In contrast to the single top production, this is a purely QCD process. Despite this, the large cross section at the LHC, provides the opportunity to still study the $tWb$ coupling through the decays of the top quark pair. The decay modes of the top quark pair can be visualised in figure 1.12. Since, as shown in equation 1.36, the top quark decays almost exclusively

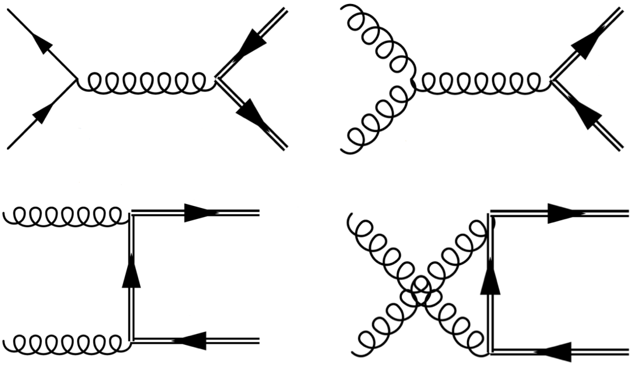

Figure 1.11: LO Feynman diagrams for top pair production. The double line just indicates the heavy (top) quark line.

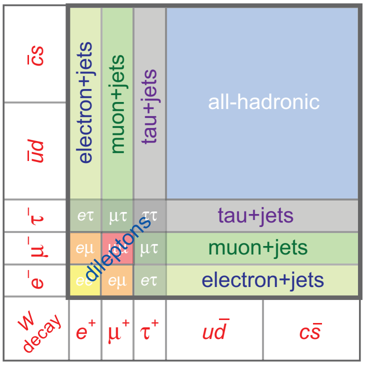

Figure 1.12: Decay modes of the top quark pair [60].

---

[4] This is due to the fact that the LHC is a $pp$ collider, whereas the Tevatron is a $p\bar{p}$ one, in combination with the fact that the LHC has higher $\sqrt{s}$ and therefore probes smaller $x$ PDFs.

to $Wb$, the different channels in figure 1.12 are driven by the $W$ boson decays. The $t\bar{t}$ branching ratios are

$$BR^{t\bar{t}}(\mathrm{h}adronic) \approx 4/9 \;, BR^{t\bar{t}}(\mathrm{s}emi-leptonic) \approx 4/9 \;, BR^{t\bar{t}}(\mathrm{l}eptonic) \approx 1/9 \;. \tag{1.38}$$

On top of that if we remove the $\tau$'s from the leptonic part, as a non final state lepton, the branching ratios become

$$BR^{t\bar{t}}(\mathrm{h}adronic) \approx 46\% \;, BR^{t\bar{t}}(\mathrm{s}emi-leptonic) \approx 30\% \;, BR^{t\bar{t}}(\mathrm{l}eptonic) \approx 5\% \;. \tag{1.39}$$

The semi-leptonic channel, despite the fact that it is not the dominant one, is preferred in many experimental analyses. The reason is that the leptonic part provides a clean signature and the hadronic part on the one hand has QCD contamination, but on the other hand increases the $BR$ and provides a cleaner reconstruction for the top quark.

- THE TOP QUARK MASS

Both the single top and the top pair production are used and several experimental techniques are applied in order to realise direct searches for the top quark mass determination [61]. The reconstructed mass from the final state particles is the Monte Carlo mass $m_t^{\mathrm{M}C}$, which is very close to the on shell or pole mass ($m_t$). However the quarks, being colour confined, cannot propagate freely, therefore the pole mass has an intrinsic ambiguity. The running or $\overline{\mathrm{M}S}$ mass is free from this ambiguity and it is what is used for all the quarks. But the fact that the top quark decays before hadronization gives the opportunity to treat it also as a free, bare quark. The difference between the $m_t$ and $m_t^{\overline{\mathrm{M}S}}$ (evaluated at $\mu = m_t$) is known to be at $\sim 10$ GeV [52]. Moreover, the mass of the top quark at the Lagrangian level appears to be an independent parameter. This is true, but the masses of the particles affect each other through the loop corrections (fig. 1.13). So the precise determination of the top quark mass provides a strong consistency check for the SM. It is interesting to note that

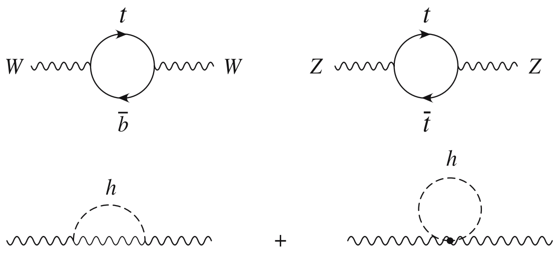

Figure 1.13: 1-loop corrections to $W, Z$ boson mass terms [53].

the top quark loop contibutions in figure 1.13 are quadratic in the top quark mass, whereas the Higgs loop contributions are logarithmic in the mass of the Higgs. Therefore the value of the $W$ mass gets corrections that are sensitive to the

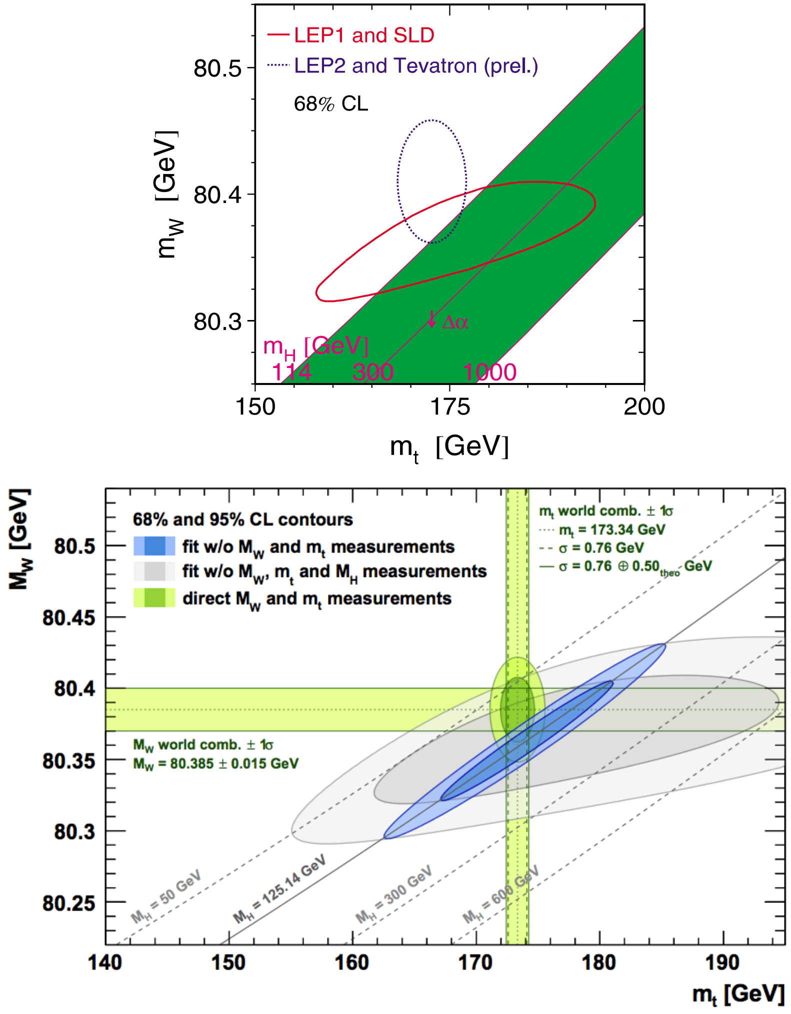

Figure 1.14: Top: Straight lines of a constant Higgs mass in a correlation plot of $m_W$ vs $m_t$. The dotted ellipse corrsponds to direct measurements, whereas the solid to indirect [53]. Bottom: The mass of the $W$ boson vs the mass of the top quark, before and after the Higgs mass determination on top of the direct measurements [61].

top quark mass. These indirect searches put extra constraints to the masses and they are used in combination to the direct searches results. This technique was already used in putting a lower limit of ~ 114 GeV to the Higgs mass from LEP2 and Tevatron (fig. 1.14). Even after the Higgs discovery, the comparison between direct and indirect results is a strong test for the SM (fig. 1.14). A deviation between these searches would imply that there is an uncontrolled part that contributes in the loop corrections, which could be a sign of BSM physics.

The other important aspect of the top quark mass is the fact that it connects it with the Higgs boson via the top Yukawa coupling. This coupling to the Higgs is $Y_t = \frac{\sqrt{2}m_t}{v} \approx 1$, suggesting that there could be an underlying connection between the top quark and the EW symmetry breaking. This value makes the $gg \to H$ via a top-quark loop the dominant production mode for the Higgs boson at the LHC. The experimental determination of this coupling will provide another precision test for the SM and for this reason the $t\bar{t}H$ production has attracted the attention of both the theoretical and experimental communities. This process has the $Y_t$ parameter appearing already at the tree level, which makes the $t\bar{t}H$ production ideal for its determination. The mass of the top quark is connected to the EW symmetry breaking also in another way. The Higgs self coupling (parameter $\lambda$ in eq. 1.19) receives top-quark loop corrections, which are dominant due to the large $Y_t$. The SM running of this parameter drives it to negative values at high energies, which in turn can lead to an unstable vacuum. The energy at which this happens is extremely sensitive to even ~ 1 GeV variations of the top-quark mass, which shows another reason for the need to its precise determination.

The main aspects of the top quark physics, mentioned in the current section, reveal the importance of the research focusing on this particle. We already saw several angles in which new physics can emerge via the top quark. In the following sections we will describe a way to parametrise the appearance of new physics in various processes in a model independent way.

## 1.5 Effective Field Theory

Having seen the structure of the SM and having sketched the calculational framework, we can proceed to introducing the BSM phsics. The weaknesses of the SM as a theory, which are pointed out at the end of section 1.2, provide the motivation for BSM searches. There are numerous models that extend the SM, mostly using the concept of symmetry. Looking at the SM symmetry as a residual of a broken more general symmetric structure, provides many BSM choices. All these models are accompanied with different predictions of particles that are heavy or weakly interacting enough to have escaped detection up to now. An exhaustively studied example of such a theory is Supersymmetry (SUSY), which is built on an extra mirror symmetry between fermions and bosons, predicting heavy spin partners for the existing SM spectrum. Another well studied BSM theory is the 2 Higgs doublet model (2HDM), which predicts the existence of two charged scalars, a CP-odd scalar and a heavier CP-even scalar accompanying the SM Higgs boson. The comparison of specific signatures of these models with experimental data, provides constraints on their parameter space. This comparison needs to be done from the experimental physics collaborations, since they have control of the extremely detailed analyses required to mimic all the technical details of the detector. However in this comparison only a finite number of BSM's can be used, for practical reasons, and they have to be decided prior to the launch of the analysis. At present, there are no theoretical or experimental signs to favour specific BSM's. On top of that, these BSM's are based on different symmetries/assumptions and they are not directly connected to each other parametrically. Even in a case of deviation w.r.t. the SM, there can be a degeneracy of BSM's, which give the same prediction. Therefore it would be advantageous to establish a common language/basis, in which every BSM can be translated into and use this to express any comparison with the SM. Expressing the results of the comparison in this common basis gives the opportunity, after the analysis, to translate them to every BSM benchmark parameter space.

Up to the current time there is no indication of any BSM state at the LHC energy range. This increases the necessity of such a model independent approach. This approach is provided in the Effective Field Theory (EFT) framework. The EFT framework is developed as a gauge invariant way to parametrise the BSM effects in the SM couplings, from any possible state, heavier than the energy probed in the experiment. This section is summary of this method and is based on the [15], [62], [63] and [64] references. The main idea behind the EFT approach is that, if there are new fields at a high energy scale $\Lambda$, they will not resonate at the energy scales of the current experiments. Whatever the BSM theory that describes these fields, they can be integrated out, if one is interested in the non resonant kinematical region. The formalism is based on expanding the SM Lagrangian with higher dimensional operators suppressed by this new energy scale. Assuming Lepton and Baryon number conservation one gets the SMEFT Lagrangian, which is

$$\mathcal{L} = \mathcal{L}_{SM} + \sum_i \frac{C_i^{(6)}}{\Lambda^2} O_i^{(6)} + \sum_j \frac{C_j^{(8)}}{\Lambda^4} O_j^{(8)} + \ldots , \tag{1.40}$$

| $X^3$ | | $\phi^6$ and $\phi^4 D^2$ | | $\psi^2\phi^3$ | |
|---|---|---|---|---|---|
| $O_G$ | $f^{ABC} G_\mu^{A\nu} G_\nu^{B\rho} G_\rho^{C\mu}$ | $O_\phi$ | $(\phi^\dagger\phi)^3$ | $O_{e\phi}$ | $(\phi^\dagger\phi)(\bar\ell_p e_r \phi)$ |
| $O_{\tilde G}$ | $f^{ABC} \tilde G_\mu^{A\nu} G_\nu^{B\rho} G_\rho^{C\mu}$ | $O_{\phi\Box}$ | $(\phi^\dagger\phi)\Box(\phi^\dagger\phi)$ | $O_{u\phi}$ | $(\phi^\dagger\phi)(\bar q_p u_r \tilde\phi)$ |
| $O_W$ | $\varepsilon^{IJK} W_\mu^{I\nu} W_\nu^{J\rho} W_\rho^{K\mu}$ | $O_{\phi D}$ | $(\phi^\dagger D^\mu\phi)^*(\phi^\dagger D^\mu\phi)$ | $O_{d\phi}$ | $(\phi^\dagger\phi)(\bar q_p d_r \phi)$ |
| $O_{\widetilde W}$ | $\varepsilon^{IJK} \widetilde W_\mu^{I\nu} W_\nu^{J\rho} W_\rho^{K\mu}$ | | | | |

| $X^2\phi^2$ | | $\psi^2 X\phi$ | | $\psi^2\phi^2 D$ | |
|---|---|---|---|---|---|
| $O_{\phi G}$ | $\phi^\dagger\phi G_{\mu\nu}^A G^{A\mu\nu}$ | $O_{eW}$ | $(\bar\ell_p\sigma^{\mu\nu}e_r)\tau^I\phi W_{\mu\nu}^I$ | $O_{\phi\ell}^{(1)}$ | $(\phi^\dagger i\overleftrightarrow{D}_\mu\phi)(\bar\ell_p\gamma^\mu\ell_r)$ |
| $O_{\phi\tilde G}$ | $\phi^\dagger\phi \tilde G_{\mu\nu}^A G^{A\mu\nu}$ | $O_{eB}$ | $(\bar\ell_p\sigma^{\mu\nu}e_r)\phi B_{\mu\nu}$ | $O_{\phi\ell}^{(3)}$ | $(\phi^\dagger i\overleftrightarrow{D}_\mu^I\phi)(\bar\ell_p\tau^I\gamma^\mu\ell_r)$ |
| $O_{\phi W}$ | $\phi^\dagger\phi W_{\mu\nu}^I W^{I\mu\nu}$ | $O_{uG}$ | $(\bar q_p\sigma^{\mu\nu}T^A u_r)\tilde\phi G_{\mu\nu}^A$ | $O_{\phi e}$ | $(\phi^\dagger i\overleftrightarrow{D}_\mu\phi)(\bar e_p\gamma^\mu e_r)$ |
| $O_{\phi\widetilde W}$ | $\phi^\dagger\phi \widetilde W_{\mu\nu}^I W^{I\mu\nu}$ | $O_{uW}$ | $(\bar q_p\sigma^{\mu\nu}u_r)\tau^I\tilde\phi W_{\mu\nu}^I$ | $O_{\phi q}^{(1)}$ | $(\phi^\dagger i\overleftrightarrow{D}_\mu\phi)(\bar q_p\gamma^\mu q_r)$ |
| $O_{\phi B}$ | $\phi^\dagger\phi B_{\mu\nu}B^{\mu\nu}$ | $O_{uB}$ | $(\bar q_p\sigma^{\mu\nu}u_r)\tilde\phi B_{\mu\nu}$ | $O_{\phi q}^{(3)}$ | $(\phi^\dagger i\overleftrightarrow{D}_\mu^I\phi)(\bar q_p\tau^I\gamma^\mu q_r)$ |
| $O_{\phi\widetilde B}$ | $\phi^\dagger\phi \widetilde B_{\mu\nu}B^{\mu\nu}$ | $O_{dG}$ | $(\bar q_p\sigma^{\mu\nu}T^A d_r)\phi G_{\mu\nu}^A$ | $O_{\phi u}$ | $(\phi^\dagger i\overleftrightarrow{D}_\mu\phi)(\bar u_p\gamma^\mu u_r)$ |
| $O_{\phi WB}$ | $\phi^\dagger\tau^I\phi W_{\mu\nu}^I B^{\mu\nu}$ | $O_{dW}$ | $(\bar q_p\sigma^{\mu\nu}d_r)\tau^I\phi W_{\mu\nu}^I$ | $O_{\phi d}$ | $(\phi^\dagger i\overleftrightarrow{D}_\mu\phi)(\bar d_p\gamma^\mu d_r)$ |
| $O_{\phi\widetilde WB}$ | $\phi^\dagger\tau^I\phi \widetilde W_{\mu\nu}^I B^{\mu\nu}$ | $O_{dB}$ | $(\bar q_p\sigma^{\mu\nu}d_r)\phi B_{\mu\nu}$ | $O_{\phi ud}$ | $i(\tilde\phi^\dagger D_\mu\phi)(\bar u_p\gamma^\mu d_r)$ |

| $(\bar LL)(\bar LL)$ | | $(\bar RR)(\bar RR)$ | | $(\bar LL)(\bar RR)$ | |
|---|---|---|---|---|---|
| $O_{\ell\ell}$ | $(\bar\ell_p\gamma_\mu\ell_r)(\bar\ell_s\gamma^\mu\ell_t)$ | $O_{ee}$ | $(\bar e_p\gamma_\mu e_r)(\bar e_s\gamma^\mu e_t)$ | $O_{\ell e}$ | $(\bar\ell_p\gamma_\mu\ell_r)(\bar e_s\gamma^\mu e_t)$ |
| $O_{qq}^{(1)}$ | $(\bar q_p\gamma_\mu q_r)(\bar q_s\gamma^\mu q_t)$ | $O_{uu}$ | $(\bar u_p\gamma_\mu u_r)(\bar u_s\gamma^\mu u_t)$ | $O_{\ell u}$ | $(\bar\ell_p\gamma_\mu\ell_r)(\bar u_s\gamma^\mu u_t)$ |
| $O_{qq}^{(3)}$ | $(\bar q_p\gamma_\mu\tau^I q_r)(\bar q_s\gamma^\mu\tau^I q_t)$ | $O_{dd}$ | $(\bar d_p\gamma_\mu d_r)(\bar d_s\gamma^\mu d_t)$ | $O_{\ell d}$ | $(\bar\ell_p\gamma_\mu\ell_r)(\bar d_s\gamma^\mu d_t)$ |
| $O_{\ell q}^{(1)}$ | $(\bar\ell_p\gamma_\mu\ell_r)(\bar q_s\gamma^\mu q_t)$ | $O_{eu}$ | $(\bar e_p\gamma_\mu e_r)(\bar u_s\gamma^\mu u_t)$ | $O_{qe}$ | $(\bar q_p\gamma_\mu q_r)(\bar e_s\gamma^\mu e_t)$ |
| $O_{\ell q}^{(3)}$ | $(\bar\ell_p\gamma_\mu\tau^I\ell_r)(\bar q_s\gamma^\mu\tau^I q_t)$ | $O_{ed}$ | $(\bar e_p\gamma_\mu e_r)(\bar d_s\gamma^\mu d_t)$ | $O_{qu}^{(1)}$ | $(\bar q_p\gamma_\mu q_r)(\bar u_s\gamma^\mu u_t)$ |
| | | $O_{ud}^{(1)}$ | $(\bar u_p\gamma_\mu u_r)(\bar d_s\gamma^\mu d_t)$ | $O_{qu}^{(8)}$ | $(\bar q_p\gamma_\mu T^A q_r)(\bar u_s\gamma^\mu T^A u_t)$ |
| | | $O_{ud}^{(8)}$ | $(\bar u_p\gamma_\mu T^A u_r)(\bar d_s\gamma^\mu T^A d_t)$ | $O_{qd}^{(1)}$ | $(\bar q_p\gamma_\mu q_r)(\bar d_s\gamma^\mu d_t)$ |
| | | | | $O_{qd}^{(8)}$ | $(\bar q_p\gamma_\mu T^A q_r)(\bar d_s\gamma^\mu T^A d_t)$ |

| $(\bar LR)(\bar RL)$ and $(\bar LR)(\bar LR)$ | | $B$-violating | |
|---|---|---|---|
| $O_{\ell edq}$ | $(\bar\ell_p^j e_r)(\bar d_s q_t^j)$ | $O_{duq}$ | $\varepsilon^{\alpha\beta\gamma}\varepsilon_{jk}[(d_p^\alpha)^T C u_r^\beta][(q_s^{\gamma j})^T C\ell_t^k]$ |
| $O_{quqd}^{(1)}$ | $(\bar q_p^j u_r)\varepsilon_{jk}(\bar q_s^k d_t)$ | $O_{qqu}$ | $\varepsilon^{\alpha\beta\gamma}\varepsilon_{jk}[(q_p^{\alpha j})^T C q_r^{\beta k}][(u_s^\gamma)^T C e_t]$ |
| $O_{quqd}^{(8)}$ | $(\bar q_p^j T^A u_r)\varepsilon_{jk}(\bar q_s^k T^A d_t)$ | $O_{qqq}$ | $\varepsilon^{\alpha\beta\gamma}\varepsilon_{jn}\varepsilon_{km}[(q_p^{\alpha j})^T C q_r^{\beta k}][(q_s^{\gamma m})^T C\ell_t^n]$ |
| $O_{\ell equ}^{(1)}$ | $(\bar\ell_p^j e_r)\varepsilon_{jk}(\bar q_s^k u_t)$ | $O_{duu}$ | $\varepsilon^{\alpha\beta\gamma}[(d_p^\alpha)^T C u_r^\beta][(u_s^\gamma)^T C e_t]$ |
| $O_{\ell equ}^{(3)}$ | $(\bar\ell_p^j\sigma_{\mu\nu}e_r)\varepsilon_{jk}(\bar q_s^k\sigma^{\mu\nu}u_t)$ | | |

Table 1.5: Top: 6-dim operators mixing fermionic with bosonic fields . Bottom: 6-dim 4-fermion operators. Table taken from [66].

where the parameters $C_i^{(d)}$ are called Wilson coefficients and they quantify the significance of each operator in this expansion. On top of being gauge invariant, this framework is renormalisable under QCD and EW corrections order by order in the $(1/\Lambda)$ expansion. However this series is infinite and the number of operators, even at the lowest order of the expansion, is of the order of $\sim 3000$ [65], [66]. Using the equations of motion one can establish a basis of an independent set of operators at each dimension. As mentioned before, any BSM heavy state is supposed to be integrated out, therefore all the operators are constructed from the SM fields. Any possible combination is allowed as long as the SM symmetries and the corresponding dimensionality are respected. This is what makes even the final independent operator-basis to be of the size of 59 operators. In table 1.5 one can see the 6-dimensional SMEFT operators mixing the fermions with the bosons and separately the pure fermionic ones. The 8-dimensional corresponding basis is much larger, but this group of terms is subleading in the $(1/\Lambda)$ expansion w.r.t. the 6-dimensional one, so it is not included in the EFT analyses. The same is done in the current research and from now on we will focus only to the dim-6 leading group of terms of equation 1.40. One should note that this is true only if the main assumption holds, i.e. the scale $\Lambda$ is higher than the energy probed in the experiment.

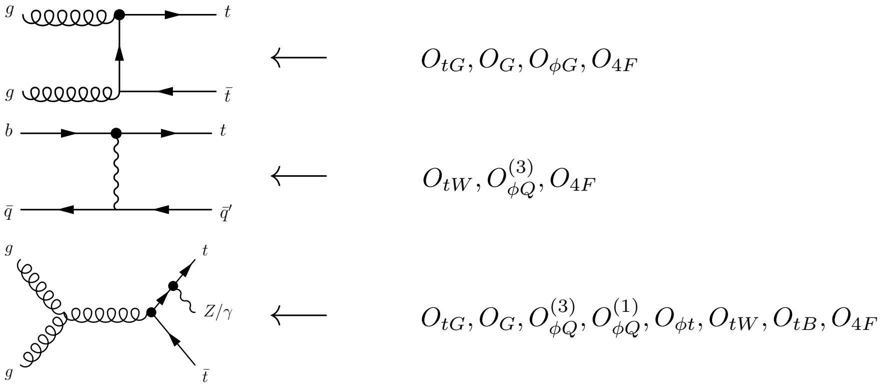

Figure 1.15: Representative Feymnan diagrams of $t\bar{t}$, $t$-channel single top and $t\bar{t}Z/\gamma$ processes with the relevant operators in each case. The black blobs indicate possible vertices in which some of the operators contribute.

Being model independent requires a price to pay, which is connected to the number of the independent operators. There is no physical reason to assume *a priori* that one or more $C_i^{(d)}$'s are zero at the $\Lambda$ or the EW scale. Since one cannot be selective on the effect of a possible new heavy state, the EFT analysis should be global. This implies that in a process by process basis one needs to include all the relevant operators that enter the corresponding couplings. As an example we show in figure 1.15 the 6-dimensional operators entering the $t\bar{t}$, $t$-channel single top and $t\bar{t}$ associated with a neutral vector boson. The more the operators contributing to a process, the more difficult is to constrain them, because naturally one needs more observables for a global fit.

As a result, in many cases, in order to simplify the analysis and the calculation some of the Wilson coefficients are assumed to be zero at the scale $\Lambda$. However, as we will see in the following, this assumption is not valid if there are mixing effects with other operators. At this stage one needs to be careful because the $C_i$'s can be understood as new coupling constants. Once we proceed to the NLO QCD corrections in the Lagrangian of equation 1.40, not only the SM coupling contants, but also the $C_i$'s will be renormalised and the corresponding RGEs will emerge as following

$$\frac{dC_i}{d\log\mu} = \gamma_{ij} C_j \ . \tag{1.41}$$

This set of equations describes the running of the $C_i$'s from the high scale $\Lambda$ down to the process scale $\sqrt{\hat{s}}$ and during this the mixing among the operators occurs as

$$C_i(\sqrt{\hat{s}}) = \left(\delta_{ij} + \gamma_{ij} \log \frac{\sqrt{\hat{s}}}{\Lambda}\right) C_j(\Lambda) \ . \tag{1.42}$$

The anomalous dimension matrix $\gamma$ is neither diagonal nor symmetric. This implies that even if one assumes that a Wilson coefficient $C_i$ is zero at the scale $\Lambda$, it may no longer be zero at the low $\sqrt{\hat{s}}$ scale due to $\propto \gamma_{ij} C_j(\Lambda)$ contributions from other operators. In this sense we say that a $C_i$ operator mixes into the $C_j$ one (see [67] for detailed examples). On top of that, this does not imply also the opposite. As a result, the assumption that $C_i = 0$ is meaningful only if this operator does not mix into others (non zero ones), because the latter would imply that from their contributions it will not be zero at the low scale.

Moving from the Lagrangian level to the observables, the limits on the Wilson coefficients are set after fitting the global and differential level cross sections of one or more processes with the experimental data. It is interesting to notice that these limits for each coefficient are not applied only to the $C_i$, but actually to the $C_i/\Lambda^2$. These two quantities cannot be disentangled unless one considers a specific UV BSM theory that describes the physics at the scale $\Lambda$. The mapping between the Wilson coefficients and the parameters of the UV theory is called matching. Having done this, the constraints acquire a physical meaning, since they are translated to the parameter space of the UV theory, describing BSM heavy particles of masses at the order of $\Lambda$.

In this chapter we have introduced the mathematical framework of the SM. We briefly discussed the features of the higher order calculations and the tools, which were used for this research. Finally we have introduced the EFT framework as a model independent BSM approach. In the following chapters we proceed with presenting and discussing the results of this research.

# 2 | $t\bar{t}$ production with QCD+EW corrections

There are great efforts which have been put in place in order to improve the accuracy of theoretical predictions: inclusive and differential cross-sections have been calculated up to Next-to-Next-to-Leading-Order (NNLO) accuracy in QCD [58,68], and soft gluon effects have been included up to Next-to-Next-to-Leading-Logarithmic (NNLL) accuracy [69–80]. Notably, higher-order QCD corrections lead to the reduction of scale uncertainties down to very few percents. At this level of accuracy effects due to Electro-Weak (EW) corrections cannot be neglected, especially for differential distributions, where the expected hierarchy between the strong and electroweak interactions may not be respected. On the one hand, when large scales are probed ($Q \gg m_W$), the so-called Sudakov logarithms render EW corrections large and negative. On the other hand, EW corrections receive also contributions from channels that feature photons in the initial state, thus they depend on the PDF of the photon. As we will show in this chapter, the impact of photons in the initial state strongly depends on the PDF set employed and can give a positive contribution of non-negligible size, leading to possible compensations of the corrections induced by Sudakov logarithms. It should be stressed that when these kind of compensations appear, they are not theoretically expected. These two effects are of different nature, hence the possible compensations are accidental. While weak [81–89], QED [90] and EW (weak+QED) [91–94] corrections to $t\bar{t}$ production at hadron colliders have been known for quite some time and the effect of Sudakov logarithms has been quantified and studied, the impact of photon-induced subprocesses has been addressed only in [90] for only the $g\gamma \to t\bar{t}$ channel at LO and using the only PDF set with the photon distribution available at that time, *i.e.*, MRST2004QED [95].

In this chapter we firstly evaluate, besides the NLO QCD corrections, the complete set of NLO EW corrections to top-quark pair production and carefully assess their impact on differential distributions for proton–proton collisions at 8, 13 and 100 TeV centre-of-mass energy. For the first time, photon-induced contributions are taken into account both at $\mathcal{O}(\alpha_s\alpha)$, from the $g\gamma$-channel at tree-level, and at $\mathcal{O}(\alpha_s^2\alpha)$, from the $g\gamma$ as well as the $q\gamma(\bar{q}\gamma)$ initial states arising in the NLO EW corrections. In order to have a reliable estimate of the photon-induced contribution and of its uncertainties, we evaluate the impact of electroweak corrections with both the NNPDF2.3QED [96] and CT14QED [97] PDF sets, the only modern sets that include LO QED contribution in the

DGLAP evolution and, with very different assumptions and strategies in the extraction from data, the photon distribution [5].

We show that, besides higher-order QCD corrections, it is also necessary to take into account EW corrections, including photon-induced contributions, for a correct determination of both the central value and the uncertainty of theoretical predictions. This is particularly important in the context of the ongoing discussion on NLO-accurate event generators and the compatibility with experimental data for the $p_T(t)$ distribution at the LHC 8-TeV measurements [100] and in view of the measurements at 13 TeV. Furthermore, we show that differential observables in top-pair production, in particular top-quark and $t\bar{t}$ rapidities, can be used to improve the determination of the photon PDF within the NNPDF approach, while in the CT14QED approach $t\bar{t}$ production is not sensitive to the photon-induced contributions. Finally we proceed to consistently merging existing NNLO QCD predictions with EW corrections into a single coherent prediction and to study its phenomenological impact. Using the same calculation framework of sec 2.1, NNLO QCD predictions from ref [101] are combined with the complete LO and NLO contributions.

The structure of this chapter is the following: in sect. 2.1 we present the framework employed to perform our calculation and discuss relevant input parameters. In sect. 2.2 we discuss differences among existing PDF sets which provide a photon distribution (NNPDF2.3QED, CT14QED and the older MRST-2004QED set). We describe the different theoretical approaches employed in the sets, and we compare central values and uncertainties for the photon PDF and the parton luminosities relevant for our calculation. In sect. 2.3 we show predictions at 13 and 100 TeV, and we compare results with and without the contribution of photon-induced processes and using the NNPDF2.3QED or the CT14QED PDF set. In sect. 2.4 we analyse the impact of EW corrections and the photon PDF for specific measurements performed by ATLAS and CMS at 8 TeV. We compare the usage of NNPDF2.3QED with a standard modern set with QCD-only partons and DGLAP evolution. In section 2.5 we discuss the results at NNLO QCD + NLO EW accuracy. We present predictions for top-pair differential distributions at the LHC based on the LUXQED [98] and NNPDF3.0QED [102] PDF sets. We give our conclusions and outlook in sect. 2.6.

This chapter includes results that are public and available at [9, 13], and are obtained in collaboration with D. Pagani and M. Zaro. The results of section 2.5 are obtained in further collaboration with M. Czakon, D. Heymes and A. Mitov and are available in [10].

---

[5] We acknowledge that two new studies on the determination of the photon PDF [98, 99] have appeared during the publication of the results of the first part of the chapter and are used in section 2.5.

## 2.1 Calculation setup and input parameters

The calculation has been performed in a completely automated way and we do not describe here the technical details; they can be found in [40,41], where the $t\bar{t}H$ process has been calculated in the same framework. In the following, we only want to match the notation of this chapter to the one introduced in [40] and precisely define the quantities included in our calculation, specifying those that depend on the photon PDF.

In the case of $pp \to t\bar{t}$ process a generic observable $\Sigma^{t\bar{t}}$ can be expanded simultaneously in the QCD and EW coupling constants as:

$$\Sigma^{t\bar{t}}(\alpha_s,\alpha) = \sum_{m+n\geq 2} \alpha_s^m \alpha^n \Sigma_{m+n,n}\,. \tag{2.1}$$

Following this notation, one can separate the LO ($m+n = 2$) and NLO ($m+n = 3$) contributions as follows:

$$\begin{aligned}
\Sigma^{t\bar{t}}_{\mathrm{LO}}(\alpha_s,\alpha) &= \alpha_s^2\Sigma_{2,0} + \alpha_s\alpha\Sigma_{2,1} + \alpha^2\Sigma_{2,2} \equiv \\
&\equiv \Sigma_{\mathrm{LO},1} + \Sigma_{\mathrm{LO},2} + \Sigma_{\mathrm{LO},3}\,, \\
\Sigma^{t\bar{t}}_{\mathrm{NLO}}(\alpha_s,\alpha) &= \alpha_s^3\Sigma_{3,0} + \alpha_s^2\alpha\Sigma_{3,1} + \alpha_s\alpha^2\Sigma_{3,2} + \alpha^3\Sigma_{3,3} \equiv \\
&\equiv \Sigma_{\mathrm{NLO},1} + \Sigma_{\mathrm{NLO},2} + \Sigma_{\mathrm{NLO},3} + \Sigma_{\mathrm{NLO},4}\,.
\end{aligned} \tag{2.2}$$

In our results we include the $\Sigma_{\mathrm{LO},1}$, $\Sigma_{\mathrm{LO},2}$, $\Sigma_{\mathrm{NLO},1}$ and $\Sigma_{\mathrm{NLO},2}$ terms. We checked that the remaining terms are subleading as expected, giving results of the order or below 1% of the LO,1 contribution both in the total cross section and at the differential level. In order to help the reader we further define the quantities

$$\Sigma_{\mathrm{LO\ QCD}} \equiv \Sigma_{\mathrm{LO},1}\,, \qquad \Sigma_{\mathrm{NLO\ QCD}} \equiv \Sigma_{\mathrm{NLO},1}\,, \tag{2.3}$$

$$\Sigma_{\mathrm{LO\ EW}} \equiv \Sigma_{\mathrm{LO},2}\,, \qquad \Sigma_{\mathrm{NLO\ EW}} \equiv \Sigma_{\mathrm{NLO},2}\,, \tag{2.4}$$

$$\Sigma_{\mathrm{QCD}} \equiv \Sigma_{\mathrm{LO\ QCD}} + \Sigma_{\mathrm{NLO\ QCD}}\,, \tag{2.5}$$

$$\Sigma_{\mathrm{EW}} \equiv \Sigma_{\mathrm{LO\ EW}} + \Sigma_{\mathrm{NLO\ EW}}\,, \tag{2.6}$$

$$\Sigma_{\mathrm{QCD+EW}} \equiv \Sigma_{\mathrm{QCD}} + \Sigma_{\mathrm{EW}}\,. \tag{2.7}$$

In the following text with the term “EW corrections” we will in general refer to the quantity $\Sigma_{\mathrm{EW}}$, while we will use “NLO EW corrections” for $\Sigma_{\mathrm{NLO\ EW}}$. At variance with refs. [40, 41], in our calculation we do not consider the effect due to the Heavy-Boson-Radiation (HBR). Although the LO cross sections of

$pp \to t\bar{t}V$, $V = W^{\pm}, Z, H$ processes may in principle contribute at the same perturbative order of $\Sigma_{\text{NLO EW}}$ to the inclusive $t\bar{t}$ production, in this chapter we assume that $t\bar{t}$ and $t\bar{t}V$ final states can always be distinguished. However this effect is calculated and discussed in section 2.5.

The quantities that depend on the photon PDF are $\Sigma_{\text{LO EW}}$ and $\Sigma_{\text{NLO EW}}$. The $g\gamma \to t\bar{t}$ process contributes to $\Sigma_{\text{LO EW}}$ and to $\Sigma_{\text{NLO EW}}$. In addition, $\Sigma_{\text{NLO EW}}$ receives contributions from the $q\gamma \to t\bar{t}q$ and $\bar{q}\gamma \to t\bar{t}\bar{q}$ processes at the tree level, which feature initial-state singularities that have to be subtracted. As in the case of $q\bar{q} \to t\bar{t}\gamma$ processes, the subtracted QED singularities are taken into account in the DGLAP evolution in MRST2004QED, NNPDF-2.3QED and CT14QED. Thus, for theoretical consistency, these three PDF sets should be preferred whenever NLO EW corrections are computed. However, since the QED accuracy of DGLAP evolution is only LO in all the three PDF sets, one could not technically claim at the moment NLO QED and thus NLO EW accuracy for hadronic predictions. Even before considering the numerical results in sects. 2.3 and 2.4, this issue points to the necessity of a better determination of the photon PDF by means of fits which include NLO QED effects in the DGLAP evolution [103, 104].

Our calculation is performed using the following input parameters

$$\begin{aligned} m_t &= 173.3 \text{ GeV}, \quad m_H = 125.09 \text{ GeV}, \\ m_W &= 80.385 \text{ GeV}, \quad m_Z = 91.1876 \text{ GeV}, \end{aligned} \tag{2.8}$$

and setting all the other fermion masses to zero. All masses are renormalised on-shell and all decay widths are set to zero. The renormalisation of $\alpha_s$ is performed in the five-flavour scheme, while EW parameters are chosen in the $G_\mu$-scheme, with

$$G_\mu = 1.1663787 \cdot 10^{-5} \text{ GeV}^{-2}. \tag{2.9}$$

Since NLO EW corrections of $\mathcal{O}(\alpha_s^2\alpha)$ to $t\bar{t}$ hadroproduction do not involve the renormalisation of $\alpha$, the choice of a different EW scheme will not change our results in a visible way. The CKM matrix is approximated by the identity.

Unless differently specified, we use a dynamical reference scale for the central values of the renormalisation ($\mu_r$) and factorisation ($\mu_f$) scales defined as

$$\mu = \frac{H_T}{2} = \frac{1}{2}\sum_i m_{T,i}\,, \tag{2.10}$$

where the sum of the transverse masses runs over all the final-state particles. In all cases theoretical uncertainties due to missing higher orders are estimated via independent variations of $\mu_r$ and $\mu_f$ in the interval $\{\mu/2, 2\mu\}$.

It is worth to note that the NNPDF2.3QED set is in the variable-flavour scheme with six active flavours, which for $\mu > m_t$ is equivalent to the six-flavour

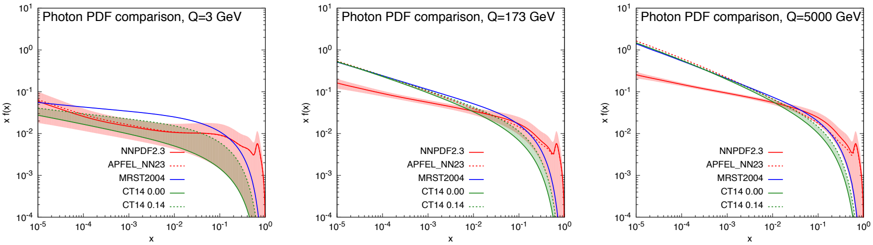

Figure 2.1: Comparison of the photon PDF for MRST2004QED, CT14QED, NNPDF2.3QED and APFEL_NN23 sets at $Q = 3$ GeV, $Q = 173$ GeV and $Q = 5000$ GeV.

scheme. On the contrary, in CT14QED the active flavours are five, leading to the five-flavour scheme also for $\mu > m_t$. As we said, we renormalise $\alpha_s$ in the five-flavour scheme for all the predictions; for the comparison between the NNPDF2.3QED and CT14QED results we simply change the PDF set without modifying the calculation framework. The change of scheme can be easily performed by following the recipe described in [105] and based on [106], which, at NLO QCD + NLO EW accuracy, has a direct effect only on the $q\bar{q}$-induced contribution to $\Sigma_{\text{NLO QCD}}$. We explicitly verified that the numerical impact of such a change of renormalisation scheme is always much smaller of the scale uncertainty and furthermore cancels in any ratio involving $\Sigma_{\text{NLO QCD}}$ both at the numerator and the denominator. Thus, it has not any influence on the discussion presented in this chapter.

## 2.2 Photon PDF and parton luminosities

In this section we discuss in some details the different modelling of the photon PDF in the NNPDF2.3QED, CT14QED[6] and MRST2004QED sets.

Although for all the three PDF sets the DGLAP evolution is performed at NLO QCD + LO QED accuracy [7], very different and crucial assumptions un-

---

[6] CT14QED provides two kinds of sets, one with only the incoherent component of the photon PDF and another one with both the coherent and incoherent components. In this work we have used the first set. We have checked that the inclusion of the coherent component in the photon PDF does not significantly alter our findings. The predictions obtained with the photon PDF with momentum fraction $p_0^\gamma = 0.00\%$ including both components are very similar, in the $x$ and $Q$ ranges relevant for our study, to those from the incoherent-only photon PDF with $p_0^\gamma = 0.14\%$.

[7] In the case of NNPDF2.3QED, PDFs at NNLO QCD + LO QED accuracy as well as at LO QCD + LO QED accuracy are also available. However we considered here only the NLO QCD + LO QED case, consistently with the other PDF sets discussed.

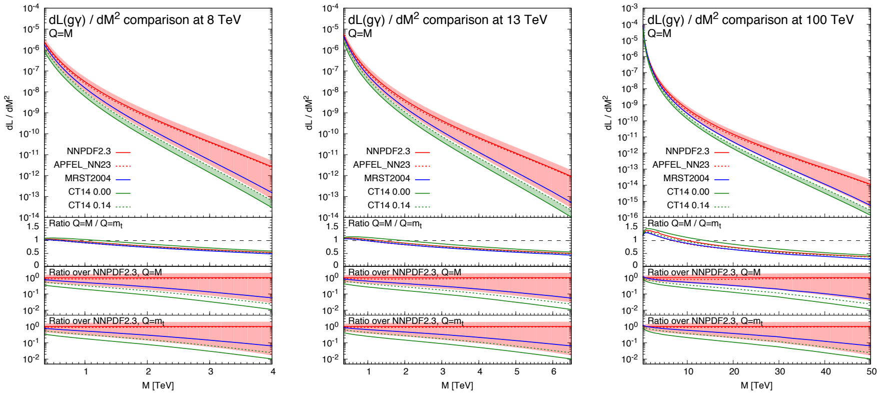

Figure 2.2: Comparison of the $g\gamma$ luminosity for MRST2004QED, CT14QED, NNPDF2.3QED and APFEL_NN23 sets at 8, 13 and 100 TeV.

derlie the determination of the photon PDF $\gamma(x, Q)$. These differences mainly concern the following three aspects. First, the ansatz for $\gamma(x, Q)$ at the initial scale $Q = Q_0$. Second, the different datasets which are used in the fit. Third, the practical implementation of the DGLAP evolution from the initial scale $Q_0$ to the scale $Q$.

In fig. 2.1 we show the photon PDF for the different sets at the scales $Q = (3, 173, 5000)$ GeV. As it can be seen, these assumptions affect the dependence on $x$ and $Q$ for both the central value and the uncertainty band [8]. The main reasons for the differences can be traced to the different assumption for the photon PDF at the initial scale and in differences in the QCD+QED evolution. In particular:

- Consistently with the approach pursued for coloured partons, in NNPDF-2.3QED no functional form is specified for the photon PDF at the initial scale, $\gamma(x, Q_0)$. The photon PDF is only constrained to be positive. In a first step, PDF replicas for all the partons are fit together from DIS-data only. Afterwards, they are further constrained by Drell-Yan data form the LHC Run-I at 7 TeV. At variance with DIS, neutral-current Drell-Yan (fig. 2.4) is sensitive to the photon PDF already at LO, and it can put stronger constraints on $\gamma(x, Q_0)$. Because of the positivity requirement for the photon PDF, the replicas distribute in a very non-Gaussian way around the central value. The prescription suggested in order to determine a 68% CL uncertainty band consists in the evaluation of the symmetric error including 68 of the 100 replicas around the central value. Since no model is assumed for the photon PDF and no data are

---

[8] The red dotted curve labelled as APFEL_NN23 will be explained after in the text.

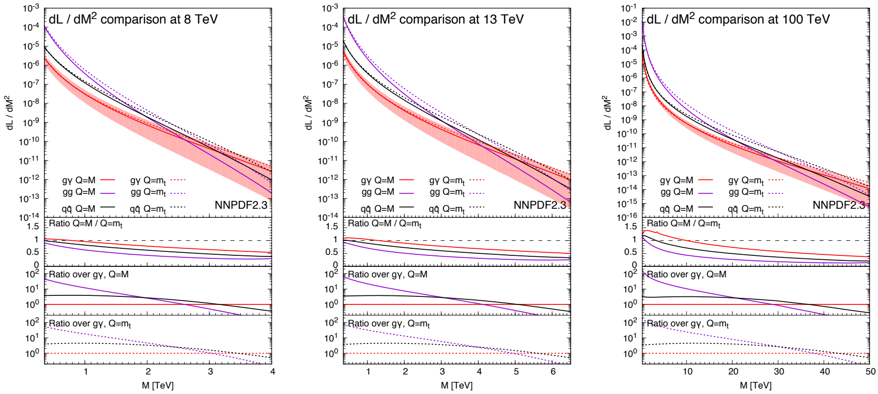

Figure 2.3: Comparison of the $g\gamma$, $gg$ and $q\bar{q}$ luminosities for the NNPDF2.3-QED set at 8, 13 and 100 TeV.

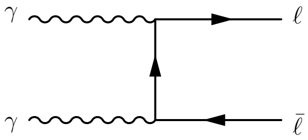

Figure 2.4: Photon-induced neutral current Drell-Yan LO diagram.

present for large $x$, in this region uncertainties are very large and the central value alone can be misleading, leading even to an unphysical peak at very large $x$, which can be seen in fig. 2.1.

- The CT14QED and MRST2004QED sets are based on a completely different assumption for $\gamma(x, Q)$ at the initial scale $Q = Q_0$. Since the amount of data for constraining the shape of the photon PDF is limited, $\gamma(x, Q_0)$ is chosen to be described by an ansatz; the photon PDF at $Q = Q_0$ is assumed to be completely determined by the valence quark distributions. Specifically, in CT14QED and MRST2004QED the photon parameterisation at the initial scale $Q_0$ GeV reads

$$f_{\gamma/p}(x, Q_0) \;=\; \frac{\alpha}{2\pi}\left(A_u e_u^2 \tilde{P}_{\gamma q} \otimes u^0(x) + A_d e_d^2 \tilde{P}_{\gamma q} \otimes d^0(x)\right) . \qquad (2.11)$$

In eq. (2.11) $\tilde{P}_{\gamma q} \otimes f^0(x)$ corresponds to the convolution of the splitting function $\tilde{P}_{\gamma q}(x)$ with the so-called "primordial" quark distributions $f^0(x)$. In the case of MRST2004QED, $f^0(x)$ are valence-like model distributions, *i.e.*, they are not those fitted within the global MRST2004 [107] analysis.

In the case of CT14QED, $f^0(x)$ correspond to the initial up and down valence distributions from CT14NLO [108].

More importantly, in CT14QED $A_u$ is set equal to $A_d$ in order to obtain a dependence on a single parameter. Conversely, in MRST2004QED, the coefficients $A_i$ are given by $A_i = \ln\left(Q_0^2/m_i^2\right)$, where $m_i$ are the "Current Mass" (CM) of the quarks ($m_u = 6$ MeV and $m_d = 10$ MeV). Thus, the case of CT14QED is a generalisation of the original ansatz used in MRST2004QED, where the photon PDF is simply determined by the CM for the up and the down quark. The CT14QED set leaves freedom for the value of $m_i$ in the $A_i$ coefficients, which can be alternatively parameterised by the momentum fraction $p_\gamma^0$ carried by the photon at the initial scale. The constraints on $p_\gamma^0$ and consequently on the photon PDF are then obtained by fitting the ZEUS data [109] for the production of isolated photons in Deep-Inelastic-Scattering (DIS), $ep \to e\gamma + X$, a process which is sensitive to the photon PDF already at LO. In this way, the constraint $p_0^\gamma \lesssim 0.14\%$ is set at 90% CL for the photon PDF, at the initial scale of $Q_0 = 1.295$ GeV. For this reason, the uncertainty band in CT14QED corresponds to the area between the $p_0^\gamma = 0.14\%$ and $p_0^\gamma = 0\%$ predictions; no central, or preferred value is given in this approach. Since in MRST2004QED the photon PDF is simply determined from the quark PDF assuming CM for the up and the down quark, no uncertainty band is provided. Moreover, for this set, no constraints from data enter in the determination of the photon PDF.

- All three PDF sets implement the DGLAP evolution at NLO QCD+LO QED accuracy. However, while the scale is evolved simultaneously with the same value for the QCD and QED evolution in CT14QED and MRST2004QED, in NNPDF2.3QED the two evolutions are done independently. The effect from the different evolution can be seen by comparing the plots in fig. 2.1, which display the same quantities at different factorisation scales. At $Q = 3$ GeV the central values of the three sets are different, although the CT14QED and NNPDF2.3QED photons are well compatible within the uncertainty. At large $Q$, while CT14QED and MRST2004QED converge to similar values, the prediction from NNPDF-2.3QED is different. This trend is particularly visible at small $x$ and for large scales, where the photon PDF mostly stems from the quark densities via the DGLAP evolution. However, it is worth to remind that a new correct implementation of the coupled QCD+QED DGLAP equations is now also available in APFEL [110] and has been described in [111] in the context of the determination of new sets of PDFs including also lepton members. [9] In fig. 2.1 we included also a red dashed line labelled APFEL_NN23, which corresponds to the central value for the set denoted as "C2" in [111]. This set is the same of NNPDF2.3QED at the initial scale $Q_0 = 1$ GeV, but it is different at larger scales due to the different treatment of the evolution. Indeed, the photon PDF in APFEL_NN23 is very close to the one of NNPDF2.3QED only at large $x$, while for small $x$ and large $Q$ it converges to the values of CT14QED and MRST2004QED. This proves that the discrepancy between the different sets at small $x$ and large $Q$ is completely driven by the different treatment of the DGLAP evolution.

In fig. 2.2 we show the photon-gluon luminosity as function of the invariant mass $M$ for the three PDF sets considered at 8, 13 and 100 TeV, with the factorisation scale $Q$ set equal to $M$. In the first inset we show for every luminosity the ratio of their values at $Q = M$ and $Q = m_t$, while in the second(third) inset we show at $Q = M(Q = m_t)$ the ratio of every luminosity over the corresponding central value with NNPDF2.3QED. For the entire range in $M$ considered at the three different proton-proton-collision energies, the CT14QED and NNPDF2.3QED photon-gluon luminosities are barely compatible or not compatible at all. The slightly better compatibility with $Q = m_t$ is mainly due to the larger uncertainty band in NNPDF2.3QED.

It is important to note that the behaviour of the photon PDF at small $x$ and large $Q$, the region where differences among the PDF sets are the largest (see fig. 2.1) and are determined by the different QCD+QED DGLAP evolution, is not of particular interest for our study. Indeed, as can be seen in fig. 2.2, the APFEL_NN23 $g\gamma$ luminosity is very close to the NNPDF2.3QED one and inside its uncertainty band. The insensitivity of our study on the different treatment of QCD+QED DGLAP running is in principle expected for most of the predictions at the LHC, since large factorisation scales $Q$ are typically not correlated with small values of $x$. Moreover, at small values of $M$, where small values of $x$ can be probed, the PDFs of quarks and gluons are much larger than the photon PDF, leading to a relative suppression of photon-initiated contributions.

In order to determine at which values of $M$ the photon–gluon luminosity is actually expected to be relevant in $t\bar{t}$ hadroproduction, in fig. 2.3 we show the photon-gluon, gluon-gluon and quark-antiquark luminosities for NNPDF-

---

[9] During the writing of this chapter also a new set NNPDF3.0QED has been released [112] and it includes the correct DGLAP running at (N)NLO QCD + LO QED accuracy.

2.3QED sets at 8, 13 and 100 TeV. These plots will also become useful to understand the dependence of $\Sigma_{\mathrm{EW}}/\Sigma_{\mathrm{LO\ QCD}}$ on the scale definition. [10]

The solid lines refer to the luminosities with $Q = M$, with the uncertainty band shown only for the photon-gluon case. The same-colour dashed lines are the corresponding quantities with $Q = m_t$. The ratios between predictions with $Q = M$ and with $Q = m_t$ is shown in the first inset. The luminosities at $Q = M$ are in general of the same order or smaller than at $Q = m_t$, with the exception of the 100 TeV case for $M \lesssim 10$ TeV. In particular at 8 and 13 TeV, in the range of $M \lesssim 1$ TeV the luminosities of $gg$ and $q\bar{q}$ strongly reduce at $Q = M$ with respect to $Q = m_t$, while the photon-gluon luminosity is less sensitive to the value of $Q$. Since in the TeV range the negative contributions from Sudakov logarithms in the $gg$ and $q\bar{q}$ channels and the positive photon-gluon contribution tend to cancel each other, larger scales lead to larger values of $\Sigma_{\mathrm{EW}}/\Sigma_{\mathrm{LO\ QCD}}$. This effect will be discussed both in sect. 2.3 for predictions at 13 TeV and in sect. 2.4, where the $\Sigma_{\mathrm{QCD+EW}}/\Sigma_{\mathrm{QCD}}$ ratio will be compared to the experimental accuracy reached at the LHC measurements at 8 TeV. In the second(third) insets we also show the ratios of the $gg$ and $q\bar{q}$ luminosities over the $g\gamma$ luminosity at $Q = M(Q = m_t)$ in order to better identify at which scales the $g\gamma$ contribution is expected to be relevant. From these insets, the hierarchy between $gg$ and $q\bar{q}$ channels can also be easily derived.

In conclusion, the different results for photon-induced processes and consequently for EW corrections obtained with the different PDF sets discussed in this chapter have to be attributed mainly to the different assumptions that underlie the determination of $\gamma(x, Q)$ at the initial scale $Q = Q_0$ and the choice of the factorisation scale, but not to the different treatment of the DGLAP NLO QCD+LO QED evolution.

## 2.3 Predictions at 13 and 100 TeV

In this section we discuss the impact of the EW corrections and the photon PDF on several distributions at 13 and 100 TeV. In particular, we focus on the top-pair invariant mass $m(t\bar{t})$, the transverse momentum of the top quark $p_T(t)$, and the rapidities of the top quark $y(t)$ and $t\bar{t}$ pair $y(t\bar{t})$. Predictions for the LHC at 13 TeV are shown in figs. 2.5-2.10, while those for a Future Circular Collider (FCC) at 100 TeV are shown in figs. 2.11-2.16. Unless differently specified, results are obtained with no cut imposed on the final-state particles.

---

[10] In our calculation there are also contribution from quark-photon initial states, however, as it will be discussed in sect. 2.3, their contribution is small so we decided to exclude the corresponding luminosities from the discussion in this section for the sake of clarity.

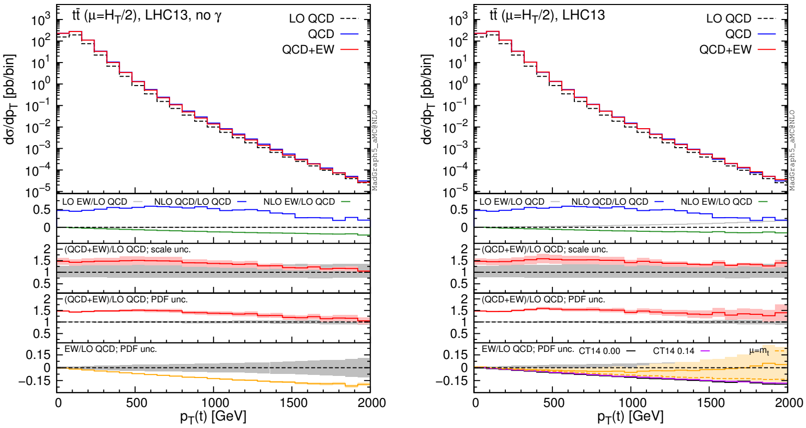

Figure 2.5: Differential distributions for the $p_T(t)$ at 13 TeV. The format of the plots is described in detail in the text.

In each figure we show two plots for the same observable, displaying in the left plot, denoted as "no $\gamma$", predictions with the photon PDF artificially set equal to zero. The reason behind this choice is manifold. First of all, the comparison of left and right plots allows to gauge the impact of the photon PDF on both the central value and PDF uncertainties of the electroweak contributions. Furthermore, in the plots on the left it is possible to observe the impact of the Sudakov logarithms, which can be hidden by the compensation given by the photon-induced processes included in the plots on the right. Last but not least, whereas the EW corrections in the right plots strongly depend on the PDF set used and may possibly change with future improved determination of the photon PDF, the plots on the left display the subset of the EW corrections that is expected to be stable under future PDF determination.

In each plot the main panel includes the distributions for $\Sigma_{\mathrm{LO\ QCD}}$, $\Sigma_{\mathrm{QCD}}$ and $\Sigma_{\mathrm{QCD+EW}}$ predictions as defined in equations (2.3)-(2.7). The four insets below the main panel display ratios of several quantities over the $\Sigma_{\mathrm{LO\ QCD}}$ central value. In the first inset we plot this ratio for the central values of $\Sigma_{\mathrm{LO\ EW}}$, $\Sigma_{\mathrm{NLO\ QCD}}$ and $\Sigma_{\mathrm{NLO\ EW}}$, *i.e.*, the other perturbative orders which we consider. The second and third inset respectively present the $\Sigma_{\mathrm{QCD+EW}}/\Sigma_{\mathrm{LO\ QCD}}$ ratio including the scale and PDF uncertainties for the numerator. In the last inset we present the $\Sigma_{\mathrm{EW}}/\Sigma_{\mathrm{LO\ QCD}}$ ratio with the PDF uncertainties for the numerator. All the results in the plots are obtained with the NNPDF2.3QED PDF set, with the PDF uncertainty computed at the 68% CL. However, plots on the right, including effects due to the photon PDF, also show (in the last

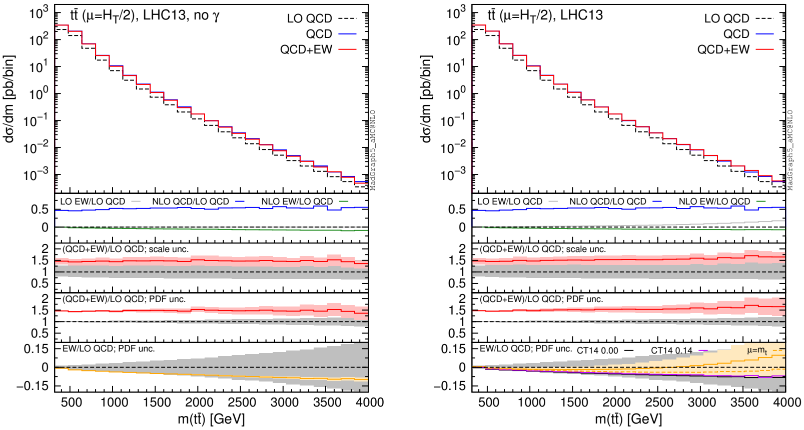

Figure 2.6: Differential distributions for the $m(t\bar{t})$ at 13 TeV. The format of the plots is described in detail in the text.

inset) the ratio $\Sigma_{\rm EW}/\Sigma_{\rm LO\ QCD}$ computed with the CT14QED PDF set. [11] For this particular set two predictions are shown, which correspond to a momentum fraction carried by the photon at the initial scale of 0% and 0.14%; as explained in sect. 2.2 this interval corresponds to the uncertainty band of CT14QED.

The first general feature that can be noticed in all the distributions for the LHC at 13 TeV is the different behaviour of the EW corrections with NNPDF2.3QED and CT14QED in the plots on the right. The effects induced by the photon PDF with CT14QED is much smaller with respect to. the case of NNPDF2.3QED. Indeed, by comparing the last inset in equivalent plots with (right) and without (left) photon-induced contributions, it is easy to see that effects due to the CT14QED photon PDF are essentially invisible, regardless of the momentum fraction (in the 0%-0.14% range). Furthermore, by comparing the first inset in the two plots of each figure, it is possible to notice how the dominant contribution from photon-induced processes originates from the $\Sigma_{\rm LO\ EW}$ contribution of the $g\gamma$ channel. As anticipated in sect. 2.2, the $q\gamma$ contribution is negligible [12] and will not be further discussed in the following. Moreover, when we will refer to the effect of photon PDF, unless differently specified, we will always understand the case of NNPDF2.3QED PDF set in order to be conservative.

---

[11] Only for this ratio, also the $\Sigma_{\rm LO\ QCD}$ quantity has been evaluated with the CT14QED PDF set.

[12] This statement could be done only *a posteriori*, after having performed the calculation and cannot be generalised to other processes. See for instance ref. [113].

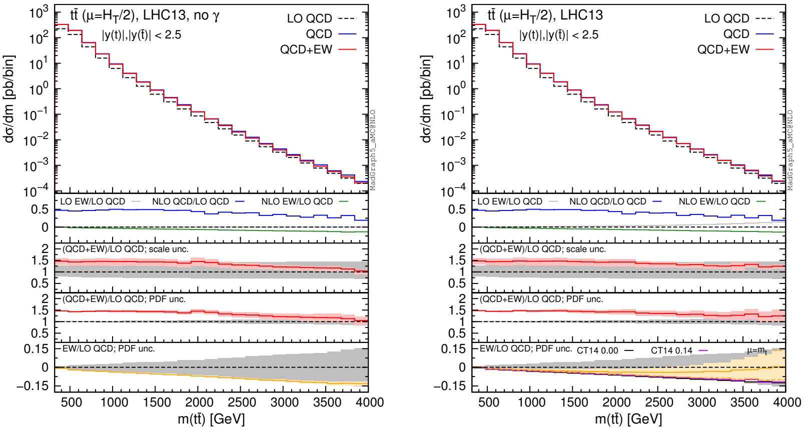

Figure 2.7: Differential distributions for the $m(t\bar{t})$ at 13 TeV with $|y(t)|, |y(\bar{t})| < 2.5$ cuts applied. The format of the plots is described in detail in the text.

As can be seen in figs. 2.5 and 2.6, at 13 TeV the photon-initiated contributions can accidentally compensate the Sudakov suppression in the top-pair invariant mass and top-quark transverse momentum distributions. At very large scales ($p_T(t) >$ 1.7 TeV or $m(t\bar{t}) >$ 3 TeV) their size is larger than the effect due to Sudakov logarithms. In all the figures at 13 TeV, in the last inset of the plots on the right, we also included the central value of the ratio $\Sigma_{\rm EW}/\Sigma_{\rm LO\ QCD}$ with both quantities evaluated at the scale $\mu = m_t$. This quantity indicates that the cancellation between Sudakov logarithms strongly depends also on the scale choice, thus the scale dependence of $\Sigma_{\rm EW}$ should also be taken into account as a source of uncertainties. The origin of this dependence will be discussed in detail in sect. 2.4, in the context of the measurements at 8 TeV.

In the last inset, the PDF uncertainties of the $\Sigma_{\rm EW}$ term alone are directly compared with the $\Sigma_{\rm LO\ QCD}$ PDF uncertainties, the grey band. In the tail of the $p_T(t)$ and $m(t\bar{t})$ distributions on the right, PDF uncertainties for separately $\Sigma_{\rm EW}$ and $\Sigma_{\rm LO\ QCD}$ are of the same size. This is consistent with the difference between the PDF uncertainty for the total prediction $\Sigma_{\rm QCD+EW}$ with and without effects form photon in the initial state, which is shown in the third inset and, in the plots on the right, is much larger with respect to the case of $\Sigma_{\rm LO\ QCD}$. Just for reference, we decided to show in the second inset the ratio $\Sigma_{\rm QCD+EW}/\Sigma_{\rm LO\ QCD}$ with scale uncertainties, which are reduced with respect to. the $\Sigma_{\rm LO\ QCD}$ case, the grey band. The effects due to the EW corrections and the impact of the photon PDF is in general smaller than the scale uncertainty of $\Sigma_{\rm QCD+EW}$. However, one should consider that the scale uncertainty is

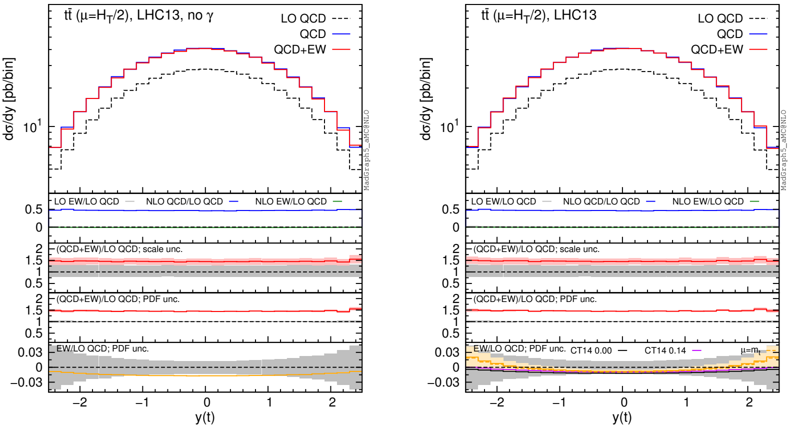

Figure 2.8: Differential distributions for the $y(t)$ at 13 TeV. The format of the plots is described in detail in the text.

further reduced to very few percents by NNLO corrections, which have already been calculated [58, 68]. Moreover, when normalised distributions ($d\sigma/\sigma$) are considered, even at NLO accuracy scale uncertainties are strongly reduced. In sect. 2.4 we will comment both effects for specific distributions measured at the LHC at 8 TeV by ATLAS and CMS, where we will also investigate the impact of EW corrections and of the photon PDF.

While $p_T(t)$ distributions do not change by requiring $|y(t)|$, $|y(\bar{t})| < 2.5$, *i.e.* top and anti-top produced in the central region of the detector, these cuts have an effect on predictions for high $m(t\bar{t})$. This is shown in fig. 2.7, which is equivalent to fig. 2.6, but with $|y(t)|, |y(\bar{t})| < 2.5$ cuts. At large invariant masses, tops are preferably produced in the forward or backward region, due to the $t$- and $u$-channel diagrams in the $gg$-channel, which is much less suppressed than the $q\bar{q}$ channels featuring only $s$-channel diagrams at LO QCD. Rapidity cuts suppress the $gg$ contribution, as well as $g\gamma$ contributions, but also enhance the typical value of the partonic Mandelstam variables $\hat{t}$ and $\hat{u}$. Consequently, with those cuts, we observe larger values for the Sudakov logarithms (plot on the left) and a similar behaviour for the photon-induced contributions. Moreover, we can notice that, as in the $p_T(t)$ distributions in fig. 2.5, also in the tails of the plots in fig. 2.7 the ratio $\Sigma_{\rm NLO\ QCD}/\Sigma_{\rm LO\ QCD}$ in the first insets decrease, at variance with fig. 2.6, where cuts are not applied. This trend is correlated with the fraction of the cross section originating from the $gg$ initial state, which is decreasing in the tail of $p_T(t)$ distribution and, only with rapidity cuts applied, of the $m(t\bar{t})$ distribution.

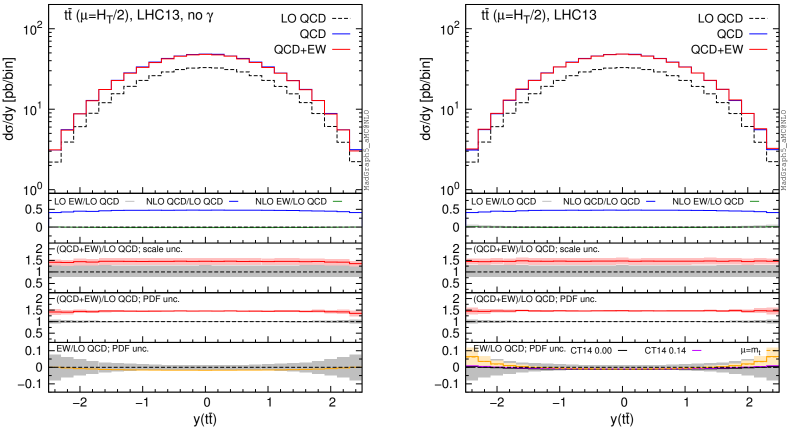

Figure 2.9: Differential distributions for the $y(t\bar{t})$ at 13 TeV. The format of the plots is described in detail in the text.

In figs. 2.8 and 2.9 we show predictions for $y(t)$ and $y(t\bar{t})$ distributions. EW corrections are quite flat in the plots on the left, while in the plots on the right they are enhanced by the $g\gamma$ initial state in the peripheral region, especially for the $y(t\bar{t})$ distribution. In this region photon-initiated contributions and their uncertainties become relevant since the photon PDF is sampled at rather large $x$, where the suppression with respect to the quark and gluon PDFs is reduced. At variance with the tail of $p_T(t)$ or $m(t\bar{t})$, where the $g\gamma$ contribution is also sizeable, the cross section in the peripheral region is not largely suppressed with respect to to the total cross section. For these reasons, large-rapidity bins can be exploited to set additional constraints on the photon PDF in a theoretical framework such as the one adopted in NNPDF2.3QED, while with an assumption *à la* CT14QED the sensitivity on the photon PDF remains very small. Given the large cross section in $t\bar{t}$ production at the LHC 13 TeV, in fig. 2.10 we also show the same plots of fig. 2.8 with a $m(t\bar{t}) > 1$ TeV cut applied. EW corrections in the left plot are larger in the central region, where, due to large values of the $\hat{t}$ and $\hat{u}$ Mandelstam variables, the effect of Sudakov logarithms is enhanced. Again, this effect can be accidentally compensated by photon-induced processes as shown in the plot on the right. As already observed for all the previous distributions, only in the plots on the left the PDF uncertainties related to $\Sigma_{\rm EW}$ are negligible, while they are sizeable in the plots on the right. Also in this case the trend of the ratio $\Sigma_{\rm NLO\ QCD}/\Sigma_{\rm LO\ QCD}$ displayed in the first inset is correlated with the fraction of the cross section originating from the $q\bar{q}$ initial state, as discussed for figs. 2.5 and 2.7.

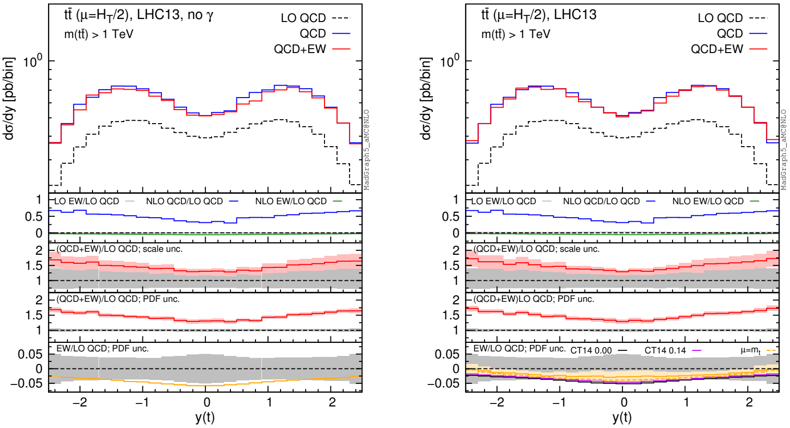

Figure 2.10: Differential distributions for the $y(t)$ at 13 TeV with the cut $m(t\bar{t}) > 1$ TeV. The format of the plots is described in detail in the text.

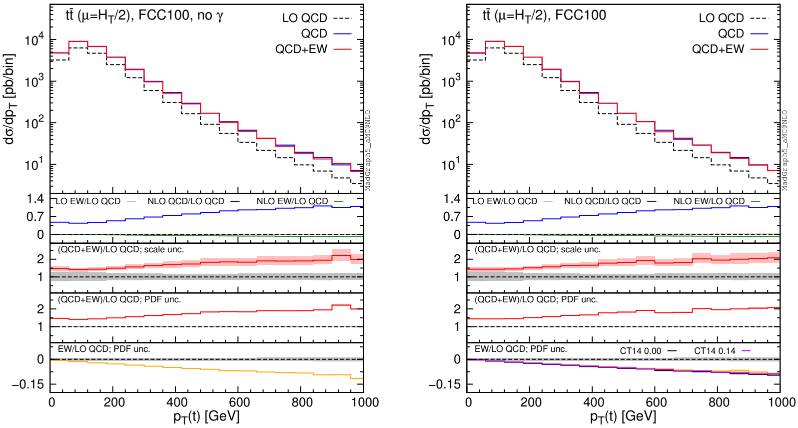

Figure 2.11: Differential distributions for the $p_T(t)$ at 100 TeV. The format of the plots is described in detail in the text.

It is worth to notice that while plots in fig. 2.5 would be identical in the case of $p_T(\bar{t})$ distributions, the transverse momentum of the antitop, the $y(\bar{t})$ distribution is different from $y(t)$ when $\Sigma_{\mathrm{QCD+EW}}$ terms are included, because of the charge asymmetry [21, 92–94]. However, we observed the same qualitative behaviour for the photon PDF and the EW corrections in $y(t)$ and $y(\bar{t})$ distributions. Moreover, the $g\gamma$ channel cannot give a contribution to

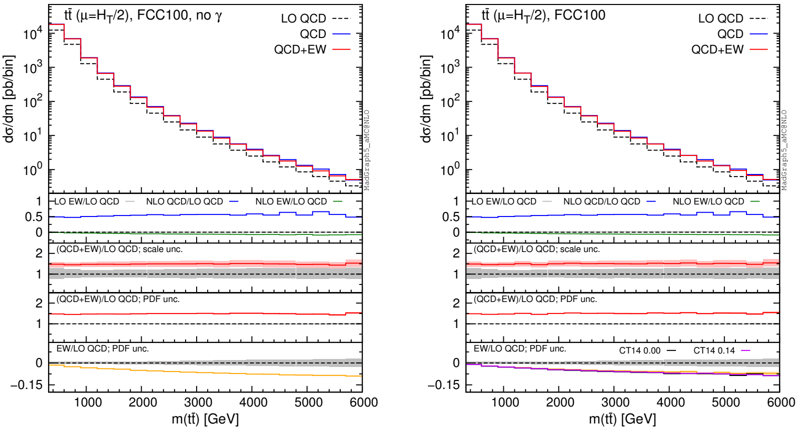

Figure 2.12: Differential distributions for the $m(t\bar{t})$ at 100 TeV. The format of the plots is described in detail in the text.

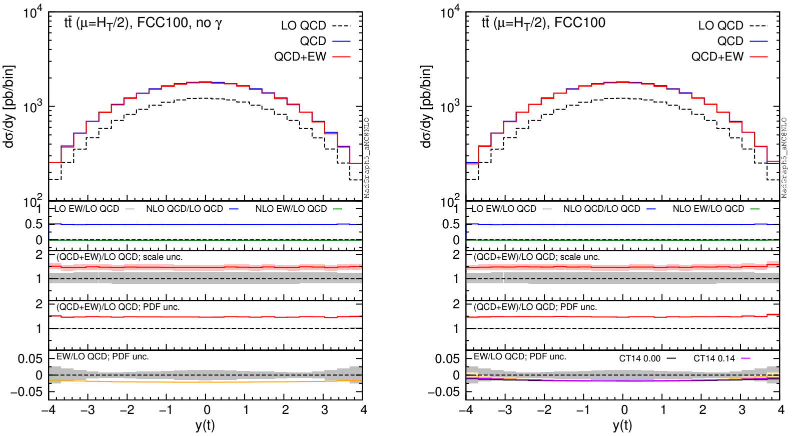

Figure 2.13: Differential distributions for the $y(t)$ at 100 TeV. The format of the plots is described in detail in the text.

the numerator of the charge asymmetry (see also ref. [114]), and all the other contributions to the asymmetry have already been investigated in ref. [94].

The distributions that have been discussed for the LHC at 13 TeV are also presented for a FCC at 100 TeV, with larger ranges for the abscissae. [13] By comparing plots in figs. 2.11-2.14 with their corresponding ones at 13 TeV, it can be noticed that the impact of the photon PDF is strongly reduced at 100

---

[13] We provided a few representative results also in [11].

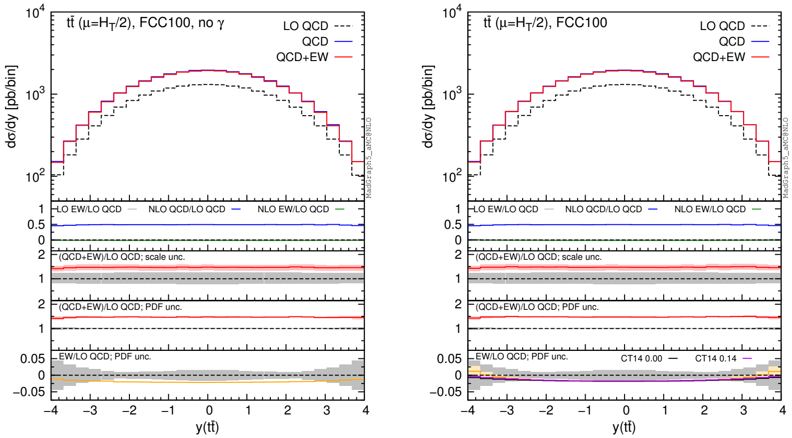

Figure 2.14: Differential distributions for the $y(t\bar{t})$ at 100 TeV. The format of the plots is described in detail in the text.

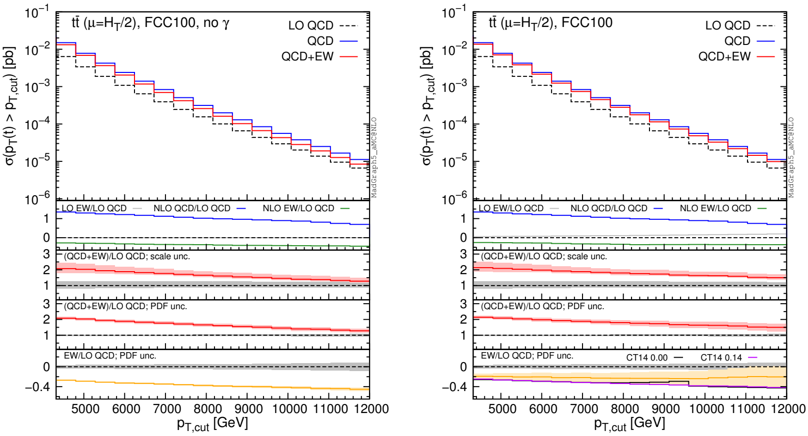

Figure 2.15: Integrated distributions for the $p_T(t)$ at 100 TeV. The format of the plots is described in detail in the text.

TeV. In each figure, the plot on the right (with photons in the initial state) does not exhibit any qualitatively different behaviour with respect to. the plot on the left. The smaller impact of the photon-induced contributions at 100 TeV with respect to the 13 TeV case is due to the different range of $x$ spanned in the PDFs; keeping the hardness of the process fixed, a larger energy of the hadronic collisions corresponds to probing smaller values of $x$, where parton luminosities involving photons are suppressed with respect to those involving

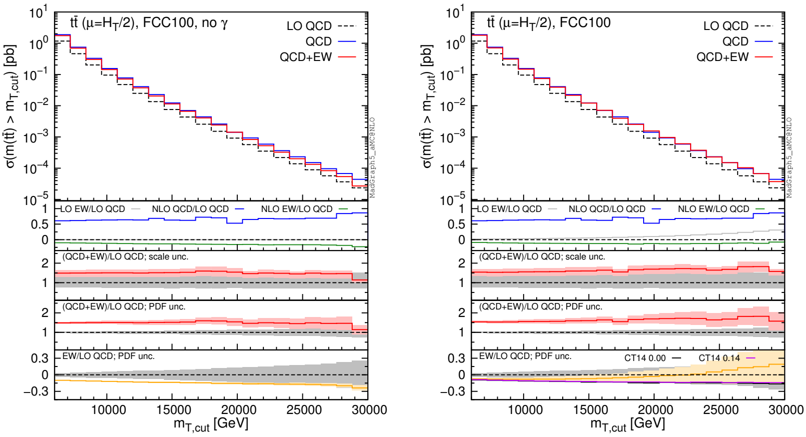

Figure 2.16: Integrated distributions for the $m(t\bar{t})$ at 100 TeV. The format of the plots is described in detail in the text.

QCD partons, as shown in fig. 2.3. For the same reason, the impact of the photon PDF at the LHC at 8 TeV is even larger than at 13 TeV, as it will be discussed in the next session. Moreover, at 100 TeV, for a given value of $p_T(t)$ or $m(t\bar{t})$, EW corrections are slightly smaller than at 13 TeV also in the plots on the left, *i.e.*, without considering photon-induced contributions.

In order to find a large contribution from the $g\gamma$ initial state at a FCC, it is necessary to probe very large scales. In figs. 2.15 and 2.16 we respectively plot, using the same layout of the previous plots, the cumulative distributions $\sigma(p_T(t) > p_{T,\mathrm{cut}})$ and $\sigma(m(t\bar{t}) > m_{\mathrm{cut}})$ with $p_{T,\mathrm{cut}}$ up to 12 TeV and $m_{\mathrm{cut}}$ up to 30 TeV. First of all, we remind that at a FCC it would be possible with 10 ab$^{-1}$ integrated luminosity to probe such small cross sections and large hard-scales. Thus, the following discussion is not purely academic. Sudakov logarithms can induce up to $\sim -40\%$ corrections for $\sigma(p_T(t) > 12~\mathrm{TeV})$ and $\sim -30\%$ for $\sigma(m(t\bar{t}) > 30~\mathrm{TeV})$, rendering EW corrections not only important for precision physics, but essential for obtaining a sensible result. For precision physics, Sudakov logarithms have to be considered also beyond the NLO EW accuracy and possibly resummed. The central role of EW corrections at a FCC at 100 TeV is not peculiar for the $t\bar{t}$ final state; it is a general feature for all the production processes (see also the EW section in [11]). At such large scales, also the $g\gamma$ luminosity is not negligible, and indeed the size and the PDF uncertainty of the EW corrections is very different in the left and right plots. Once again, the prediction obtained with CT14QED is similar to the case where the photon PDF has been set to zero. As in the case of 13 TeV, we observed similar changes in the tail of the $m(t\bar{t})$ distribution by applying the $|y(t)|, |y(\bar{t})| < 4$ cuts, *i.e.*, mimicking the expected coverage of the future detector. Sudakov logarithms are enhanced, photon contributions are not visibly changed, and the $\Sigma_{\rm NLO\ QCD}/\Sigma_{\rm LO\ QCD}$ ratio in the first inset decreases in the tail as observed in fig. 2.15.

## 2.4 Impact on ATLAS and CMS measurements at 8 TeV

In this section we discuss the relevance of the photon PDF and EW corrections for experimental measurements at the LHC. Specifically, we will consider their impact on the analyses already published both by ATLAS and CMS for the $t\bar{t}$ differential distributions at 8 TeV.

We want to stress that our aim is not to perform a direct comparison of the SM "best prediction" with experimental data. Indeed, at differential level, the best accuracy reached in perturbative QCD is NNLO or NLO+NNLL. Terms beyond NLO in QCD are not taken into account in this analysis, but they are crucial both for a correct determination of the central value and for reducing the scale uncertainty. Here, we want to show that a reliable comparison between SM predictions and experimental data in $t\bar{t}$ production cannot be based only on purely QCD corrections. Indeed, the contribution of EW corrections, especially the uncertainty due to the photon PDF and the scale choice, cannot be ignored and has to be taken into account. In particular cases, such as the normalised distributions discussed in the following, they can yield the largest effect, playing a primary role in the determination of precise SM predictions.

After the discussion and the results presented in the previous section, it is clear that EW corrections at 8 TeV are expected to show a larger dependence on the photon PDF with respect to. the 13 TeV case. On the other hand, smaller cross sections and integrated luminosities may in practice not lead to enough events to probe this effect. In order to evaluate their real impact at the experimental level, we take in to account in our analysis both the theory uncertainties (scale and PDF) and the errors from the experimental measurements. Moreover, this study serves also as a motivation to perform this kind of analysis for future 13 TeV data, where larger cross sections and luminosities should considerably decrease the experimental errors.

In the following, we consider CMS data from ref. [115], which are based on the dilepton and lepton+jets events collected at 8 TeV with an integrated luminosity of 19.7 $\mathrm{fb}^{-1}$. In particular, we focus on the distributions of the transverse momentum and rapidity of the top quark, [14] and of the rapidity of the $t\bar{t}$ pair. Moreover, we consider ATLAS data based on lepton+jets events collected with an integrated luminosity of $20.3\,\mathrm{fb}^{-1}$. Distributions for the top quark transverse momentum in the boosted regime are taken from ref. [116], while those for the invariant mass of the $t\bar{t}$ pair, the absolute value of the rapidity of the top and of the $t\bar{t}$ pair are taken from ref. [117]. In the ATLAS analyses, part of the electroweak corrections (the purely weak contribution calculated in [84]) has been taken into account via an updated version of HATHOR [118]. Thus, although the Sudakov enhancement has been taken into account, the QED corrections and especially the dependence on the photon PDF, which is a crucial aspect of our discussion, have not been considered yet.

For each differential measurement of ATLAS and CMS, we show two plots with the corresponding theoretical predictions obtained with the MMHT2014 PDF set [119] (plot on the left), and with NNPDF2.3QED (plots on the right), respectively. At variance with what has been done in sect. 2.3, we do not set the photon PDF to zero in the left plots, but we directly use a PDF set that does not include neither LO QED contribution in the DGLAP running nor the photon PDF, as typically done in the experimental analyses and in QCD-only predictions. In the plots on the right we decided to use NNPDF2.3QED in order to be conservative, since the effects due to the photon PDF are the largest for this PDF set. We explicitly verified that, as it could be expected from the discussion in sect. 2.3, using the CT14QED PDFs or setting the photon PDF in NNPDF2.3QED to zero, the relative corrections induced by $\Sigma_{\mathrm{EW}}$, *e.g.* the $\Sigma_{\mathrm{QCD+EW}}/\Sigma_{\mathrm{QCD}}$ ratio, are the same as those obtained with MMHT2014. Indeed the effect of the LO QED terms in the DGLAP running, which is present in CT14QED and NNPDF2.3QED but not in MMHT2014, cancels in the ratio. On the other hand, this effect can have an impact on the cross section, especially on the $\Sigma_{\mathrm{LO\ QCD}}$ term, and may be important for a direct comparison with data. This is another reason, besides the theoretical consistency, for which NNPDF2.3QED or CT14QED should be in general preferred when NLO EW calculations are performed.

In each plot we present our predictions for a specific measurement, using three different definitions for the renormalisation and factorisation scales, *i.e.*, $\mu = m(t\bar{t})$ (blue), $\mu = H_T/2$ (as in sect. 2.3, red) and $\mu = m_t$ (green). In the main panel of each plot we present the $\Sigma_{\mathrm{QCD+EW}}$ predictions, without theory uncertainties, compared to data. In the first inset we display the ratio

---

[14] In the plots of this section, the $p_T(t)$ distribution is actually the average of the distribution of the transverse momentum of the top quark and antiquark, consistently with what has been done in the experimental analyses. Similarly, the $y(t)$ distribution is the average of the distribution of the rapidity of the top quark and antiquark. However, differences with real $p(t)$ and $y(t)$ distributions are in practice invisible.

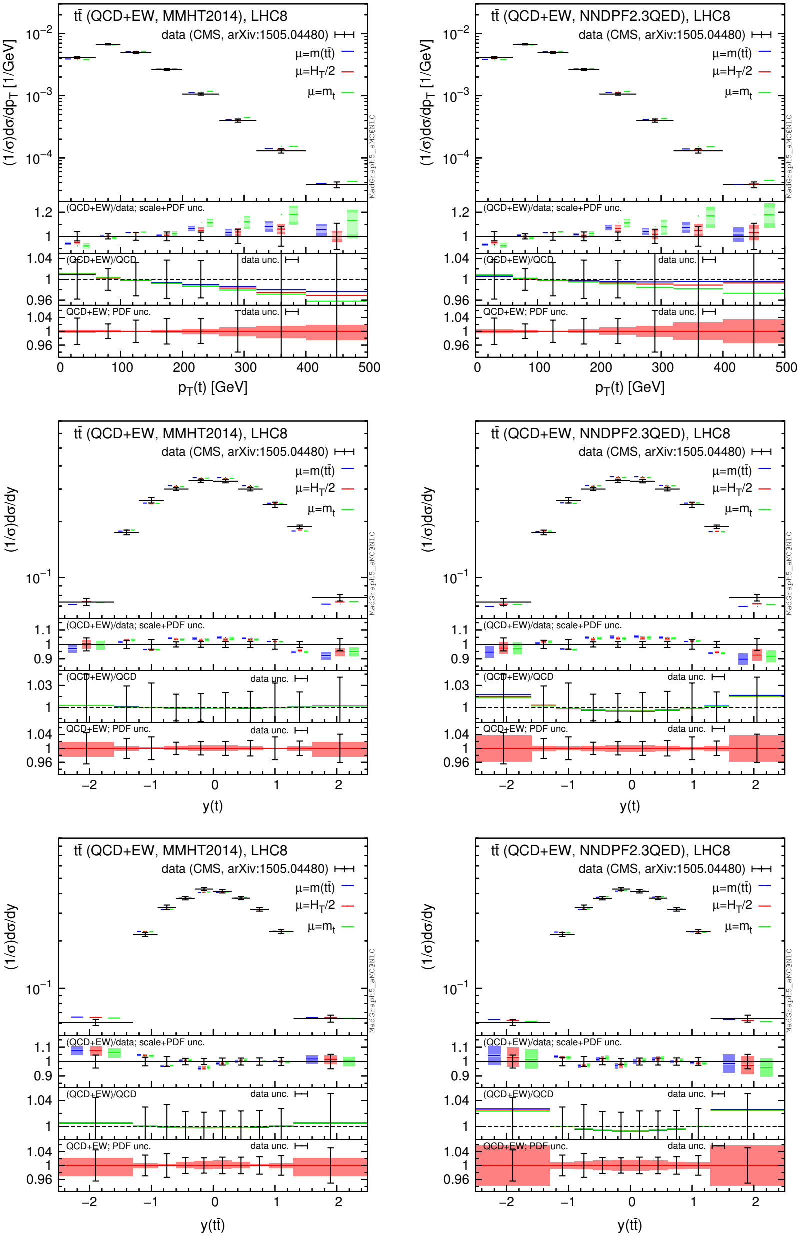

Figure 2.17: Comparison of CMS data from ref. [115] and NLO QCD+EW predictions computed with MMHT2104 (left) and NNPDF2.3QED (right) PDF sets.

of the $\Sigma_{\mathrm{QCD+EW}}$ over data, including scale (light band) and PDF (dark band) uncertainties linearly added. In the second inset we show the central value of the ratio $\Sigma_{\mathrm{QCD+EW}}/\Sigma_{\mathrm{QCD}}$ for the three different scales and also the relative error in the measurement for each bin, with the error bar centred around one. In the third inset we zoom the PDF uncertainty already included in the main panel. Specifically, we show the PDF uncertainty band of the $\Sigma_{\mathrm{QCD+EW}}$ predictions with $\mu = H_T/2$ normalised to their central value and we compare them again with the relative error in the measurement for each bin. Distributions corresponding to CMS analyses [115] are shown in fig. 2.17, while ATLAS distributions taken from ref. [116] and ref. [117] are shown in fig. 2.18 and fig. 2.19, respectively.

Before discussing each plot, it is important to note that two different kinds of distributions are shown here, namely, absolute differential distributions ($d\sigma/dx$) and normalised distributions ($d\sigma/(\sigma dx)$).[15] The $m(t\bar{t})$ distribution in fig. 2.18 and the boosted $p_T(t)$ distribution in fig. 2.19 are differential distributions, while all the other plots actually display normalised distributions, which exhibit much smaller scale and PDF uncertainties. Indeed, for normalised distributions both types of uncertainties are calculated directly for the $d\sigma/\sigma$ ratio, yielding large cancellations between the numerator and the denominator. As we said, our aim is not to perform a direct comparison of data and SM predictions, which would need QCD corrections beyond the NLO. Nevertheless, it is interesting to note how the scale uncertainty shown in the main panel and in the first inset of the plots, which reflects the typical QCD accuracy (NLO) of available Monte Carlo event generators, is of the same order of the experimental precision for all the distributions considered here. Thus, although NNLO and NLO+NNLL have shown to reduce the dependence of the predictions on the renormalisation and factorisation scale, a few comments can be done about the scale choice for NLO simulations. The plot for the $m(t\bar{t})$ distribution in fig. 2.18 suggests that $m(t\bar{t})$ is not the natural scale for this process and indeed it artificially leads to particularly large corrections also beyond NLO (see ref. [80]). Similarly, the discrepancy between data and predictions observed in ref. [68] at NLO QCD for large $p_T(t)$, but not at NNLO QCD with fixed scale $\mu = m_t$, can be simply reduced at NLO using the scale $\mu = H_T/2$, as shown in the plots in the first line of fig. 2.17.

The most important information of the plots is however contained in the second and third insets. In the former we compare the experimental precision with the relative corrections induced by $\Sigma_{\mathrm{EW}}$ on the predictions at NLO

---

[15] Consistently with what is done in the experimental analyses, we use as $\sigma$ the sum of the values of the bins of the distribution considered, without including overflows.

QCD accuracy via the ratio $\Sigma_{\mathrm{QCD+EW}}/\Sigma_{\mathrm{QCD}}$. [16] In the latter we compare the experimental precision with the relative PDF uncertainties for the $\Sigma_{\mathrm{QCD+EW}}$ predictions. In the following, we discuss these comparisons for every measurement analysed here.

In the plots of the first line in fig. 2.17, we can see that the size of electroweak corrections is always smaller than the precision of the experimental measurement for $p_T(t)$ distributions. However, it is reasonable to expect that in the Run-II at 13 TeV, with larger cross sections and higher luminosities, it will be possible to reach an experimental precision such that this effect could be probed, as it is also discussed in ref. [84] and supported by the first CMS analyses [120,121] on 13 TeV data collected with only $2.3\,\mathrm{fb}^{-1}$ integrated luminosity. Nevertheless, it is important to note how results obtained with MMHT2014 and NNPDF2.3QED are qualitatively different; the cancellation between photon-induced contributions and Sudakov logarithms at large $p_T(t)$ also strongly depends on the factorisation scale used. This is particularly important because the dependence of the $\Sigma_{\mathrm{QCD+EW}}/\Sigma_{\mathrm{QCD}}$ ratio on the PDF set and on the central scale choice is of the same order, or even exceeds, the scale uncertainty of the NNLO QCD predictions, which is at the percent level. [17] The PDF uncertainties for $\Sigma_{\mathrm{QCD+EW}}$ predictions are smaller than the experimental precision both in the right and left plot, although slightly larger values appear in the NNPDF2.3QED case at large $p_T(t)$ due to the photon-induced contribution.

The case of the $y(t)$ and $y(t\bar{t})$ distributions in the plots in the second and third lines of both figs. 2.17 and 2.18 clearly shows the relevance of EW corrections and photon-initiated processes for a trustworthy comparison of theory predictions and data measurements at the LHC. As can be seen in the first insets, scale uncertainties are smaller than the experimental errors and, for the $y(t)$ distribution, they are further reduced to 1% level or even less by NNLO QCD corrections, thus they are negligible. The theory uncertainties, as can be noted in the second insets, are completely dominated by PDF uncertainties. What is not negligible is the impact of the electroweak corrections. In the case of MMHT2014, without photon-induced processes, EW corrections are flat and thus their impact cancels in the $d\sigma/\sigma$ ratio. On the contrary, in the case of NNPDF2.3QED, for large rapidities their impact is comparable to the experimental error, with a negligible dependence on the factorisation scale. Also, the enhancement in the peripheral region induces a small negative effect in the

---

[16] In the case of normalised distributions, we actually display the ratio of $d\sigma/\sigma$ with both numerator and the denominator evaluated at QCD+EW accuracy over the same quantity at QCD accuracy $(d\sigma/\sigma)|_{\mathrm{QCD+EW}}/(d\sigma/\sigma)|_{\mathrm{QCD}}$, in order to correctly identify the effect of the electroweak corrections on the observable considered.

[17] The size of NNLO scale uncertainties quoted in this section are taken from ref. [68]. In particular the authors of ref. [68] explicitly considered the same $p_T(t)$ and the $y(t)$ CMS distributions of fig. 2.17 that are discussed in detail in the text.

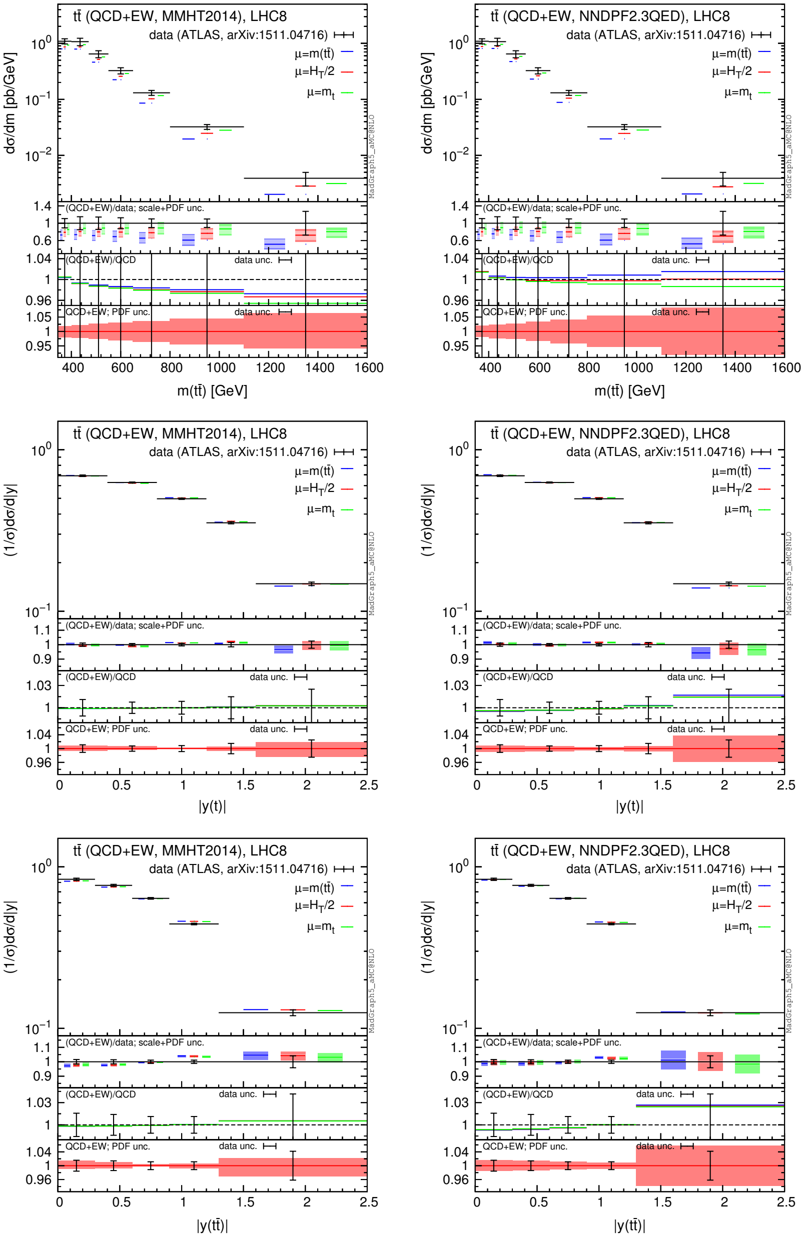

Figure 2.18: Comparison of ATLAS data from ref. [117] and NLO QCD+EW predictions computed with MMHT2104 (left) and NNPDF2.3QED (right) PDF sets.

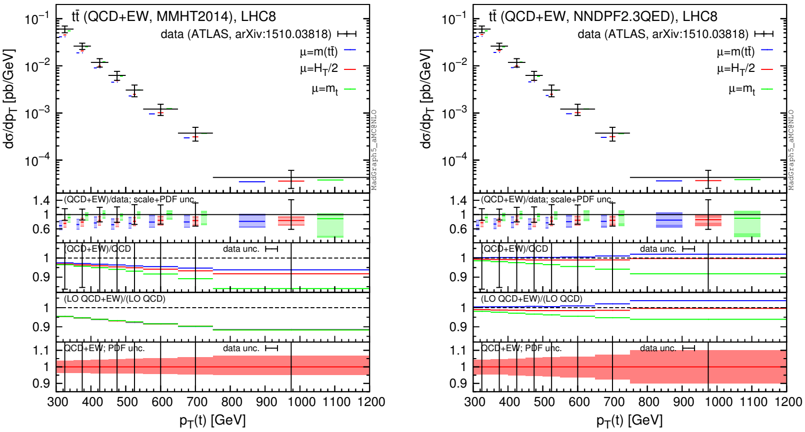

Figure 2.19: Comparison of ATLAS data from ref. [116] and NLO QCD+EW predictions computed with MMHT2104 (left) and NNPDF2.3QED (right) PDF sets.

central region because of the fixed normalisation. PDF uncertainties for the $\Sigma_{\rm QCD+EW}$ are smaller or of the same order of the experimental precision in the case of MMHT2014, while they are larger in the case of NNPDF2.3QED for large rapidities. All these effects are more prominent in the case of the ATLAS measurement (fig. 2.18), where experimental errors are smaller. It is also worth to note that for rapidity distributions EW corrections do not receive Sudakov enhancements and, at this level of accuracy, besides the photon-induced contributions, *a priori* QED effects cannot be neglected.

The situation for the $m(t\bar{t})$ distribution in the first line of fig. 2.18 is very similar to the one for the $p_T(t)$ distribution, which has been already discussed for the CMS measurement (first line of fig. 2.17) and it is also shown for the boosted regime in the ATLAS analysis in fig. 2.19. However, these two *differential* distributions exhibit much larger scale uncertainties than the normalised $p_T(t)$ distribution in fig. 2.17. The inclusion of NNLO QCD corrections is crucial in order to pin down the scale uncertainties below the 5% level, pointing to the necessity of a combination of EW and NNLO QCD corrections for a reliable comparison of theory predictions and data measurements at the LHC. In all the $p_T(t)$ and $m(t\bar{t})$ distributions with the NNPDF2.3QED set, the dependence of the EW corrections on the factorisation scale is also particularly evident and in the following we describe the reason of this feature.

The dependence of the size (and possibly of the sign) of EW corrections on the scale choice can be traced to different effects. First of all, unlike QCD corrections, EW corrections to $q\bar{q}$ and $gg$ initial states do not involve neither $\alpha_s$ renormalisation nor the $\mathcal{O}(\alpha_s)$ PDF counter terms that stabilise the $\mu_f$ dependence. Thus, without photon-initiated contributions, both the $\mu_r$ and $\mu_f$ dependence of $\Sigma_{\mathrm{LO\ QCD}}$ and $\Sigma_{\mathrm{NLO\ EW}}$ is the same; it is different for $\Sigma_{\mathrm{QCD}}$. This can be clearly seen in the left plot of fig. 2.19, where in addition to the $\Sigma_{\mathrm{QCD+EW}}/\Sigma_{\mathrm{QCD}}$ ratio in the third inset we included also the $(\Sigma_{\mathrm{LO\ QCD}}+\Sigma_{\mathrm{EW}})/\Sigma_{\mathrm{LO\ QCD}}$ ratio [18], where the scale dependence is the same in the numerator and the denominator. On top of this, as anticipated in the last point in sect. 2.2, $gg$, $q\bar{q}$ and $g\gamma$ luminosities have a different dependence on $\mu_f$. Moreover, at LO the $g\gamma$ channel contributes only to $\Sigma_{\mathrm{LO\ EW}}$, which features only one power of $\alpha_s$ and thus a different dependence on $\mu_r$ with respect to. $\Sigma_{\mathrm{LO\ QCD}}$. While the Sudakov logarithms are negative and proportional to the $gg$ and $q\bar{q}$ contributions to $\Sigma_{\mathrm{LO\ QCD}}$, the $g\gamma$ contributions to $\Sigma_{\mathrm{EW}}$ are positive. Consequently, the cancellation of this two classes of contributions both entering $\Sigma_{\mathrm{EW}}$ depends on $\mu$. All these effects are present in any distribution on the right with NNPDF2.3QED. However, in the rapidity distributions there is no Sudakov enhancement and $m_t \sim H_T/2$, especially for large rapidities, so only a small difference for the case $\mu = m(t\bar{t})$ is visible.

In conclusion, the impact of the photon PDF and also its dependence on the scale choice should be in general taken into account for the determination of the theory uncertainties.

## 2.5 Combined NNLO QCD predictions and EW corrections in $t\bar{t}$ production

The goal of this part of the work is to consistently merge existing NNLO QCD predictions with EW corrections into a single coherent prediction and to study its phenomenological impact. Using the same calculation framework of sec 2.1, NNLO QCD predictions from ref [101] are combined with the complete LO and NLO contributions, *i.e.*, not only with NLO EW effects of $\mathcal{O}(\alpha_s^2\alpha)$, but also with all the subleading NLO ($\mathcal{O}(\alpha_s\alpha^2)$ and $\mathcal{O}(\alpha^3)$) and LO ($\mathcal{O}(\alpha_s\alpha)$ and $\mathcal{O}(\alpha^2)$) contributions. To this end, we present predictions for top-pair differential distributions at the LHC based on the LUXQED [98] and

---

[18] It is worth to note that without photon PDF this ratio corresponds to the NLO EW $K$-factor, $K^{\mathrm{EW}} \equiv (\Sigma_{\mathrm{LO\ QCD}} + \Sigma_{\mathrm{NLO\ EW}})/\Sigma_{\mathrm{LO\ QCD}}$, which can be also seen as the ratio $\Sigma_{\mathrm{QCD\times EW}}/\Sigma_{\mathrm{QCD}}$, where $\Sigma_{\mathrm{QCD\times EW}} \equiv \Sigma_{\mathrm{LO\ QCD}} \times K^{\mathrm{QCD}} \times K^{\mathrm{EW}}$ is the multiplicative combination of results at NLO QCD and EW accuracy and we have defined as usual $K^{\mathrm{QCD}} = \Sigma_{\mathrm{QCD}}/\Sigma_{\mathrm{LO\ QCD}}$. Thus the second and third insets in the left plot can be seen as a comparison of $\Sigma_{\mathrm{QCD+EW}}$ and $\Sigma_{\mathrm{QCD\times EW}}$. On the other hand, the inclusion of $g\gamma$-channels in $\Sigma_{\mathrm{LO\ EW}}$, such as in the right plot, invalidates the previous argument introducing a non-negligible contribution to $\Sigma_{\mathrm{LO\ EW}}$.

NNPDF3.0QED [102] PDF sets. Our goal in this part is twofold: we aim at providing detailed phenomenological predictions for LHC observables as well as input to future PDF determinations including EW effects.

This section is organised as follows: in sec. 2.5.1 we provide for all main top-pair differential distributions the combination of NNLO QCD predictions with the EW corrections, by consistently adding the different perturbative orders. We provide predictions in the multiplicative approach in sec. 2.5.2, assuming factorisation of NLO QCD and NLO EW contributions. Section 2.5.3 is dedicated to studying the impact of the photon PDF on top-pair spectra. In sec. 2.5.4 we provide an estimate of the impact of inclusive Heavy Boson Radiation (HBR), namely the contribution from $t\bar{t}V$ with $V = H, W^{\pm}, Z$. While most of the notation is introduced in sec 2.1, technical details are delegated to Appendix A.1.

### 2.5.1 Additive combination of NNLO QCD predictions and EW corrections

In the following we present predictions for $t\bar{t}$ distributions for the LHC at 13 TeV at NNLO QCD accuracy including also EW corrections. We focus on the following distributions: the top-pair invariant mass $m(t\bar{t})$, the top/antitop average transverse momentum ($p_{T,\mathrm{avt}}$) and rapidity ($y_{\mathrm{avt}}$), and the rapidity $y(t\bar{t})$ of the $t\bar{t}$ system. The $p_{T,\mathrm{avt}}$ ($y_{\mathrm{avt}}$) distributions are calculated *not* on an event-by-event basis, but by averaging the results of the histograms for the transverse momentum (rapidity) of the top and the antitop.

In this section we *additively* combine the NNLO QCD predictions (defined as the complete set of $\mathcal{O}(\alpha_s^n)$ terms up to $n = 4$) with all the possible remaining LO and NLO terms arising from QCD and electroweak interactions in the Standard Model. In other words, at LO we include not only the purely QCD $\mathcal{O}(\alpha_s^2)$ contribution, but also all $\mathcal{O}(\alpha_s\alpha)$ and $\mathcal{O}(\alpha^2)$ terms. Similarly, at NLO we take into account not only the NLO QCD $\mathcal{O}(\alpha_s^3)$ contribution but also the $\mathcal{O}(\alpha_s^2\alpha)$ one, the so-called NLO EW, as well as the subleading contributions of $\mathcal{O}(\alpha_s\alpha^2)$ and $\mathcal{O}(\alpha^3)$. For brevity, we will denote as "EW corrections" the sum of all LO and NLO terms of the form $\mathcal{O}(\alpha_s^m\alpha^n)$ with $n > 0$. Moreover, when we will refer to "QCD" results, we will understand predictions at NNLO QCD accuracy.

For a generic observable $\Sigma$ we denote the prediction at this level of accuracy as $\Sigma_{\mathrm{QCD+EW}}$. The alternative combination of QCD and EW corrections assuming complete factorisation of NLO QCD and NLO EW effects is presented in sec. 2.5.2 and is denoted as $\Sigma_{\mathrm{QCD}\times\mathrm{EW}}$. For brevity, we will refer to the former as *additive* approach and to the latter as *multiplicative* approach.

The precise definition of the various quantities mentioned in the text is given in appendix A.1, where an appropriate notation for the classification of the different contributions is introduced.

Our calculation is performed using the same input parameters as shown in section 2.1. For this part however, we work with dynamical renormalisation ($\mu_r$) and factorisation ($\mu_f$) scales, for which the common central value is defined as

$$\mu = \frac{m_{T,t}}{2} \quad \text{for the } p_{T,t} \text{ distribution,} \tag{2.12}$$

$$\mu = \frac{m_{T,\bar{t}}}{2} \quad \text{for the } p_{T,\bar{t}} \text{ distribution,} \tag{2.13}$$

$$\mu = \frac{H_T}{4} = \frac{1}{4}\left(m_{T,t} + m_{T,\bar{t}}\right) \quad \text{for all other distributions,} \tag{2.14}$$

where $m_{T,t}$ and $m_{T,\bar{t}}$ are the transverse masses of the top and antitop quarks. As already mentioned, $p_{T,\text{avt}}$ and $y_{\text{avt}}$ distributions are obtained by averaging the top and antitop distributions for the transverse momentum and rapidity, respectively.

These scale choices have been lengthly studied and motivated in ref. [101]. In all cases theoretical uncertainties due to missing higher orders are estimated via the 7-point variation of $\mu_r$ and $\mu_f$ in the interval $\{\mu/2, 2\mu\}$ with $1/2 \leq \mu_r/\mu_f \leq 2$. We remark that the combination of QCD and EW corrections is independently performed for each value of $\mu_{f,r}$.

At the moment, the only two NNLO QCD accurate PDF sets that include them are NNPDF3.0QED and LUXQED[19]. Both sets have a photon density, which induces the additional contributions to the $t\bar{t}$ production. As it has been discussed in the previous sections of this chapter, the usage of different PDF sets leads to a very different impact of photon-induced contributions on $t\bar{t}$ distributions. While in the case of NNPDF3.0QED the impact of photon-induced contributions is relatively large and with very large uncertainties, in the case of LUXQED it is expected to be negligible. For this reason we always show predictions with both PDF sets.

Distributions for $p_{T,\text{avt}}$ and $m(t\bar{t})$ are shown in fig. 2.20, while the $y_{\text{avt}}$ and $y(t\bar{t})$ distributions are shown in fig. 2.21. The format of the plots for all distributions is as follows: for each observable, we show two plots side-by-side, with the same layout. The plot on the left-hand side shows predictions obtained using the LUXQED set, while for the one on the right the NNPDF3.0QED set is employed. In each plot, the main panel displays the central scale predictions

---

[19] The PDF sets MRST2004QED [95] and CT14QED [97] also include QED effects in the DGLAP evolution, but they are not NNLO QCD accurate. A PDF set including full SM LO evolution (not only QCD and QED but also weak effects) has also recently become available [122].

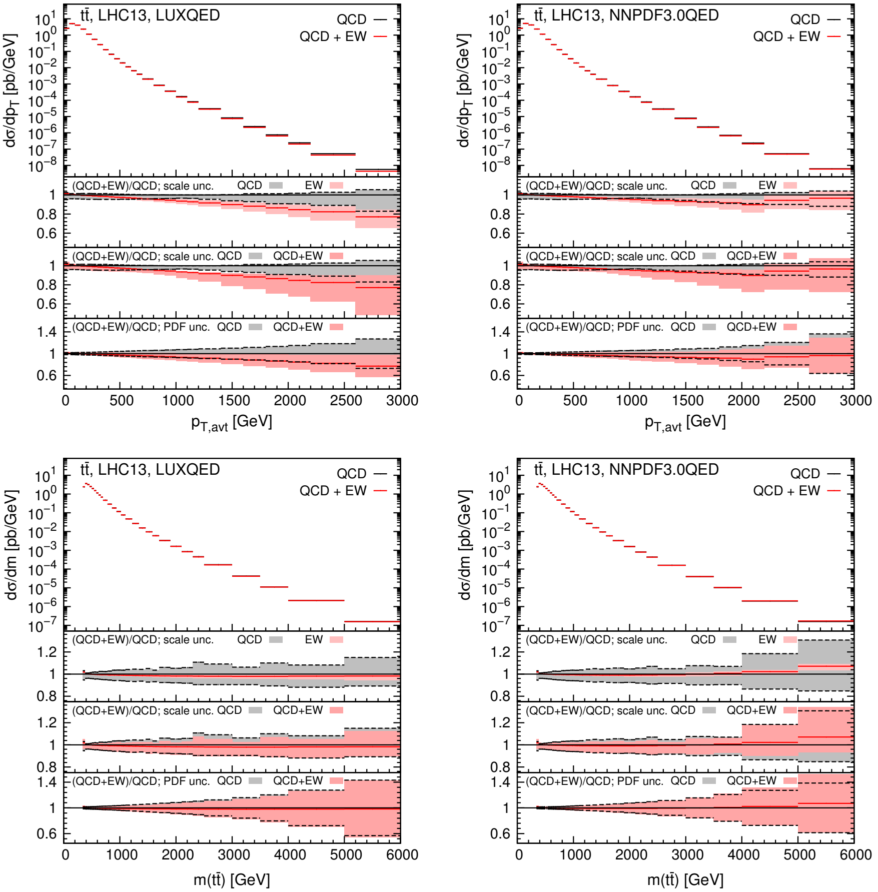

Figure 2.20: Differential distributions for $p_{T,\mathrm{avt}}$ and $m(t\bar{t})$ at 13 TeV. Predictions are based on the additive approach. The format of the plots is described in the text.

for the corresponding differential cross section at NNLO QCD accuracy (black line labelled "QCD") as well as the combination of NNLO QCD predictions and EW corrections in the additive approach (red line labelled "QCD+EW").

The three insets display ratios of different quantities [20] over the central-scale QCD result (i.e. with respect to the black line in the main panel). In the first inset we show the scale uncertainty due to EW corrections alone (red band), without QCD contributions ($\Sigma_{\mathrm{EW}}$ using the notation of Appendix A.1).

---

[20] It is actually in all cases the $\Sigma_{\mathrm{QCD+EW}}/\Sigma_{\mathrm{QCD}}$ ratio, but the bands refer to three different quantities, as explained in the text.

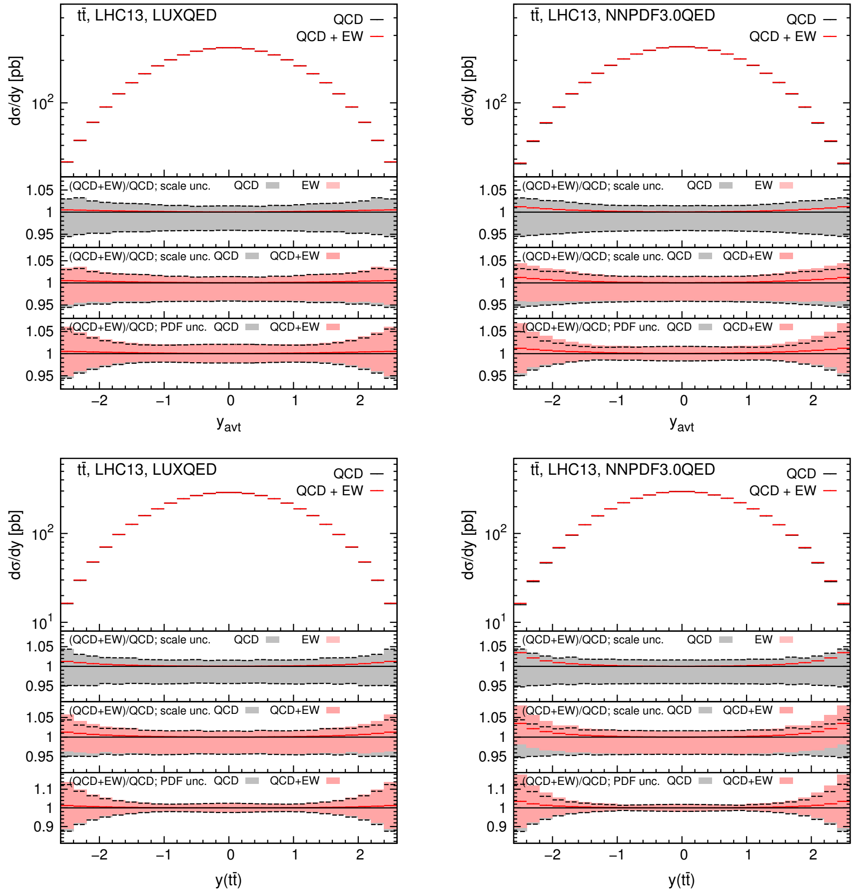

Figure 2.21: As in fig.2.20 but for the $y_{\mathrm{avt}}$ and $y(t\bar{t})$ differential distributions.

This quantity can be compared to the scale uncertainty of the QCD prediction at NNLO accuracy (grey band). In the second inset we present the scale-uncertainty band (red) for the combined QCD+EW prediction. The grey band corresponds to the NNLO QCD scale-uncertainty band already shown in the first inset. The third inset is equivalent to the second one, but it shows the PDF uncertainties. We combine, for each one of the PDF members, the QCD prediction and the EW corrections into the QCD+EW result. The PDF uncertainty band of the QCD+EW prediction is shown in red while the grey band corresponds to the PDF uncertainty of the QCD prediction. For all insets, when the grey band is covered by the red one, its borders are displayed as black dashed lines.

As can be seen in figs. 2.20 and 2.21, the effect of EW corrections is, in general, within the NNLO QCD scale uncertainty. A notable exception is the case of the $p_{T,\mathrm{avt}}$ distribution with LUXQED. In the tail of this distribution the effect of Sudakov logarithms is large and negative, of the order of -(10–20%), and is not compensated by the photon-induced contributions. On the contrary, in the case of NNPDF3.0QED, photon-induced contributions mostly compensate the negative corrections due to Sudakov logarithms. As it was expected, with this PDF set, the effect of photon-induced contributions is not negligible also for large values of $m(t\bar{t})$, $y_{\mathrm{avt}}$ and $y(t\bar{t})$.

As it can be seen in the first inset, in the large $p_{T,\mathrm{avt}}$ regime the scale dependence of the EW corrections alone is of the same size of or even larger than the scale variation at NNLO QCD accuracy. For this reason, as evident from the second inset, the scale uncertainty of the combined QCD+EW prediction is much larger than the purely QCD case, both with the LUXQED and NNPDF3.0QED PDF sets. This feature is only present in the tail of the $p_{T,\mathrm{avt}}$ distribution.

The PDF uncertainties (third inset) for all distributions do not exhibit large differences between QCD and QCD+EW predictions, despite the fact that the photon-induced contribution in NNPDF3.0QED is large and has very large PDF uncertainty (relative to LUXQED).

### 2.5.2 Multiplicative combination of NNLO QCD predictions and EW corrections

The additive approach $\Sigma_{\mathrm{QCD+EW}}$ for combining QCD and EW corrections, which has been discussed in sec. 2.5.1, is the exact result originating from a fixed-order perturbative expansion of the production cross section. An alternative possibility for combining QCD and EW corrections is what we already called the multiplicative approach $\Sigma_{\mathrm{QCD}\times\mathrm{EW}}$, which is designed for estimating the leading EW corrections at NNLO accuracy, namely, the $\mathcal{O}(\alpha_s^3\alpha)$ contribution in $t\bar{t}$ production. This approximation is based on the fact that Sudakov logarithms, which are typically associated with large EW corrections, and soft QCD effects factorise. Thus, when dominant NLO EW and NLO QCD corrections are at the same time induced by these two different kind of effects, the desired order of accuracy can be very well approximated via rescaling NLO EW corrections with NLO QCD $K$-factors. [21] Otherwise, the difference between the multiplicative and additive approach (the term $\Sigma_{\mathrm{mixed}}$ defined in eq. (A.8)) can be adopted as theory uncertainty. It must be stressed that the perturbative orders involved in the additive approach are exactly included also in the

---

[21] The precise definitions of $\Sigma_{\mathrm{QCD}\times\mathrm{EW}}$ is given in eq. (A.13)

multiplicative approach; the only addition is the presence of the approximated $\mathcal{O}(\alpha_s^3\alpha)$ contribution.

One of the advantages of the multiplicative approach is the stabilisation of the scale dependence, which, as we saw in sec. 2.5.1, for large $p_{T,\mathrm{avt}}$ can be larger then at NNLO QCD accuracy when EW corrections are combined in the additive approach. This is exactly the kinematic regime where the multiplicative approach is a good approximation and can be trusted.

In the following, for all observables $\Sigma$ considered in the previous section, we present predictions in the multiplicative approach, denoted as $\Sigma_{\mathrm{QCD}\times\mathrm{EW}}$. As a further check of the stability of multiplicative approach we display also the quantity $\Sigma_{\mathrm{QCD}^2\times\mathrm{EW}}$, which is precisely defined in appendix A.1. The quantity $\Sigma_{\mathrm{QCD}^2\times\mathrm{EW}}$ is defined analogously to $\Sigma_{\mathrm{QCD}\times\mathrm{EW}}$, but rescaling NLO EW corrections via NNLO QCD $K$-factors. By comparing $\Sigma_{\mathrm{QCD}\times\mathrm{EW}}$ and $\Sigma_{\mathrm{QCD}^2\times\mathrm{EW}}$ one can further estimate the uncertainty due to mixed QCD-EW higher orders.

Figure 2.22 shows the $p_{T,\mathrm{avt}}$ and $m(t\bar{t})$ distributions, while fig. 2.23 refers to $y_{\mathrm{avt}}$ and $y(t\bar{t})$. As in sec. 2.5.1, the plots on the left are produced using the LUXQED PDF set, while those on the right using the NNPDF3.0QED PDF set. We next describe the format of the plots.

Each plot consists of five insets, which all show ratios of different quantities over the central value of $\Sigma_{\mathrm{QCD}}$. In the first inset we compare the central-scale results for the three alternative predictions: $\Sigma_{\mathrm{QCD+EW}}/\Sigma_{\mathrm{QCD}}$ (red line), $\Sigma_{\mathrm{QCD}\times\mathrm{EW}}/\Sigma_{\mathrm{QCD}}$ (green line) and $\Sigma_{\mathrm{QCD}^2\times\mathrm{EW}}/\Sigma_{\mathrm{QCD}}$ (violet line). These quantities are further displayed in the second, third and fourth inset, respectively, where not only the central value but also the scale dependence of the numerator is shown. In all cases we calculate the scale-uncertainty band as a scale-by-scale combination and subsequent variation in the 7-point approach. Scale variation bands have the same colour as the corresponding central-value line. For comparison we also display (grey band) the relative scale uncertainty of $\Sigma_{\mathrm{QCD}}$. Thus, the second inset is exactly the same of the second inset in the corresponding plots in sec. 2.5.1. The last inset shows a comparison of the ratio $\Sigma_{\mathrm{QCD+EW}}/\Sigma_{\mathrm{QCD}}$ with (red line) or without (orange line) including the contribution $\Sigma_{\mathrm{res}}$, where "res" stands for residual and denotes the fact that $\Sigma_{\mathrm{res}}$ are contributions of $\Sigma_{\mathrm{EW}}$ that are expected to be small, regardless of the PDF set used (see eq. (2.7)).

The multiplicative approach shows much smaller dependence on the scale variation. This is particularly relevant for the tail of the $p_{T,\mathrm{avt}}$ distribution, where the scale uncertainty of $\Sigma_{\mathrm{EW}}$ alone is comparable in size with the one of $\Sigma_{\mathrm{QCD}}$; with the reduction of the scale uncertainty $\Sigma_{\mathrm{QCD}\times\mathrm{EW}}$ and $\Sigma_{\mathrm{QCD}}$ uncertainty bands do not overlap, when LUXQED is used. In the case of $m(t\bar{t})$ and $y_{\mathrm{avt}}$ distributions, the $\Sigma_{\mathrm{QCD}\times\mathrm{EW}}$ central-value predictions are typically

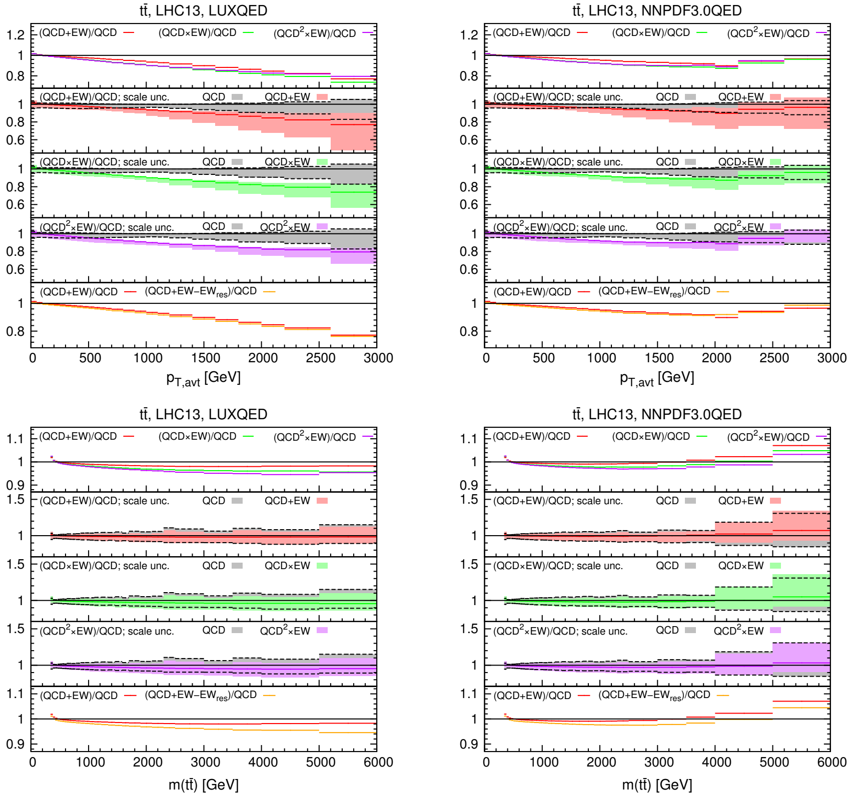

Figure 2.22: Additive ($\Sigma_{\mathrm{QCD+EW}} \equiv \mathrm{QCD}+\mathrm{EW}$) versus multiplicative ($\Sigma_{\mathrm{QCD}\times\mathrm{EW}} \equiv \mathrm{QCD}\times\mathrm{EW}$) approach: $p_{T,\mathrm{avt}}$ and $m(t\bar{t})$ differential distributions at 13 TeV. The format of the plots is described in the text.

larger in absolute value than those of $\Sigma_{\mathrm{QCD+EW}}$, while they are all almost of the same size for the $y(t\bar{t})$ distribution. However, in the case of $y_{\mathrm{avt}}$ the difference between the additive and multiplicative approach is completely negligible compared to their scale uncertainty. Thus, besides the kinematic region where Sudakov effects are the dominant contribution, multiplicative and additive approach are equivalent. Moreover, the difference between $\Sigma_{\mathrm{QCD}\times\mathrm{EW}}$ and $\Sigma_{\mathrm{QCD}^2\times\mathrm{EW}}$ is in general small; a sizeable difference for their scale dependence can be noted only in the tail of the $p_{T,\mathrm{avt}}$ distribution.

For all the reasons mentioned before we believe that the multiplicative approach should be preferred to the additive approach and considered as our best prediction. This conclusion strongly relies also on our choice of the scale, which is based on the principle of fastest convergence, as explained in detail in

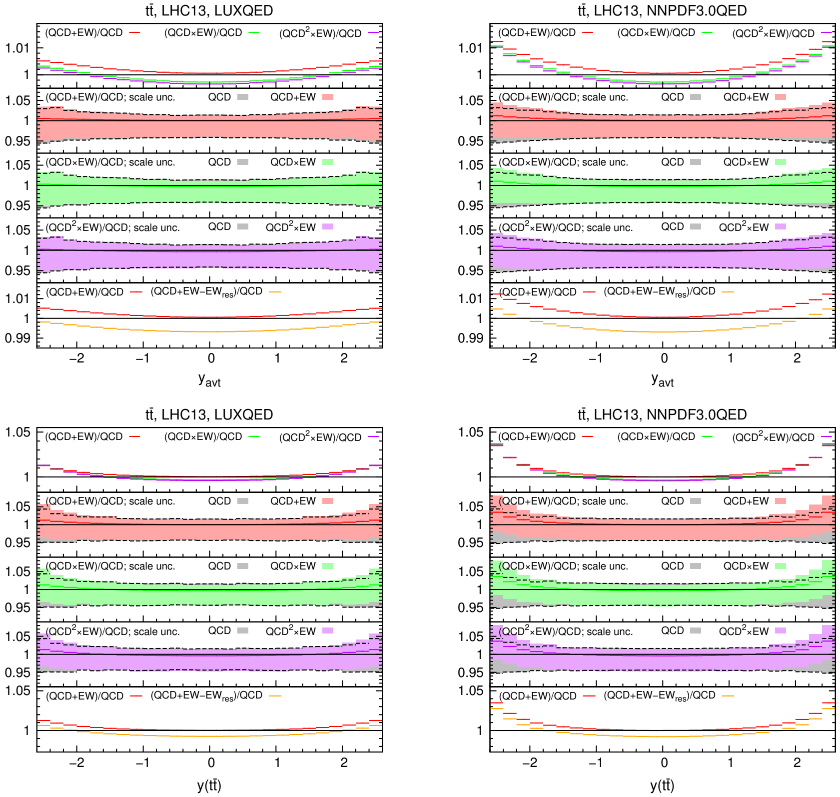

Figure 2.23: As in fig. 2.22 but for the $y_{\mathrm{avt}}$ and $y(t\bar{t})$ differential distributions.

ref. [101]. A scale choice leading to larger $K$ factors would have led to different results, artificially enhancing the difference between $\Sigma_{\mathrm{QCD+EW}}$ and $\Sigma_{\mathrm{QCD\times EW}}$ and jeopardising the conclusion that the multiplicative approach should be preferred.

In the last inset of the plots in figs. 2.22 and 2.23 we also display the quantities $\Sigma_{\mathrm{EW}}$ and $\Sigma_{\mathrm{EW}} - \Sigma_{\mathrm{res}}$. As expected, one can see that the $\Sigma_{\mathrm{res}}$ contribution is typically flat and very small. The only exceptions are the plots for $m(t\bar{t})$, where a visible difference between the two curves ($\Sigma_{\mathrm{EW}}$ and $\Sigma_{\mathrm{EW}} - \Sigma_{\mathrm{res}}$) is present, especially in the tail. The $\Sigma_{\mathrm{res}}$ contributions are exactly included both in the additive and multiplicative approach.

### 2.5.3 Impact of the photon PDF

In this section we explicitly compare the different impact of the photon density provided by the LUXQED and NNPDF3.0QED PDF sets. In other words, we repeat the study performed in section 2.3 for these two PDF sets that were not explicitly considered in that work. We compare the size of the electroweak corrections with and without the photon PDF for both PDF sets. In each plot of fig. 2.24 we show the relative impact induced by the electroweak corrections (the ratio $\Sigma_{\rm EW}/\Sigma_{\rm QCD}$ according to the notation in Appendix A.1) for four cases: NNPDF3.0QED setting the photon PDF equal to zero (red) or not (green), and LUXQED setting the photon PDF equal to zero (violet) or not (blue). For the cases including the photon PDF, we also show the PDF uncertainty band of $\Sigma_{\rm EW}$.

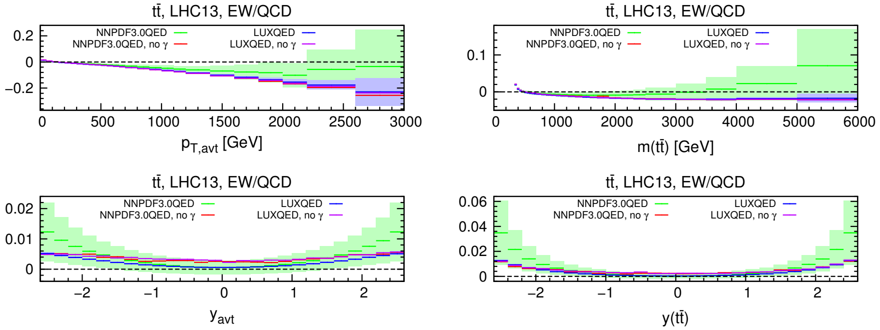

Figure 2.24: Impact of the photon PDF on the $p_{T,\rm avt}$, $m(t\bar{t})$, $y_{\rm avt}$ and $y(t\bar{t})$ differential distributions at 13 TeV. The format of the plots is described in the text.

The impact of the photon-induced contributions can be evaluated via the difference between the green and red line in the case of NNPDF3.0QED and the difference between the blue and violet line in the case of LUXQED. As can be seen from fig. 2.24, which includes this kind of plots for $p_{T,\rm avt}$, $m(t\bar{t})$, $y_{\rm avt}$ and $y(t\bar{t})$, the impact of the photon PDF is negligible for these $t\bar{t}$ distributions in the case of LUXQED, while it is large and with very large uncertainties for the case of NNPDF3.0QED, as already pointed out in section 2.3 for NNPDF2.3QED. At very large $p_{T,\rm avt}$ and $m(t\bar{t})$ also LUXQED show a non-negligible relative PDF uncertainty, which is not induced by the photon but from the PDFs of the coloured partons at large $x$. We checked that a similar behaviour happens also for NNPDF3.0QED when the photon PDF is set to zero.

### 2.5.4 Contributions from heavy boson radiation

In the calculation of EW corrections to QCD processes the inclusion of real emissions of massive gauge bosons (heavy boson radiation or HBR) is not mandatory since, due to the finite mass of the gauge bosons, real and virtual corrections are separately finite (albeit the virtual corrections are enhanced by large Sudakov logarithms). Furthermore, such emissions are typically resolved in experimental analyses and are generally considered as a different process $t\bar{t}V(+X)$ with $V = H, W^{\pm}, Z$.

It is, nonetheless, interesting to estimate the contribution of HBR to inclusive $t\bar{t}$ production. Our motivation is threefold: First, resolved or not, HBR is a legitimate contribution to the $t\bar{t}(+X)$ final state considered in this work. Secondly, it is clear that one cannot guarantee that HBR is resolved with 100% efficiency. Therefore, it is mandatory to have a prior estimate of an upper bound of the size of the effect. Finally, at the best of our knowledge there is no prior work where the HBR contribution has been estimated in inclusive $t\bar{t}$ production. Recently, refs. [40, 41] have provided estimates for HBR in the processes $t\bar{t}V(+X)$, with $V = H, Z, W$.

We have investigated the impact of HBR on all four distributions considered in this work: $p_{T,\mathrm{avt}}$, $m(t\bar{t})$, $y_{\mathrm{avt}}$ and $y(t\bar{t})$. Our results are shown in fig. 2.25, where we plot the effect of HBR for the central scale normalised to the QCD prediction. We show separately the LO HBR effect ($\mathcal{O}(\alpha_s^2\alpha)$), as well as its NLO QCD prediction, which includes corrections order $\mathcal{O}(\alpha_s^3\alpha)$. As a reference we also show the EW corrections for $t\bar{t}$.

In our calculations we include HBR due to $H, W$ and $Z$. We are fully inclusive in HBR, *i.e.*, no cuts on the emitted heavy bosons are applied. Clearly, any realistic experimental analysis will require an estimate of HBR subject to experimental cuts but such an investigation would be well outside the scope of the present work.

From fig. 2.25 we conclude that the effect of HBR is generally much smaller than the EW corrections. In particular, higher order QCD corrections to HBR are completely negligible, i.e. HBR is well described in LO for all the $t\bar{t}$ inclusive distributions and for the full kinematic ranges considered here. The absolute effect of HBR on the $p_{T,\mathrm{avt}}$ distribution is positive and small; it never exceeds 2-3% (relative to the $t\bar{t}$ prediction at NNLO QCD accuracy) and is always much smaller than the virtual EW corrections. The only distribution where the HBR contribution is not negligible compared to the EW corrections is the $m(t\bar{t})$ with LUXQED. For this distribution the HBR correction is positive and only about half the absolute size of the (negative) EW correction. Still, the absolute size

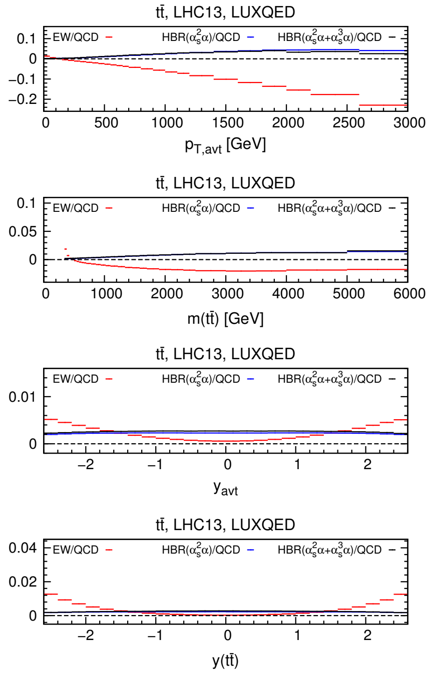

Figure 2.25: Impact of heavy boson radiation (HBR) on the $p_{T,\mathrm{avt}}$, $m(t\bar{t})$, $y_{\mathrm{avt}}$ and $y(t\bar{t})$ differential distributions at 13 TeV. The format of the plots is described in the text.

of the HBR, relative to the prediction at NNLO QCD accuracy, is within 1% and so its phenomenological relevance is unclear. The impact of HBR on the two rapidity distributions is tiny, typically within 3 permil of the NNLO QCD prediction.

## 2.6 Summary

In this chapter we studied the impact of EW corrections and photon-induced contributions on top-quark differential distributions at 8, 13 and 100 TeV. We compared predictions with two different modern PDF sets including the photon density and DGLAP evolution at NLO QCD + LO QED accuracy: the CT14QED and NNPDF2.3QED PDF sets. While contributions due to the photon PDF are negligible with CT14QED, this is not the case for NNPDF2.3-QED, where such contributions at 13 TeV are sizeable and are affected by large PDF uncertainties. At high $p_T(t)$ and $m(t\bar{t})$, the photon-induced contributions can accidentally compensate the negative contributions of Sudakov logarithms or even change the sign of the EW corrections. Furthermore, we have shown that such a compensation strongly depends on the scale choice. In rapidity distributions, the impact of the $g\gamma$ initial state is sizeable in the peripheral region and much larger than NLO EW corrections, which do not receive large Sudakov enhancements in these kinematical configurations.

Increasing the energy of the collider, photon-induced channels become less relevant for a fixed value of $p_T(t)$ or $m(t\bar{t})$, since smaller values of $x$ are probed and consequently the quark and gluon PDFs are much larger than the photon PDF. At 100 TeV, photon-induced channels are important only in the very boosted regime ($p_T(t) \gtrsim 5$ TeV or $m(t\bar{t}) \gtrsim 10$ TeV), where Sudakov logarithms are negative and above the 20% level.

For the same reason, at the LHC photon-induced contributions are relatively larger at 8 TeV than at 13 TeV. We computed their size for the same differential (and normalised) distributions already analysed by ATLAS and CMS, taking into account both experimental errors and theory uncertainties. Data from 8 TeV at large rapidities already appear to be sensitive to the photon PDF; with smaller experimental errors, as expected at 13 TeV, such a sensitivity may be reached also at large $p_T(t)$ and $m(t\bar{t})$.

The first part of our analyses showed two important points. First, differential observables in top-pair production, in particular $y(t)$ and $y(t\bar{t})$ rapidities, can be used to improve the determination of the photon PDF within the NNPDF approach. Second, given the status of the current available PDF sets, both EW corrections and photon-induced contribution have to be taken into account for a correct determination of both central values and uncertainties of theoretical predictions. The first point is particularly relevant for a future fit with LHC 13 TeV data at (N)NLO QCD as well NLO QED accuracy, which will presumably return a better determination of the photon PDF and consequently, with smaller uncertainties, a more solid comparison with the ansatz for $\gamma(x, Q_0)$ used in CT14QED. The second point suggests also that *a priori* not only EW corrections but also photon-induced contributions may be in general important for processes at the LHC and must not be neglected. For the case of $t\bar{t}$ production, given the experimental precision that has been reached at the LHC and especially will be achieved in the Run-II, a combination of higher-order QCD corrections, beyond the NLO, and EW corrections, including photon-induced contributions, is mandatory for providing a precise and reliable SM predictions. This is relevant not only for top physics but also for all the analyses that feature $t\bar{t}$ production as background, notably those related to the Higgs boson and new physics.

In the last part of this work we derive for the first time predictions for all main top-quark pair differential distributions [22] with stable top quarks at the LHC at NNLO QCD accuracy and including EW corrections beyond the NLO EW level. We find that, depending on the specific distribution and kinematics, EW corrections can be significant relative to the scale uncertainty of the NNLO QCD prediction. We present a detailed analysis of top-pair production at the 13 TeV LHC. We have checked that similar conclusions apply also for LHC at 8 TeV.

Providing phenomenological predictions for the LHC is only one of the motivations for the present study. In this work we also study the difference between the additive and multiplicative approaches for combining QCD and EW corrections. Moreover, we analyse the contribution from inclusive Heavy Boson Radiation on inclusive top-pair differential distributions.

In order to quantify the impact of the photon PDF, we use two recent PDF sets whose photon components are constructed within very different approaches. The first set, LUXQED, is based on the PDF4LHC15 set [123] and adds to it a photon contribution that is derived from the structure function approach of ref. [98]. This approach leads to very small photon PDF with tiny PDF error. The second set, NNPDF3.0QED, is based on the NNPDF3.0 family of PDFs and adds a photon component that is extracted from a fit to collider data. NNPDF3.0QED's photon PDF is much larger than that of LUXQED and has much larger PDF error. The two sets are compatible within PDF errors and they both include QED effects in the DGLAP evolution on top of the NNLO QCD.

We confirm the observations already made for the NLO QCD+EW accuracy, namely, the way the photon PDF is included impacts all differential distributions. The size of this impact is different for the various distributions; the most significant impact can be observed in the $p_{T,\mathrm{avt}}$ distribution at moderate and large $p_T$ where the net effect from EW corrections based on NNPDF3.0QED is rather small and with large PDF uncertainties, while using LUXQED is negative, with small PDF uncertainties and comparable to the size of the NNLO QCD scale error. The $m(t\bar{t})$ distribution displays even larger effects, but only at extremely high $m(t\bar{t})$. The $y(t\bar{t})$ distribution is also affected at large $y(t\bar{t})$ values. It seems to us that a consensus is emerging around the structure-function approach of ref. [98]. Given its appealing predictiveness, this approach will likely be utilised in the future in other PDF sets. Therefore, at present, it seems to us that predictions based on the LUXQED set should be preferred – at least as far as the photon PDF is concerned.

---

[22] One distribution we do not consider is $p_{T,t\bar{t}}$ which is not known in NNLO QCD, and for which resummation is mandatory in order to have reliable predictions.

Our best predictions in this work are based on the so-called multiplicative approach for combining QCD and EW corrections. We have also presented predictions based on the standard additive approach. In general, we find that the difference between the two approaches is small and well within the scale uncertainty band. The difference between the two approaches is more pronounced for the $m(t\bar{t})$ and $p_{T,\mathrm{avt}}$ distribution. Nevertheless, both approaches agree within the scale variation. On the other hand, the scale uncertainty band within the multiplicative approach is smaller. Especially, in the case of the $p_{T,\mathrm{avt}}$ distribution it does not overlap with the NNLO QCD uncertainty band. We stress also here, that all these features are sensitive to the factorisation and renormalisation scale choice, thus cannot be generalised to other scale definitions.

Since at the best of our knowledge there is no past study of Heavy Boson Radiation (i.e. $H, W$ and $Z$) in inclusive $t\bar{t}$ production, for completeness, we have also presented the impact of inclusive HBR on the inclusive top-pair differential spectrum. While it is often assumed that additional HBR emissions can be removed in the measurements, it is nevertheless instructive to consider the contribution of such final states. We find that, typically, the HBR contribution is negligible, except for the $m(t\bar{t})$ distribution, where it tends to partially offset the EW correction (when computed with LUXQED). We have also checked that NLO QCD corrections to the LO HBR result are negligible for all the studied in this chapter $t\bar{t}$ distributions. Being independently resolved processes, we focus to the HBR in the next chapter.

# 3 | Associated production of top-quark pairs with bosons

With the second run of the LHC at 13 TeV of centre of mass energy, the Standard Model (SM) is being probed at the highest energy scale ever reached in collider experiments. At these energies, heavy particles and high-multiplicity final states are abundantly produced, offering the opportunity to scrutinise the dynamics and the strength of the interactions among the heaviest particles discovered so far: the $W$ and $Z$ bosons, the top quark and the recently observed Higgs boson [124, 125]. The possibility of measuring the couplings of the top quark with the $W$ and $Z$ bosons and the triple (quadruple) gauge-boson couplings will further test the consistency of the SM and in case quantify possible deviations. In addition, the couplings of the Higgs with the $W$ and $Z$ bosons and the top quark, which are also crucial to fully characterise the scalar sector of the SM, could possibly open a window on BSM interactions.

Besides the study of their interactions, final states involving the heaviest states of the SM are an important part of the LHC program, because they naturally lead to high-multiplicity final states (with or without missing transverse momentum). This kind of signatures are typical in BSM scenarios featuring new heavy states that decay via long chains involving, e.g., dark matter candidates. Thus, either as signal or as background processes, predictions for this class of SM processes need to be known at the best possible accuracy and precision to maximise the sensitivity to deviations from the SM. In other words, the size of higher-order corrections and the total theoretical uncertainties have to be under control. In the case of future (hadron) colliders, which will typically reach higher energies and luminosities, the phenomenological relevance of this kind of processes and the impact of higher-order corrections on the corresponding theoretical predictions are expected to become even more relevant [126].

In this chapter we focus on a specific class of high-multiplicity production process in the SM, i.e., the associated production of a top-quark pair with either one ($t\bar{t}V$) or two gauge vector bosons ($t\bar{t}VV$). The former includes the processes $t\bar{t}W^{\pm}(t\bar{t}W^{+}+t\bar{t}W^{-})$, $t\bar{t}Z$ and $t\bar{t}\gamma$, while the latter counts six different final states, i.e., $t\bar{t}W^{+}W^{-}$, $t\bar{t}ZZ$, $t\bar{t}\gamma\gamma$, $t\bar{t}W^{\pm}\gamma$, $t\bar{t}W^{\pm}Z$ and $t\bar{t}Z\gamma$. In addition, we consider also the associated production of two top-quark pairs ($t\bar{t}t\bar{t}$), since it will be relevant for the phenomenological analyses that are presented in this chapter.

The aim of this chapter is twofold. Firstly, we perform a detailed study of the predictions at NLO QCD accuracy for all the $t\bar{t}V$ and $t\bar{t}VV$ processes, together with $t\bar{t}H$ and $t\bar{t}t\bar{t}$ production, within the same calculation framework and using the same input parameters. This approach allows to investigate, for the first time, whether either common features or substantial differences exist among the theoretical predictions for different final states. More specifically, we investigate the impact of NLO QCD corrections on total cross sections and differential distributions. We systematically study the residual theoretical uncertainties due to missing higher orders by considering the dependence of key observables on different definitions of central renormalisation and factorisation scales and on their variations. NLO QCD corrections are known for $t\bar{t}H$ in [127–130], for $t\bar{t}\gamma$ in [35, 131], for $t\bar{t}Z$ in [35, 132–135], for $t\bar{t}W^{\pm}$ in [6,35,135,136] and for $t\bar{t}t\bar{t}$ in [32,137]. NLO electroweak and QCD corrections have also already been calculated for $t\bar{t}H$ in [40,41,138] and for $t\bar{t}W^{\pm}$ and $t\bar{t}Z$ in [41]. Moreover, in the case of $t\bar{t}H$, NLO QCD corrections have been matched to parton showers [139, 140] and calculated for off-shell top (anti)quarks with leptonic decays in [141]. In the case of $t\bar{t}\gamma$, NLO QCD corrections have been matched to parton showers in [142]. For the $t\bar{t}VV$ processes a detailed study of NLO QCD corrections has been performed only for $t\bar{t}\gamma\gamma$ [143, 144]. So far, only representative results at the level of total cross sections have been presented for the remaining $t\bar{t}VV$ processes [32, 126]. When possible, i.e. for $t\bar{t}V$, $t\bar{t}H$ and $t\bar{t}\gamma\gamma$, our results have been checked against those available in the literature in previous works [32, 35, 41, 135, 136, 139, 140, 142, 143], and we have found perfect agreement with them. This cross-check can also be interpreted as a further verification of the correctness of both the results in the literature and of the automation of the calculation of NLO QCD corrections in MadGraph5_aMC@NLO.

Secondly, we perform a complete analysis, at NLO QCD accuracy including the matching to parton shower and decays, in a realistic experimental setup, for both signal and background processes involved in the searches for $t\bar{t}H$ at the LHC. Specifically, we consider the cases where the Higgs boson decays either into two photons ($H \to \gamma\gamma$), or into leptons (via $H \to WW^*$, $H \to ZZ^*$, $H \to \tau^+\tau^-$), which have already been analysed by the CMS and ATLAS collaborations at the LHC with 7 and 8 TeV [145–147]. In the first case, the process $t\bar{t}\gamma\gamma$ is the main irreducible background. In the second case, the processes $t\bar{t}W^+W^-$, $t\bar{t}ZZ$, $t\bar{t}W^{\pm}Z$ are part of the background, although their rates are very small, as we will see. However, $t\bar{t}W^+W^-$ production, e.g, has already been taken into account at LO in the analyses of the CMS collaboration at 7 and 8 TeV, see for instance [145]. A contribution of similar size can originate also from $t\bar{t}t\bar{t}$ production [148], which consequently has to be included for a correct estimation of the background.[23] Furthermore, depending on the exact final state signature, the $t\bar{t}V$ processes can give the dominant contribu-

---

[23] Triple top-quark production, $t\bar{t}tW$ and $t\bar{t}tj$, a process mediated by a weak current, is characterised by a cross section that is one order of magnitude smaller than $t\bar{t}t\bar{t}$ at the LHC and it is usually neglected in the analyses.

tion, which is typically one order of magnitude larger than in $t\bar{t}VV$ and $t\bar{t}t\bar{t}$ production.

The current chapter is organised as follows. In section 3.1 we present a detailed study of the predictions at NLO QCD accuracy for the total cross sections of $t\bar{t}V$, $t\bar{t}VV$ and $t\bar{t}t\bar{t}$ production. We study their dependences on the variation of the factorisation and renormalisation scales. Furthermore, we investigate the differences among the use of a fixed scale and two possible definitions of dynamical scales. Inclusive and differential $K$-factors are also shown. As already mentioned above, these processes are backgrounds to the $t\bar{t}H$ production with the Higgs boson decaying into leptons, which is also considered in this chapter. To this purpose, we show also the same kind of results for $t\bar{t}H$ production. In addition, in the case of $t\bar{t}V$ and $t\bar{t}H$, we provide predictions at NLO in QCD for the corresponding top-charge asymmetries and in order to investigate the behaviour of the perturbative expansion for some key observables, we also compute $t\bar{t}Vj$ and $t\bar{t}Hj$ cross sections at NLO in QCD. Such results appear here for the first time.

In section 3.2 we study the dependence of the total cross sections and of global $K$-factors for $t\bar{t}VV$ and $t\bar{t}V$ processes as well as for $t\bar{t}H$ and $t\bar{t}t\bar{t}$ production on the total energy of the proton–proton system, providing predictions in the range from 8 to 100 TeV. Specifically for the $t\bar{t}V$ processes we also present diferential distributions at 100 TeV.

In section 3.3 we present results at NLO accuracy for the background and signal relevant for $t\bar{t}H$ production. In section 3.3.1 we consider the signature where the Higgs decays into photons. In our analysis we implement a selection and a definition of the signal region that are very similar to those of the corresponding CMS study [145]. For the signal and background processes $t\bar{t}\gamma\gamma$, we compare LO, NLO results and LO predictions rescaled by a global flat $K$-factor for production only, as obtained in section 3.1. We discuss the range of validity and the limitations of the last approximation, which is typically employed in the experimental analyses. In section 3.3.2 we present an analysis at NLO in QCD accuracy for the searches of $t\bar{t}H$ production with the Higgs boson subsequently decaying into leptons (via vector bosons), on the same lines of section 3.3.1. In this case, we consider different signal regions and exclusive final states, which can receive contributions from $t\bar{t}t\bar{t}$ production and from all the $t\bar{t}V$ and $t\bar{t}VV$ processes involving at least a heavy vector boson. Also here, we compare LO, NLO results and LO predictions rescaled by a global flat $K$-factor for production only. In section 3.4 we draw our conclusions and present an outlook.

This chapter includes results that are public and available at [6, 7], [11, ch. 13], [12, sec. I.6.7], and are obtained in collaboration with F. Maltoni, M.L. Mangano, D. Pagani and M. Zaro.

## 3.1 Fixed-order corrections at the production level

In this section we describe the effects of fixed-order NLO QCD corrections at the production level for $t\bar{t}V$ processes and $t\bar{t}H$ production (subsection 3.1.1), for $t\bar{t}VV$ processes (subsection 3.1.3) and then for $t\bar{t}t\bar{t}$ production (subsection 3.1.4). All the results are shown for 13 TeV collisions at the LHC. In section 3.2.1 we provide total cross sections and global $K$-factors for proton–proton collision energies from 8 to 100 TeV. With the exception of $t\bar{t}\gamma\gamma$, detailed studies at NLO for $t\bar{t}VV$ processes are presented here for the first time. The other processes have already been investigated in previous works, whose references have been listed in introduction. Here, we (re-)perform all such calculations within the same framework, MadGraph5_aMC@NLO, using a consistent set of input parameters and paying special attention to features that are either universally shared or differ among the various processes. Moreover, we investigate aspects that have been only partially studied in previous works, such as the dependence on (the definition of) the factorisation and renormalisation scales, both at integrated and differential level. To this aim we define the variables that will be used as renormalisation and factorisation scales.

Besides a fixed scale, we will in general explore the effect of dynamical scales that depend on the transverse masses ($m_{T,i}$) of the final-state particles. Specifically, we will employ the arithmetic mean of the $m_{T,i}$ of the final-state particles ($\mu_a$) and the geometric mean ($\mu_g$), which are defined as

$$\mu_a = \frac{H_T}{N} := \frac{1}{N} \sum_{i=1,N(+1)} m_{T,i}\,, \tag{3.1}$$

$$\mu_g := \left( \prod_{i=1,N} m_{T,i} \right)^{1/N} . \tag{3.2}$$

In these two definitions $N$ is the number of final-state particles at LO and with $N(+1)$ in eq. 3.1 we understand that, for the real-emission events contributing at NLO, we take into account the transverse mass of the emitted parton.[24] There are two key aspects in the definition of a dynamical scale: the normalisation and the functional form. We have chosen a "natural" average

---

[24] This cannot be done for $\mu_g$; soft real emission would lead to $\mu_g \sim 0$. Conversely, $\mu_a$ can also be defined excluding the partons from real emission and, in the region where $m_{T,i}$'s are of the same order, is numerically equivalent to $\mu_g$. We remind that by default in MadGraph5_aMC@NLO the renormalisation and factorisation scales are set equal to $H_T/2$.

normalisation in both cases leading to a value close to $m_t$ when the transverse momenta in the Born configuration can be neglected. This is somewhat conventional in our approach as the information on what could be considered a good choice (barring the limited evidence that a NLO calculation can give for that in first place) can be only gathered a posteriori by explicitly evaluating the scale dependence of the results. For this reason, in our studies of the total cross section predictions, we vary scales over a quite extended range, $\mu_c/8 < \mu < 8\mu_c$. More elaborate choices of event-by-event scales, such as a CKKW-like one [149] where factorisation and renormalisation scales are "local" and evaluated by assigning a parton-shower like history to the final state configuration, could be also considered. Being ours the first comprehensive study for this class of processes and our aim that of gaining a basic understanding of the dynamical features of these processes, we focus on the simpler definitions above and leave possible refinements to specific applications.

All the NLO and LO results have been produced with the MSTW2008 (68% c.l.) PDFs [27] respectively at NLO or LO accuracy, in the five-flavour-scheme (5FS) and with the associated values of $\alpha_s$. $t\bar{t}W^+W^-$ production, however, has been calculated in the four-flavour-scheme (4FS) with 4FS PDFs, since the 5FS introduces intermediate top-quark resonances that need to be subtracted and thus unnecessary technical complications. The mass of the top quark has been set to $m_t = 173\,\mathrm{GeV}$, the mass of the Higgs boson to $m_H = 125\,\mathrm{GeV}$ and the CKM matrix is approximated as diagonal. NLO computations are performed by leaving the top quark and the vector bosons stable. In simulations at NLO+PS accuracy, they are decayed by employing MADSPIN [150, 151] or by PYTHIA8. If not stated otherwise photons are required to have a transverse momentum larger than 20 GeV ($p_T(\gamma) > 20\,\mathrm{GeV}$) and Frixione isolation [152] is imposed for jets and additional photons, with the technical cut $R_0 = 0.4$. The fine structure constant $\alpha$ is set equal to its corresponding value in the $G_\mu$-scheme for all the processes.[25]

### 3.1.1 $t\bar{t}V$ processes and $t\bar{t}H$ production

As first step, we show for $t\bar{t}H$ production and all the $t\bar{t}V$ processes the dependence of the NLO total cross sections, at 13 TeV, on the variation of the renormalisation and factorisation scales $\mu_r$ and $\mu_f$. This dependence is shown in fig. 3.2 by keeping $\mu = \mu_r = \mu_f$ and varying it by a factor eight around the central value $\mu = \mu_g$ (solid lines), $\mu = \mu_a$ (dashed lines) and

---

[25] This scheme choice for $\alpha$ is particularly suitable for processes involving $W$ bosons [153]. Anyway, in our calculation, no renormalisation is involved in the electroweak sector, so results with different values of $\alpha$ can be obtained by simply rescaling the numbers listed in this chapter.

$\mu = m_t$ (dotted lines). The scales $\mu_a$ and $\mu_g$ are respectively defined in eqs. 3.1 and 3.2. As typically $\mu_a$ is larger than $\mu_g$ and $m_t$, the bulk of the cross sections originates from phase-space regions where $\alpha_s(\mu_a) < \alpha_s(\mu_g)$, $\alpha_s(m_t)$. Consequently, such choice gives systematically smaller cross sections. On the other hand, the dynamical scale choice $\mu_g$ leads to results very close in shape and normalisation to a fixed scale of order $m_t$. Driven by the necessity of making a choice, in the following of this section and in the analyses of section 3.3 we will use $\mu_g$ as reference scale. Also, we will independently vary $\mu_f$ and $\mu_r$ by a factor of two around the central value $\mu_g$, $\mu_g/2 < \mu_f, \mu_r < 2\mu_g$, in order to estimate the uncertainty of missing higher orders. This generally includes, e.g., almost the same range of values spanned by varying $\mu = \mu_r = \mu_f$ by a factor of four around the central value $\mu = \mu_a$, $\mu_a/4 < \mu < 4\mu_a$ (cf. fig. 3.2) and thus it can be seen as a conservative choice. In any case, while certainly justified a priori as well as a posteriori, we stress that the $\mu = \mu_g$ choice is an operational one, i.e. we do not consider it as our “best guess” but just use it as reference for making meaningful comparisons with other possible scale definitions and among different processes.

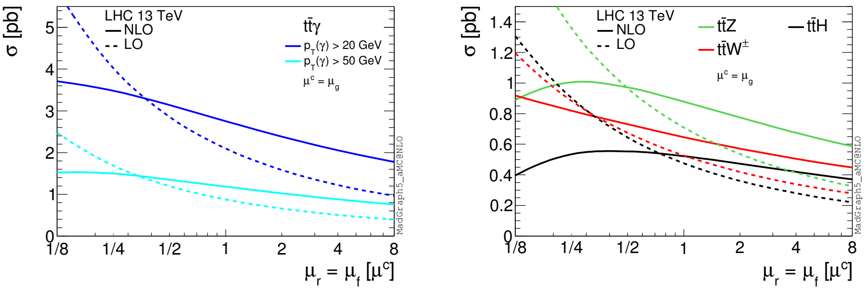

Figure 3.1: LO and NLO cross sections at 13 TeV. Scale dependence in the interval $\mu^c/8 < \mu < 8\mu^c$ with $\mu^c = \mu_g$. The upper plot refers to $t\bar{t}\gamma$ production, the lower plot to $t\bar{t}W^\pm$, $t\bar{t}Z$ and $t\bar{t}H$ production.

Using the procedure described before, in table 3.1 we list, for all the processes, LO and NLO cross sections together with PDF and scale uncertainties, and $K$-factors for the central values. The dependence of the LO and NLO cross sections on $\mu = \mu_r = \mu_f$ is also shown in fig. 3.1 in the range $\mu_g/8 < \mu < 8\mu_g$. As expected, for all the processes, the scale dependence is strongly reduced from LO to NLO predictions both in the standard 9-point interval $\mu_g/2 < \mu < 2\mu_g$ as well as in the full diagonal range $\mu_g/8 < \mu < 8\mu_g$. For $t\bar{t}\gamma$ process (left plots in figs. 3.2 and 3.1), we find that in general the dependence of the cross-section scale variation is not strongly affected by the minimum $p_T$ of the photon, giving

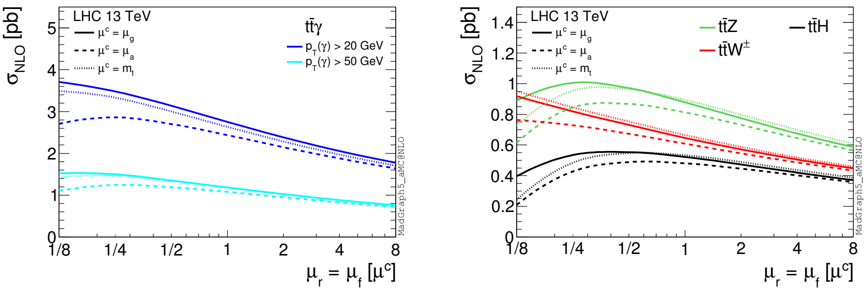

Figure 3.2: Cross sections at 13 TeV. Comparison of the NLO scale dependence in the interval $\mu^c/8 < \mu < 8\mu^c$ for the three different choices of the central value $\mu^c$: $\mu_g$, $\mu_a$, $m_t$. The upper plot refers to $t\bar{t}\gamma$ production, the lower plot to $t\bar{t}W^\pm$, $t\bar{t}Z$ and $t\bar{t}H$ production.

similar results for $p_T(\gamma) > 20\,\mathrm{GeV}$ and $p_T(\gamma) > 50\,\mathrm{GeV}$. With $t\bar{t}W^\pm$ we refer to the sum of the $t\bar{t}W^+$ and $t\bar{t}W^-$ contributions.

We now show the impact of NLO QCD corrections on important distributions and we discuss their dependence on the scale variation as well as on the definition of the scales. For all the processes we analysed the distribution of the invariant mass of the top-quark pair and the $p_T$ and the rapidity of the (anti)top quark, of the top-quark pair and of the vector or scalar boson. For each figure, we display together the same type of distributions for the four different processes: $t\bar{t}\gamma$, $t\bar{t}H$, $t\bar{t}W^\pm$ and $t\bar{t}Z$. Most of the plots for each individual process will be displayed in the format described in the following.

In each plot, the main panel shows the specific distribution at LO (blue) and NLO QCD (red) accuracy, with $\mu = \mu_f = \mu_r$ equal to the reference scale $\mu_g$. In the first inset we display scale and PDF uncertainties normalised to the blue curve, i.e., the LO with $\mu = \mu_g$. The light-grey band indicates the scale variation at LO in the standard range $\mu_g/2 < \mu_f, \mu_r < 2\mu_g$, while the dark-grey band shows the PDF uncertainty. The black dashed line is the central value of the grey band, thus it is by definition equal to one. The solid black line is the NLO QCD differential $K$-factor at the scale $\mu = \mu_g$, the red band around it indicates the scale variation in the standard range $\mu_g/2 < \mu_f, \mu_r < 2\mu_g$. The additional blue borders show the PDF uncertainty. We stress that in the plots, as well as in the tables, scale uncertainties are always obtained by the independent variation of the factorisation and renormalisation scales, via the reweighting technique introduced in [154]. The second and third insets show the same content of the first inset, but with different scales. In the second panel both LO and NLO have been evaluated with $\mu = \mu_a$, in the third panel with $\mu = m_t$.

| 13 TeV $\sigma$[fb] | $t\bar{t}H$ | $t\bar{t}Z$ |
|---|---|---|
| NLO | $522.2^{+6.0\%\ +2.1\%}_{-9.4\%\ -2.6\%}$ | $873.6^{+10.3\%\ +2.0\%}_{-11.7\%\ -2.5\%}$ |
| LO | $476.6^{+35.5\%\ +2.0\%}_{-24.2\%\ -2.1\%}$ | $710.3^{+36.1\%\ +2.0\%}_{-24.5\%\ -2.1\%}$ |
| $K$-factor | 1.10 | 1.23 |

| 13 TeV $\sigma$[fb] | $t\bar{t}W^{\pm}$ | $t\bar{t}\gamma$ |
|---|---|---|
| NLO | $644.8^{+13.0\%\ +1.7\%}_{-11.6\%\ -1.3\%}$ | $2746^{+14.2\%\ +1.6\%}_{-13.5\%\ -1.9\%}$ |
| LO | $526.9^{+28.1\%\ +1.7\%}_{-20.4\%\ -1.8\%}$ | $2100^{+36.2\%\ +1.8\%}_{-24.5\%\ -1.9\%}$ |
| $K$-factor | 1.22 | 1.31 |

Table 3.1: NLO and LO cross sections for $t\bar{t}V$ processes and $t\bar{t}H$ production at 13 TeV for $\mu = \mu_g$. As already stated in the text, with $t\bar{t}W^{\pm}$ we refer to the sum of the $t\bar{t}W^{+}$ and $t\bar{t}W^{-}$ contributions. The first uncertainty is given by the scale variation within $\mu_g/2 < \mu_f, \mu_r < 2\mu_g$, the second one by PDFs. The relative statistical integration error is equal or smaller than one permille.

The fourth and the fifth panels show a direct comparison of NLO QCD predictions using the scale $\mu_g$ and, respectively, $\mu_a$ and $m_t$. All curves are normalised to the red curve in the main panel, i.e., the NLO with $\mu = \mu_g$. The light-grey band now indicates the scale variation dependence of NLO QCD with $\mu = \mu_g$. Again the dashed black line, the central value, is by definition equal to one and the dark-grey borders represent the PDF uncertainties. The black solid line in the fourth panel is the ratio of the NLO QCD predictions at the scale $\mu_a$ and $\mu_g$. The red band shows the scale dependence of NLO QCD predictions at the scale $\mu_a$, again normalised to the central value of NLO QCD at the scale $\mu_g$, denoted as $R(\mu_a)$. Blue bands indicate the PDF uncertainties. The fifth panel, $R(m_t)$, is completely analogous to the fourth panel, but it compares NLO QCD predictions with $\mu_g$ and $m_t$ as central scales.

We start with fig. 3.3, which shows the distributions for the invariant mass of the top-quark pair ($m(t\bar{t})$) for the four production processes. From this distribution it is possible to note some features that are in general true for most of the distributions. As can be seen in the fourth insets, the use of $\mu = \mu_a$ leads to NLO values compatible with, but systematically smaller than, those obtained with $\mu = \mu_g$. Conversely, the using $\mu = m_t$ leads to scale uncertainties bands that overlap with those obtained with $\mu = \mu_g$. By

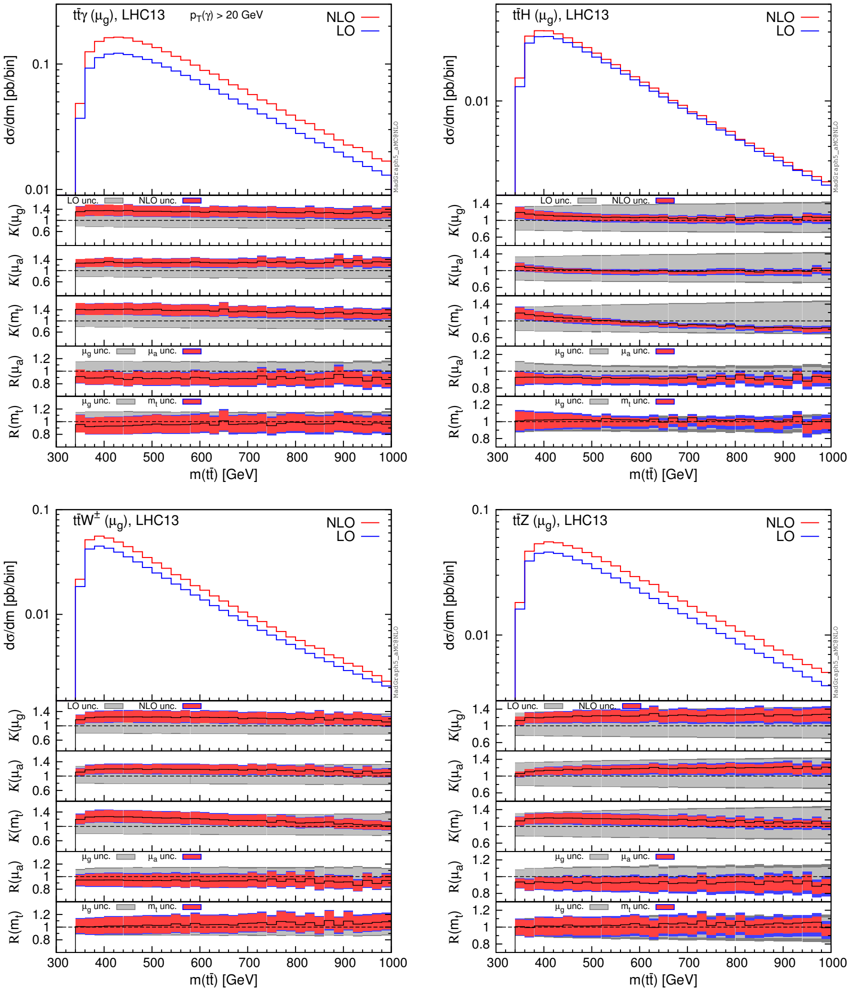

Figure 3.3: Differential distributions for the invariant mass of top-quark pair, $m(t\bar{t})$. The format of the plots is described in detail in the text.

comparing the first three insets for the different processes, it can be noted that the reduction of the scale dependence from LO to NLO results is stronger in $t\bar{t}H$ production than for the $t\bar{t}V$ processes. As we said, all these features are not peculiar for the $m(t\bar{t})$ distribution, and are consistent with the total cross section analysis presented before, see fig. 3.2 and table 3.1. From fig. 3.3 one can see that the two dynamical scales $\mu_g$ and $\mu_a$ yield flatter $K$-factors than those from the fixed scale $m_t$, supporting a posteriori such a reference scale. While this feature is general, there are important exceptions. This is particular

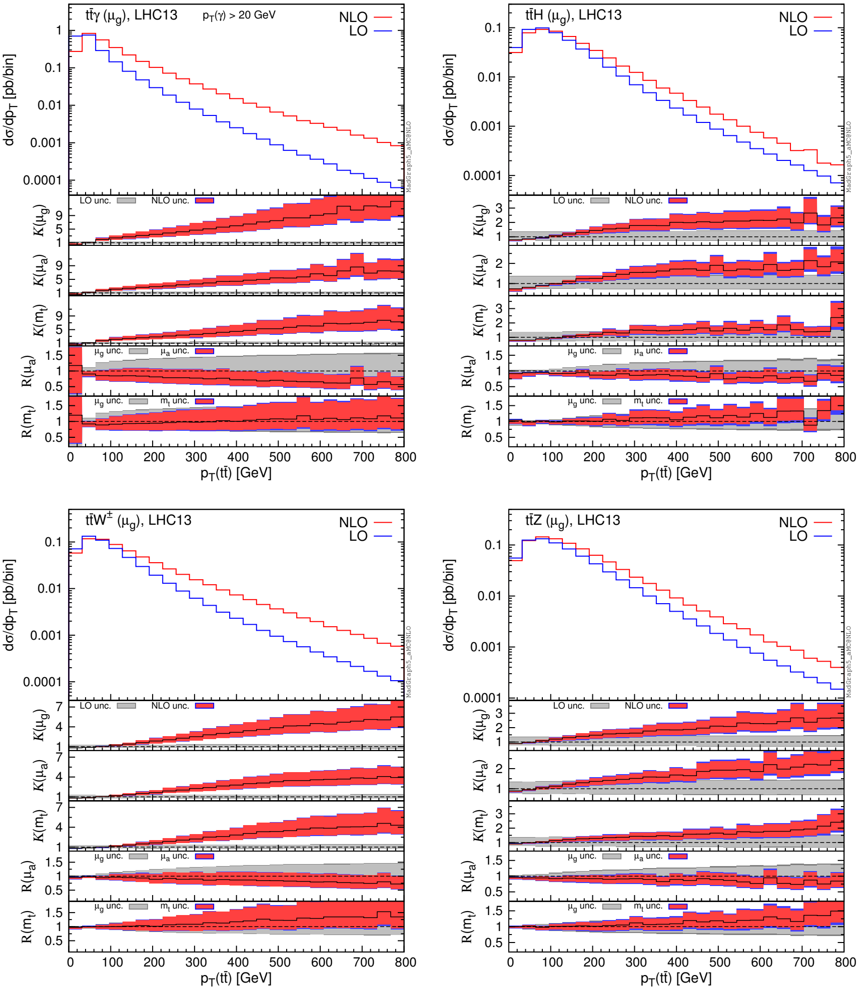

Figure 3.4: Differential distributions for the $p_T$ of top-quark pair, $p_T(t\bar{t})$. The format of the plots is described in detail in the text.

evident for the distributions of the $p_T$ of the top-quark pair ($p_T(t\bar{t})$) in fig. 3.4, where the differential $K$-factors strongly depend on the value of $p_T(t\bar{t})$ for both dynamical and fixed scales. The relative size of QCD corrections grows with the values of $p_T(t\bar{t})$ and this effect is especially large in $t\bar{t}W^{\pm}$ and $t\bar{t}\gamma$ production. In the following we investigate the origin of these large $K$-factors. Top-quark pairs with a large $p_T$ originate at LO from the recoil against a hard vector or scalar boson. Conversely, at NLO, the largest contribution to this kinetic configuration emerges from the recoil of the top-quark pair against a

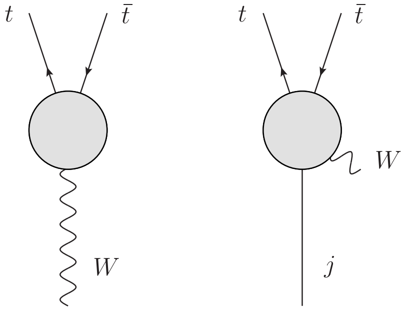

Figure 3.5: Representative kinematical configurations for $t\bar{t}W$ final state. At LO (left) a high-$p_T$ $t\bar{t}$ pair recoils against the $W$ boson. At NLO (right), the dominant configuration is the one where the jet takes most of the recoil and the $W$ boson is soft.

hard jet and a soft scalar or vector boson (see the sketches in fig. 3.5). In particular, the cross section for a top-quark pair with a large $p_T$ receives large corrections from (anti)quark–gluon initial state, which appears for the first time in the NLO QCD corrections. This effect is further enhanced in $t\bar{t}W^{\pm}$ production for two different reasons. First, at LO $t\bar{t}W^{\pm}$ production does not originate, unlike the other production processes, form the gluon–gluon initial state, which has the largest partonic luminosity. Thus, the relative corrections induced by (anti)quark–gluon initial states have a larger impact. Second, the emission of a $W$ collinear to the final-state (anti)quark in $qg \to t\bar{t}W^{\pm}q'$ can be approximated as the $qg \to t\bar{t}q$ process times a $q \to q'W^{\pm}$ splitting. For the $W$ momentum, the splitting involves a soft and collinear singularity which is regulated by the $W$ mass. Thus, once the $W$ momentum is integrated, the $qg \to t\bar{t}W^{\pm}q'$ process yields contributions to the $p_T(t\bar{t})$ distributions that are proportional to $\alpha_s \log^2 [p_T(t\bar{t})/m_W]$ [26]. The same effect has been already observed for the $p_T$ distribution of one vector boson in NLO QCD and EW corrections to $W^{\pm}W^{\mp}, W^{\pm}Z$ and $ZZ$ bosons hadroproduction [113, 155, 156]. The argument above clarifies the origin of the enhancement at high $p_T$ of the $t\bar{t}$ pair, yet it raises the question of the reliability of the NLO predictions for $t\bar{t}V$ in this region of the phase space. In particular the giant $K$-factors and the large scale dependence call for better predictions. At first, one could argue that only a complete NNLO calculation for $t\bar{t}V$ would settle this issue. However, since

---

[26] In $t\bar{t}Z$ the same argument holds for the $q \to qZ$ splitting in $qg \to t\bar{t}Zq$. However, the larger mass of the $Z$ boson and especially the presence of the gluon–gluon initial state at LO suppress this effect.

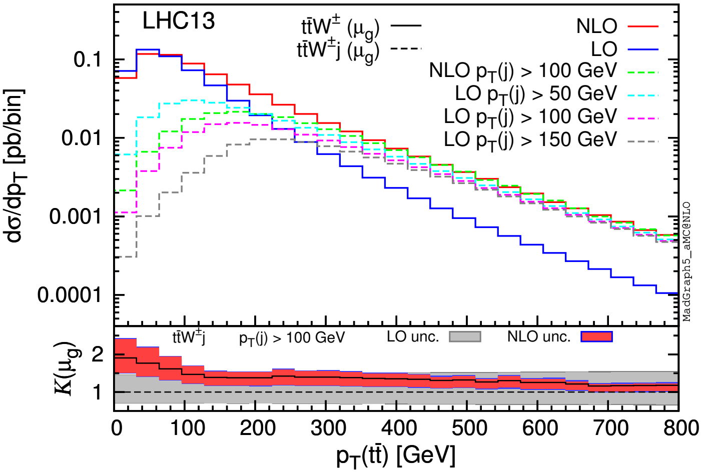

Figure 3.6: Comparison between differential distribution of the $t\bar{t}$ transverse momentum in $t\bar{t}W^{\pm}$ as obtained from calculations performed at different orders in QCD. The blue and red solid histograms are obtained from the $t\bar{t}W^{\pm}$ calculation at LO and NLO respectively. The dashed histograms are obtained from the $t\bar{t}W^{\pm}j$ calculation at LO (light blue, purple, and light-grey) and at NLO (green), for different minimum cuts (50, 100, 150 GeV) on the jet $p_T$. The lower inset shows the differential $K$-factor as well as the residual uncertainties as given by the $t\bar{t}W^{\pm}j$ calculation.

the dominant kinematic configurations (see the sketch on the right in fig. 3.5) feature a hard jet, it is possible to start from the $t\bar{t}Vj$ final state and reduce the problem to the computation of NLO corrections to $t\bar{t}Vj$. Such predictions can be automatically obtained within MadGraph5_aMC@NLO. We have therefore computed results for different minimum $p_T$ for the extra jet both at NLO and LO accuracy. In fig. 3.6 we summarise the most important features of the $t\bar{t}W^{\pm}(j)$ cross section as a function of the $p_T(t\bar{t})$ as obtained from different calculations and orders. Similar results, even though less extreme, hold for $t\bar{t}Z$ and $t\bar{t}H$ final states and therefore we do not show them for sake of brevity. In fig. 3.6, the solid blue and red curves correspond to the predictions of $p_T(t\bar{t})$ as obtained from $t\bar{t}W^{\pm}$ calculation at LO and NLO, respectively. The dashed light blue, purple and light-grey curves are obtained by calculating $t\bar{t}W^{\pm}j$ at LO (yet with NLO PDFs and $\alpha_s$ and same scale choice in order to consistently compare them with NLO $t\bar{t}W^{\pm}$ results) with a minimum $p_T$ cut for the jets of 50, 100, 150 GeV, respectively. The three curves, while having a different threshold behaviour, all tend smoothly to the $t\bar{t}W^{\pm}$ prediction at NLO at high

$p_T(t\bar{t})$, clearly illustrating the fact that the dominant contributions come from kinematic configurations featuring a hard jet, such as those depicted on the right of fig. 3.5. Finally, the dashed green line is the $p_T(t\bar{t})$ as obtained from $t\bar{t}W^{\pm}j$ at NLO in QCD with a minimum $p_T$ cut of the jet of 100 GeV. This prediction for $p_T(t\bar{t})$ at high $p_T$ is stable and reliable, and in particular does not feature any large $K$-factor, as can be seen in the lower inset which displays the differential $K$-factor for $t\bar{t}W^{\pm}j$ production with $p_T$ cut of the jet of 100 GeV. For large $p_T(t\bar{t})$, NLO corrections to $t\bar{t}W^{\pm}j$ reduce the scale dependence of LO predictions, but do not increase their central value. Consequently, as we do not expect large effects from NNLO corrections in $t\bar{t}W^{\pm}$ production at large $p_T(t\bar{t})$, a simulation of NLO $t\bar{t}V$+jets merged sample à la FxFx [157] should be sufficient to provide reliable predictions over the full phase space (see app. B.1). For completeness, we provide in table 3.2 the total cross sections at LO

| 13 TeV $\sigma$[fb] | $t\bar{t}Hj$ | $t\bar{t}Zj$ | $t\bar{t}Wj$ |
|---|---|---|---|
| NLO | $148.3^{+3.3\%}_{-10.1\%}\ ^{+3.0\%}_{-3.6\%}$ | $230.7^{+6.6\%}_{-13.4\%}\ ^{+2.8\%}_{-3.2\%}$ | $202.9^{+11.6\%}_{-15.6\%}\ ^{+1.4\%}_{-1.1\%}$ |
| LO | $174.5^{+57.8\%}_{-33.9\%}\ ^{+2.8\%}_{-2.9\%}$ | $243.1^{+58.2\%}_{-34.0\%}\ ^{+2.7\%}_{-2.8\%}$ | $197.6^{+53.7\%}_{-32.4\%}\ ^{+1.5\%}_{-1.5\%}$ |
| $K$-factor | 0.85 | 0.95 | 1.03 |

Table 3.2: Cross sections with $p_T(j) > 100$ GeV. The renormalisation and factorisation scales are set to $\mu_g$ of $t\bar{t}V$. The (N)LO cross sections are calculated with (N)LO PDFs, the relative statistical integration error is equal or smaller than one permil.

and NLO accuracy for $t\bar{t}W^{\pm}j$, as well as $t\bar{t}Zj$ and $t\bar{t}Hj$ production, with a cut $p_T(j) > 100$ GeV. At variance with what has been done in fig. 3.6, LO cross sections are calculated with LO PDFs and the corresponding $\alpha_s$, as done in the rest of the article.

The mechanism discussed in detail in previous paragraphs is also the source of the giant $K$-factors for large $p_T(t\bar{t})$ in $t\bar{t}\gamma$ production, see fig. 3.4. This process can originate from the gluon–gluon initial state at LO, however, the emission of a photon involves soft and collinear singularities, which are not regulated by physical masses. When the photon is collinear to the final-state (anti)quark, the $qg \to t\bar{t}\gamma q$ process can be approximated as the $qg \to t\bar{t}q$ process times a $q \to q\gamma$ splitting. Here, soft and collinear divergencies are regulated by both the cut on the $p_T$ of the photon ($p_T^{\mathrm{cut}}$) and the Frixione isolation parameter $R_0$. We checked that, increasing the values of $p_T^{\mathrm{cut}}$ and/or $R_0$, the size of the $K$-factors is reduced. It is interesting to note also that corrections in the tail are much larger for $\mu = \mu_g$ than $\mu = \mu_a$. This is due to the fact that the

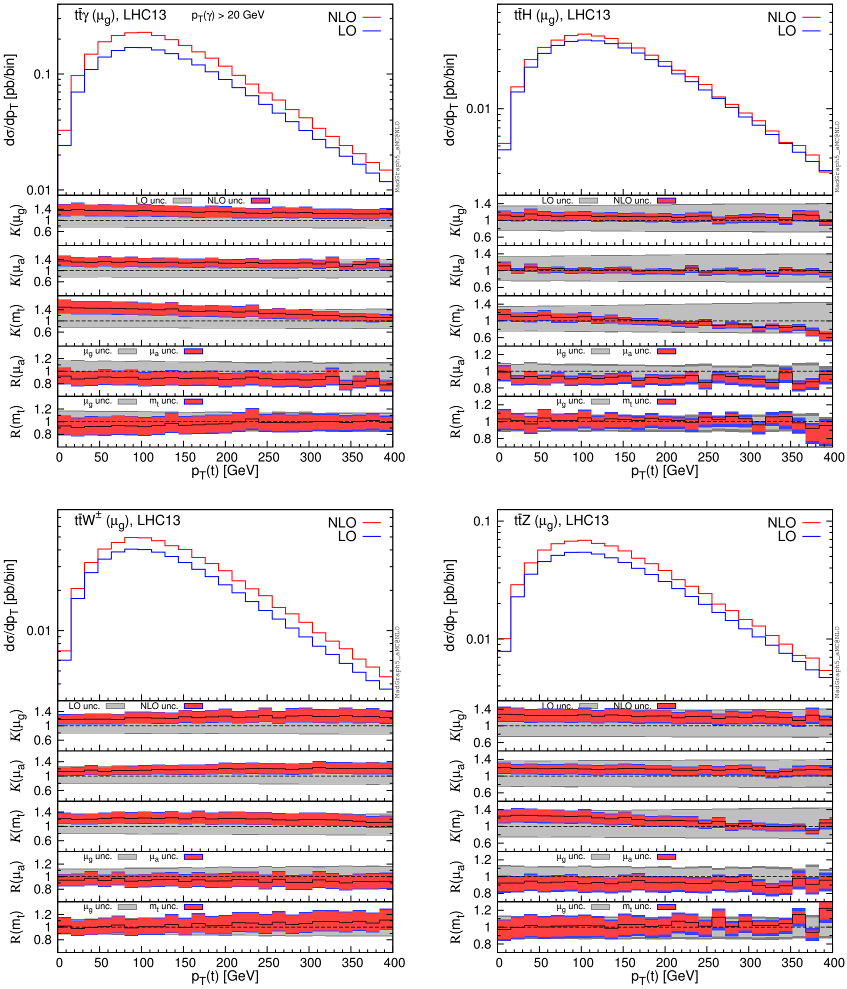

Figure 3.7: Differential distributions for the $p_T$ of top-quark, $p_T(t)$. The format of the plots is described in detail in the text.

softest photons, which give the largest contributions, sizeably reduce the value of $\mu_g$, whereas $\mu_a$ is by construction larger than $2p_T(t\bar{t})$. This also suggests that $\mu_g$ might be an appropriate scale choice for this process only when the minimum $p_T$ cut and the isolation on the photon are harder.[27]

---

[27] Assuming $m_T(t) \sim m_T(\bar{t})$ and $m_T(\gamma) = p_T^{\rm cut}$, the ratio $\mu_a/\mu_g$ increases by increasing $p_T(t)$ and, when $m_T(t) > p_T^{\rm cut}$, decreases by increasing $p_T^{\rm cut}$. Moreover, under the same assumption, $\mu_a = \mu_g$ at $m_T(t) = p_T^{\rm cut}$. For these reasons, especially for large $p_T(t\bar{t})$, $\mu_g$ may underestimate the value of the scale.

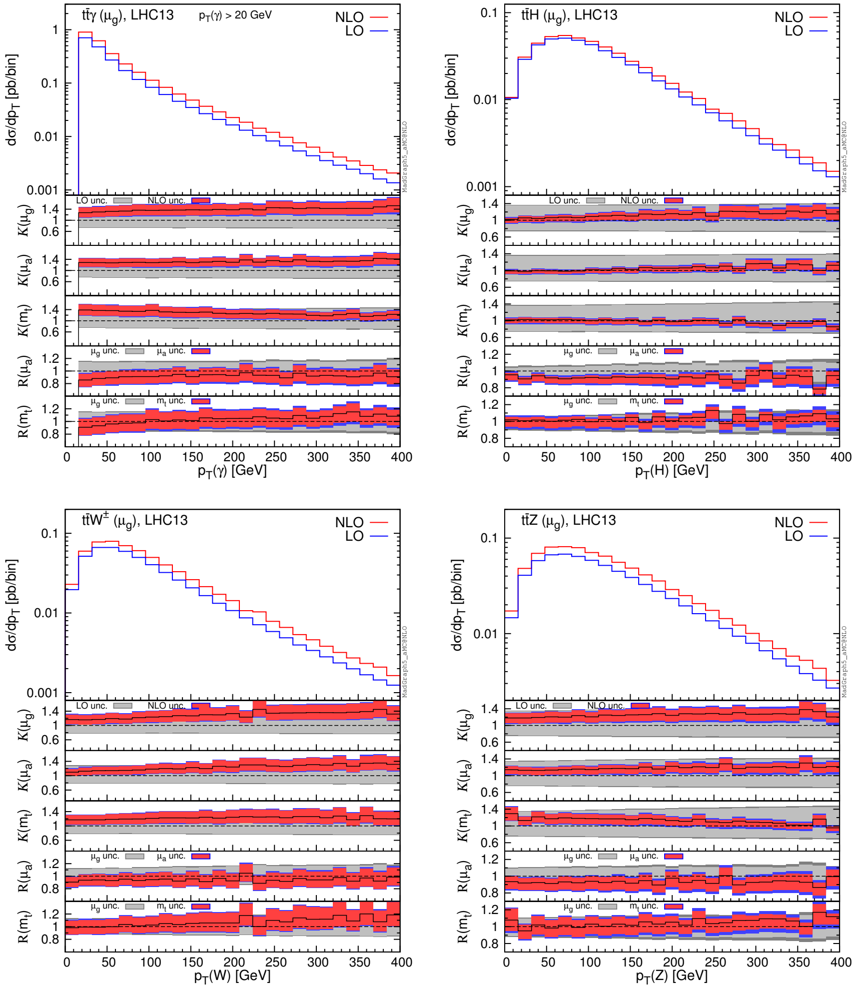

Figure 3.8: Differential distributions for the $p_T$ of the vector or scalar boson, $p_T(V)$. The format of the plots is described in detail in the text.

In figs. 3.7 and 3.8 we show the $p_T$ distributions for the top quark and the vector or scalar boson, $p_T(t)$ and $p_T(V, H)$, respectively. For these two observables, we find the general features which have already been addressed for the $m(t\bar{t})$ distributions in fig. 3.3. In fig. 3.9 we display the distributions for the rapidity of the vector or scalar boson, $y(V, H)$. In the four processes considered here, the vector or scalar boson is radiated in different ways at LO. In $t\bar{t}H$ production, the Higgs boson is never radiated from the initial state. In $t\bar{t}Z$ and $t\bar{t}\gamma$ production, in the quark–antiquark channel the vector boson can be

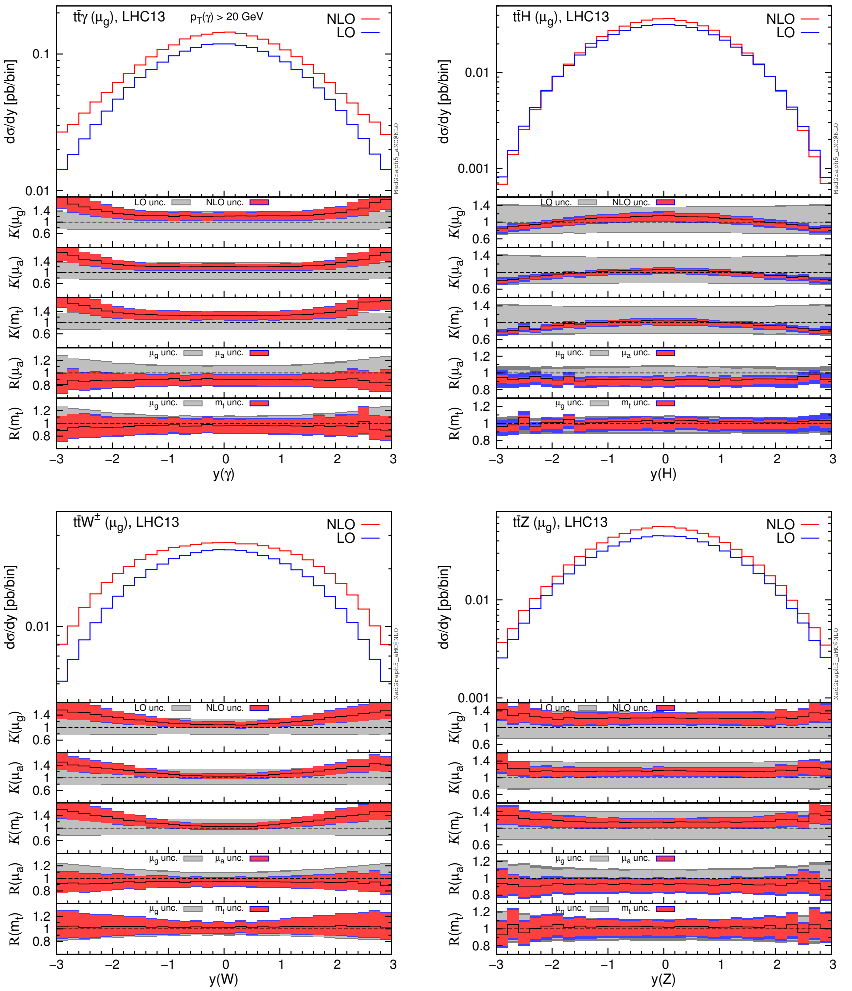

Figure 3.9: Differential distributions for the rapidity of the vector or scalar boson, $y(V)$. The format of the plots is described in detail in the text.

emitted from the initial and final states, but in the gluon–gluon channel it can be radiated only from the final state. In $t\bar{t}W^{\pm}$ production, the $W$ is always emitted from the initial state. The initial-state radiation of a vector boson is enhanced in the forward and backward direction, i.e., when it is collinear to the beam-pipe axis. Consequently, the vector boson is more peripherally distributed in $t\bar{t}W^{\pm}$ production, which involves only initial state radiation, than in $t\bar{t}\gamma$ and especially $t\bar{t}Z$ production. In $t\bar{t}H$ production, large values of $|y(V)|$ are not related to any enhancement and indeed the $y(V)$ distribution

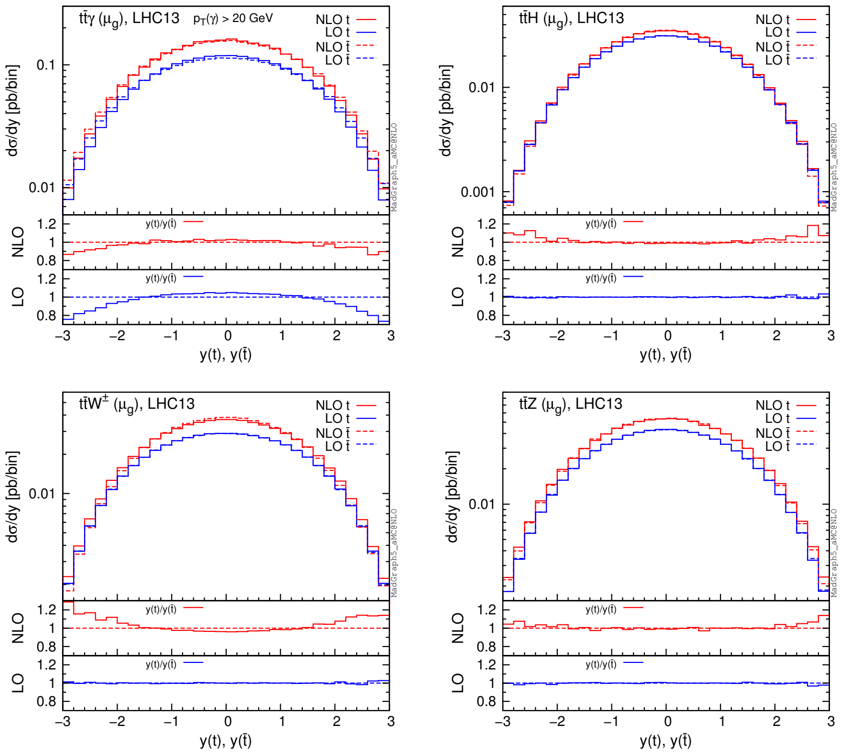

Figure 3.10: Differential distributions for the rapidity of the top quark and antiquark, $y(t)$ and $y(\bar{t})$.

is much more central than in $t\bar{t}V$ processes. These features can be quantified by looking, e.g., at the ratio $r(V) := \frac{d\sigma}{dy}(|y|=0)/\frac{d\sigma}{dy}(|y|=3)$. At LO we find, $r(W) \sim 5$, $r(\gamma) \sim 8.5$, $r(Z) \sim 17.5$ and $r(H) \sim 40$. As can be seen in the first three insets of the plots of fig. 3.9, NLO QCD corrections decrease the values of $r(V)$ for $t\bar{t}W^{\pm}$ and $t\bar{t}\gamma$ production, i.e. the vector bosons are even more peripherally distributed ($r(W) \sim 3.5$, $r(\gamma) \sim 5.5$). A similar but milder effect is observed also in $t\bar{t}Z$ production ($r(Z) \sim 16$). On the contrary, NLO QCD corrections make the distribution of the rapidity of the Higgs boson even more central ($r(H) \sim 53$). In fig. 3.9 one can also notice how the reduction of the scale dependence from LO to NLO results is much higher in $t\bar{t}H$ production than in $t\bar{t}V$ type processes. Furthermore, for this observable, $K$-factors are in general not flat also with the use of dynamical scales. From a phenomenological point of view, this is particularly important for $t\bar{t}W^{\pm}$ and $t\bar{t}\gamma$, since the cross section originating from the peripheral region is not extremely suppressed, as can be seen from the aforementioned values of $r(W)$ and $r(\gamma)$. In fig. 3.10 we show distributions for the rapidities of the top quark and antiquark, $y(t)$ and $y(\bar{t})$. In this case we use a slightly different format for the plots. In the main panel, as in the format of the previous plots, we show LO results in blue and NLO results in red. Solid lines correspond to $y(t)$, while dashed lines refer to $y(\bar{t})$. In the first and second inset we plot the ratio of the $y(t)$ and $y(\bar{t})$ distributions respectively at NLO and LO accuracy. This ratio is helpful to easily identify which distribution is more central(peripheral) and if there is a central asymmetry for the top-quark pair. Also here, although it is not shown in the plots, $K$-factors are not in general flat.

### 3.1.2 The $t\bar{t}$ asymmetry

In the case of $t\bar{t}$ production the central asymmetry, or the forward-backward asymmetry in proton–antiproton collisions, originates from QCD and EW corrections. At NLO, the asymmetry arises from the interference of initial- and final-state radiation of neutral vector bosons (gluon in QCD corrections, and photons or $Z$ bosons in EW corrections) [21, 91–94, 158]. It is not present to the $gg$ initiated subprocesses, which are symmetric. Thus, the real radiation contributions involve, at LO, the processes $pp \to t\bar{t}Z$ and $pp \to t\bar{t}\gamma$, which are studied here both at LO and at NLO accuracy. As can be seen from fig. 3.10, $t\bar{t}\gamma$ production yields an asymmetry already at LO, a feature studied in [159]. The $t\bar{t}Z$ production central asymmetry is also expected to be non vanishing at LO, but the results plotted in fig. 3.10 tell us that the actual value is very small. The asymmetry is instead analytically zero in $t\bar{t}W^{\pm}$ ($t\bar{t}H$) production, where the interference of initial- and final- state $W$(Higgs) bosons is not possible.[28]

At NLO, all the $t\bar{t}V$ processes and the $t\bar{t}H$ production have an asymmetry, as can be seen in fig. 3.10 from the ratios of the $y(t)$ and $y(\bar{t})$ distributions at NLO. In the case of $t\bar{t}W^{\pm}$ production the asymmetry, which is generated by NLO QCD corrections, has been studied in detail in [6] and will be discussed in the following. In all the other cases it is analysed for the first time here. NLO and LO results at 13 TeV for the charge asymmetry $A_c$ defined as

$$A_c = \frac{\sigma(|y_t| > |y_{\bar{t}}|) - \sigma(|y_t| < |y_{\bar{t}}|)}{\sigma(|y_t| > |y_{\bar{t}}|) + \sigma(|y_t| < |y_{\bar{t}}|)} \tag{3.3}$$

are listed in table 3.3, which clearly demonstrates that NLO QCD effects cannot be neglected, once again, in the predictions of the asymmetries. For $t\bar{t}W^{\pm}$

---

[28] In principle, when the couplings of light-flavour quarks are considered non-vanishing, initial-state radiation of a Higgs boson is possible and also a very small asymmetry is generated. However, this possibility is ignored here.

and $t\bar{t}H$ production, an asymmetry is actually generated only at NLO. Furthermore, NLO QCD corrections change sign and increase by a factor $\sim 7$ the asymmetry in $t\bar{t}Z$ production and they decrease it by a factor larger than two in $t\bar{t}\gamma$ production. Thus, NLO results point to the necessity of reassessing the phenomenological impact of the $t\bar{t}\gamma$ signature, which is based on a LO calculation [159]. Moreover, we have also checked that for $p_T(\gamma) > 50\,\mathrm{GeV}$ both the LO and NLO central values of the asymmetry are very similar (within 5 per cent) to the results in table 3.3, where $p_T(\gamma) > 20\,\mathrm{GeV}$. At the LHC, for the $t\bar{t}$ process, it is measured to be $A_c^{exp.} = 0.9 \pm 0.5(\%)$ at 8 TeV [160] and within the SM at NLO QCD+EW accuracy it is calculated to be $A_c^{th.} = 1.11 \pm 0.04(\%)$ [94]. The two parts that consist the asymmetry effect (interference between born and box diagrams as well as interference between ISR and FSR diagrams [21]) are competitive. The former is positive, whereas the latter is negative. This explains the behaviour of this observable for $t\bar{t}\gamma$ and $t\bar{t}Z$ processes from LO to NLO in QCD (table 3.3).

| 13 TeV $A_c$ [%] | $t\bar{t}W^{\pm}$ | $t\bar{t}\gamma$ |
|---|---|---|
| LO | - | $-3.93^{+0.26}_{-0.23}\,^{+0.14}_{-0.11} \pm 0.03$ |
| NLO | $2.90^{+0.67}_{-0.47}\,^{+0.06}_{-0.07} \pm 0.07$ | $-1.79^{+0.50}_{-0.39}\,^{+0.06}_{-0.09} \pm 0.06$ |
| 13 TeV $A_c$ [%] | $t\bar{t}H$ | $t\bar{t}Z$ |
| LO | - | $-0.12^{+0.01}_{-0.01}\,^{+0.01}_{-0.02} \pm 0.03$ |
| NLO | $1.00^{+0.30}_{-0.20}\,^{+0.06}_{-0.04} \pm 0.02$ | $0.85^{+0.25}_{-0.17}\,^{+0.06}_{-0.05} \pm 0.03$ |

Table 3.3: NLO and LO central asymmetries for $t\bar{t}V$-type processes and $t\bar{t}H$ production at 13 TeV for $\mu = \mu_g$. The first uncertainty is given by the scale variation within $\mu_g/2 < \mu_f, \mu_r < 2\mu_g$, the second one by PDFs. The assigned error is the absolute statistical integration error.

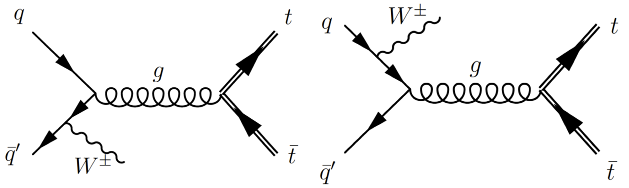

Figure 3.11: Feynman diagrams for the $t\bar{t}W^{\pm}$ production at leading order in QCD.

Looking at table 3.3, we can notice that the charge asymmetry is significantly larger in the $t\bar{t}W^{\pm}$ process. The reason for this is that the symmetric $gg$ channel is absent up to NLO in QCD for this process. The presence of the $W$ boson provides another important property to the $t\bar{t}W^{\pm}$ process. At LO the $W$ boson couples only to the initial quark line (fig. 3.11) and the presence of the $\frac{1}{2}(1-\gamma^5) \equiv P_L$ in the $qW^{\pm}q'$ coupling polarises the quark line. As a result the top-quark resulting pair is also polarised (see app. B.2). This cannot be seen in the top or antitop distributions, but in the subsequent decay products. As a result already at LO, there are large asymmetries for the final leptons and $b$ quarks. In order to access the decay products including the spin correlations, we realise the decays using the MadSpin [150] framework and apply the parton shower with HERWIG6 [46], imposing a $k_T$ algorithm for the jets with $R = 0.7$ and minimum $p_T$ of 20 GeV. We decay leptonically the top-quark pair and extend the definition of the asymmetry of equation 3.3 to the b-jets and the resulting leptons, which we show in table 3.4.

| 13 TeV, $t\bar{t}W^{\pm}$ | $A_c^b$ [%] | $A_c^{\ell}$ [%] |
|---|---|---|
| NLO+PS | $7.54^{+0.19}_{-0.17}$ | $13.16^{+0.81}_{-1.12}$ |

Table 3.4: NLO+PS central asymmetries for $t\bar{t}W^{\pm}$ production at 13 TeV for $\mu = m_t$. The uncertainty is given by the scale variation within $m_t/2 < \mu_f, \mu_r < 2m_t$. The integration error is less than 0.1 (absolute value in %).

### 3.1.3 $t\bar{t}VV$ processes

We start showing for all the $t\bar{t}VV$ processes the dependence of the NLO total cross sections, at 13 TeV, on the variation of the renormalisation and factorisation scales $\mu_r$ and $\mu_f$. This dependence is shown in fig. 3.12 and it is obtained by varying $\mu = \mu_r = \mu_f$ by a factor eight around the central value $\mu = \mu_g$ (solid lines), $\mu = \mu_a$ (dashed lines) and $\mu = m_t$ (dotted lines). Again, for all the processes and especially for those with a photon in the final state, we find that $\mu_a$ typically leads to smaller cross sections than $\mu_g$ and $m_t$. For this class of processes we also investigated the effect of the independent variation of factorisation and renormalisation scales. We found that the condition $\mu_r = \mu_f$ captures the full dependence in the $(\mu_r, \mu_f)$ plane in the range $\mu_a/2 < \mu_f, \mu_r < 2\mu_a$. On the other hand, in the full $\mu_a/8 < \mu_f, \mu_r < 8\mu_a$ region off-diagonal values might differ from the values spanned at $\mu_f = \mu_r$.

In table 3.5 we list, for all the processes, LO and NLO cross sections together with PDF and scale uncertainties, and $K$-factors for the central values.

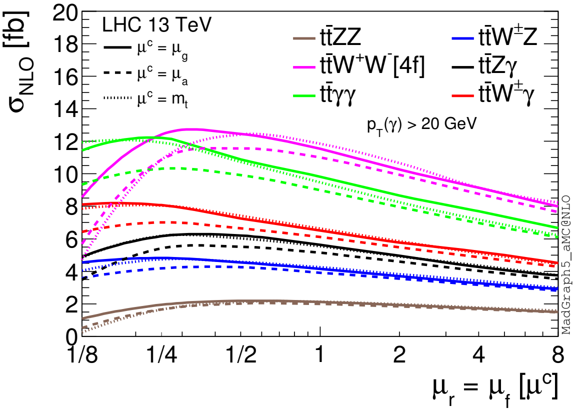

Figure 3.12: Cross sections of $t\bar{t}VV$ processes at 13 TeV. Comparison of NLO scale dependence in the interval $\mu^c/8 < \mu < 8\mu^c$ for the three different choices of the central value $\mu^c$: $\mu_g$, $\mu_a$, $m_t$.

| 13 TeV $\sigma$[fb] | $t\bar{t}ZZ$ | $t\bar{t}W^+W^-$[4f] | $t\bar{t}\gamma\gamma$ |
|---|---|---|---|
| NLO | $2.117^{+3.8\%\ +1.9\%}_{-8.6\%\ -1.8\%}$ | $11.84^{+8.3\%\ +2.3\%}_{-11.2\%\ -2.4\%}$ | $10.26^{+13.9\%\ +1.3\%}_{-13.3\%\ -1.3\%}$ |
| LO | $2.137^{+36.1\%\ +1.9\%}_{-24.4\%\ -1.9\%}$ | $10.78^{+38.3\%\ +2.2\%}_{-25.4\%\ -2.2\%}$ | $8.838^{+36.5\%\ +1.5\%}_{-24.5\%\ -1.6\%}$ |
| $K$-factor | 0.99 | 1.10 | 1.16 |

| 13 TeV $\sigma$[fb] | $t\bar{t}W^\pm Z$ | $t\bar{t}Z\gamma$ | $t\bar{t}W^\pm\gamma$ |
|---|---|---|---|
| NLO | $4.157^{+9.8\%\ +2.2\%}_{-10.7\%\ -1.6\%}$ | $5.771^{+10.5\%\ +1.8\%}_{-12.1\%\ -1.9\%}$ | $6.734^{+12.0\%\ +1.8\%}_{-11.6\%\ -1.4\%}$ |
| LO | $3.921^{+32.6\%\ +2.3\%}_{-22.8\%\ -2.2\%}$ | $5.080^{+38.0\%\ +1.9\%}_{-25.3\%\ -1.9\%}$ | $6.145^{+32.4\%\ +2.1\%}_{-22.6\%\ -2.0\%}$ |
| $K$-factor | 1.06 | 1.14 | 1.10 |

Table 3.5: NLO and LO cross sections for $t\bar{t}VV$ processes at 13 TeV for $\mu = \mu_g$. The first uncertainty is given by the scale variation within $\mu_g/2 < \mu_f, \mu_r < 2\mu_g$, the second one by PDFs. The relative statistical integration error is equal or smaller than one permille.

Again scale uncertainties are evaluated by varying independently the factorisation and the renormalisation scales in the interval $\mu_g/2 < \mu_f, \mu_r < 2\mu_g$. The dependence of the LO and NLO cross sections on $\mu = \mu_r = \mu_f$ is shown in fig. 3.13 in the range $\mu_g/8 < \mu < 8\mu_g$. As expected, for all the processes, the scale dependence is strongly reduced from LO to NLO predictions both in the standard interval $\mu_g/2 < \mu < 2\mu_g$ as well as in the full range $\mu_g/8 < \mu < 8\mu_g$.

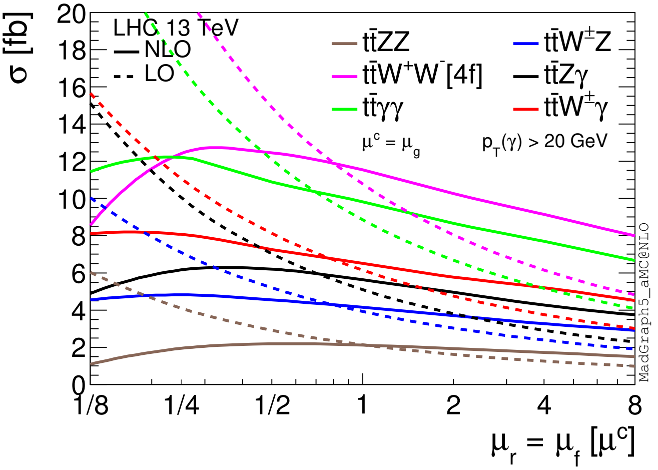

Figure 3.13: NLO and LO cross sections at 13 TeV. Scale dependence in the interval $\mu^c/8 < \mu < 8\mu^c$ with $\mu^c = \mu_g$ for the $t\bar{t}VV$ processes.

For the central scale $\mu = \mu_g$, $K$-factors are very close to unity. It is interesting to note that NLO curves display a plateau around $\mu_g/2$ or $\mu_g/4$, corresponding to $H_T/8$ and $H_T/16$, respectively.

We show now the impact of NLO QCD corrections for relevant distributions and we discuss their dependence on scale choice and its variation. For all the processes we have considered the distribution of the invariant mass of the top-quark pair and the $p_T$ and the rapidity of the (anti)top quark, of the top-quark pair and of the vector bosons.

For each figure, we display together the same type of distributions for the six different processes: $t\bar{t}\gamma\gamma$, $t\bar{t}ZZ$, $t\bar{t}W^+W^-$, $t\bar{t}W^\pm Z$, $t\bar{t}W^\pm\gamma$ and $t\bar{t}Z\gamma$. We start with fig. 3.14, which shows the $m(t\bar{t})$ distributions. The format of the plot is the same used for most of the distribution plots in section 3.1.1, where it is also described in detail. For $m(t\bar{t})$ distributions, we notice features that are in general common to all the distributions and have already been addressed for $t\bar{t}V$ processes in section 3.1.1. For instance, the use of $\mu = \mu_a$ leads to NLO values compatible with, but systematically smaller than, those obtained with $\mu = \mu_g$. Conversely, the choice $\mu = m_t$ leads to scale uncertainties bands that overlaps with those obtained with $\mu = \mu_g$. The NLO corrections in $t\bar{t}ZZ$ production are very close to zero, for $\mu = \mu_g$, and very stable under scale variation (see also table 3.5). For all the processes, the two dynamical scales $\mu_g$ and $\mu_a$ yield flatter $K$-factors than those from the fixed scale $m_t$.

In fig. 3.15 we show the distributions for $p_T(t\bar{t})$. As for $t\bar{t}V$ processes (see fig. 3.4), these distributions receive large corrections in the tails. This effect is especially strong for the processes involving a photon in the final state, namely, $t\bar{t}\gamma\gamma$, $t\bar{t}Z\gamma$ and $t\bar{t}W^{\pm}\gamma$. Also, for all the three choices of $\mu$ employed here, $K$-factors are not flat. Surprisingly, the $K$-factors for $t\bar{t}ZZ$, $t\bar{t}W^{\pm}Z$ and $t\bar{t}W^+W^-$ production show a larger dependence on the value of $p_T(t\bar{t})$ when $\mu$ is a dynamical quantity, as can be seen from a comparison of the first ($\mu = \mu_g$) and second ($\mu = \mu_a$) insets with the third insets ($\mu = m_t$). From the fourth insets of all the six plots, it is possible to notice how the scale dependence at NLO for $\mu = \mu_g$ it is much larger than for $\mu = \mu_a$. Exactly as we argued for $t\bar{t}V$ processes, NLO $t\bar{t}VV$+jets merged sample à la FxFx should be used for an accurate prediction of these tails.

In fig. 3.16 we show the distributions for $p_T(t)$. Most of the features discussed for $m(t\bar{t})$ in fig. 3.14 appear also for these distributions. The same applies to the distributions of the $p_T$ of the two vector bosons, which are displayed in fig. 3.17. In the plots of fig. 3.17 and in all the remaining figures of this section we use the same format used in section 3.1.1 for fig. 3.10. Thus, differential $K$-factors will not be explicitly shown. In the first and second inset we show the ratio of the distributions of the $p_T$ of the two vector bosons, respectively at NLO and LO accuracies. In the case of $t\bar{t}\gamma\gamma$ production, $\gamma_1$ is the hardest photon, while $\gamma_2$ is the softest one. Similarly, in $t\bar{t}ZZ$ production, $Z_1$ is the hardest $Z$ boson, while $Z_2$ is the softest one. As can be noticed, for each process this ratio is the same at LO and NLO accuracy and thus it is not sensitive to NLO QCD corrections.

In fig. 3.18 we show the distributions for $y(t)$ and $y(\bar{t})$. The $t\bar{t}VV$ processes, with the exception of $t\bar{t}W^+W^-$ [29], at LO exhibit a central asymmetry for top (anti-)quarks. Top quarks are more centrally distributed than top antiquarks in $t\bar{t}\gamma\gamma$, $t\bar{t}W^{\pm}\gamma$ and $t\bar{t}Z\gamma$ productions, while they are more peripherally distributed in $t\bar{t}ZZ$ and $t\bar{t}W^{\pm}Z$ production. In all the $t\bar{t}VV$ processes, NLO QCD corrections lead to a relatively more peripheral distribution of top quarks than antiquarks. This effects yield to a non-vanishing central asymmetry for $t\bar{t}W^+W^-$ production and almost cancel the LO central asymmetry of $t\bar{t}Z\gamma$ production. Here, we refrain to present results for the central asymmetries of $t\bar{t}VV$ processes, since it is extremely unlikely that at the LHC it will be possible to accumulate enough statistics to perform these measurements.

---

[29] Analytically, this process is supposed to give an asymmetry. Numerically, it turns out that it can be safely considered as zero.

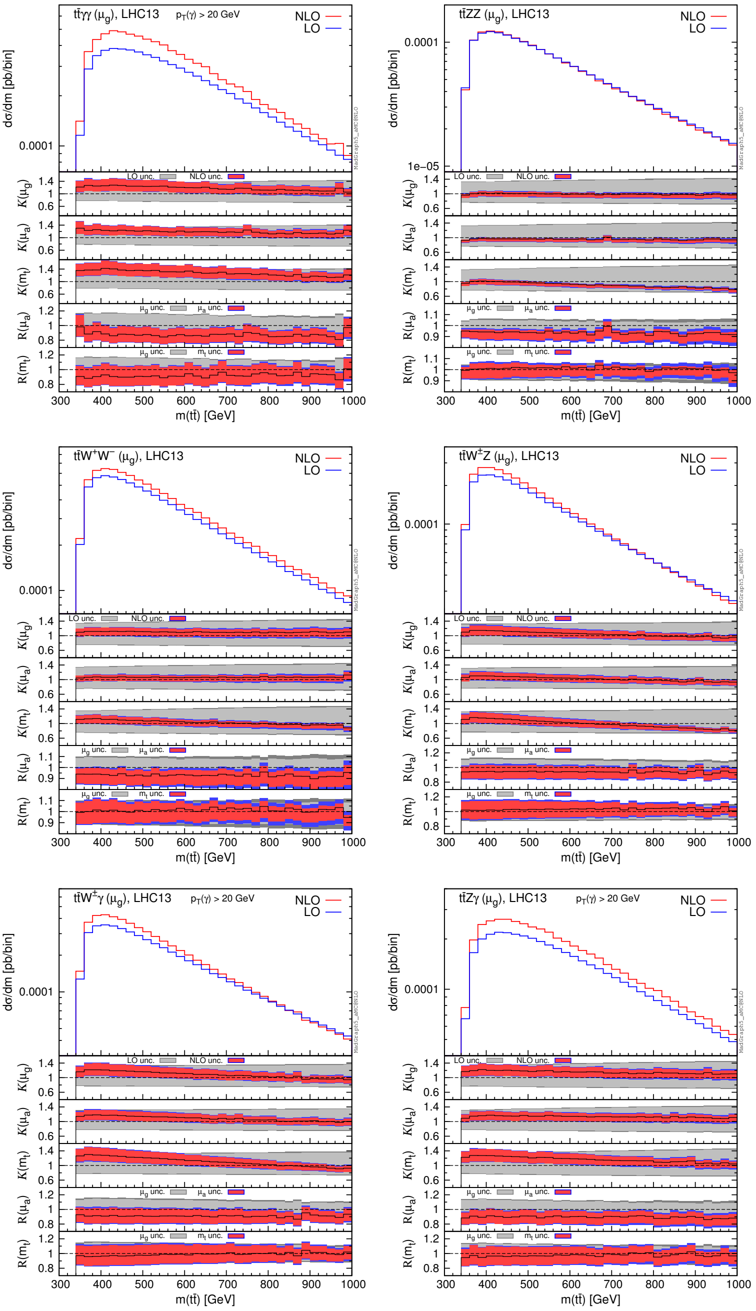

Figure 3.14: Differential distributions for the invariant mass of top-quark pair, $m(t\bar{t})$. The format of the plots is described in detail in section 3.1.1.

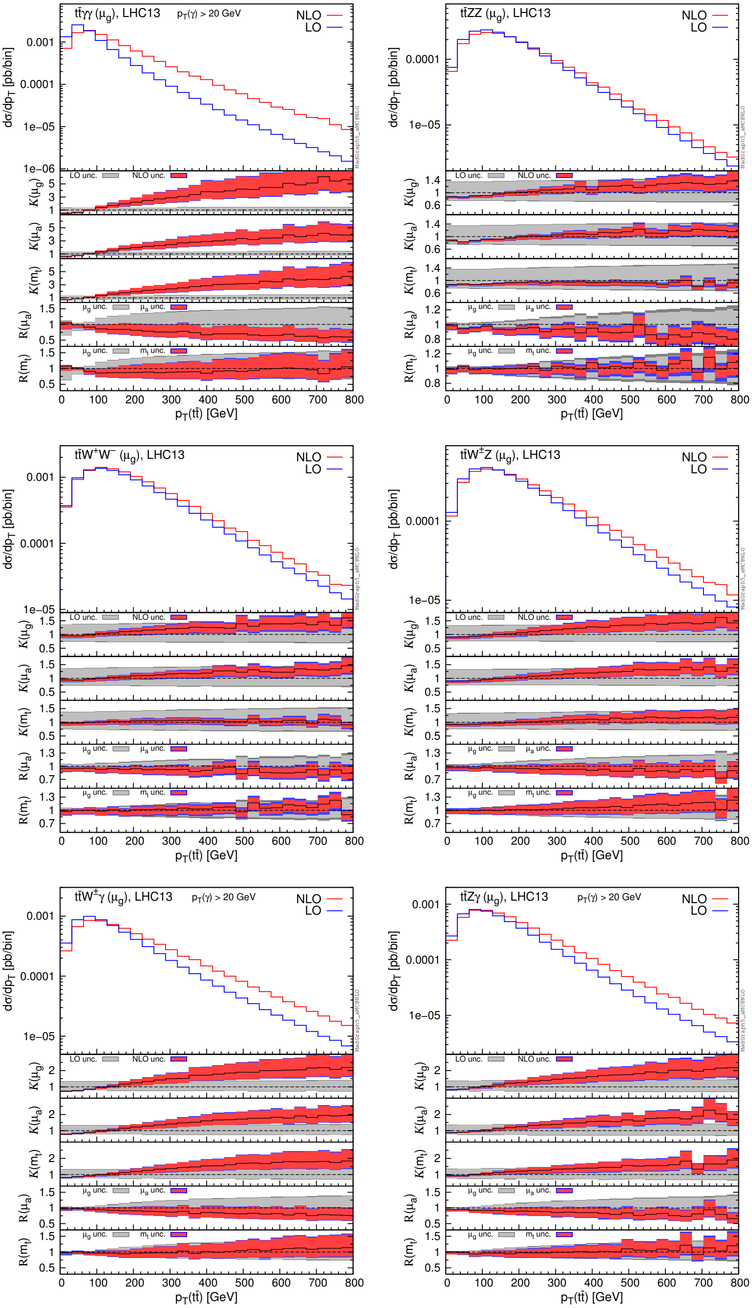

Figure 3.15: Differential distributions for the $p_T$ of top-quark pair, $p_T(t\bar{t})$. The format of the plots is described in detail in section 3.1.1.

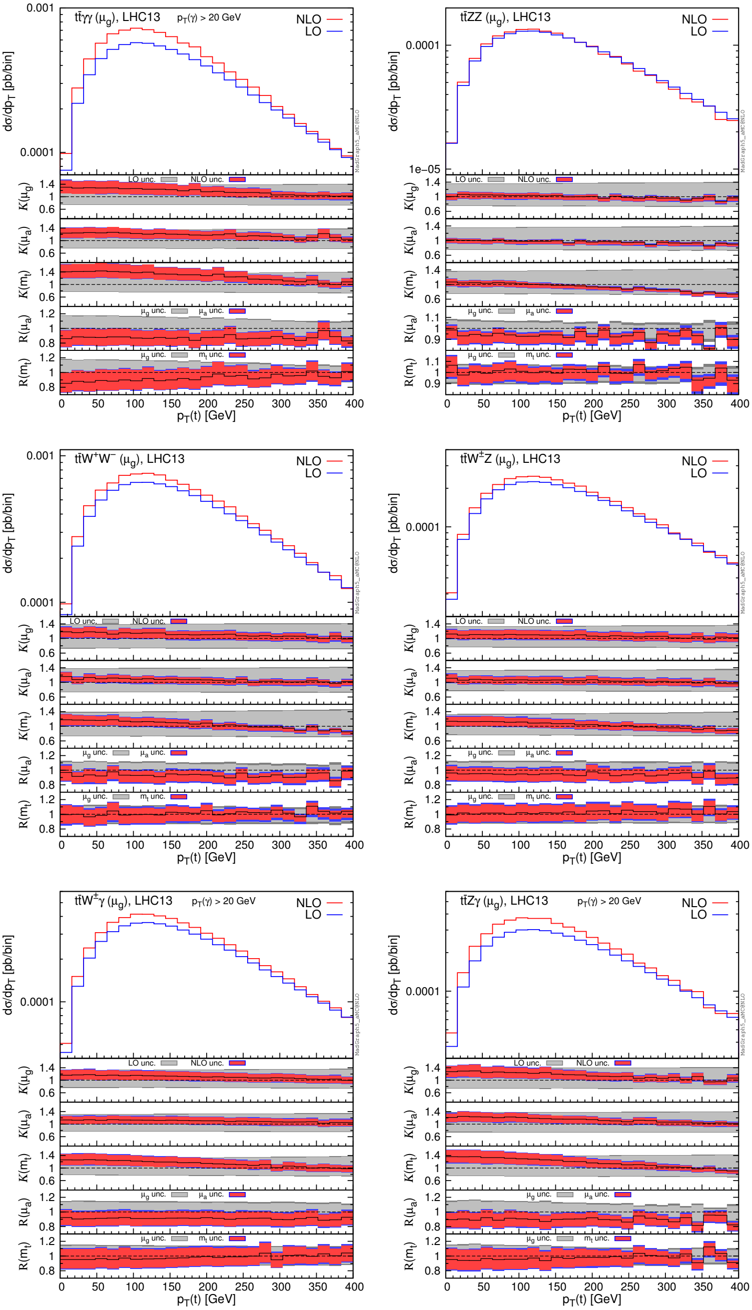

Figure 3.16: Differential distributions for the $p_T$ of top-quark, $p_T(t)$. The format of the plots is described in detail in section 3.1.1.

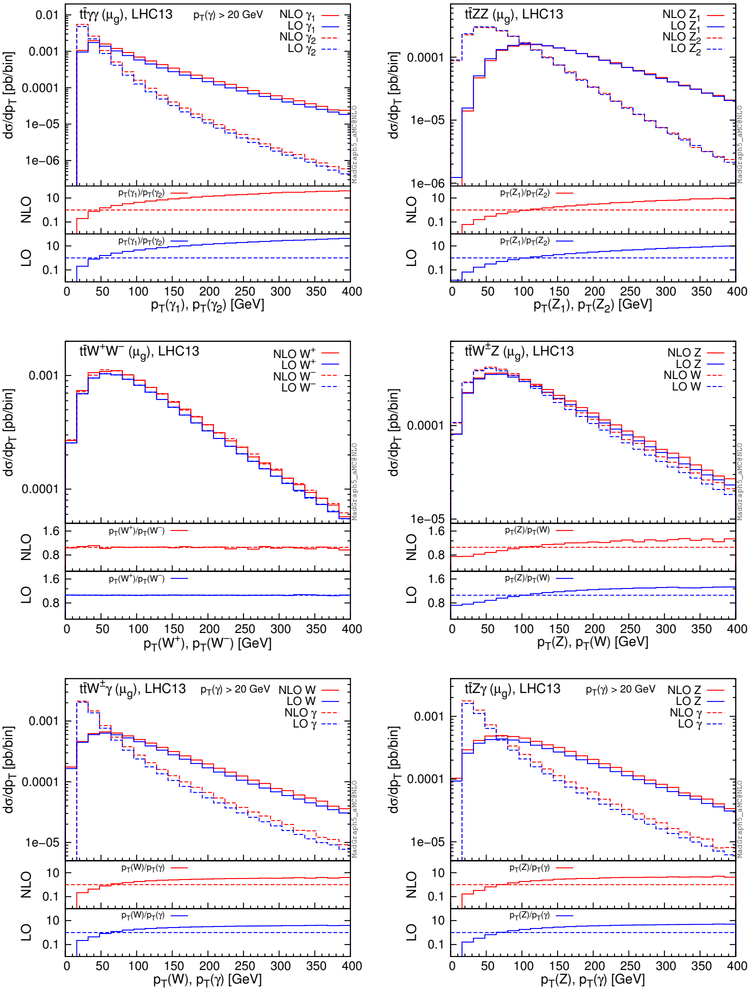

Figure 3.17: Differential distributions for the $p_T$ of the first and second vector boson, $p_T(V_1)$ and $p_T(V_2)$.

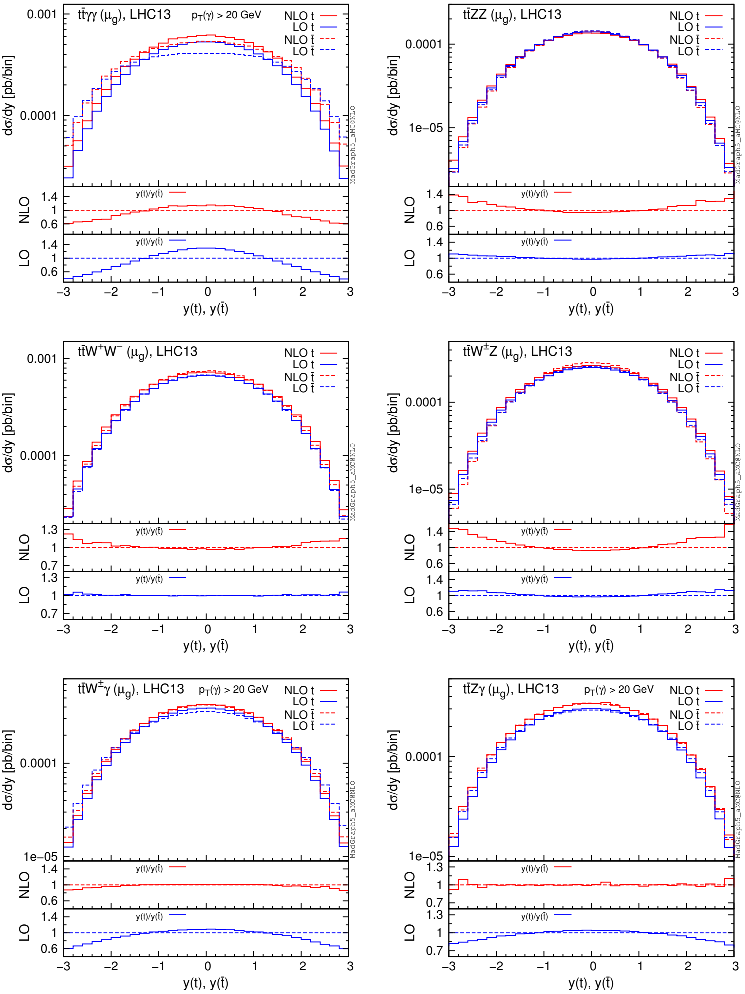

Figure 3.18: Differential distributions for the rapidity of the top quark and antiquark, $y(t)$ and $y(\bar{t})$.

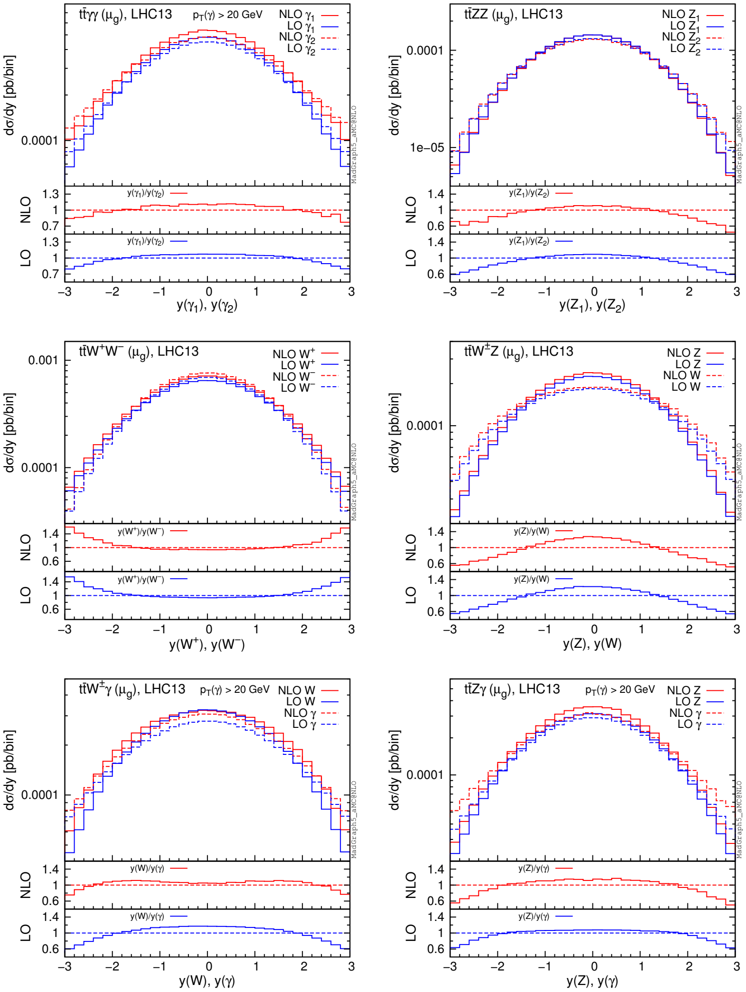

Figure 3.19: Differential distributions for the rapidity of the first and second vector boson, $y(V_1)$ and $y(V_2)$.

In fig. 3.19 we show the distributions for $y(V_1)$ and $y(V_2)$. Comparing the first and second insets, only small differences can be seen for the ratios of the distributions at LO and NLO. Thus, unlike for the top quark and antiquark, the rapidity of the first and the second vector boson receive NLO relative differential corrections that are very similar in size. Both in the distributions of the rapidities of the top (anti)quark and of the vector bosons, NLO QCD corrections in general induce non-flat $K$-factors, also with the use of dynamical scales.

### 3.1.4 $t\bar{t}t\bar{t}$ production

In this section we present results for $t\bar{t}t\bar{t}$ production. We start by showing in fig. 3.20 the scale dependence of the LO (blue lines) and NLO (red lines) total cross section at 13 TeV. As for the previous cases, we vary $\mu = \mu_r = \mu_f$ by a factor eight around the central value $\mu = \mu_g$ (solid lines), $\mu = \mu_a$ (dashes lines) and, due to the much heavier final state, $\mu = 2m_t$ (dotted lines). In this case we also show with a dot-dashed line the dependence of the NLO cross section on an alternative definition of average scale $\mu_a^{\rm LO} = \frac{1}{N}\sum_{i=1,N} m_{T,i}$, where possible additional partons appearing in the final state do not contribute.

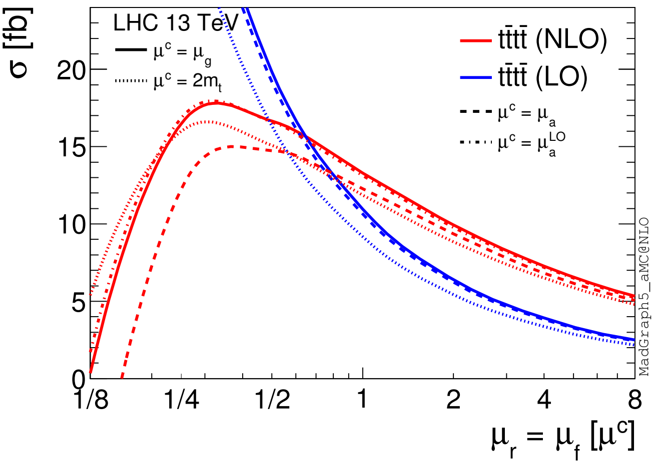

Figure 3.20: NLO and LO cross sections for $t\bar{t}t\bar{t}$ production at 13 TeV. Comparison of the scale dependence in the interval $\mu^c/8 < \mu < 8\mu^c$ for the four different choices of the central value $\mu^c$: $\mu_g$, $\mu_a$, $\mu_a^{\rm LO}$, $2m_t$.

As expected, predictions relative to $\mu_g$ and $\mu_a^{\rm LO}$ are very close. Conversely, $\mu_a$ and $\mu_a^{\rm LO}$ show a non-negligible difference. Note that the value of $\mu_a$ and $\mu_a^{\rm LO}$ is the same for Born and and virtual contributions for any kinematic configuration. Thus, the difference between dashed and dot-dashed lines is formally an NNLO effect that arise from differences in the scale renormalisation for real radiation events only. To investigate the origin of this effect, we have explicitly checked that the difference is mainly induced by the corresponding change in the renormalisation scale and not of the factorisation scale. Similar behaviour is also found in $t\bar{t}V$ and $t\bar{t}VV$ processes, yet since the masses of the final-state particles are different and the $\alpha_s$ coupling order lower, $\mu_g$ and $\mu_a^{\rm LO}$ lines are more distant than in $t\bar{t}t\bar{t}$ production.

Since the LO cross section is of $\mathcal{O}(\alpha_s^4)$, it strongly depends on the value of the renormalisation scale, as can be seen in fig. 3.20. This dependence is considerably reduced at NLO QCD accuracy in the standard interval $\mu_g/2 < \mu < 2\mu_g$. Conversely, for $\mu < \mu_g/4$ the value of the cross section falls down rapidly, reaching zero for $\mu \sim \mu_g/8$. This is a signal that in this region the dependence of the cross section on $\mu$ is not under control. Qualitatively similar considerations apply also for the different choices of scales, as can be seen in fig. 3.20.

In eqs. 3.4 and 3.5, we list the NLO and LO cross sections evaluated at the scale $\mu = \mu_g$ together with scale and PDF uncertainties. As done in previous sections, scale uncertainties are evaluated by varying the factorisation and renormalisation scales in the standard 9-point interval $\mu_g/2 < \mu_f, \mu_r < 2\mu_g$. As a result the total cross section at LHC 13 TeV for the $\mu = \mu_g$ central scale choice reads

$$\begin{aligned}
\sigma_{\rm NLO} &= 13.31^{+25.8\%}_{-25.3\%}\,{}^{+5.8\%}_{-6.6\%}\ \text{fb}\,, && (3.4)\\
\sigma_{\rm LO} &= 10.94^{+81.1\%}_{-41.6\%}\,{}^{+4.8\%}_{-4.7\%}\ \text{fb}\,, && (3.5)\\
K\text{-factor} &= 1.22\,. && (3.6)
\end{aligned}$$

Different choices for the central value and functional form of the scales, as well as the interval of variation, lead to predictions that are compatible with the result above, see also e.g. [137].

We now discuss the effect of NLO QCD corrections on differential distributions. We analysed the distribution of the invariant mass, the $p_T$ and the rapidity of top (anti-)quark and the possible top-quark pairs. Again, given the large amount of distributions, we show only representative results. All the distributions considered and additional ones can be produced via the public code MadGraph5_aMC@NLO. For this process the scale dependence of many distributions has been studied also in [137] and our results are in agreement with those therein. In fig. 3.21 we show plots with the same formats as those used and described in the previous sections. Specifically, we display the distributions for the total $p_T$ of the two hardest top quark and antiquark ($p_T(t_1\bar{t}_1)$), their invariant mass ($m(t_1\bar{t}_1)$), the rapidity of the hardest top quark $y(t_1)$ and the invariant mass of the $t\bar{t}t\bar{t}$ system ($m(t\bar{t}t\bar{t})$). Also, in the last plot of fig. 3.21, we show the $p_T$ distributions of the hardest together with the softest top quarks, $p_T(t_1)$ and $p_T(t_2)$, and their ratios at NLO and LO.

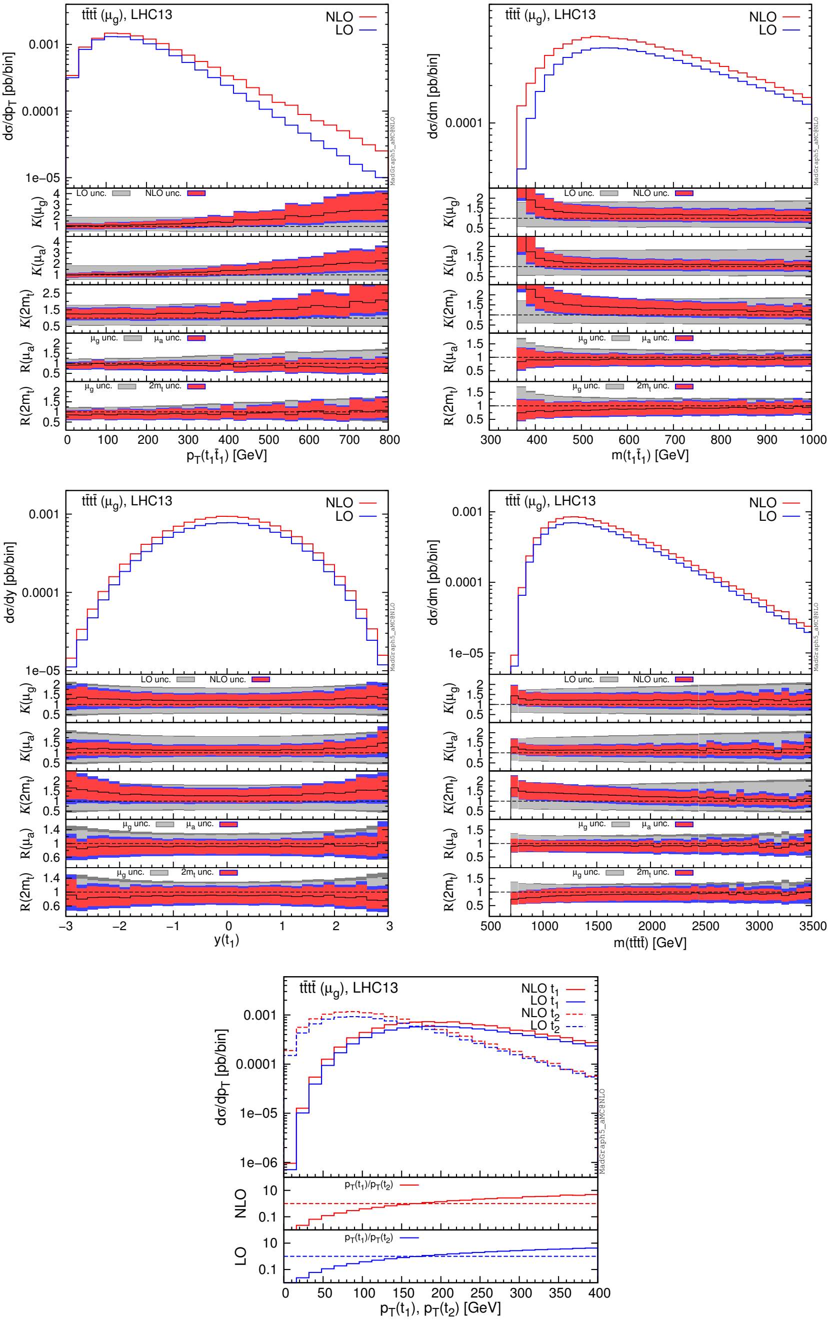

Figure 3.21: Differential distributions for $t\bar{t}t\bar{t}$ production.

We avoid repeating once again the general features that have already been pointed out several times in the previous two sections; they are still valid for $t\bar{t}t\bar{t}$ production. Here we have found, interestingly, that NLO corrections give a sizeable enhancement in the threshold region for $m(t_1\bar{t}_1)$. It is worth to notice that also for this process NLO QCD corrections are very large in the tail of the $p_T(t_1\bar{t}_1)$ distribution, especially with the use of dynamical scales. We have verified that in these regions of phase space the $qg \to t\bar{t}t\bar{t}q$ contributions are important. Finally, as can be seen in the last plot, we find that the ratios of $p_T(t_1)$ and $p_T(t_2)$ distributions are not sensitive to NLO QCD corrections.

## 3.2 FCC studies

### 3.2.1 Total cross sections from 8 to 100 TeV

In addition to the studies performed for the LHC at 13 TeV, in this section we discuss and show results for the dependence of the total cross section on the energy of the proton–proton collision. In fig. 3.22 NLO QCD total cross sections are plotted from 8 to 100 TeV, as bands including scale and PDF uncertainties. The corresponding numerical values are listed in table 3.6. As usual, central values refers to $\mu = \mu_g$, and scale uncertainties are obtained by varying independently $\mu_r$ and $\mu_f$ in the standard interval $\mu_g/2 < \mu_f, \mu_r < 2\mu_g$.

In the left plot of fig. 3.22 we show the results for $t\bar{t}H$ production and $t\bar{t}V$ processes, whereas $t\bar{t}t\bar{t}$ production and $t\bar{t}VV$ processes results are displayed in the right plot. In both plots we show the dependence of the $K$-factors at $\mu = \mu_g$ on the energy (the first and the second inset). The first insets refer to processes with zero-total-charge final states, whereas the second insets refer to processes with charged final states. The very different qualitative behaviours between the two classes of processes is due to the fact that the former include already at LO an initial state with gluons, whereas the latter do not. The gluon appears in the partonic initial states of charged processes only at NLO via the (anti)quark–gluon channel. At small Bjorken-$x$'s, the gluon PDF grows much faster than the (anti)quark PDF. Thus, increasing the energy of the collider, the relative corrections induced by the (anti)quark–gluon initial states leads to the growth of the $K$-factors and dominates in their energy dependence. Also, as can be seen in fig. 3.22 and table 3.6, these processes present a larger dependence on the scale variation than the uncharged processes.

| $\sigma$ [fb] | 8 TeV | 13 TeV | 14 TeV | 25 TeV | 33 TeV | 50 TeV | 100 TeV |
|---|---|---|---|---|---|---|---|
| $t\bar{t}ZZ$ | $0.502^{+2.9\%\ +2.7\%}_{-8.6\%\ -2.2\%}$ | $2.12^{+3.8\%\ +1.9\%}_{-8.6\%\ -1.8\%}$ | $2.59^{+4.3\%\ +1.8\%}_{-8.7\%\ -1.8\%}$ | $11.1^{+6.9\%\ +1.2\%}_{-9.1\%\ -1.4\%}$ | $21.1^{+8.1\%\ +1.1\%}_{-9.4\%\ -1.3\%}$ | $51.6^{+9.9\%\ +0.9\%}_{-9.8\%\ -1.1\%}$ | $204^{+11.3\%\ +0.8\%}_{-9.9\%\ -1.0\%}$ |
| $t\bar{t}W^+W^-$[4f] | $2.67^{+6.2\%\ +2.9\%}_{-11.1\%\ -2.7\%}$ | $11.8^{+8.3\%\ +2.3\%}_{-11.2\%\ -2.4\%}$ | $14.4^{+12.2\%\ +2.6\%}_{-12.8\%\ -2.9\%}$ | $66.6^{+9.5\%\ +1.6\%}_{-10.8\%\ -2.0\%}$ | $130^{+10.2\%\ +1.5\%}_{-10.8\%\ -1.8\%}$ | $327^{+10.9\%\ +1.3\%}_{-10.6\%\ -1.6\%}$ | $1336^{+10.3\%\ +1.0\%}_{-9.9\%\ -1.3\%}$ |
| $t\bar{t}\gamma\gamma$ | $2.77^{+6.4\%\ +1.9\%}_{-10.5\%\ -1.5\%}$ | $10.3^{+13.9\%\ +1.3\%}_{-13.3\%\ -1.3\%}$ | $12^{+12.5\%\ +1.2\%}_{-12.6\%\ -1.2\%}$ | $44.8^{+15.7\%\ +0.9\%}_{-13.5\%\ -0.9\%}$ | $78.2^{+16.4\%\ +0.8\%}_{-13.6\%\ -0.9\%}$ | $184^{+19.2\%\ +0.8\%}_{-14.7\%\ -0.9\%}$ | $624^{+15.5\%\ +0.7\%}_{-13.4\%\ -1.0\%}$ |
| $t\bar{t}W^{\pm}Z$ | $1.13^{+5.8\%\ +3.1\%}_{-9.8\%\ -2.1\%}$ | $4.16^{+9.8\%\ +2.2\%}_{-10.7\%\ -1.6\%}$ | $4.96^{+10.4\%\ +2.1\%}_{-10.8\%\ -1.6\%}$ | $17.8^{+15.1\%\ +1.5\%}_{-12.6\%\ -1.1\%}$ | $30.2^{+18.3\%\ +1.2\%}_{-14.1\%\ -0.9\%}$ | $66^{+18.9\%\ +1.1\%}_{-14.3\%\ -0.8\%}$ | $210^{+21.6\%\ +1.0\%}_{-15.8\%\ -0.8\%}$ |
| $t\bar{t}Z\gamma$ | $1.39^{+6.9\%\ +2.5\%}_{-11.2\%\ -2.2\%}$ | $5.77^{+10.5\%\ +1.8\%}_{-12.1\%\ -1.9\%}$ | $6.95^{+10.7\%\ +1.8\%}_{-12.1\%\ -1.9\%}$ | $29.9^{+12.9\%\ +1.3\%}_{-12.4\%\ -1.5\%}$ | $56.5^{+13.2\%\ +1.2\%}_{-12.2\%\ -1.4\%}$ | $138^{+13.7\%\ +1.0\%}_{-12.0\%\ -1.1\%}$ | $533^{+13.3\%\ +0.8\%}_{-11.1\%\ -1.0\%}$ |
| $t\bar{t}W^{\pm}\gamma$ | $2.01^{+7.9\%\ +2.6\%}_{-10.5\%\ -1.8\%}$ | $6.73^{+12.0\%\ +1.8\%}_{-11.6\%\ -1.4\%}$ | $7.99^{+12.8\%\ +1.7\%}_{-11.9\%\ -1.3\%}$ | $27.6^{+18.7\%\ +1.2\%}_{-14.4\%\ -0.9\%}$ | $46.3^{+20.2\%\ +1.1\%}_{-15.1\%\ -0.8\%}$ | $98.4^{+21.9\%\ +1.0\%}_{-15.9\%\ -0.7\%}$ | $318^{+22.5\%\ +1.0\%}_{-17.7\%\ -0.7\%}$ |
| $t\bar{t}t\bar{t}$ | $1.71^{+24.9\%\ +7.9\%}_{-26.2\%\ -8.4\%}$ | $13.3^{+25.8\%\ +5.8\%}_{-25.3\%\ -6.6\%}$ | $17.8^{+26.6\%\ +5.5\%}_{-25.4\%\ -6.4\%}$ | $130^{+26.7\%\ +3.8\%}_{-24.3\%\ -4.6\%}$ | $297^{+25.5\%\ +3.1\%}_{-23.3\%\ -3.9\%}$ | $929^{+24.9\%\ +2.4\%}_{-22.4\%\ -3.0\%}$ | $4934^{+25.0\%\ +1.7\%}_{-21.3\%\ -2.1\%}$ |

| $\sigma$ [pb] | 8 TeV | 13 TeV | 14 TeV | 25 TeV | 33 TeV | 50 TeV | 100 TeV |
|---|---|---|---|---|---|---|---|
| $t\bar{t}Z$ | $0.226^{+9.0\%\ +2.6\%}_{-11.9\%\ -3.0\%}$ | $0.874^{+10.3\%\ +2.0\%}_{-11.7\%\ -2.5\%}$ | $1.057^{+10.4\%\ +1.9\%}_{-11.7\%\ -2.4\%}$ | $4.224^{+11.0\%\ +1.5\%}_{-11.0\%\ -1.8\%}$ | $7.735^{+11.2\%\ +1.3\%}_{-10.8\%\ -1.5\%}$ | $18^{+11.1\%\ +1.1\%}_{-10.2\%\ -1.3\%}$ | $64.07^{+10.8\%\ +0.9\%}_{-10.9\%\ -1.2\%}$ |
| $t\bar{t}W^{\pm}$ | $0.23^{+9.6\%\ +2.3\%}_{-10.6\%\ -1.7\%}$ | $0.645^{+13.0\%\ +1.7\%}_{-11.6\%\ -1.3\%}$ | $0.745^{+13.5\%\ +1.6\%}_{-11.8\%\ -1.3\%}$ | $2.188^{+17.0\%\ +1.3\%}_{-13.2\%\ -0.9\%}$ | $3.534^{+18.1\%\ +1.2\%}_{-13.7\%\ -0.8\%}$ | $7.03^{+19.2\%\ +1.1\%}_{-14.3\%\ -0.8\%}$ | $20.65^{+21.5\%\ +1.1\%}_{-18.0\%\ -0.8\%}$ |
| $t\bar{t}\gamma$ | $0.788^{+12.7\%\ +2.1\%}_{-13.5\%\ -2.4\%}$ | $2.746^{+14.2\%\ +1.6\%}_{-13.5\%\ -1.9\%}$ | $3.26^{+14.2\%\ +1.6\%}_{-13.4\%\ -1.9\%}$ | $11.77^{+14.5\%\ +1.2\%}_{-12.7\%\ -1.4\%}$ | $20.84^{+14.9\%\ +1.1\%}_{-12.5\%\ -1.3\%}$ | $45.68^{+14.2\%\ +1.0\%}_{-11.7\%\ -1.2\%}$ | $152.6^{+14.3\%\ +0.9\%}_{-13.7\%\ -1.2\%}$ |
| $t\bar{t}H$ | $0.136^{+3.3\%\ +2.8\%}_{-9.1\%\ -3.2\%}$ | $0.522^{+6.0\%\ +2.1\%}_{-9.4\%\ -2.6\%}$ | $0.631^{+6.3\%\ +2.0\%}_{-9.4\%\ -2.5\%}$ | $2.505^{+8.3\%\ +1.6\%}_{-9.4\%\ -1.9\%}$ | $4.567^{+8.8\%\ +1.4\%}_{-9.2\%\ -1.7\%}$ | $10.55^{+9.5\%\ +1.2\%}_{-9.0\%\ -1.4\%}$ | $37.56^{+9.9\%\ +1.0\%}_{-9.8\%\ -1.3\%}$ |

Table 3.6: NLO cross sections for $t\bar{t}VV, t\bar{t}t\bar{t}, t\bar{t}V, t\bar{t}H$ processes using the geometrical average scale. The first uncertainty is given by scale variation, the second by PDFs. For final states with photons the $p_T(\gamma) > 20$ GeV cut is applied. The cross sections for the four final-state particle processes are calculated with percent accuracy, whereas for the processes with three final-state particles with per mill.

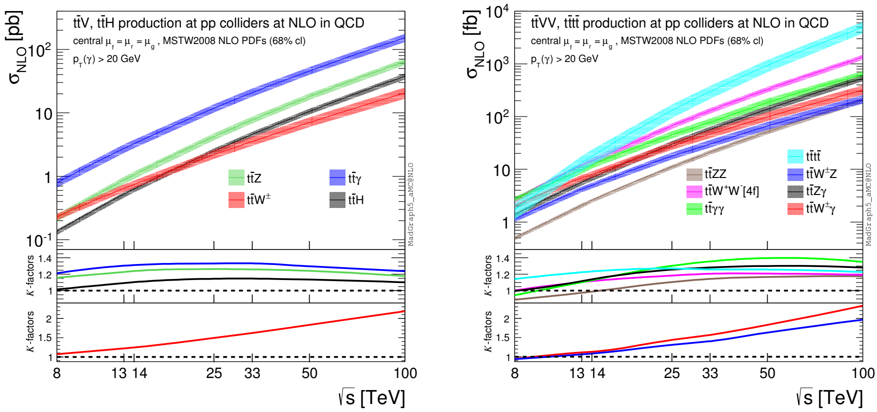

Figure 3.22: NLO total cross sections from 8 to 100 TeV. The error bands include scale and PDF uncertainties (added linearly). The upper plot refers to $t\bar{t}V$ processes and $t\bar{t}H$ production, the lower plot to $t\bar{t}VV$ processes and $t\bar{t}t\bar{t}$ production. For final states with photons the $p_T(\gamma) > 20$ GeV cut is applied.

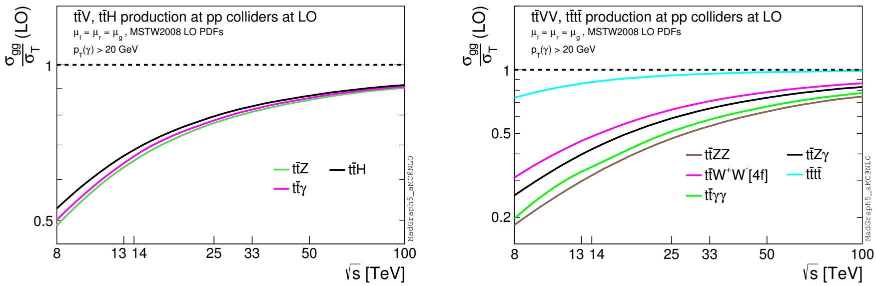

Figure 3.23: Relative contribution of the $gg$ channel to the total cross section at LO for $t\bar{t}V, t\bar{t}H, t\bar{t}VV$ and $t\bar{t}t\bar{t}$ processes for $pp$ collisions from 8 to 100 TeV centre-of-mass energy. For final states with photons the $p_T(\gamma) > 20$ GeV cut is applied.

The differences in the slopes of the curves in the main panels of the plots are also mostly due to the gluon PDF. Charged processes do not originate from the gluon–gluon initial state neither at LO nor at NLO. For this reason, their growth with the increasing of the energy is smaller than for the uncharged processes. All these arguments point to the fact that, at 100 TeV collider, it will be crucial to have NNLO QCD corrections for $t\bar{t}W^{\pm}$, $t\bar{t}W^{\pm}\gamma$ and $t\bar{t}W^{\pm}Z$ processes, if precise measurements to be compared with theory will be available. The fact that $t\bar{t}t\bar{t}$ production is the process with the rapidest growth is again due to percentage content of gluon–gluon-initiated channels, which is higher than for all the other processes, see fig. 3.23. From the right plot of fig. 3.22, it is easy also to note that the scale uncertainty of $t\bar{t}t\bar{t}$ production is larger than for the $t\bar{t}VV$ processes. In this case, the difference originates from the different powers of $\alpha_s$ at LO; $t\bar{t}t\bar{t}$ production is of $\mathcal{O}(\alpha_s^4)$ whereas $t\bar{t}VV$ processes are of $\mathcal{O}(\alpha_s^2\alpha^2)$.

## 3.2.2 Differential distributions at 100 TeV

Based on the previous section, we now focus on results for the $t\bar{t}V$ processes at 100 TeV. We keep the parameter and scale settings from the 13 TeV analysis with the only difference that the photons are required to have a transverse momentum larger than 50 GeV ($p_T(\gamma) > 50\,\text{GeV}$). As a first step, we show for all the $t\bar{t}V$ processes the dependence of the NLO total cross sections on the variation of the renormalisation and factorisation scales $\mu_r$ and $\mu_f$ in analogy to the fig. 3.2 of the 13 TeV. This dependence, which is shown in fig. 3.24, is now monotone over this broad range for all scale choices. This is due to the $qg$ initial states, which give a very large contribution and appear only at NLO. Consequently, no renormalisation and stabilisation of the $\mu_r$ is present for the numerically dominant contribution.

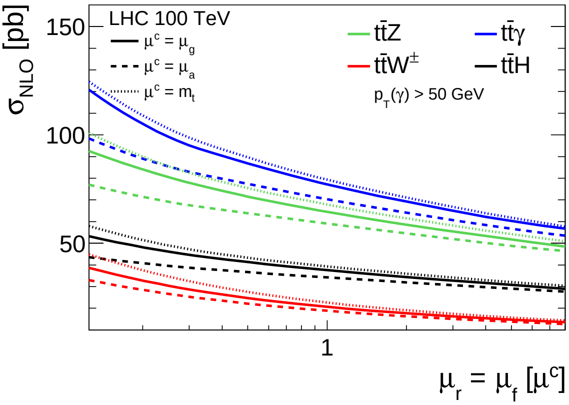

Figure 3.24: Comparison of the NLO scale dependence in the interval $\mu^c/8 < \mu < 8\mu^c$ for the three different choices of the central value $\mu^c$: $\mu_g$, $\mu_a$, $m_t$.

In table table 3.7 we list LO and NLO cross sections, with PDF and scale uncertainties, and $K$-factors for the central values. As expected, the scale dependence is strongly reduced from LO to NLO predictions. $K$-factors are very similar and close to 1, with the exception of $t\bar{t}W^{\pm}$ production. For

| 100 TeV $\sigma$[pb] | $t\bar{t}H$ | $t\bar{t}Z$ |
|---|---|---|
| NLO | $37.56^{+9.9\%\ +1.0\%}_{-9.8\%\ -1.3\%}$ | $64.07^{+10.8\%\ +0.9\%}_{-10.9\%\ -1.2\%}$ |
| LO | $34.26^{+25.6\%\ +0.9\%}_{-19.6\%\ -1.6\%}$ | $54.57^{+25.3\%\ +0.9\%}_{-19.3\%\ -1.7\%}$ |
| $K$-factor | 1.10 | 1.17 |

| 100 TeV $\sigma$[pb] | $t\bar{t}W^{\pm}$ | $t\bar{t}\gamma$ |
|---|---|---|
| NLO | $20.65^{+21.5\%\ +1.1\%}_{-18.0\%\ -0.8\%}$ | $76.68^{+13.3\%\ +0.9\%}_{-12.6\%\ -1.2\%}$ |
| LO | $9.39^{+34.1\%\ +0.9\%}_{-25.1\%\ -1.4\%}$ | $61.51^{+26.8\%\ +0.9\%}_{-20.3\%\ -1.7\%}$ |
| $K$-factor | 2.20 | 1.25 |

Table 3.7: NLO and LO cross sections for $t\bar{t}V$ processes and $t\bar{t}H$ production for $\mu = \mu_g$. The first uncertainty is given by the scale variation within $\mu_g/2 < \mu_f, \mu_r < 2\mu_g$, the second one by PDFs (MSTW2008). The minimum photon $p_T$ is set to 50 GeV. The relative statistical integration error is equal or smaller than one permille.

this process, which at LO only includes $q\bar{q}$ initial states, the opening of $gq$ channels in the initial state has a huge effect. Similar effects may be expected at NNLO, i.e., the first perturbative order including the $gg$ initial state. We further focus on differential distributions and we discuss their dependence on the scale variation as well as on the definition of the scales. For all the processes we analysed the distribution of the invariant mass of the top-quark pair and the $p_T$ and the rapidity of the (anti)top quark, of the top-quark pair and of the vector or scalar boson. We keep the same format as for the 13 TeV distributions.

We start with fig. 3.25, which shows the distributions for the invariant mass of the top-quark pair ($m(t\bar{t})$) for the four production processes. We deduce similar conclusion for the scale uncertainties and behaviour with the 13 TeV distributions. However, at 100 TeV the $K-$factor for the ($m(t\bar{t})$) distribution in $t\bar{t}W^{\pm}$ production is not flat, independently of the scale definition employed, as can be seen in fig. 3.25. This effect is induced by the $qg(\bar{q}g)$ initial states, which have at 100 TeV a relative large PDF luminosity also for high values of $m(t\bar{t})$ and especially $t$-channel-like diagrams for the top-quark pair, at variance with LO $q\bar{q}'$ production. In fig. 3.26 we display for the same observable cumulative plots, i.e., we plot the dependence of the total cross sections on the cut $m(t\bar{t}) > m_{\text{cut}}$ by varying $m_{\text{cut}}$. We can notice that at very high values of $m_{\text{cut}}$ the luminosities of the $qg(\bar{q}g)$ initial states are not the dominant ones, for example the $K$-factor of $t\bar{t}W^{\pm}$ decreases accordingly. For cumulative distributions we show in the

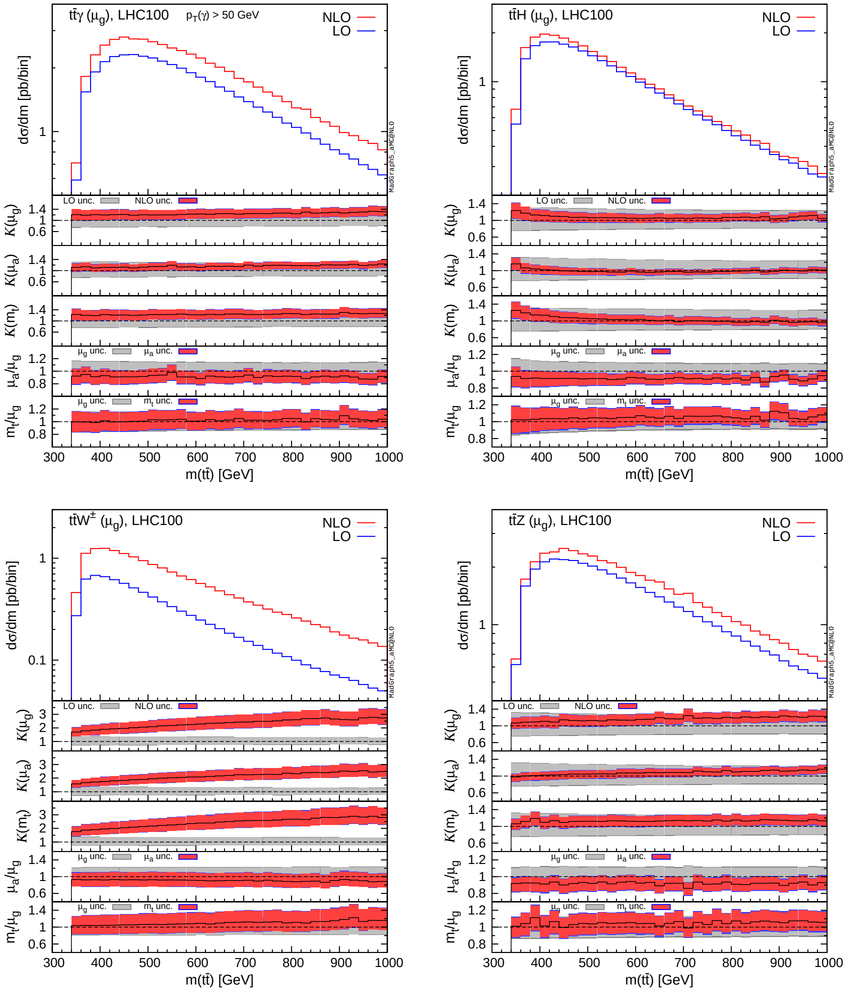

Figure 3.25: Differential distributions for the invariant mass of top-quark pair, $m(t\bar{t})$ at 100 TeV. The format of the plots is described in detail in the text.

plots only results obtained by using $\mu_g$ as central scale. After the $m(t\bar{t})$, we show the $p_T(t\bar{t})$ distributions, where we observe the same, but much more enhanced, behaviour for the NLO corrections as for the 13 TeV case. The $K$-factors become giant at the tails of the distributions already in a phase space region, which will be accurately reached experimentally at an 100 TeV collider. We show this effect in both the cumulative (fig. 3.27) and the differential distributions (fig. 3.28). For further verification of our conclusions for the 13 TeV kinematics (fig. 3.5), we show explicitly the kinematical behaviour of the

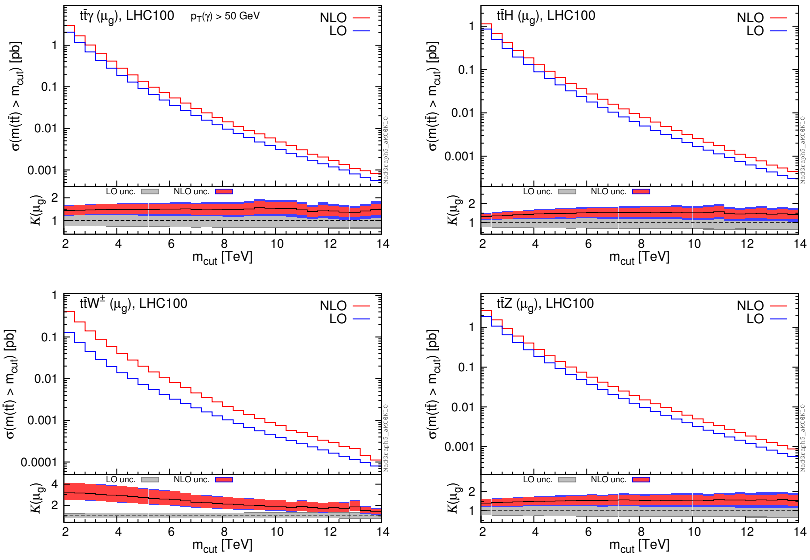

Figure 3.26: Cumulative distributions for the invariant mass of top-quark pair, $m(t\bar{t})$ at 100 TeV. The format of the plots is described in detail in the text.

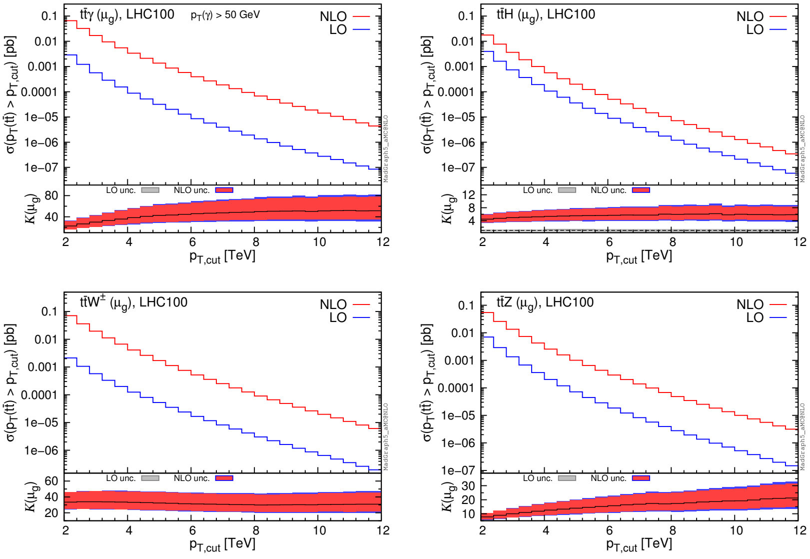

Figure 3.27: Cumulative distributions for the $p_T$ of top-quark pair, $p_T(t\bar{t})$ at 100 TeV. The format of the plots is described in detail in the text.

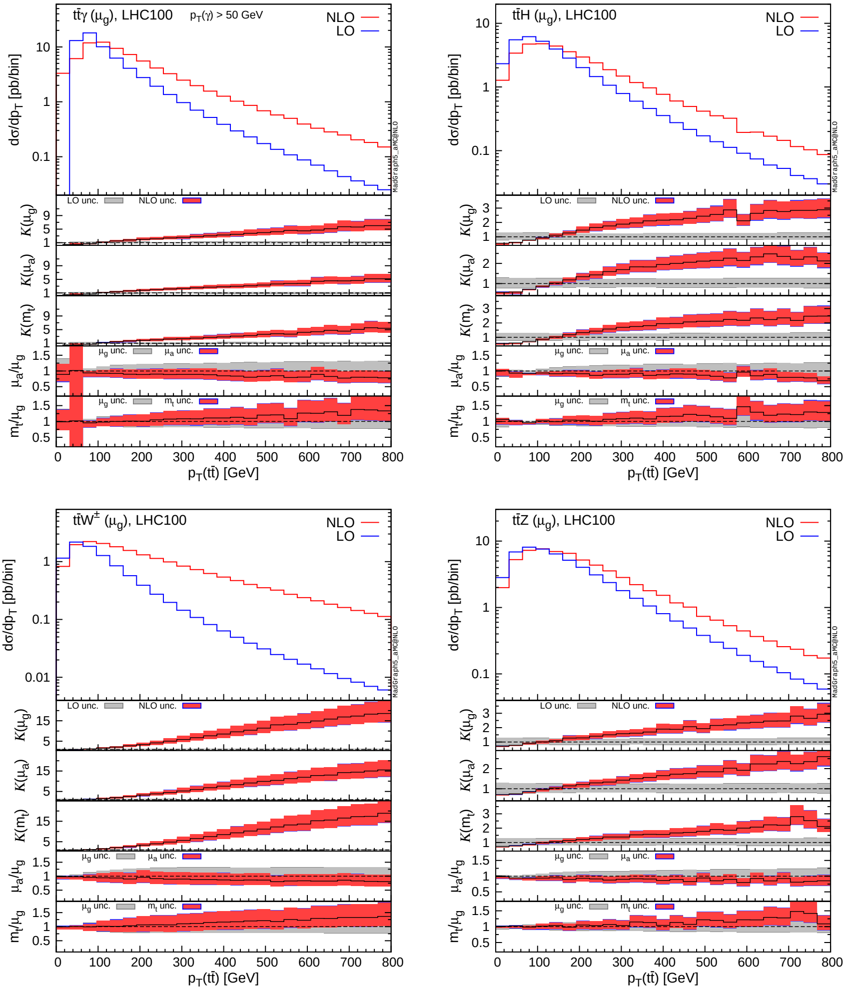

Figure 3.28: Differential distributions for the $p_T$ of top-quark pair, $p_T(t\bar{t})$ at 100 TeV. The format of the plots is described in detail in the text.

$t\bar{t}W^{\pm}j$ process at 100 TeV. In fig. 3.29 we show these additional proofs for the argument discussed so far. We plot relevant distributions for the $t\bar{t}W^{\pm}j$ production. One can see that the $W$ and the jet tend to be collinear, especially for large $p_T(t\bar{t})$, and that the $W$ is typically soft. In fig. 3.30 we summarise the most important features of the $t\bar{t}W^{\pm}(j)$ cross section as a function of the $p_T(t\bar{t})$ as obtained from different calculations and orders. Comparing this figure with the figure 3.6 of 13TeV, we see a similar behavour, with the difference that now the $t\bar{t}W^{\pm}j$@NLO (green dashed), which opens up the $gg$ channel provides a

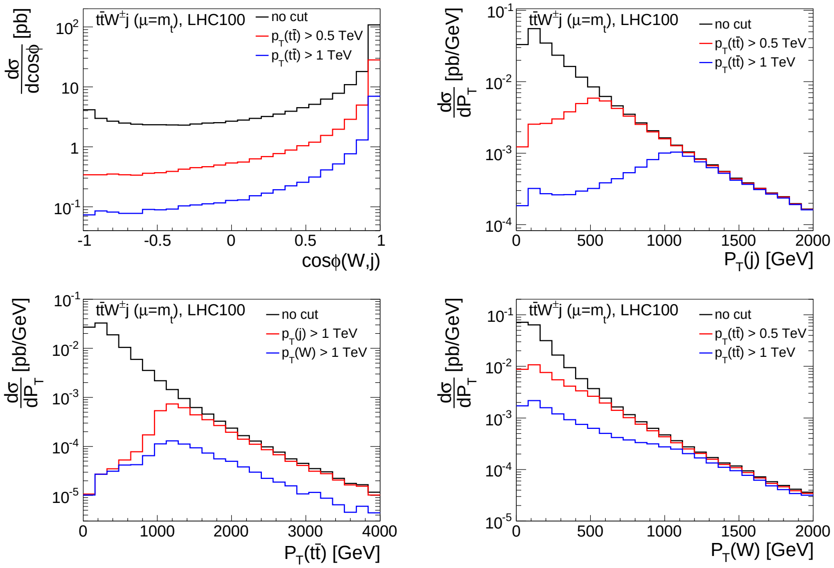

Figure 3.29: Relevant distributions for $t\bar{t}W^{\pm}j$ production, where the fixed scale $\mu = m_t$ has been used. Black lines are without cuts, red and blue lines are with cuts.

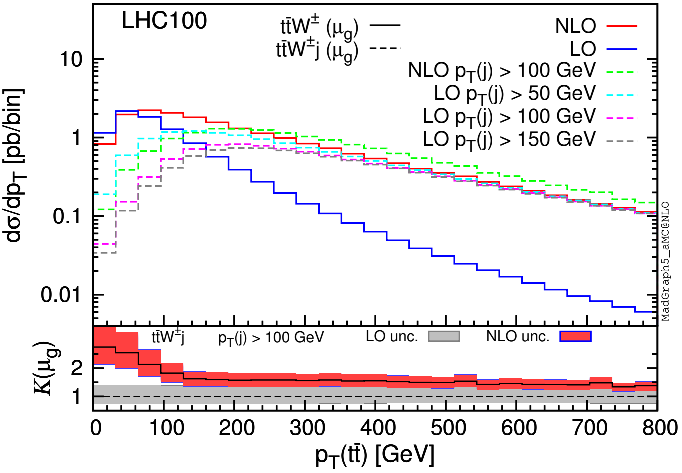

Figure 3.30: Comparison at 100 TeV between differential distribution of the $t\bar{t}$ transverse momentum in $t\bar{t}W^{\pm}$. The format of the plot is as in fig. 3.6.

| 100 TeV $\sigma$[pb] | $t\bar{t}Hj$ | $t\bar{t}Zj$ | $t\bar{t}W^{\pm}j$ |
|---|---|---|---|
| NLO | $19.42^{+0.7\%}_{-4.9\%}{}^{+1.0\%}_{-1.2\%}$ | $32.38^{+2.4\%}_{-7.4\%}{}^{+0.9\%}_{-1.1\%}$ | $17.16^{+14.9\%}_{-13.7\%}{}^{+0.7\%}_{-0.6\%}$ |
| LO | $27.02^{+39.3\%}_{-26.4\%}{}^{+1.1\%}_{-1.6\%}$ | $39.81^{+39.8\%}_{-26.7\%}{}^{+1.1\%}_{-1.6\%}$ | $15.67^{+37.7\%}_{-25.5\%}{}^{+0.5\%}_{-1.1\%}$ |
| $K$-factor | 0.72 | 0.81 | 1.10 |

Table 3.8: Cross sections with $p_T(j) > 100$ GeV. The renormalisation and factorisation scales are set to $\mu_g$ of $t\bar{t}V$. The (N)LO cross sections are calculated with (N)LO PDFs, the relative statistical integration error is equal or smaller than one permil.

positive non-negligible flat correction to the $t\bar{t}W^{\pm}$@NLO (red solid). This is due to the fact that at 100 TeV, the $gg$ luminosity is larger than at 13 TeV. Finally, we provide in table 3.8 the total cross sections at LO and NLO accuracy for $t\bar{t}W^{\pm}j$, as well as $t\bar{t}Zj$ and $t\bar{t}Hj$ production, with a cut $p_T(j) > 100$ GeV (for these results the LO cross sections are calculated with LO PDFs and the corresponding $\alpha_s$). We close this 100 TeV study, by calculating the asymmetry of equation 3.3 for all the $t\bar{t}V$ processes, which we show in table 3.9. All the asymmetries are reduced in comparison to the 13 TeV ones, due to the large symmetric $gg$ luminosity. The NLO QCD corrections decrease the asymmetry by $\sim$ 40% in $t\bar{t}\gamma$ production. Only in the $t\bar{t}W^{\pm}$ process the asymmetry remains to be of the order of $\sim$ 1%, due to the absence of the $gg$ channel even at NLO.

| 100 TeV $A_c$ [%] | $t\bar{t}W^{\pm}$ | $t\bar{t}\gamma$ |
|---|---|---|
| LO | - | $(-0.70 \pm 0.05)^{+0.04}_{-0.04}{}^{+0.03}_{-0.02}$ |
| NLO | $(1.3 \pm 0.1)^{+0.23}_{-0.16}{}^{+0.05}_{-0.03}$ | $(-0.45 \pm 0.04)^{+0.05}_{-0.04}{}^{+0.01}_{-0.02}$ |
| 100 TeV $A_c$ [%] | $t\bar{t}H$ | $t\bar{t}Z$ |
| LO | - | $(0.03 \pm 0.05)^{+0.001}_{-0.004}{}^{+0.003}_{-0.01}$ |
| NLO | $(0.17 \pm 0.01)^{+0.06}_{-0.04}{}^{+0.01}_{-0.01}$ | $(0.22 \pm 0.04)^{+0.06}_{-0.04}{}^{+0.01}_{-0.01}$ |

Table 3.9: NLO and LO central asymmetries for $t\bar{t}V$-type processes and $t\bar{t}H$ production at 100 TeV for $\mu = \mu_g$. The first uncertainty is due to the limited integration statistics. The second and third uncertainties reflect the scale variation within $\mu_g/2 < \mu_f, \mu_r < 2\mu_g$, and the PDFs.

# 3.3 Analyses of $t\bar{t}H$ signatures

In this section we provide numerical results for the contributions of signal and irreducible background processes to two different classes of $t\bar{t}H$ signatures at the LHC. In section 3.3.1 we consider a signature involving two isolated photons emerging from the decay of the Higgs boson into photons, $H \to \gamma\gamma$. In section 3.3.2 we analyse three different signatures involving two or more leptons, where $t\bar{t}H$ production can contribute via the $H \to ZZ^*$, $H \to WW^*$ and $H \to \tau^+\tau^-$ decays. We perform both the analyses at 13 TeV and we adopt the cuts of [145].[30] The preselection cuts, which are common for both the analyses, are:

$$\begin{aligned} &p_T(e) > 7\,\text{GeV}\,, \qquad |\eta(e) < 2.5|\,, \qquad p_T(\mu) > 5\,\text{GeV}\,, \quad |\eta(\mu)| < 2.4\,, \\ &|\eta(\gamma)| < 2.5\,, \qquad p_T(j) > 25\,\text{GeV}\,, \qquad |\eta(j)| < 2.4\,, \end{aligned} \tag{3.7}$$

where jets are clustered via anti-$k_T$ algorithm [161] with the distance parameter $R = 0.5$. Event by event, only particles satisfying the preselection cuts in eq.3.7 are considered and, for each jet $j$ and lepton $\ell$, if $\Delta R(j,\ell) < 0.5$ the lepton $\ell$ is clustered into the jet $j$. With the symbol $\ell$, unless otherwise specified, we always refer to electrons(positrons) and (anti)muons, not to $\tau$ (anti)leptons.

All the simulations for the signal and the background processes have been performed at NLO QCD accuracy matched with parton shower effects (NLO + PS). Events are generated via MadGraph5_aMC@NLO, parton shower and hadronization effects are realised in Pythia8 [45], and jets are clustered via FastJet [162].[31] Unless differently specified, decays of the heavy states, including $\tau$ leptons, are performed in Pythia8. In the showering, only QCD effects have been included; QED and purely weak effects are not included. Furthermore, multi-parton interaction and underlying event effects are not taken into account.

In order to discuss NLO effects at the analysis level, in the following we will also report results for events generated at LO accuracy including shower and hadronization effects (LO + PS). As done for the fixed-order studies in section 3.1, LO + PS and NLO + PS central values are evaluated at $\mu_f = \mu_r = \mu_g$ and scale uncertainties are obtained by varying independently the factorisation and the renormalisation scale in the interval $\mu_g/2 < \mu_f, \mu_r < 2\mu_g$.

---

[30] In our simulation we do not take into account particle identification efficiencies and possible misidentification effects.

[31] In our simulation, $b$-tagging is performed by looking directly at $B$ hadrons, which we keep stable.

### 3.3.1 Signature with two photons

The present analysis focuses on the Higgs boson decaying into two photons in $t\bar{t}H$ production, which presents as irreducible background the $t\bar{t}\gamma\gamma$ production. In our simulation, top quark pairs are decayed via MADSPIN for both the signal and the background, whereas the loop-induced $H \to \gamma\gamma$ decay is forced in PYTHIA8 and event weights are rescaled by the branching ratio $\mathrm{BR}(H \to \gamma\gamma) = 2.28 \times 10^{-3}$, which is taken from [163].

| 13 TeV $\sigma$[fb] | $t\bar{t}H \times \mathrm{BR}(H \to \gamma\gamma)$ | $t\bar{t}\gamma\gamma$ |
|---|---|---|
| NLO | $1.191^{+6.0\%\ +2.1\%}_{-9.4\%\ -2.6\%}$ | $1.466^{+8.7\%\ +1.6\%}_{-11.0\%\ -1.8\%}$ |
| LO | $1.087^{+35.5\%\ +2.0\%}_{-24.2\%\ -2.1\%}$ | $1.340^{+37.0\%\ +1.7\%}_{-24.8\%\ -1.8\%}$ |
| $K$ | 1.10 | 1.09 |
| 13 TeV $\sigma$[fb] | $t\bar{t}H(H \to \gamma\gamma)$ | $t\bar{t}\gamma\gamma$ |
| NLO+PS | $0.194^{+5.9\%\ +2.0\%}_{-9.3\%\ -2.6\%} \pm 0.002$ | $0.374^{+11.4\%\ +1.5\%}_{-12.2\%\ -1.7\%} \pm 0.004$ |
| LO+PS | $0.172^{+35.2\%\ +2.0\%}_{-24.1\%\ -2.2\%} \pm 0.001$ | $0.310^{+36.4\%\ +1.7\%}_{-24.5\%\ -1.8\%} \pm 0.002$ |
| $K^{\mathrm{PS}}$ | $1.13 \pm 0.01$ | $1.21 \pm 0.01$ |

Table 3.10: NLO and LO cross sections for $t\bar{t}H(H \to \gamma\gamma), t\bar{t}\gamma\gamma$ processes at 13 TeV. The first uncertainty is given by scale variation, the second by PDFs. The assigned error is the statistical Monte Carlo uncertainty.

In this analysis, at least two jets are required and one of them has to be $b$-tagged. In addition, the following cuts are applied:

$$\begin{gathered} 100\,\mathrm{GeV} < m(\gamma_1\gamma_2) < 180\,\mathrm{GeV}\,, \quad p_T(\gamma_1) > \frac{m(\gamma_1\gamma_2)}{2}\,, \quad p_T(\gamma_2) > 25\,\mathrm{GeV}\,, \\ \Delta R(\gamma_1,\gamma_2),\ \Delta R(\gamma_{1,2},j) > 0.4\,, \quad \Delta R(\gamma_{1,2},\ell) > 0.4\ , \quad p_T(\ell_1) > 20\,\mathrm{GeV}\,, \end{gathered} \tag{3.8}$$

and an additional cut

$$\Delta R(\ell_i,\ell_j) > 0.4 \tag{3.9}$$

is applied if leptons are more than one. With $\gamma_1$ and $\gamma_2$ we respectively denote the hard and the soft photon, analogously $\ell_1$ indicates the hardest lepton. Cuts on lepton(s) imply that the fully and semileptonic decays of the top-quark pair are selected.

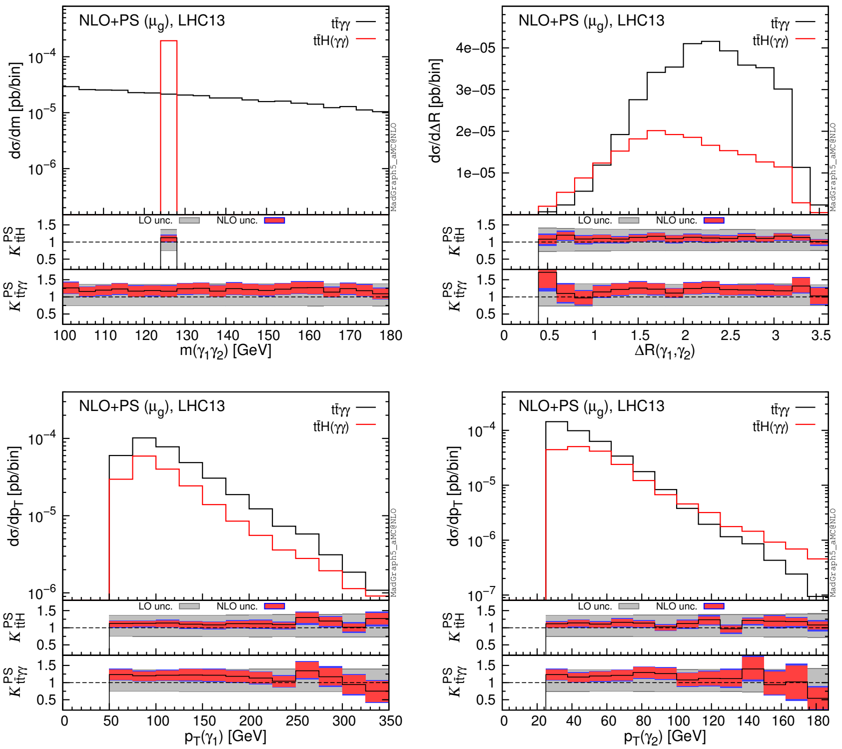

Figure 3.31: Differential distributions for signal and background processes for the diphoton analysis.

Results at LO + PS and NLO + PS accuracy are listed in table 3.10 for the signal and the $t\bar{t}\gamma\gamma$ background. Also, we display fixed order results (LO, NLO) at production level only, without including top decays, shower and hadronization effects. In order to be as close as possible to the analyses level, we apply the cuts in eqs. 3.7 and 3.8 that involve only photons. Thus, the difference between LO and NLO results of $t\bar{t}\gamma\gamma$ in tables 3.5 and 3.10 are solely due to these cuts.

In table 3.10, we show global $K$-factors both at fixed order ($K :=$ NLO/LO) and including decays, shower and hadronization effects, and all the cuts employed in the analysis ($K^{\rm PS} :=$ NLO + PS/LO + PS). Comparing $K^{\rm PS}$ and $K$ it is possible to directly quantify the difference between a complete NLO simulation ($K^{PS}$) and the simulation typically performed at experimental level, i.e., a LO + PS simulation rescaled by a $K$-factor from production only ($K$). As shown in table 3.10, e.g., the second approach would underestimate the prediction for $t\bar{t}\gamma\gamma$ production with respect to a complete NLO + PS simulation. This difference is not of particular relevance at the level of discovery, which mostly relies on an identification of a peak in the $m(\gamma_1\gamma_2)$ (see also fig. 3.31), but could be important in the determination of signal rates and in the extraction of Higgs couplings. Conversely, the difference between $K$ and $K^{\mathrm{PS}}$ is much smaller for the signal.

In fig. 3.31 we show representative differential distributions at NLO + PS accuracy for the signal (red) and background (black) processes. In the two insets we display the differential $K$-factor for the signal ($K^{\mathrm{PS}}_{t\bar{t}H}$) and the background ($K^{\mathrm{PS}}_{t\bar{t}\gamma\gamma}$) using the same layout and conventions adopted in the plots of section 3.1. In particular, we plot the invariant mass of the two photons ($m(\gamma_1\gamma_2)$) their distance ($\Delta R(\gamma_1,\gamma_2)$) and the transverse momentum of the hard ($p_T(\gamma_1)$) and the soft ($p_T(\gamma_2)$) photon. We note that predictions for key discriminating observables, such as the $\Delta R(\gamma_1,\gamma_2)$ and $p_T(\gamma_2)$ are in good theoretical control.

### 3.3.2 Signatures with leptons

This analysis involves three different signatures and signal regions that includes two or more leptons and it is specifically designed for $t\bar{t}H$ production with subsequent $H \to ZZ^*$, $H \to WW^*$ and $H \to \tau^+\tau^-$ decays. In the simulation, all the decays of the massive particles are performed in Pythia8. In the case of the signal processes, the Higgs boson is forced to decay to the specific final state ($H \to ZZ^*$, $H \to WW^*$ or $H \to \tau^+\tau^-$) and event weights are rescaled by the corresponding branching ratios, which are taken from [163]: $\mathrm{BR}(H \to WW^*) = 2.15 \times 10^{-1}$, $\mathrm{BR}(H \to ZZ^*) = 2.64 \times 10^{-2}$, $\mathrm{BR}(H \to \tau^+\tau^-) = 6.32 \times 10^{-2}$. The isolation of leptons from the hadronic activity is performed by directly selecting only prompt leptons in the analyses, i.e., only leptons emerging from $Z$, $W$ or from $\tau$ leptons which emerge from $Z$, $W$ or Higgs bosons.[32]

We consider as irreducible background the contribution from $t\bar{t}W^\pm$, $t\bar{t}Z/\gamma^*$, $t\bar{t}W^+W^-$, $t\bar{t}ZZ$, $t\bar{t}W^\pm Z$ and $t\bar{t}t\bar{t}$ production.[33] Precisely, with the notation $t\bar{t}Z/\gamma^*$ we mean the full process $t\bar{t}\ell^+\ell^-(\ell = e,\mu,\tau)$, where $Z$ and photon propagators, from which the $\ell^+\ell^-$ pair emerges, can both go off-shell and interfere.[34]

---

[32] We observed that applying hadronic isolation cuts as done in [145] we obtain results with at most 10% difference with those presented here by selecting prompt leptons. $K$-factors are independent of the application of hadronic isolation cuts.

[33] In principle also $t\bar{t}W\gamma$ and $t\bar{t}Z\gamma$ production can contribute to the signatures specified in the following. However, they are a small fraction of $t\bar{t}W$ and $t\bar{t}Z$ production and indeed are not taken into account in the analyses of [145].

[34] To this purpose, we excluded Higgs boson propagators in order to avoid a double count of the $t\bar{t}H(H \to \tau^+\tau^-)$ contributions.

All the processes, with the exception of $t\bar{t}Z/\gamma^*$, have also been studied at fixed-order accuracy in section 3.1.

In the analyses the following common cuts are applied in order to select at least two leptons

$$m(\ell_1\ell_2) > 12\,, \qquad \Delta R(\ell_i,\ell_j) > 0.4\,. \tag{3.10}$$

Then, the three signatures and the corresponding signal regions are defined as described in the following:

- **Signal region one (SR1): two same-sign leptons**

Exactly two same-sign leptons with with $p_T(\ell) > 20$ GeV are requested. The event is selected if it includes at least four jets with one or more of them that are $b$-tagged. Furthermore it is required that $p_T(\ell_1)+p_T(\ell_2)+E_T^{\rm miss} > 100\,\text{GeV}$ and, for the dielectron events, $|m(e^\pm e^\pm) - m_Z| > 10$ GeV and $E_T^{\rm miss} > 30$ GeV, in order to suppress background from electron sign misidentification in $Z$ boson decays.

- **Signal region two (SR2): three leptons**

Exactly three leptons with $p_T(\ell_1) > 20$ GeV, $p_T(\ell_2) > 10$ GeV, $p_T(\ell_3 = e(\mu)) > 7(5)$ GeV are requested. The event is selected if it includes at least two jets with one or more of them that are $b$-tagged. For a $Z$ boson background suppression, events with an opposite-sign same-flavour lepton pair are required to have $|m(\ell^+\ell^-) - m_Z| > 10$ GeV. Also, for this kind of events if the number of jets is equal or less than three, the cut $E_T^{\rm miss} > 80$ GeV is applied.

- **Signal region three (SR3): four leptons**

Exactly four leptons with $p_T(\ell_1) > 20$ GeV, $p_T(\ell_2) > 10$ GeV, $p_T(\ell_{3,4} = e(\mu)) > 7(5)$ GeV are requested. The event is selected if it includes at least two jets with one or more of them that are $b$-tagged. Also here, for a $Z$ boson background suppression, events with an opposite-sign same-flavor lepton pair are required to have $|m(\ell^+\ell^-) - m_Z| > 10$ GeV.

For both signal and background processes, results at LO + PS and NLO + PS accuracy as well as $K^{\rm PS}$-factors are listed in table 3.11 for the three signal regions. Also, for each process we display the value of the global $K$-factor (listed also in section 3.1), which does not take into account shower effects, cuts and decays. A posteriori, we observe that in these analyses the $K$-factors are almost insensitive of shower effects and the applied cuts. This is evident from a comparison of the values of $K$ and $K^{\rm PS}$ in table 3.11, where the largest discrepancy stems from the $t\bar{t}Z/\gamma^*$ process in SR1. We also verified, with the help of MADSPIN, that results in the SR3 (SR2 for $t\bar{t}W^\pm$) do not change when spin

| 13 TeV $\sigma$[fb] | | SR1 | SR2 | SR3 |
|---|---|---|---|---|
| | NLO+PS | $1.54(2)^{+5.1\%}_{-9.0\%}$ | $1.47(2)^{+5.2\%}_{-9.0\%}$ | $0.095(2)^{+7.4\%}_{-9.7\%}$ |
| $t\bar{t}H(H \to WW^*)$ | LO+PS | $1.401(8)^{+35.6\%}_{-24.4\%}$ | $1.355(8)^{+35.2\%}_{-24.1\%}$ | $0.0855(7)^{+34.9\%}_{-24.0\%}$ |
| $K = 1.10$ | $K^{\mathrm{PS}}$ | $1.10 \pm 0.02$ | $1.09 \pm 0.02$ | $1.11 \pm 0.02$ |
| | NLO+PS | $0.0437(4)^{+5.5\%}_{-9.2\%}$ | $0.119(2)^{+6.3\%}_{-9.6\%}$ | $0.0170(3)^{+5.0\%}_{-8.5\%}$ |
| $t\bar{t}H(H \to ZZ^*)$ | LO+PS | $0.0404(2)^{+36.1\%}_{-24.6\%}$ | $0.1092(8)^{+35.3\%}_{-24.2\%}$ | $0.0152(1)^{+34.7\%}_{-23.9\%}$ |
| $K = 1.10$ | $K^{\mathrm{PS}}$ | $1.08 \pm 0.01$ | $1.09 \pm 0.02$ | $1.12 \pm 0.02$ |
| | NLO+PS | $0.563(7)^{+4.6\%}_{-8.8\%}$ | $0.669(8)^{+6.0\%}_{-9.4\%}$ | $0.0494(7)^{+7.1\%}_{-9.9\%}$ |
| $t\bar{t}H(H \to \tau^+\tau^-)$ | LO+PS | $0.513(3)^{+35.9\%}_{-24.5\%}$ | $0.611(3)^{+35.4\%}_{-24.2\%}$ | $0.0438(3)^{+35.1\%}_{-24.1\%}$ |
| $K = 1.10$ | $K^{\mathrm{PS}}$ | $1.10 \pm 0.02$ | $1.10 \pm 0.01$ | $1.13 \pm 0.02$ |
| | NLO+PS | $5.77(7)^{+15.1\%}_{-12.7\%}$ | $2.44(1)^{+13.1\%}_{-11.6\%}$ | - |
| $t\bar{t}W^{\pm}$ | LO+PS | $4.57(3)^{+27.7\%}_{-20.2\%}$ | $1.989(7)^{+27.5\%}_{-20.0\%}$ | - |
| $K = 1.22$ | $K^{\mathrm{PS}}$ | $1.26 \pm 0.02$ | $1.23 \pm 0.01$ | - |
| | NLO+PS | $1.61(2)^{+7.7\%}_{-10.5\%}$ | $2.70(3)^{+9.0\%}_{-11.2\%}$ | $0.280(3)^{+9.8\%}_{-11.0\%}$ |
| $t\bar{t}Z/\gamma^*$ | LO+PS | $1.422(8)^{+36.8\%}_{-24.9\%}$ | $2.21(1)^{+36.4\%}_{-24.7\%}$ | $0.221(1)^{+35.8\%}_{-24.4\%}$ |
| $K = 1.23$ | $K^{\mathrm{PS}}$ | $1.13 \pm 0.02$ | $1.23 \pm 0.01$ | $1.27 \pm 0.01$ |
| | NLO+PS | $0.288(3)^{+8.0\%}_{-11.1\%}$ | $0.201(3)^{+7.4\%}_{-10.7\%}$ | $0.0116(2)^{+6.9\%}_{-10.2\%}$ |
| $t\bar{t}W^+W^-$ | LO+PS | $0.260(1)^{+38.4\%}_{-25.5\%}$ | $0.181(1)^{+38.0\%}_{-25.3\%}$ | $0.01073(8)^{+37.7\%}_{-25.1\%}$ |
| $K = 1.10$ | $K^{\mathrm{PS}}$ | $1.11 \pm 0.01$ | $1.11 \pm 0.01$ | $1.08 \pm 0.02$ |
| | NLO+PS | $0.340(4)^{+27.5\%}_{-25.8\%}$ | $0.211(3)^{+27.4\%}_{-25.6\%}$ | $0.0110(2)^{+27.0\%}_{-25.5\%}$ |
| $t\bar{t}t\bar{t}$ | LO+PS | $0.271(1)^{+80.9\%}_{-41.5\%}$ | $0.166(1)^{+80.3\%}_{-41.4\%}$ | $0.00871(7)^{+79.8\%}_{-41.2\%}$ |
| $K = 1.22$ | $K^{\mathrm{PS}}$ | $1.26 \pm 0.02$ | $1.27 \pm 0.02$ | $1.26 \pm 0.03$ |
| 13 TeV $\sigma$[ab] | | SR1 | SR2 | SR3 |
| | NLO+PS | $9.60(6)^{+3.5\%}_{-8.4\%}$ | $5.02(4)^{+3.7\%}_{-8.3\%}$ | $0.249(9)^{+7.2\%}_{-9.6\%}$ |
| $t\bar{t}ZZ$ | LO+PS | $9.71(2)^{+36.3\%}_{-24.5\%}$ | $5.08(2)^{+35.9\%}_{-24.3\%}$ | $0.250(4)^{+35.5\%}_{-24.2\%}$ |
| $K = 0.99$ | $K^{\mathrm{PS}}$ | $0.99 \pm 0.01$ | $0.99 \pm 0.01$ | $1.00 \pm 0.04$ |
| | NLO+PS | $62.0(7)^{+9.0\%}_{-10.2\%}$ | $27.9(5)^{+9.2\%}_{-10.3\%}$ | $0.91(2)^{+7.2\%}_{-9.2\%}$ |
| $t\bar{t}W^{\pm}Z$ | LO+PS | $60.2(3)^{+32.2\%}_{-22.6\%}$ | $26.4(2)^{+32.0\%}_{-22.5\%}$ | $0.893(9)^{+31.9\%}_{-22.4\%}$ |
| $K = 1.06$ | $K^{\mathrm{PS}}$ | $1.03 \pm 0.01$ | $1.06 \pm 0.02$ | $1.02 \pm 0.02$ |

Table 3.11: NLO and LO cross sections for signal and background processes for $t\bar{t}H$ to multileptons at 13 TeV. The assigned error is the statistical Monte Carlo uncertainty. The uncertainty is given by scale variation. The PDF uncertainties in all processes are of the order of $\sim 2\%$ except the $t\bar{t}t\bar{t}$ production, where they are at $\sim 5\%$.

correlation effects are taken into account in the decays.[35]. It is important to note that, a priori, with different cuts and/or at different energies, $K$ and $K^{\mathrm{PS}}$ could be in principle different and spin correlation effects may be not negligible. Thus, a genuine NLO+PS simulation is always preferable.

## 3.4 Summary

In this chapter we have presented a thorough study at NLO QCD accuracy for $t\bar{t}V$ and $t\bar{t}VV$ processes as well as for $t\bar{t}H$ and $t\bar{t}t\bar{t}$ production within the same computational framework and using the same input parameters. In the case of $t\bar{t}VV$ processes, with the exception of $t\bar{t}\gamma\gamma$ production, NLO cross sections have been studied for the first time here. Moreover, we have performed a complete analysis with realistic selection cuts on final states at NLO QCD accuracy including the matching to parton shower and decays, for both signal and background processes relevant for searches at the LHC for the $t\bar{t}H$ production. Specifically, we have considered the cases where the Higgs boson decays either into leptons, where $t\bar{t}V$ and $t\bar{t}VV$ processes and $t\bar{t}t\bar{t}$ production provide backgrounds, or into two photons giving the same signature as $t\bar{t}\gamma\gamma$ production.

We have investigated the behaviour of fixed order NLO QCD corrections for several distributions and we have analysed their dependence on (the definition of) the renormalisation and factorisation scales. We have found that QCD corrections on key distributions cannot be described by overall $K$-factors. However, dynamical scales in general, even though not always, reduce the dependence of the corrections on kinematic variables and thus lead to flatter $K$-factors. In addition, our study shows that while it is not possible to identify a "best scale" choice for all processes and/or differential distributions in $t\bar{t}V$ and $t\bar{t}VV$, such processes present similar features and can be studied together. For all the processes considered, NLO QCD corrections are in general necessary in order to provide precise and reliable predictions at the LHC. In particular cases they are also essential for a realistic phenomenological description. Notable examples discussed in the text are, e.g., the giant corrections in the tails of $p_T(t\bar{t})$ distributions for $t\bar{t}V$ processes and the large decrement of the top-quark central asymmetry for $t\bar{t}\gamma$ production. In the case of future (hadron) colliders also inclusive cross sections receive sizeable corrections, which lead, e.g., to $K$-factors larger than two at 100 TeV for $t\bar{t}V$ and $t\bar{t}VV$ processes with a charged final state. Differences between a 13 and 100 TeV collider are pointed

---

[35] SR2 and especially SR1 involves a rich combinatoric of leptonic and hadronic $Z$, $W$ and $\tau$ decays, which render the simulation with spin-correlation non-trivial. However, we checked also here for representative cases that spin-correlation effects do not sensitively alter the results.

out at the total cross section scale dependence and at differential level, for the $t\bar{t}V$ processes.

In the searches at the LHC for the $t\bar{t}H$ production with the Higgs boson decaying either into leptons or photons, NLO QCD corrections are important for precise predictions of the signal and the background. We have explicitly studied the sensitivity of NLO+PS QCD corrections on experimental cuts by comparing genuine NLO+PS QCD predictions with LO+PS predictions rescaled by global $K$-factors from the fixed order calculations without cuts. *A posteriori*, we have verified that these two approximations give compatible results for analyses at the 13 TeV Run-II of the LHC with the cuts specified in the text. *A priori*, this feature is not guaranteed for analyses with different cuts and/or at different energies. In general, a complete NLO+PS prediction for both signal and background processes is more reliable an thus preferable for any kind of simulation.

Having established the necessity of the NLO accuracy for these processes, we proceed to the next chapter on an EFT analysis, focusing on the $t\bar{t}\gamma$ and $t\bar{t}Z$ processes. Since the EFT is a framework for non resonant BSM searches, it focuses on deviations in the shapes of differential distributions rather than resonant peaks. For this reason NLO accuracy is necessary also there, in order to compare in detail the obtained distributions with respect to the SM ones. The improvement of the EFT approach due to NLO corrections will be shown explicitly in the following chapter.

# 4 | Probing the neutral top-quark couplings in the EFT

The $t\bar{t}V$ processes, which are studied in detail in the previous chapter, are particularly interesting, as they provide the first probe of the neutral couplings of the top quark to the electroweak gauge bosons, which were not accessible at the Tevatron due to their high production thresholds. Therefore these channels could give important information about the top quark, which are complementary to top-pair and single-top production measurements as well as the top decay measurements. Measurements of $t\bar{t}\gamma$ have been performed at the Tevatron by CDF [164], and at the LHC by CMS [165] and by ATLAS [166]. Results for $t\bar{t}Z$ and $t\bar{t}W$ by CMS appear in [167,168] and by ATLAS in [169].

With Run-II of the LHC, more and more precise measurements in the top-quark sector can be expected. In this respect, theoretical predictions matching the foreseeable precision of the experimental determinations are required to extract correct and useful information about deviations in the top-quark sector. For this reason, recently fully differential NLO QCD corrections to top-quark processes within the top quark EFT have started to become available, for example for the top-decay processes including the main decay channel and the flavor-changing channels [170,171], and for single-top production triggered by flavor-changing neutral interactions of the top [172]. More recently, the two main production channels in the SM, top-quark pair production and single top production, have also become available at dimension-six at NLO in QCD [173,174]. QCD corrections are found to have nontrivial impact on SMEFT analyses [174].

In this chapter, we pursue this line of research further. We provide NLO QCD predictions for the $t\bar{t}Z$ and $t\bar{t}\gamma$ channels at the LHC and $t\bar{t}$ production at the ILC, including the full set of dimension-six operators that parametrise the interactions between the top-quark and the SM gauge bosons. Note that results for $pp \to t\bar{t}\gamma$ at NLO appear here for the first time, while $pp \to t\bar{t}Z$ and $e^+e^- \to t\bar{t}$ have been calculated at NLO in QCD in Refs. [175,176] in the anomalous coupling approach, albeit with the omission of the chromomagnetic dipole operator. As we will see, this operator gives a very important contribution to both the $t\bar{t}Z$ and $t\bar{t}\gamma$ processes. In addition, we also present results for the top-loop induced $HZ$ production, which involves the same operators. An important feature of our approach is that NLO predictions matched to the parton shower (PS) are provided in an automatic way. Our results are important not only because predictions are improved in accuracy and in precision, but also because NLO results can be used directly in an experimental simulation, allowing for a more dedicated investigation of all the features of any potential deviations, with possibly optimised selections and improved sensitivities to probe EFT signals.

This chapter is organised as follows. In section 4.1, we present the relevant dimension-six operators. In section 4.2, we present our calculation setup. Results for the $t\bar{t}Z$, $t\bar{t}\gamma$, $gg \to HZ$ processes at the LHC and $t\bar{t}$ production at the ILC are given in sections 4.3-4.5, followed by a discussion about theoretical uncertainties in section 4.6. In section 4.7, we discuss the sensitivity of the various processes on the operators in light of the corresponding LHC measurements. We draw our conclusions and discuss the outlook in section 4.8.

The results of this chapter have been published and are available at [8]. They are obtained in collaboration with O. Bessidskaia Bylund, F. Maltoni, E. Vryonidou and C. Zhang.

## 4.1 Effective operators

In an EFT approach, SM deviations are described by higher-dimensional operators. Up to dimension-six, we consider the following operators [66, 177]:

$$O_{\varphi Q}^{(3)} = i\frac{1}{2}y_t^2 \left(\varphi^\dagger \overleftrightarrow{D}^I_\mu \varphi\right)(\bar{Q}\gamma^\mu \tau^I Q) \tag{4.1}$$

$$O_{\varphi Q}^{(1)} = i\frac{1}{2}y_t^2 \left(\varphi^\dagger \overleftrightarrow{D}_\mu \varphi\right)(\bar{Q}\gamma^\mu Q) \tag{4.2}$$

$$O_{\varphi t} = i\frac{1}{2}y_t^2 \left(\varphi^\dagger \overleftrightarrow{D}_\mu \varphi\right)(\bar{t}\gamma^\mu t) \tag{4.3}$$

$$O_{tW} = y_t g_w (\bar{Q}\sigma^{\mu\nu}\tau^I t)\tilde{\varphi} W^I_{\mu\nu} \tag{4.4}$$

$$O_{tB} = y_t g_Y (\bar{Q}\sigma^{\mu\nu} t)\tilde{\varphi} B_{\mu\nu} \tag{4.5}$$

$$O_{tG} = y_t g_s (\bar{Q}\sigma^{\mu\nu} T^A t)\tilde{\varphi} G^A_{\mu\nu}\,, \tag{4.6}$$

where $Q$ is the third generation left-handed quark doublet, $\varphi$ is the Higgs field, $g_W$, $g_Y$ and $g_s$ are the SM gauge coupling constants, $y_t$ is the top-Yukawa coupling, defined by $y_t = \sqrt{2}m_t/v$ where $v$ is the Higgs vacuum expectation value and $m_t$ is the pole mass (and so $y_t$ does not run). At lowest order in perturbation expansion, the Lagrangian is modified by these operators as follows:

$$\Delta\mathcal{L} = \sum_i \frac{C_i}{\Lambda^2} O_i + h.c. \tag{4.7}$$

Note that the Hermitian conjugate of each operator is added.

The above operators form a complete set that parameterises the top-quark couplings to the gluon and the electroweak gauge bosons of the SM, which could contribute at $\mathcal{O}(\Lambda^{-2})$. In this chapter, we focus on their contributions to top

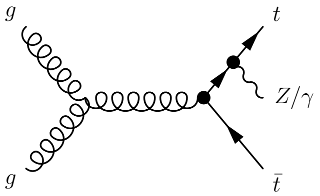

Figure 4.1: Example Feyman diagram for $t\bar{t}Z$ and $t\bar{t}\gamma$ production. The operators we consider can enter the $gt\bar{t}$ vertex ($O_{tG}$), the $t\bar{t}\gamma$ vertex ($O_{tW}, O_{tB}$) or the $t\bar{t}Z$ vertex ($O_{\phi t}, O^{(3)}_{\phi Q}, O^{(1)}_{\phi Q}, O_{tW}, O_{tB}$).

production processes at colliders calculated at NLO in QCD. The first three operators are tree-level generated current-current operators. They modify the vector and axial-vector coupling of the top quark to the electroweak gauge bosons. The other three are dipole operators, that are more likely to be loop induced. $O_{tW}$ and $O_{tB}$ give rise to electroweak dipole moments, and $O_{tG}$ is the chromomagnetic dipole operator, relevant for the interaction of the top quark with gluons. Up to order $\Lambda^{-2}$, the cross sections and differential observables considered in this chapter do not receive CP-odd contributions, so in the following we assume the coefficients of $O_{tW,tB,tG}$ to be real. The three current operators are Hermitian so their coefficients are always real. The operators enter the vertices are marked out on the example Feynman diagram for the $t\bar{t}Z$, $t\bar{t}\gamma$ processes in Fig. 4.1.

A complete study of the processes considered here involve more operators at dimension-six. For example, four-fermion operators featuring top-quark pairs will also contribute to these processes. They are the same set of seven operators that contribute to top pair production as discussed in [178,179]. Additional four-fermion operators could enter and modify the $t\bar{t}Z$ vertex through loops. In this chapter, we will not consider this kind of operators, postponing this to future studies. Operators involving the gauge bosons and light quarks could in principle contribute to these processes, but as they receive stringent constraints from precision observables, we consider their effect to these processes to be negligible compared to the top operators. Another operator that contributes to the $t\bar{t}Z/t\bar{t}\gamma$ processes is $O_G$, which would enter by modifying the gluon self-interactions. As this is not a top-quark operator, we will not consider it further here, assuming also that its contribution is sufficiently suppressed due to constraints from the accurately measured $t\bar{t}$ and dijet cross sections.

In our approach, we also take into account an additional operator, $O_{\varphi b}$ (identical to $O_{\varphi t}$ with $b$ replacing $t$), which does not involve a top quark, but does contribute to, for example, NLO $t\bar{t}Z$ production through a bottom loop or $b-$quarks in the initial state as well as $HZ$ production in gluon fusion through the bottom loops. We include it in this study mainly as an option to cancel the $ggZ$ chiral anomaly induced by modifications to the $ttZ$ interaction.

Various constraints can be placed on the Wilson coefficients of the top quark operators of Eqs. (4.1-4.6) both from direct measurements and from electroweak precision measurements. For $\Lambda = 1$ TeV, at 95% confidence level, $C_{tG}$ is constrained from top pair production to be within the range [-0.77,0.4] in Ref. [180], and in Ref. [173] [-0.56,0.41] at leading order (LO) and [-0.42,0.30] at NLO. $C_{tW}$ is constrained from $W$ helicity fractions in top-decay measurements and single top production, to be in the interval [-0.15,1.9] [181]. The $Z \to b\bar{b}$ decay constrains the sum of $C^{(3)}_{\phi Q} + C^{(1)}_{\phi Q}$ to be [-0.026, 0.059] [182]. The other three operator coefficients, $C^{(3)}_{\phi Q} - C^{(1)}_{\phi Q}$, $C_{\phi t}$ and $C_{tB}$ receive indirect constraints from precision electroweak data, which lead to the following limits [182, 183]:

$$\begin{aligned}
&C^{(3)}_{\phi Q} - C^{(1)}_{\phi Q}: \ [-3.4, 7.5] \\
&C_{\phi t}: \ [-2.5, 7] \\
&C_{tB}: \ [-16, 43] \,.
\end{aligned}$$

Note that indirect bounds should be interpreted carefully. The presented bounds here are marginalised over the $S$ and $T$ parameters, with all other operator coefficients assumed to vanish. We note here that comparable limits have been set on these operators by the recent collider based global analyses of [184, 185]. Furthermore, RG-induced limits can be found in [186].

Finally, let us stress that even though we work in the context of the SMEFT, the NLO calculations presented in this chapter can be directly used in analyses employing an anomalous couplings parametrisation, under the condition that $C_{tG} = 0$ is assumed at all scales. In this case, operators do not mix under RG flow, and they only contribute via anomalous couplings in $ttV$, $bbV$ and $tbW$ vertices, and our NLO results can be translated into the anomalous coupling approach. The relations between the anomalous couplings and the effective operator coefficients are given in appendix A.

## 4.2 Calculation setup

Like in the previous chapters, our computation is performed within the MG5_aMC framework [32], where all the elements entering the NLO computations are available automatically starting from the SMEFT Lagrangian [33, 35, 37, 38, 187, 188].

Special care needs to be taken for the UV and R2 counterterms, which are required for the virtual corrections. The R2 terms are obtained automatically through the NLOCT package [187], and have been checked against analytical calculations. The UV counterterms depend on the renormalisation scheme. For the SM part, we use $\overline{MS}$ with five-flavor running of $\alpha_s$ with the top-quark subtracted at zero momentum transfer. The bottom quark mass is neglected throughout. Masses and wave-functions are renormalised on shell. The operator $O_{tG}$ gives additional contributions to the top-quark and gluon fields, as well as $\alpha_s$ renormalisation [173]. The operator coefficients are subtracted with the $\overline{MS}$ scheme. They are renormalised by

$$C_i^0 \to Z_{ij} C_j = \left( \mathbb{1} + \frac{1}{2} \Gamma(1+\varepsilon)(4\pi)^\varepsilon \frac{1}{\varepsilon_{UV}} \gamma \right)_{ij} C_j \,, \tag{4.8}$$

where the anomalous dimension matrix $\gamma$ has non-zero components for the dipole operators $O_{tG}$, $O_{tW}$, and $O_{tB}$. The anomalous dimensions for these three operators are [171, 189–191]

$$\gamma = \frac{2\alpha_s}{\pi} \begin{pmatrix} \frac{1}{6} & 0 & 0 \\ \frac{1}{3} & \frac{1}{3} & 0 \\ \frac{5}{9} & 0 & \frac{1}{3} \end{pmatrix} . \tag{4.9}$$

The other operators do not have an anomalous dimension at order $\mathcal{O}(\alpha_s)$ due to current conservation. Results in this chapter are presented in terms of operators defined at the renormalisation scale, which we take as $m_t$ for $pp \to t\bar{t}V$ and $e^+e^- \to t\bar{t}$, and $m_H$ for $pp \to HZ$. If the operator coefficients are known at the new physics scale $\Lambda$, the above anomalous dimension matrix can be used to evolve them down to the renormalisation scale, to resum the large $\log \Lambda/m_t$ terms. Hence results presented in this chapter are free of such large log terms.

Operators that modify the $ttZ$ axial coupling may induce a chiral anomaly in the $ggZ$ three point function, which has an effect in $t\bar{t}Z$ and $gg \to HZ$ production. The cancellation of the anomaly depends on the details of the underlying model. To cancel this anomaly within the EFT framework, one option is to include the operator $O_{\phi b}$, which modifies the $bbZ$ coupling, and require

$$C_{\phi b} = 2C_{\phi Q}^{(1)} - C_{\phi t} \tag{4.10}$$

so that the change in $ttZ$ and $bbZ$ vertices cancel each other in the $ggZ$ function. In this chapter, we keep this anomaly in the calculation, and take the point of view of [192], i.e. the chiral anomaly in an effective theory is allowed, provided the corresponding gauge boson is massive. We have checked that, in either case, the numerical effect is negligible.

As a cross-check of our implementation we have compared our (LO) results with those presented in Ref. [176], and have found agreement.

## 4.3 Results for $t\bar{t}Z$, $t\bar{t}\gamma$ and $t\bar{t}\mu^+\mu^-$

### 4.3.1 Inclusive results

In this section, we consider the inclusive $t\bar{t}Z$, $t\bar{t}\gamma$ and $t\bar{t}l^+l^-$cross sections including the dimension-six operators. The $t\bar{t}l^+l^-$ cross section includes the contribution of off-shell photons and the interference of $t\bar{t}Z$ and $t\bar{t}\gamma^*$. In fact, this is the process that is experimentally accessible at the LHC, though the difference between $t\bar{t}l^+l^-$ and $t\bar{t}Z$ with leptonic $Z$ decay is small for a lepton pair invariant mass close to the $Z$ boson mass.

We work up to $\mathcal{O}(\Lambda^{-2})$, generating Feynman diagrams with at most one effective vertex. The cross section can then be expressed in the form:

$$\sigma = \sigma_{SM} + \sum_i \frac{C_i}{(\Lambda/1\mathrm{TeV})^2}\sigma_i^{(1)} + \sum_{i\leq j} \frac{C_i C_j}{(\Lambda/1\mathrm{TeV})^4}\sigma_{ij}^{(2)} , \tag{4.11}$$

with the sum running over all operators in Eqs. (4.1-4.6). Here $\sigma_i^{(1)}$ is the cross section of the interference of diagrams with one EFT vertex with diagrams from the SM. The cross section $\sigma_{ij}^{(2)}$, corresponds to the interference of two diagrams with one EFT vertex each or the squares of the amplitudes with one effective vertex for $i = j$.

Our implementation allows the extraction of the $\mathcal{O}(\Lambda^{-2})$ contribution $\sigma_i^{(1)}$ as well as the $\mathcal{O}(\Lambda^{-4})$ contribution $\sigma_{ij}^{(2)}$. While the latter is formally higher-order with respect to the $\mathcal{O}(\Lambda^{-2})$ accuracy of our computation in the SMEFT, it is important for several reasons. First, as this term is of higher-order one can decide to include it without changing the accuracy of the prediction of the central value. Arguments in favour of this approach in the SMEFT have been put forward, see e.g. [193, 194]. Finally, the $\mathcal{O}(\Lambda^{-4})$ terms are useful to associate an uncertainty to missing higher-orders in the EFT expansion. For these reasons, we quote results for $\sigma_{ii}^{(2)}$ (i.e. the squared contribution from $O_i$), to either improve the central value predictions or to (partly) assess the size of the theoretical uncertainties associated to the contribution of $\mathcal{O}(\Lambda^{-4})$ and higher terms.

In this context, we point out that the relative size of $\sigma_{ii}^{(2)}$ with respect to $\sigma_i^{(1)}$ cannot be used to infer the breaking down of the EFT expansion which even in the case where $\sigma_{ii}^{(2)} \gg \sigma_i^{(1)}$ could still be valid. One reason is that $\sigma_i^{(1)}$ is an interference term and various cancellations could occur accidentally. We will see this is indeed the case for several operators in $t\bar{t}V$ production. On the other hand, the EFT expansion in $E^2/\Lambda^2$ could still be well-behaved, or at least can be controlled by applying kinematic cuts on the total energy $E$ of the process. In this respect, as we were mentioning above, a legitimate and motivated way to proceed is to always include both interference and squared contributions, and separately estimate the theoretical error due to missing dimension-eight operators. Another interesting possibility is in the presence of "strong interactions", i.e. when $C_i^2\frac{E^4}{\Lambda^4} > C_i\frac{E^2}{\Lambda^2} > 1 > \frac{E^2}{\Lambda^2}$. In this case, the squared contribution dominates over the interference one, without invalidating the $E^2/\Lambda^2$ expansion, which is parametrically independent of the size of the coefficients. In a phenomenological analysis and in a global fit, all such cases should be always kept in mind and carefully analysed on the basis of the resulting bounds on the $C_i$'s. As the main goal of this chapter is to present a framework to perform calculations in the SMEFT at NLO accuracy and study the results for the neutral top interactions, we do not discuss any further the issue related to the size of the coefficients and the validity conditions of the EFT itself. On the other hand, we stress that our implementation/framework can provide the elements necessary to make a detailed study. For example, we present the full results at $\mathcal{O}(\Lambda^{-2})$, characterised by $\sigma_i^{(1)}$, together with $\sigma_{ii}^{(2)}$ as an estimation of uncertainties due to neglecting all $\sigma_{ij}^{(2)}$ terms. Note that if necessary, any $\sigma_{ij}^{(2)}$ term can be also computed.

In practice, to extract the values of $\sigma_i^{(1)}$, we set one of the $C_i$ coefficients to ±1 and all the others to zero. Using the two values and the SM cross-section, we can extract $\sigma_i^{(1)}$, as well as $\sigma_{ii}^{(2)}$, the contribution of the $\mathcal{O}(\Lambda^{-2})$ amplitudes squared. In order to improve the statistical significance of the interference for the operators where the interference is small, we find the value of $C_i$ which maximises it compared to the total cross-section and use that value for the runs instead of $C_i = \pm 1$.

The results are obtained using the 5-flavour scheme, with the MSTW2008 [27] parton distribution functions. The input parameters are:

$$m_t = 173.3\text{ GeV}\,, \qquad m_Z = 91.1876\text{ GeV}\,, \tag{4.12}$$

$$\alpha_{EW}^{-1} = 127.9\,, \qquad G_F = 1.16637\times 10^{-5}\text{GeV}^{-2}\,. \tag{4.13}$$

The renormalisation and factorisation scales are fixed to $\mu_R = \mu_F = \mu = m_t$. Scale variations are obtained by independently setting $\mu_R$ and $\mu_F$ to $\mu/2$, $\mu$ and $2\mu$, obtaining nine $(\mu_R, \mu_F)$ combinations. For the $t\bar{t}Z$ process no cuts are applied on the final state particles and no $Z$ or top decays are considered, while for $t\bar{t}\gamma$, $p_T(\gamma) > 20$ GeV is required. We employ the photon isolation criterium of Ref. [152] with a radius of 0.4. Finally, for the $t\bar{t}\mu^+\mu^-$ process a cut of 10 GeV is set on the minimum invariant mass of the lepton pair.

The SM predictions at LO and NLO in QCD [36] for the processes considered here are summarised as a reference in Table 4.1, where uncertainties from scale

---

[36] Note that the SM results for the $t\bar{t}Z$ process have been presented at NLO in the QCD and electroweak coupling expansion in [41].

variation, PDF uncertainties, and the $K$-factors are shown for the LHC at 8 and 13 TeV. The scale uncertainties are significantly reduced at NLO. The PDF uncertainties are small compared to the scale uncertainties even at NLO and therefore we will not consider them any further.

| SM | [fb] | $t\bar{t}Z$ | $t\bar{t}\gamma$ | $t\bar{t}\mu^+\mu^-$ |
|---|---|---|---|---|
| 8TeV | $\sigma_{SM,LO}$ | $207.0^{+41.4\%\ +2.4\%}_{-26.8\%\ -2.5\%}$ | $604.0^{+38.8\%\ +2.1\%}_{-25.6\%\ -2.2\%}$ | $8.779^{+40.9\%\ +2.4\%}_{-26.6\%\ -2.4\%}$ |
| | $\sigma_{SM,NLO}$ | $226.5^{+6.7\%\ +2.8\%}_{-11.2\%\ -3.2\%}$ | $777^{+13.4\%\ +2.1\%}_{-13.7\%\ -2.4\%}$ | $9.827^{+7.7\%\ +2.6\%}_{-11.5\%\ -2.9\%}$ |
| | $K$-factor | 1.09 | 1.29 | 1.12 |
| 13TeV | $\sigma_{SM,LO}$ | $761.8^{+37.8\%\ +2.1\%}_{-25.2\%\ -2.2\%}$ | $1998.0^{+35.5\%\ +1.8\%}_{-24.2\%\ -2.0\%}$ | $31.67^{+37.4\%\ +2.1\%}_{-25.1\%\ -2.2\%}$ |
| | $\sigma_{SM,NLO}$ | $879^{+8.0\%\ +2.0\%}_{-10.9\%\ -2.5\%}$ | $2719^{+14.2\%\ +1.6\%}_{-13.5\%\ -1.9\%}$ | $37.51^{+9.1\%\ +2.0\%}_{-11.3\%\ -2.4\%}$ |
| | $K$-factor | 1.15 | 1.36 | 1.18 |

Table 4.1: SM cross sections (in fb) for $t\bar{t}Z$, $t\bar{t}\gamma$, $t\bar{t}\mu^+\mu^-$ production at the LHC at $\sqrt{s} = 8$ TeV and $\sqrt{s} = 13$ TeV. The first percentage corresponds to scale variations and the second to PDF uncertainties.

Inclusive cross section results for $t\bar{t}Z$ production at the LHC at 8 and 13 TeV for the different operators are shown in Tables 4.2 and 4.3. We include the LO and NLO results for $\sigma_i^{(1)}$ and $\sigma_{ii}^{(2)}$, the corresponding $K$-factors, the ratio of the dimension-six contribution over the SM and the ratio of the squared $\mathcal{O}(\Lambda^{-4})$ contributions over the $\mathcal{O}(\Lambda^{-2})$ one. Statistical uncertainties are not shown unless they are comparable to the scale uncertainties. The scale uncertainties are significantly reduced at NLO similarly to the SM predictions. We note that the ratios over the SM are significantly less sensitive to scale variations compared to the cross-section numbers.

In the tables, we include the $O_{\phi Q}^{(3)}$ operator but not $O_{\phi Q}^{(1)}$. Results for these two operators differ by a sign at $\mathcal{O}(\Lambda^{-2})$ and are identical at $\mathcal{O}(\Lambda^{-4})$.[37] Similarly at $\mathcal{O}(\Lambda^{-4})$ the contributions of $O_{\phi Q}^{(3)}$ and $O_{\phi t}$ are identical. This can be traced back to the way the operators modify the $ttZ$ vertex as shown in Eq. C.1. Similarly we do not include the results for $O_{tB}$, as they can be obtained from those of $O_{tW}$ by multiplying by a factor of $-\tan^2\theta_w$ (and $\tan^4\theta_w$ for the squared contributions).

The largest contribution is given by the chromomagnetic operator both at 8 and 13 TeV, with $\sigma_i^{(1)}$ reaching almost 40% of the SM. We find that while $O_{\phi Q}^{(3)}$ and $O_{\phi t}$ give contributions of 6-10% of the SM for $C_i = 1$, $O_{tW}$ and consequently $O_{tB}$ give extremely small contributions reaching at most the per

---

[37] This is only approximately true at the cross-section level. There is a small contribution from the $bbZ$ vertex which spoils the minus sign relation between the two operators. The $bbZ$ vertex contributes as we are working in the 5-flavour scheme. Nevertheless this contribution is in practice numerically negligible and therefore the two operators give opposite contributions at $\mathcal{O}(\Lambda^{-2})$.

mille level. While the NLO predictions have significantly reduced theoretical uncertainties, we find that the various ratios of cross-sections considered are generally stable with respect to QCD corrections (apart from $O_{tW}$), and also suffer from much smaller scale uncertainties compared to the cross-sections. This fact can be exploited to extract information on the Wilson coefficients. The theoretical errors due to neglecting squared operator contributions $\sigma^{(2)}_{ii}$ are characterised by the last two rows in the table. The results indicate that for coefficients of order one, neglecting squared contributions is safe for all operators except for $O_{tB}$ and $O_{tW}$. When placing limits, this assessment should be done for the interval of where the limits are placed.

| 8TeV | $O_{tG}$ | $O^{(3)}_{\phi Q}$ | $O_{\phi t}$ | $O_{tW}$ |
|---|---|---|---|---|
| $\sigma^{(1)}_{i,LO}$ | $76.1^{+41.9\%}_{-27.1\%}$ | $18.6^{+45.2\%}_{-28.6\%}$ | $12.5^{+44.6\%}_{-28.3\%}$ | $0.077(8)^{+46.6\%}_{-43.2\%}$ |
| $\sigma^{(1)}_{i,NLO}$ | $78.1^{+4.1\%}_{-10.0\%}$ | $20.8^{+5.6\%}_{-11.5\%}$ | $13.5^{+4.9\%}_{-10.7\%}$ | $-0.32(2)^{+39.1\%}_{-67.3\%}$ |
| $K$-factor | 1.03 | 1.12 | 1.08 | -4.2 |
| $\sigma^{(2)}_{ii,LO}$ | $39.9^{+53.6\%}_{-31.8\%}$ | $0.73(2)^{+45.2\%}_{-28.8\%}$ | $0.73(2)^{+46.3\%}_{-28.8\%}$ | $4.14^{+50.1\%}_{-30.7\%}$ |
| $\sigma^{(2)}_{ii,NLO}$ | $39.8^{+4.7\%}_{-9.4\%}$ | $0.8(2)^{+5.4\%}_{-9.1\%}$ | $0.8(2)^{+7.4\%}_{-8.3\%}$ | $4.81^{+6.2\%}_{-12.5\%}$ |
| $\sigma^{(1)}_{i,LO}/\sigma_{SM,LO}$ | $0.368^{+0.4\%}_{-0.4\%}$ | $0.0899^{+2.7\%}_{-2.5\%}$ | $0.0604^{+2.3\%}_{-2.0\%}$ | $0.00037(4)^{+33.6\%}_{-42.5\%}$ |
| $\sigma^{(1)}_{i,NLO}/\sigma_{SM,NLO}$ | $0.345^{+1.3\%}_{-2.8\%}$ | $0.0918^{+0.6\%}_{-1.0\%}$ | $0.0595^{+0.8\%}_{-2.3\%}$ | $-0.0014(1)^{+31.4\%}_{-56.8\%}$ |
| $\sigma^{(2)}_{ii,LO}/\sigma^{(1)}_{i,LO}$ | $0.524^{+8.2\%}_{-6.5\%}$ | $0.039(1)^{+0.3\%}_{-0.5\%}$ | $0.058(2)^{+1.2\%}_{-0.7\%}$ | $54(6)^{+84.7\%}_{-29.1\%}$ |
| $\sigma^{(2)}_{ii,NLO}/\sigma^{(1)}_{i,NLO}$ | $0.509^{+1.4\%}_{-8.4\%}$ | $0.037(8)^{+2.7\%}_{-4.5\%}$ | $0.06(1)^{+3.2\%}_{-5.9\%}$ | $-15(1)^{+36.9\%}_{-43.5\%}$ |

Table 4.2: Cross sections (in fb) for $t\bar{t}Z$ production at the LHC at $\sqrt{s} = 8$ TeV for the different dimension-six operators. Percentages correspond to scale uncertainties. Integration errors are shown in brackets if these are comparable in size to the scale uncertainties.

We note here the extremely small contribution of the $O_{tW}$ operator, which also leads to larger statistical uncertainties as it is currently not possible to compute the interference independently of the other two contributions. In this case, the impact of the EFT amplitude squared is much larger than its interference with the SM. The small size of the interference is a result of various effects. The most important reason is that the dipole interaction, $\sigma^{\mu\nu}q_\nu$, involves the momentum of the $Z$ boson, and leads to a suppression because the $Z$ tends to be soft in $t\bar{t}Z$ production at the LHC. The same is true also for the $t\bar{t}\gamma$ production, as we will see. By crossing $\gamma$ and $g$, we have explicitly checked that in the process $g\gamma \to t\bar{t}g$ this suppression effect becomes an enhancement,

| 13TeV | $O_{tG}$ | $O_{\phi Q}^{(3)}$ | $O_{\phi t}$ | $O_{tW}$ |
|---|---|---|---|---|
| $\sigma_{i,LO}^{(1)}$ | $286.7^{+38.2\%}_{-25.5\%}$ | $78.3^{+40.4\%}_{-26.6\%}$ | $51.6^{+40.1\%}_{-26.4\%}$ | $-0.20(3)^{+88.0\%}_{-230.0\%}$ |
| $\sigma_{i,NLO}^{(1)}$ | $310.5^{+5.4\%}_{-9.7\%}$ | $90.6^{+7.1\%}_{-11.0\%}$ | $57.5^{+5.8\%}_{-10.3\%}$ | $-1.7(2)^{+31.3\%}_{-49.1\%}$ |
| $K$-factor | 1.08 | 1.16 | 1.11 | 8.5 |
| $\sigma_{ii,LO}^{(2)}$ | $258.5^{+49.7\%}_{-30.4\%}$ | $2.8(1)^{+39.7\%}_{-26.9\%}$ | $2.9(1)^{+39.7\%}_{-26.7\%}$ | $20.9^{+44.3\%}_{-28.3\%}$ |
| $\sigma_{ii,NLO}^{(2)}$ | $244.5^{+4.2\%}_{-8.1\%}$ | $3.8(3)^{+13.2\%}_{-14.4\%}$ | $3.9(3)^{+13.8\%}_{-14.6\%}$ | $24.2^{+6.2\%}_{-11.2\%}$ |
| $\sigma_{i,LO}^{(1)}/\sigma_{SM,LO}$ | $0.376^{+0.3\%}_{-0.3\%}$ | $0.103^{+1.9\%}_{-1.8\%}$ | $0.0677^{+1.7\%}_{-1.6\%}$ | $-0.00026(4)^{+89.5\%}_{-167.2\%}$ |
| $\sigma_{i,NLO}^{(1)}/\sigma_{SM,NLO}$ | $0.353^{+1.3\%}_{-2.4\%}$ | $0.103^{+0.7\%}_{-0.8\%}$ | $0.0654^{+1.1\%}_{-2.1\%}$ | $-0.0020(2)^{+22.9\%}_{-38.0\%}$ |
| $\sigma_{ii,LO}^{(2)}/\sigma_{i,LO}^{(1)}$ | $0.902^{+8.4\%}_{-6.7\%}$ | $0.036(1)^{+0.2\%}_{-1.1\%}$ | $0.056(2)^{+0.6\%}_{-0.3\%}$ | $-104(16)^{+60.8\%}_{-815.2\%}$ |
| $\sigma_{ii,NLO}^{(2)}/\sigma_{i,NLO}^{(1)}$ | $0.787^{+3.3\%}_{-12.8\%}$ | $0.042(4)^{+5.6\%}_{-3.9\%}$ | $0.067(6)^{+7.6\%}_{-4.8\%}$ | $-14(1)^{+29.0\%}_{-29.1\%}$ |

Table 4.3: Cross sections (in fb) for $t\bar{t}Z$ production at the LHC at $\sqrt{s} = 13$ TeV for the different dimension-six operators. Percentages correspond to scale uncertainties. Integration errors are shown in brackets if these are comparable in size to the scale uncertainties.

as a large momentum for $\gamma$ is guaranteed in the initial state. Apart from this, an additional suppression occurs due to an accidental cancellation between the contributions of the $gg$ and $q\bar{q}$ channels, as they are similar in size but come with an opposite sign. This cancellation leads to a final result that is an order of magnitude smaller than the individual contributions. Finally, an additional reason could be that the $O_{tW}$ vertex does not produce the $Z$ boson in its longitudinal state, which is expected to dominate if it has large momentum.

Finally, comparing 8 and 13 TeV we notice a small increase in the $K$-factors. The ratios of the $\mathcal{O}(\Lambda^{-2})$ terms over the SM do not change significantly. For $O_{tG}$ we notice a significant increase of the ratio $\mathcal{O}(\Lambda^{-4})$ over $\mathcal{O}(\Lambda^{-2})$ as the $\mathcal{O}(\Lambda^{-4})$ contribution grows rapidly with energy, as will be evident also in the differential distributions.

The corresponding $t\bar{t}\gamma$ results are shown in Table 4.4. In this case, a minimum cut of 20 GeV is set on the transverse momentum of the photon. We note that here only three operators contribute: $O_{tG}$, $O_{tW}$ and $O_{tB}$. For this process, $O_{tW}$ and $O_{tB}$ are indistinguishable and therefore only $O_{tB}$ is included in the Table. The $K$-factors in this process are larger than those of $t\bar{t}Z$, reaching 1.3 for the SM and $O_{tG}$ operator but lower for $O_{tB}$. This is due to the soft and collinear configurations between the photon and the additional jet at NLO, which however cannot happen if the photon is emitted from an $O_{tB}$ vertex.

| | $O_{tG}$ (8TeV) | $O_{tB}$ (8TeV) | $O_{tG}$ (13TeV) | $O_{tB}$ (13TeV) |
|---|---|---|---|---|
| $\sigma^{(1)}_{i,LO}$ | $171.5^{+38.6\%}_{-25.6\%}$ | $5.36^{+41.8\%}_{-27.2\%}$ | $564.6^{+35.4\%}_{-24.1\%}$ | $19.5^{+36.7\%}_{-24.9\%}$ |
| $\sigma^{(1)}_{i,NLO}$ | $218.9^{+13.3\%}_{-13.6\%}$ | $5.85^{+5.9\%}_{-9.9\%}$ | $765^{+14.0\%}_{-13.4\%}$ | $19.6^{+4.3\%}_{-6.9\%}$ |
| $K$-factor | 1.28 | 1.09 | 1.35 | 1.01 |
| $\sigma^{(2)}_{ii,LO}$ | $29.8^{+43.5\%}_{-27.8\%}$ | $1.98^{+47.5\%}_{-29.6\%}$ | $120.6^{+39.8\%}_{-26.2\%}$ | $9.14^{+42.3\%}_{-27.4\%}$ |
| $\sigma^{(2)}_{ii,NLO}$ | $39.2^{+13.1\%}_{-14.4\%}$ | $2.36^{+7.0\%}_{-12.6\%}$ | $160.4^{+12.6\%}_{-13.5\%}$ | $10.7^{+6.7\%}_{-11.2\%}$ |
| $\sigma^{(1)}_{i,LO}/\sigma_{SM,LO}$ | $0.284^{+0.04\%}_{-0.1\%}$ | $0.00888^{+2.3\%}_{-2.2\%}$ | $0.283^{+0.1\%}_{-0.1\%}$ | $0.00973^{+0.9\%}_{-1.0\%}$ |
| $\sigma^{(1)}_{i,NLO}/\sigma_{SM,NLO}$ | $0.282^{+0.13\%}_{-0.2\%}$ | $0.0075(1)^{+4.4\%}_{-8.8\%}$ | $0.281^{+0.1\%}_{-0.1\%}$ | $0.0072(1)^{+7.5\%}_{-11.9\%}$ |
| $\sigma^{(2)}_{ii,LO}/\sigma^{(1)}_{i,LO}$ | $0.174^{+3.5\%}_{-3.0\%}$ | $0.370^{+4.0\%}_{-3.3\%}$ | $0.214^{+3.3\%}_{-2.8\%}$ | $0.470^{+4.1\%}_{-3.4\%}$ |
| $\sigma^{(2)}_{ii,NLO}/\sigma^{(1)}_{i,NLO}$ | $0.179^{+0.5\%}_{-0.9\%}$ | $0.404(7)^{+3.5\%}_{-3.0\%}$ | $0.201^{+1.1\%}_{-1.3\%}$ | $0.55(1)^{+6.1\%}_{-4.6\%}$ |

Table 4.4: Cross sections (in fb) for $t\bar{t}\gamma$ production at the LHC at $\sqrt{s} =$ 8 TeV and $\sqrt{s} = 13$ TeV for the different dimension-six operators. Percentages correspond to scale uncertainties. Integration errors are shown in brackets if these are comparable in size to the scale uncertainties. A $p_T(\gamma) > 20$ GeV cut is imposed.

Similar conclusions to the $t\bar{t}Z$ can be drawn for $t\bar{t}\gamma$ regarding the operator contributions. The chromomagnetic operator contributes the most. Neglecting squared contributions is safe for $C_i \lesssim 1$, at both 8 and 13 TeV, but starts to become questionable (and therefore the corresponding uncertainty is increased) as the coefficients reach the values of $\sim 2-3$, with the relative contribution of $\sigma^{(2)}_{ii}$ increasing from 8 to 13 TeV. The contribution of the $O_{tW}$ and $O_{tB}$ operators are 1% of the SM and significantly smaller than the $O_{tG}$ one. While the $O_{tW}$ and $O_{tG}$ operators lead to the same structure in the $tt\gamma$ and $ttg$ vertices respectively, similar to $ttZ$ production, the effect of $O_{tW}$ on the $gg \to t\bar{t}\gamma$ amplitude at typical LHC energies is suppressed compared with that of $O_{tG}$. By examining the crossed amplitude, $g\gamma \to t\bar{t}g$, illustrated in Fig. 4.2, we see that the two operators give contributions of the same order, as they both enter in the production side of the process and more momentum passes through the EFT vertices. We also note here that the $K$-factors for the operators are not the same as those as for the SM contribution which implies that combining the SM $K$-factor and LO EFT predictions does not provide an accurate prediction for the EFT contribution at NLO in QCD.

We next examine $t\bar{t}l^+l^-$. For an invariant mass of the lepton pair around the $Z$ mass, this process is dominated by $t\bar{t}Z$ with leptonically decaying $Z$, the

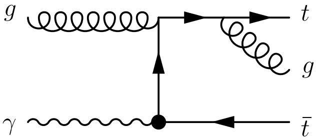

Figure 4.2: An example Feynman diagram for the crossed process $g\gamma \to t\bar{t}g$. The $t\bar{t}\gamma$ vertex, marked with a blob, has generally a higher momentum transfer here than in $t\bar{t}\gamma$ production.

| 8TeV | $O_{tG}$ | $O_{\phi Q}^{(3)}$ | $O_{\phi t}$ | $O_{tB}$ | $O_{tW}$ |
|---|---|---|---|---|---|
| $\sigma_{i,LO}^{(1)}$ | $3.07^{+41.5\%}_{-26.9\%}$ | $0.613^{+45.2\%}_{-28.6\%}$ | $0.413^{+44.6\%}_{-28.3\%}$ | $0.0101^{+43.2\%}_{-27.6\%}$ | $0.0121(6)^{+29.2\%}_{-21.5\%}$ |
| $\sigma_{i,NLO}^{(1)}$ | $3.21^{+5.1\%}_{-10.4\%}$ | $0.683^{+5.4\%}_{-11.3\%}$ | $0.447^{+4.8\%}_{-10.9\%}$ | $0.012(1)^{+8.9\%}_{-12.2\%}$ | $-0.003(2)^{+113.9\%}_{-205.9\%}$ |
| $K$-factor | 1.05 | 1.11 | 1.08 | 1.2 | -0.3 |
| $\sigma_{ii,LO}^{(2)}$ | $1.42^{+52.9\%}_{-31.6\%}$ | $0.0238^{+45.2\%}_{-28.7\%}$ | $0.0234^{+45.8\%}_{-28.7\%}$ | $0.0213^{+49.8\%}_{-30.6\%}$ | $0.147^{+50.1\%}_{-30.7\%}$ |
| $\sigma_{ii,NLO}^{(2)}$ | $1.41^{+4.5\%}_{-9.7\%}$ | $0.0275^{+6.4\%}_{-11.7\%}$ | $0.0259^{+5.0\%}_{-11.4\%}$ | $0.0249^{+6.5\%}_{-12.6\%}$ | $0.171^{+6.3\%}_{-12.5\%}$ |
| $\frac{\sigma_{i,LO}^{(1)}}{\sigma_{SM,LO}}$ | $0.350^{+0.4\%}_{-0.4\%}$ | $0.0698^{+3.1\%}_{-2.8\%}$ | $0.0470^{+2.6\%}_{-2.3\%}$ | $0.00115^{+1.6\%}_{-1.7\%}$ | $0.0014(1)^{+6.9\%}_{-8.4\%}$ |
| $\frac{\sigma_{i,NLO}^{(1)}}{\sigma_{SM,NLO}}$ | $0.327^{+1.2\%}_{-2.4\%}$ | $0.0695^{+1.0\%}_{-2.3\%}$ | $0.0455^{+1.3\%}_{-2.8\%}$ | $0.0012(1)^{+2.0\%}_{-1.5\%}$ | $-0.0004(2)^{+115.7\%}_{-184.1\%}$ |
| $\frac{\sigma_{ii,LO}^{(2)}}{\sigma_{i,LO}^{(1)}}$ | $0.461^{+8.1\%}_{-6.5\%}$ | $0.0388^{+0.0\%}_{-0.1\%}$ | $0.0567^{+0.8\%}_{-0.7\%}$ | $2.11(5)^{+5.2\%}_{-4.1\%}$ | $12.2(6)^{+16.3\%}_{-11.7\%}$ |
| $\frac{\sigma_{ii,NLO}^{(2)}}{\sigma_{i,NLO}^{(1)}}$ | $0.440^{+1.7\%}_{-8.3\%}$ | $0.0403(8)^{+1.0\%}_{-0.7\%}$ | $0.058(2)^{+0.4\%}_{-0.6\%}$ | $2.1(1)^{+2.6\%}_{-2.8\%}$ | $-49(23)^{+730.1\%}_{-332.3\%}$ |

Table 4.5: Cross sections (in fb) for $t\bar{t}\mu^+\mu^-$ production at the LHC at $\sqrt{s} =$ 8 TeV for the different dimension-six operators. An $m(\ell\ell) > 10$ GeV cut is applied to the lepton pair. Percentages correspond to scale uncertainties. Integration errors are shown in brackets if these are comparable in size to the scale uncertainties.

mode that the ATLAS and CMS experiments at the LHC are most sensitive to. Generally it also includes the contribution of $t\bar{t}\gamma^*$. As the EFT operators we study do not enter the vertices connected to leptons, we restrict our attention to $t\bar{t}\mu^+\mu^-$ [38]. We collect the results for $t\bar{t}\mu^+\mu^-$ at LO and NLO at 8 and 13 TeV in Tables 4.5 and 4.6. In this case, the photon and $Z$ amplitudes and their interference is included. For the $t\bar{t}\mu^+\mu^-$ results, the scale and PDF choices are identical to those for the inclusive $t\bar{t}Z/t\bar{t}\gamma$ processes. A lower cut of 10 GeV is

---

[38] We note here that a contribution from 4-fermion operators describing the $t\bar{t}\mu^+\mu^-$ interaction enter in this process in the off-peak regions. As the main contribution comes from the $Z-$peak we postpone the study of these operators to future work.

| 13TeV | $O_{tG}$ | $O^{(3)}_{\phi Q}$ | $O_{\phi t}$ |
|---|---|---|---|
| $\sigma^{(1)}_{i,LO}$ | $11.28^{+37.8\%}_{-25.2\%}$ | $2.584^{+40.4\%}_{-26.6\%}$ | $1.701^{+40.1\%}_{-26.4\%}$ |
| $\sigma^{(1)}_{i,NLO}$ | $12.57^{+6.7\%}_{-10.3\%}$ | $2.976^{+6.7\%}_{-10.8\%}$ | $1.891^{+5.4\%}_{-10.1\%}$ |
| $K$-factor | 1.11 | 1.15 | 1.11 |
| $\sigma^{(2)}_{ii,LO}$ | $8.957^{+49.3\%}_{-30.2\%}$ | $0.101^{+40.4\%}_{-26.6\%}$ | $0.0998^{+40.6\%}_{-26.6\%}$ |
| $\sigma^{(2)}_{ii,NLO}$ | $8.49^{+4.1\%}_{-7.4\%}$ | $0.1168^{+7.1\%}_{-11.0\%}$ | $0.112(3)^{+5.5\%}_{-10.0\%}$ |
| $\sigma^{(1)}_{i,LO}/\sigma_{SM,LO}$ | $0.356^{+0.3\%}_{-0.2\%}$ | $0.0816^{+2.2\%}_{-2.0\%}$ | $0.0537^{+2.0\%}_{-1.8\%}$ |
| $\sigma^{(1)}_{i,NLO}/\sigma_{SM,NLO}$ | $0.335^{+1.2\%}_{-2.2\%}$ | $0.0793^{+1.1\%}_{-2.2\%}$ | $0.0504^{+1.5\%}_{-3.5\%}$ |
| $\sigma^{(2)}_{ii,LO}/\sigma^{(1)}_{i,LO}$ | $0.794^{+8.4\%}_{-6.7\%}$ | $0.0390^{+0.03\%}_{-0.02\%}$ | $0.0586^{+0.5\%}_{-0.4\%}$ |
| $\sigma^{(2)}_{ii,NLO}/\sigma^{(1)}_{i,NLO}$ | $0.676^{+3.6\%}_{-13.3\%}$ | $0.0393^{+0.3\%}_{-0.2\%}$ | $0.059(1)^{+0.2\%}_{-0.2\%}$ |

| 13TeV | $O_{tB}$ | $O_{tW}$ | |
|---|---|---|---|
| $\sigma^{(1)}_{i,LO}$ | $0.034(1)^{+36.9\%}_{-25.1\%}$ | $0.025(3)^{+29.4\%}_{-24.8\%}$ | |
| $\sigma^{(1)}_{i,NLO}$ | $0.046(2)^{+13.0\%}_{-12.7\%}$ | $-0.042(9)^{+44.6\%}_{-73.2\%}$ | |
| $K$-factor | 1.3 | -1.7 | |
| $\sigma^{(2)}_{ii,LO}$ | $0.1073^{+44.3\%}_{-28.3\%}$ | $0.745^{+44.4\%}_{-28.4\%}$ | |
| $\sigma^{(2)}_{ii,NLO}$ | $0.1231^{+6.2\%}_{-11.0\%}$ | $0.851^{+5.9\%}_{-11.0\%}$ | |
| $\sigma^{(1)}_{i,LO}/\sigma_{SM,LO}$ | $0.00108(3)^{+0.3\%}_{-0.5\%}$ | $0.0008(1)^{+12.7\%}_{-16.1\%}$ | |
| $\sigma^{(1)}_{i,NLO}/\sigma_{SM,NLO}$ | $0.0012(1)^{+3.6\%}_{-1.6\%}$ | $-0.0011(2)^{+37.6\%}_{-58.7\%}$ | |
| $\sigma^{(2)}_{ii,LO}/\sigma^{(1)}_{i,LO}$ | $3.15(9)^{+5.5\%}_{-4.6\%}$ | $29(4)^{+25.3\%}_{-15.2\%}$ | |
| $\sigma^{(2)}_{ii,NLO}/\sigma^{(1)}_{i,NLO}$ | $2.7(1)^{+2.1\%}_{-6.8\%}$ | $-20(5)^{+39.2\%}_{-60.7\%}$ | |

Table 4.6: Cross sections (in fb) for $t\bar{t}\mu^+\mu^-$ production at the LHC at $\sqrt{s} =$ 13 TeV for the different dimension-six operators. An $m(\ell\ell) > 10$ GeV cut is applied to the lepton pair. Percentages correspond to scale uncertainties. Integration errors are shown in brackets if these are comparable in size to the scale uncertainties.

imposed on the invariant mass of the lepton pair. No other cuts are imposed on the leptons. All six operators contribute to this process. Results for $O^{(1)}_{\phi Q}$ differ from those of $O^{(3)}_{\phi Q}$ by a sign at $\mathcal{O}(\Lambda^{-2})$ and are identical at $\mathcal{O}(\Lambda^{-4})$, therefore we show only one of the two. The cross-section is dominated by the region close to the $Z-$mass peak and therefore the $K$-factors and relative contributions of the operators are similar to those of the $t\bar{t}Z$ process. The chromomagnetic operator contributes at the 35% level, while the other three current operators give a contribution at the 4-7% level.

The contributions of $O_{tW}$ and $O_{tB}$ at $\mathcal{O}(\Lambda^{-2})$ are at the per mille level and subdominant compared to the $\mathcal{O}(\Lambda^{-4})$ contributions. Effectively this means that with our method of extracting the interference contribution we are always very limited statistically. Even maximising the interference contribution by choosing the appropriate value of the coefficient is not enough to give us good statistics, in particular at NLO which is evident in the quoted statistical and scale uncertainties.

## 4.3.2 Differential distributions

Differential distributions are obtained at NLO for the $pp \to t\bar{t}Z$, $pp \to t\bar{t}\gamma$ and $pp \to t\bar{t}\mu^+\mu^-$ processes. This can be done also at NLO with matching to

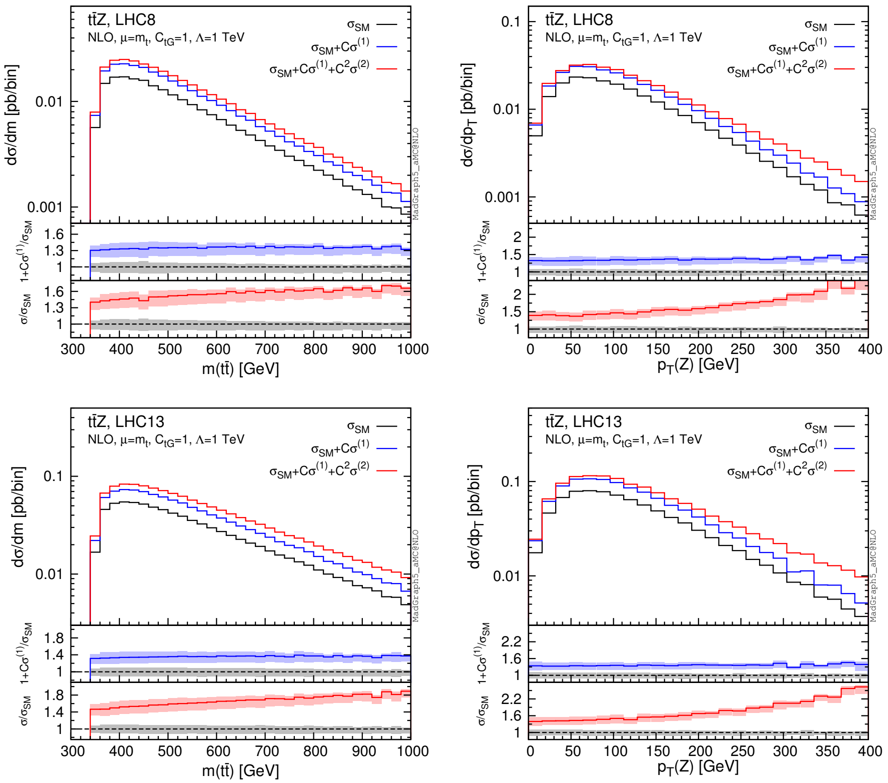

Figure 4.3: Invariant mass distributions for the top quark pair and $Z$ $p_T$ distribution at 8 and 13 TeV for the chromomagnetic operator for $C_{tG} = 1$ and $\Lambda = 1$ TeV. Scale uncertainty bands are shown.

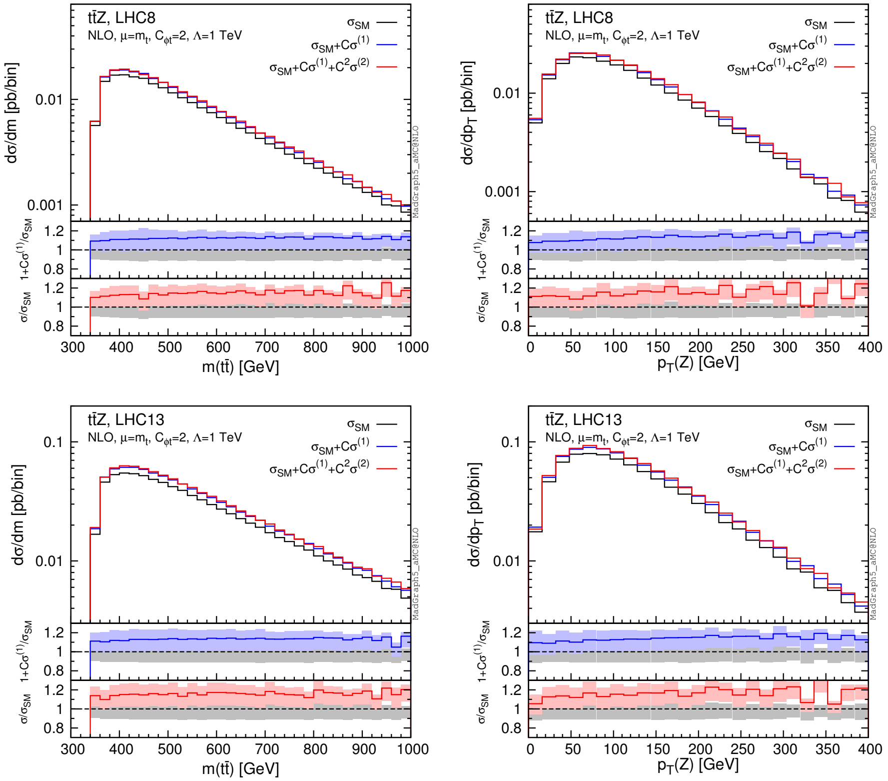

Figure 4.4: Invariant mass distributions for the top quark pair and $Z$ $p_T$ distribution at 8 and 13 TeV for the $O_{\phi t}$ operator for $C_{\phi t} = 2$ and $\Lambda = 1$ TeV. Scale uncertainty bands are shown.

the PS, and with top quarks decayed while keeping spin correlations [150], all implemented in the MG5_aMC framework. Hence our approach can be used directly in realistic experimental simulation, with NLO+PS event generation, which allows for more detailed studies of possible EFT signals. In this chapter, for illustration purpose, we keep results simple by only presenting fixed order NLO distributions. No kinematical cuts are applied except for the $m(\ell\ell) > 10$ GeV and $p_T(\gamma) > 20$ GeV generation cuts. We show results obtained with one non-zero operator coefficient at a time, with $\Lambda = 1$ TeV, and SM results are given for comparison.

We start by showing the distributions obtained for the $O_{tG}$ operator at 8 and 13 TeV in Fig. 4.3. We show as a reference the invariant mass distribution of the top quark pair and the transverse momentum of the $Z$. In the plots we

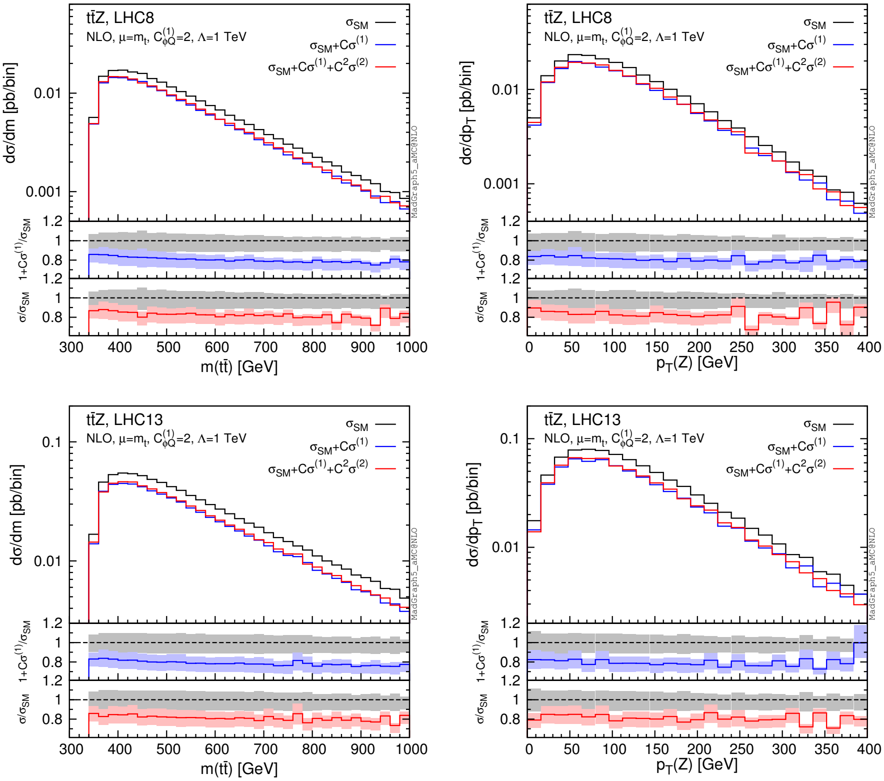

Figure 4.5: Invariant mass distributions for the top quark pair and $Z$ $p_T$ distribution at 8 and 13 TeV for the $O^{(1)}_{\phi Q}$ operator for $C^{(1)}_{\phi Q} = 2$ and $\Lambda = 1$ TeV. Scale uncertainty bands are shown.

show the SM prediction $\sigma_{\rm SM}$, the result for $C_{tG} = 1$, $\Lambda = 1$ TeV i) adding only the interference $\sigma^{(1)}_i$ and ii) adding both the interference and the squared terms $\sigma^{(2)}_{ii}$. We also include the corresponding ratios over the SM prediction and the scale uncertainty bands. It is clear that while the interference contribution is not changing the distribution shape, the $\mathcal{O}(\Lambda^{-4})$ contribution is growing fast at high energies with the effect being more evident at 13 TeV in both distributions shown here. Similar observations can be made for other observables, such as the transverse momentum of the top.

Results for the $O_{\phi t}$ and $O^{(1)}_{\phi Q}$ are shown in Fig. 4.4 and 4.5 respectively. In this case, we set the Wilson coefficients to 2, in order to obtain visible deviations from the SM. These values are allowed by the current constraints. For these operators the $\mathcal{O}(\Lambda^{-4})$ contribution is significantly smaller than the $\mathcal{O}(\Lambda^{-2})$ and

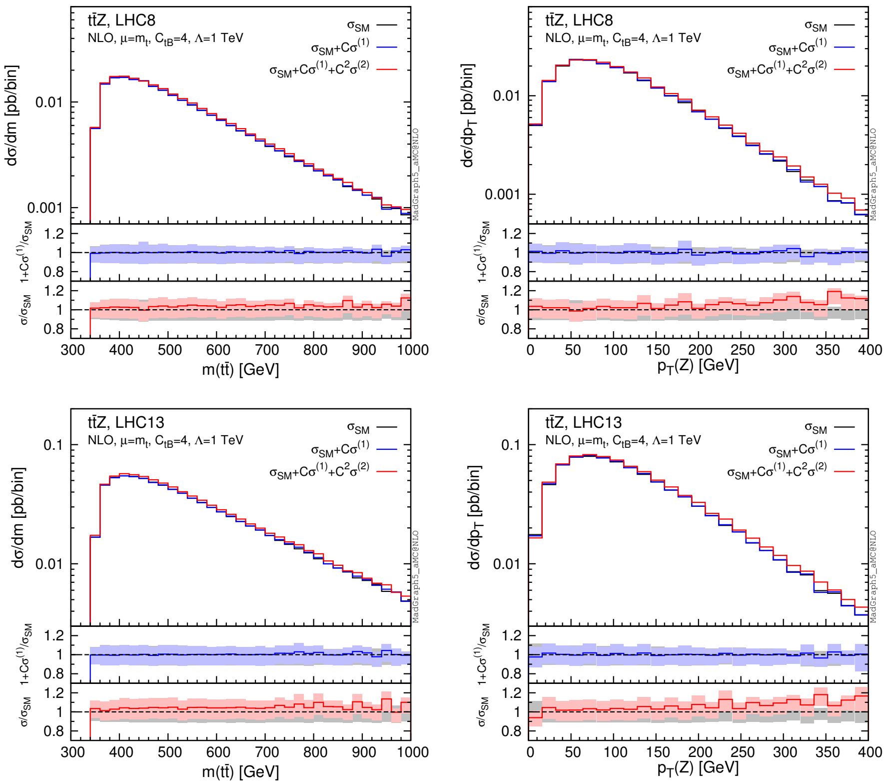

Figure 4.6: Invariant mass distributions for the top quark pair and $Z$ $p_T$ distribution at 8 and 13 TeV for the $O_{tB}$ operator for $C_{tB} = 4$ and $\Lambda = 1$ TeV. Scale uncertainty bands are shown.

does not significantly alter the shape of the differential distributions as seen in the flat ratios for both the $t\bar{t}$ invariant mass and $Z$ $p_T$ distributions. Results for $O^{(3)}_{\phi Q}$ are identical to those of $O^{(1)}_{\phi Q}$ (with a relative sign for $\sigma^{(1)}_i$), so we do not include them for brevity.

For the $O_{tW}$ and $O_{tB}$ operators the EFT contributions are very small compared to the SM. In this case, we resort to $C_{tB} = 4$ to demonstrate the effect of the $O_{tB}$ operator in Fig. 4.6. For this operator the interference with the SM is much smaller than the $\mathcal{O}(\Lambda^{-4})$ terms which are rising with the energy, as evident in the ratio plots. For $t\bar{t}\gamma$, the results for $O_{tG}$ operators are shown in Fig. 4.7 for 8 and 13 TeV. We notice that, in contrast with $t\bar{t}Z$, where the squared terms grow rapidly with the energy, that contribution is smaller for

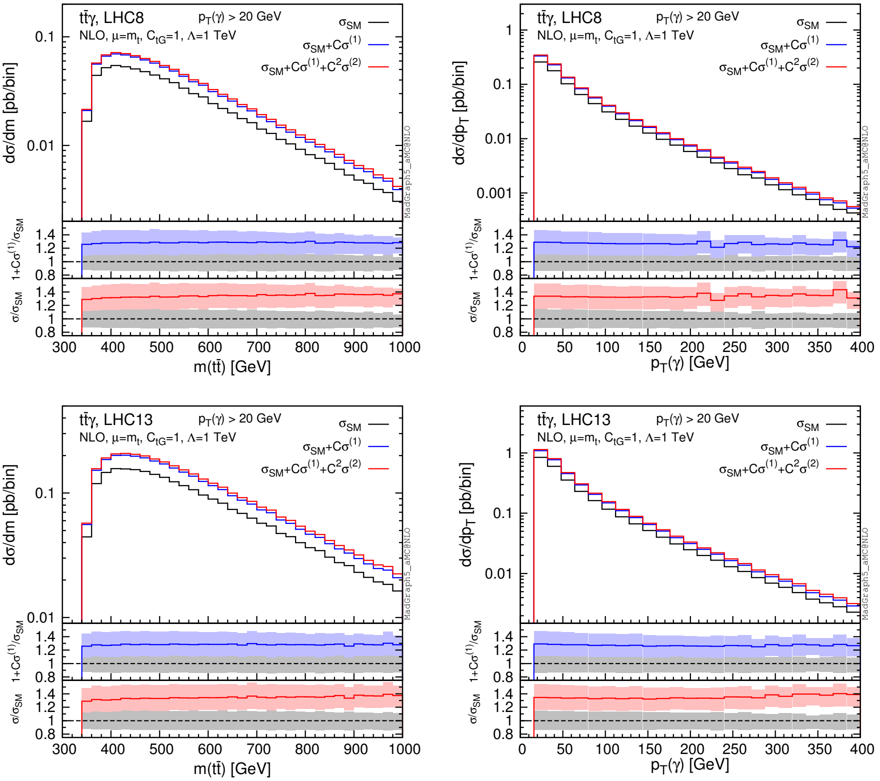

Figure 4.7: Invariant mass distributions for the top quark pair and photon $p_T$ distribution at 8 and 13 TeV for the chromomagnetic operator for $C_{tG} = 1$ and $\Lambda = 1$ TeV. Scale uncertainty bands are shown.

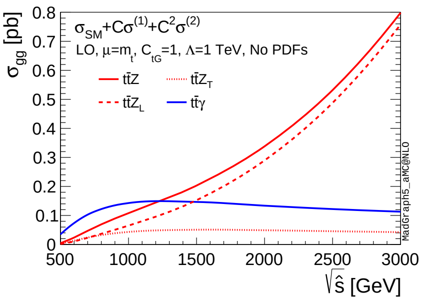

Figure 4.8: Partonic cross section for $t\bar{t}\gamma$ and $t\bar{t}Z$ as function of the centre of mass energy for the chromomagnetic operator. The $t\bar{t}Z$ cross section is decomposed to transverse and longitudinal $Z$ contributions.

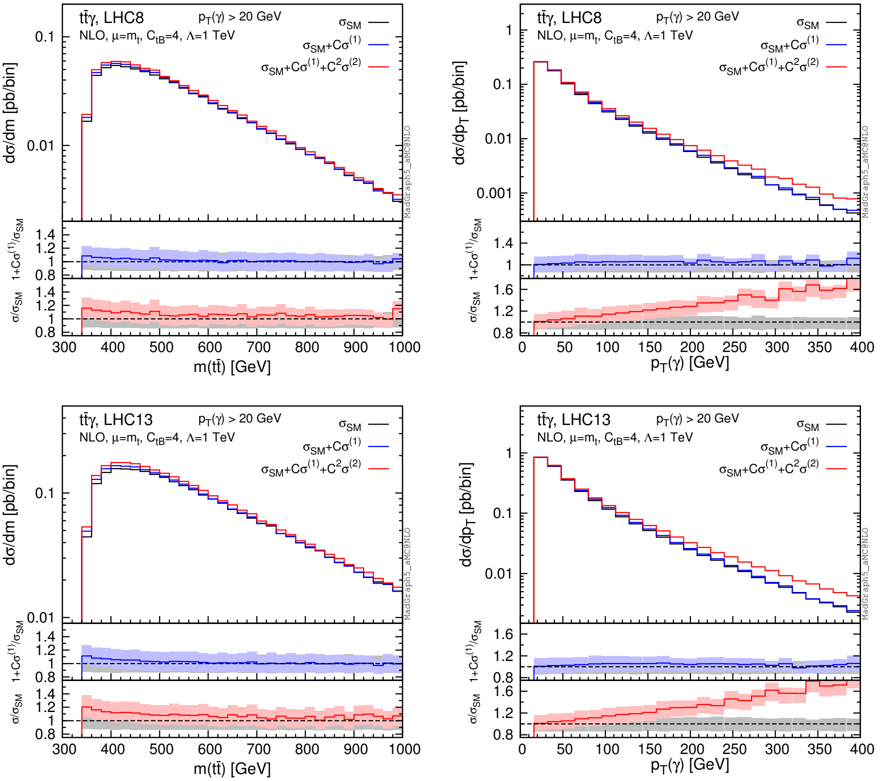

Figure 4.9: Invariant mass distributions for the top quark pair and photon $p_T$ distribution at 8 and 13 TeV for the $O_{tB}$ operator for $C_{tB} = 4$ and $\Lambda = 1$ TeV. Scale uncertainty bands are shown.

$t\bar{t}\gamma$ and does not lead to significant changes in the shapes of the two observables shown here. A comparison of the two processes can be made at the partonic cross-section level as shown in Fig. 4.8. In this plot the total cross-section is shown, i.e., schematically $\sigma_{SM} + C\sigma^{(1)} + C^2\sigma^{(2)}$ for the chromomagnetic operator. The $t\bar{t}Z$ cross-section is decomposed into the transverse and longitudinal $Z$ contributions. The only component that is rising with the energy is the longitudinal one, which explains why the photon distributions do not show any increase with the energy, while those for the $Z$ rise fast. In fact in $t\bar{t}Z$, the Higgs field in $O_{tG}$ always takes its vacuum expectation value, and so by power counting the squared amplitude scales at most as $\sim sv^2/\Lambda^4$ for $t\bar{t}Z_T$ and $t\bar{t}\gamma$, which is not enough for the cross section to rise at high energy. On the other hand, in $t\bar{t}Z_L$ the longitudinal polarisation vector contributes an

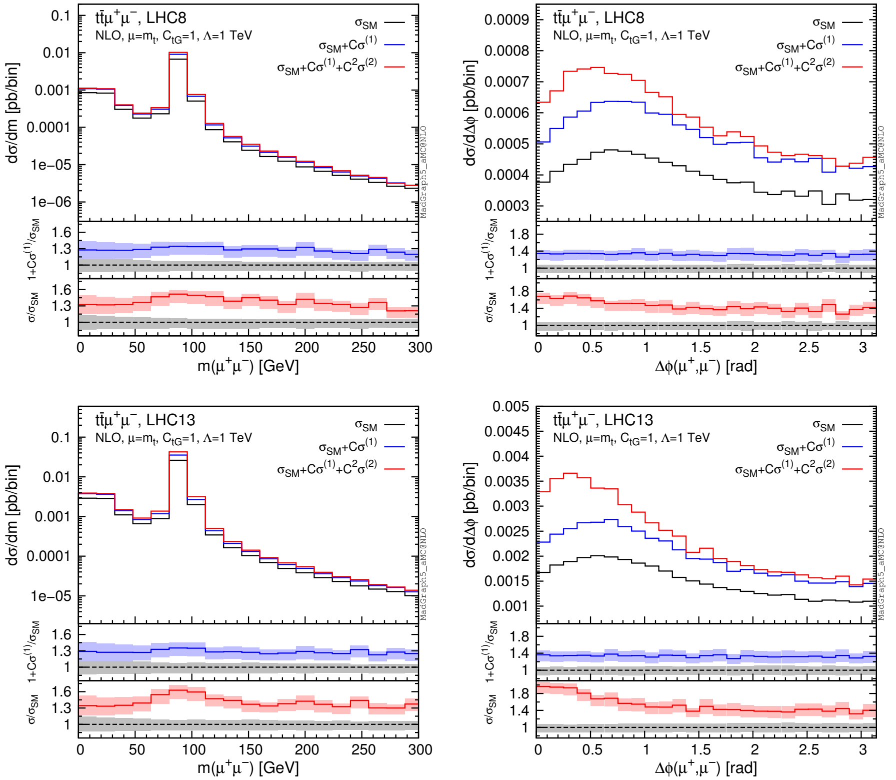

Figure 4.10: Invariant mass distributions for the lepton pair and lepton angular separation distribution at 8 and 13 TeV for the chromomagnetic operator for the $O_{tG}$ operator for $C_{tG} = 1$ and $\Lambda = 1$ TeV.

additional factor of $(E/m_Z)^2$, leading to a final $\sim s^2/\Lambda^4$ scaling of the squared amplitude.

The corresponding distributions for $O_{tB}$ are shown in Fig. 4.9 for 8 and 13 TeV. As setting $C_{tB} = 1$ does not give any visible deviations from the SM, we resort to $C_{tB} = 4$ for these plots. While the squared term does not rise with $m(t\bar{t})$, it increases fast with the photon transverse momentum. This is again related to the amount of momentum passing through the EFT vertex. High top pair invariant mass does not correspond to high momentum through the EFT vertex for the $O_{tB}$ operator, in contrast with the situation for $O_{tG}$. For $O_{tG}$ there is a strong correlation between the $m(t\bar{t})$ and the energy in the EFT vertex leading to a rising distribution.

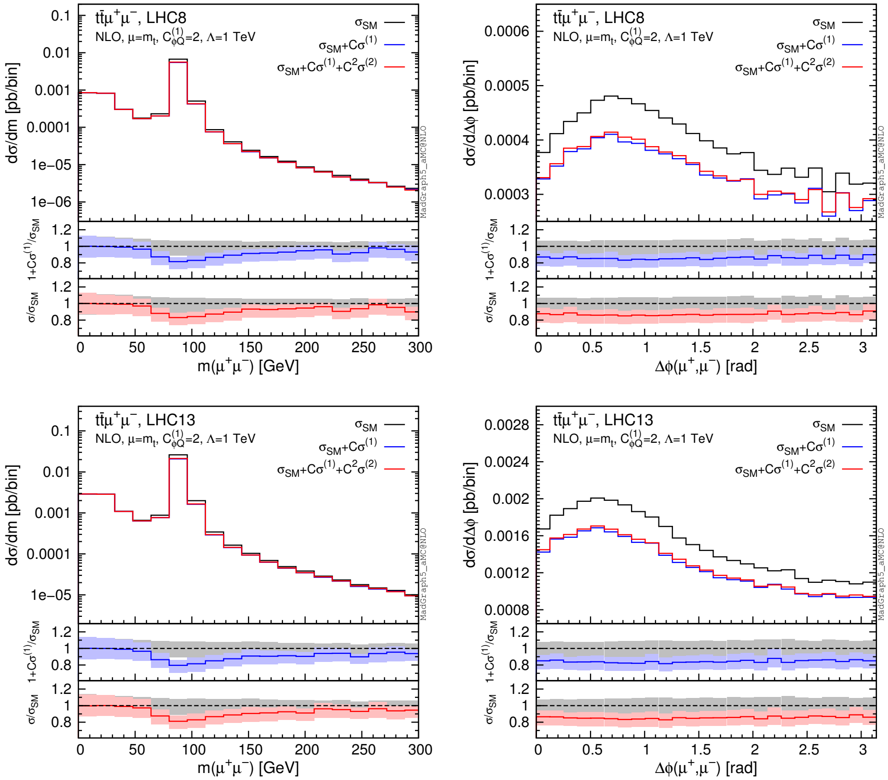

Figure 4.11: Invariant mass distributions for the lepton pair and lepton angular separation distribution at 8 and 13 TeV for the $O_{\phi Q}^{(1)}$ operator for $C_{\phi Q}^{(1)} = 2$ and $\Lambda = 1$ TeV.

For the $t\bar{t}\mu^+\mu^-$ process, we examine the angular separation between the leptons $\Delta\phi$ and the invariant mass distribution of the two leptons $m(\ell\ell)$ for the $O_{tG}$ operator in Fig. 4.10 for 8 and 13 TeV. The angular separation between the two leptons is highly correlated with the transverse momentum of the vector boson. This implies that at low $\Delta\phi$, the behaviour matches that of the high vector transverse momentum region, since for a boosted vector boson, the leptons are collimated. As expected, the behaviour close to the $Z$ mass peak resembles that of the $t\bar{t}Z$ process, while at low invariant mass of the lepton pair it approaches that of $t\bar{t}\gamma$.

The corresponding results for $O_{\phi Q}^{(1)}$ are shown in Fig. 4.11. Again the behaviour of the ratios follows that of the $t\bar{t}Z$ close to the $Z$ mass peak, while at low masses the dimension-six contribution approaches zero as this operator

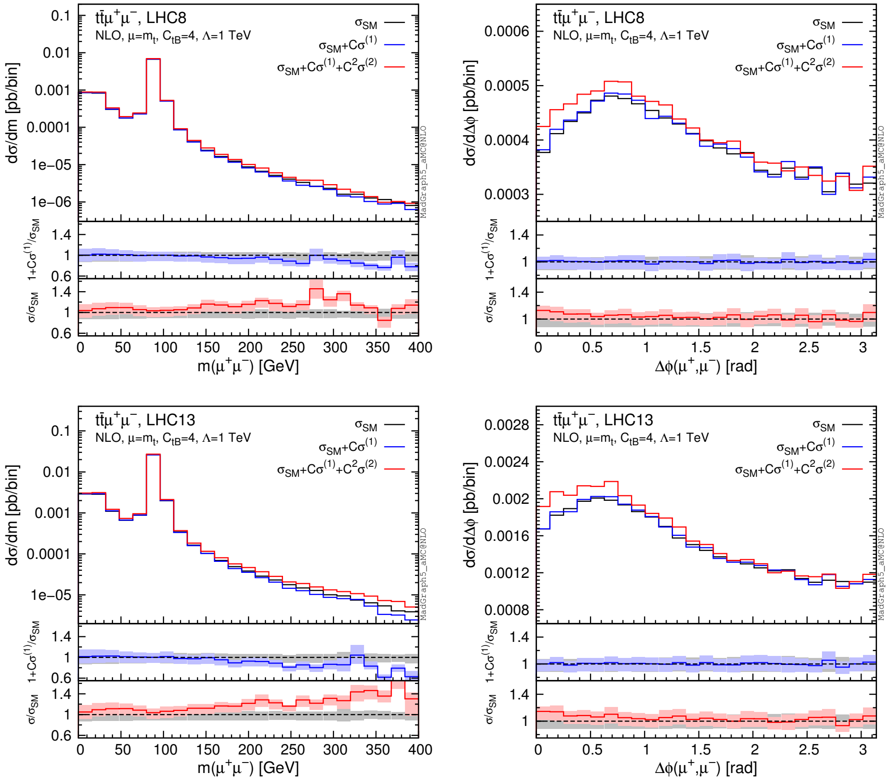

Figure 4.12: Invariant mass distributions for the lepton pair and lepton angular separation distribution at 8 and 13 TeV for the $O_{tB}$ operator for $C_{tB} = 4$ and $\Lambda = 1$ TeV.

has no effect on the $t\bar{t}\gamma^*$ process which dominates at low $m(\ell\ell)$. The $\Delta\phi$ distributions are rather flat similarly to those of the $p_T(Z)$ for the same operator. For brevity we do not show the results for the rest of the current operators, as they are similar to $O_{\phi Q}^{(1)}$.

We conclude our $t\bar{t}\mu^+\mu^-$ discussion by showing the results for the $O_{tB}$ operator operator in Fig. 4.12. The size of the interference with the SM increases at high lepton pair invariant masses while it is constant as a function of the angular separation between the leptons. The squared terms rise at high invariant mass and low angular separation in agreement with the observations made for the $t\bar{t}\gamma$ and $t\bar{t}Z$ distributions.

We conclude this section by commenting on the differential $K$-factors of the EFT contributions. As already mentioned in section 4.3.1, by comparing

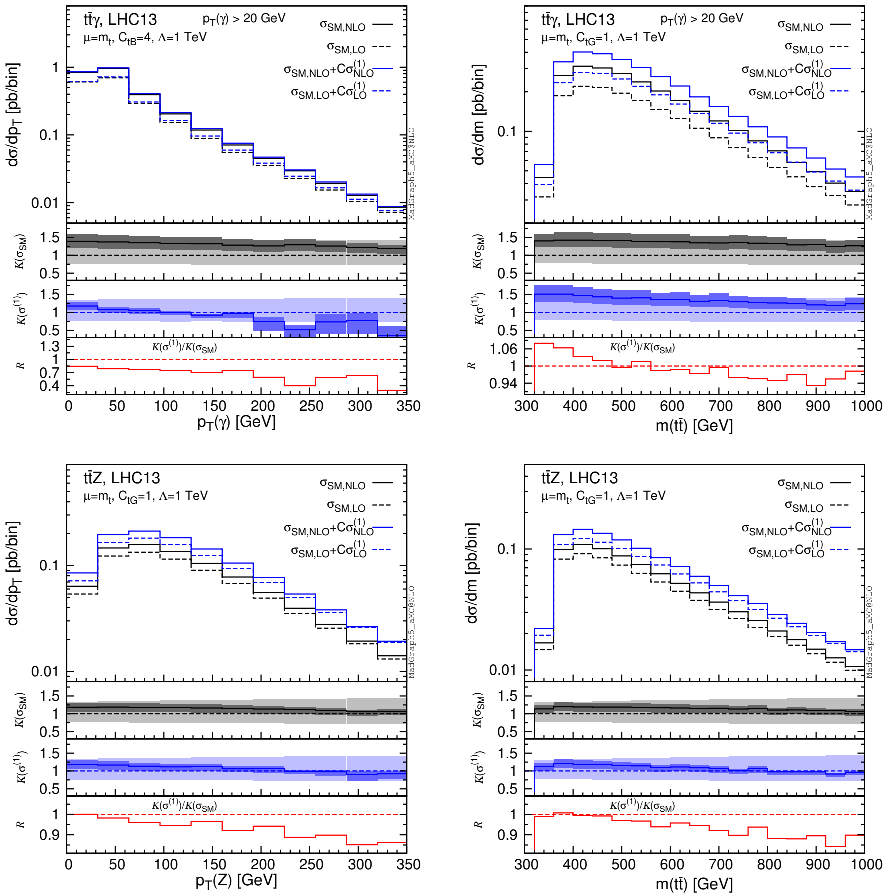

Figure 4.13: NLO and LO invariant mass of the top pair and $p_T$ of the vector boson distributions at 13 TeV for $C_{tB} = 4$, $C_{tG} = 1$ and $\Lambda = 1$ TeV. Comparison between the SM and the interference term differential $K$-factors. Scale uncertainty bands are shown.

Table 4.1 with Tables 4.2-4.6, one can see that the SM global $K$-factors are in general different from the $K$-factors of the EFT operators. This shows that already at the cross-section level, using the SM $K$-factor to estimate the NLO QCD corrections of the EFT contribution is not a reliable approximation. The same applies at the differential level. To demonstrate this observation, we present in Fig. 4.13 a comparison of the differential $K$-factors for the SM and EFT contributions. We focus on the $t\bar{t}\gamma$ and $t\bar{t}Z$ processes at 13 TeV and show four representative observables. In the main panels we show the NLO and LO results of the $\sigma_{SM}$ and $\sigma_{SM} + C\sigma^{(1)}$. In the first two insets we present the differential $K$-factors of i) the SM ($K(\sigma_{SM})$) and ii) the operator contribution ($K(\sigma^{(1)})$), while in the third inset we show the ratio ($R$) between the two. The comparison between Table 4.1 and Table 4.4 shows that the $O_{tB}$ global $K$-factor is lower than the SM one for the $t\bar{t}\gamma$ process. On top of that, in the top left plot of Fig. 4.13 we see that at differential level the ratio of $K$-factors is not flat. For the same process at the cross-section level the $O_{tG}$ contribution and the SM have similar $K$-factors. However, the top right plot reveals that the ratio $R$ is again not flat. Therefore even a bin-by-bin rescaling of the LO $O_{tG}$ distribution with the SM differential $K$-factor would lead to the mismatch depicted in the third inset. In the two lower plots we show results for the $t\bar{t}Z$ process for the $O_{tG}$ operator where similar observations can be made, highlighting the need for NLO QCD predictions for the EFT contributions.

## 4.4 Results for $gg \to HZ$

A subset of the operators affecting $t\bar{t}Z/t\bar{t}\gamma$ enter also in the associated production of a $HZ$ pair in gluon fusion, shown in the Feynman diagrams of Fig. 4.14. This process is formally part of the NNLO cross section for $HZ$ production and contributes at the 10% level. It is nevertheless particularly important in the high Higgs $p_T$ regions where the experimental searches are most sensitive. This process has been studied within the SM, also including the contribution of additional jet radiation, which turns out to be important in the high $p_T$ regions [195]. In this chapter, we consider this process as it can provide additional information on the Wilson coefficients once combined with the corresponding $HZ$ measurements at the LHC. In this section, we investigate the effect of the operators presented above on this process. We note that we consider only the operators involving the top quark and ignore all other dimension-six operators, such as those affecting the interaction of the Higgs with the vector bosons. In addition to modifying the interactions in the SM-like diagrams of Fig. 4.14, the dimension-six operators introduce additional vertices and hence Feynman diagrams as shown in Fig. 4.15.

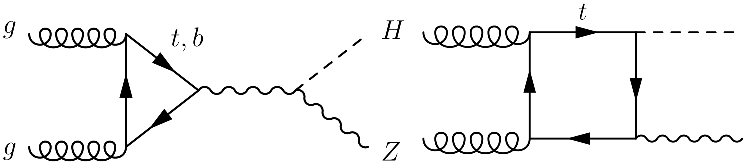

Figure 4.14: Feynman diagrams for $HZ$ production in gluon fusion in the SM.

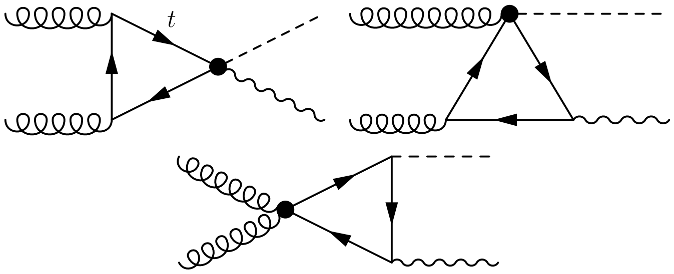

Figure 4.15: Additional types of Feynman diagrams for $HZ$ production in gluon fusion in the presence of dimension-six operators. The new vertices originating from the dimension-six operators are denoted with a blob.

| [fb] | SM | | $O_{tG}$ | $O_{\phi Q}^{(1)}$ |
|---|---|---|---|---|
| 8TeV | $29.15^{+40.0\%}_{-26.6\%}$ | $\sigma_i^{(1)}$ | $10.37^{+41.3\%}_{-27.2\%}$ | $1.719^{+42.5\%}_{-27.6\%}$ |
| | | $\sigma_{ii}^{(2)}$ | $1.621^{+45.1\%}_{-28.7\%}$ | $0.0469^{+46.5\%}_{-29.2\%}$ |
| | | $\sigma_i^{(1)}/\sigma_{SM}$ | $0.356^{+0.9\%}_{-0.8\%}$ | $0.0590^{+1.8\%}_{-1.4\%}$ |
| | | $\sigma_{ii}^{(2)}/\sigma_i^{(1)}$ | $0.156^{+2.6\%}_{-2.0\%}$ | $0.0273^{+2.8\%}_{-2.3\%}$ |
| 13TeV | $93.6^{+34.3\%}_{-23.8\%}$ | $\sigma_i^{(1)}$ | $34.6^{+35.2\%}_{-24.5\%}$ | $5.91^{+36.4\%}_{-24.9\%}$ |
| | | $\sigma_{ii}^{(2)}$ | $6.09^{+39.2\%}_{-26.1\%}$ | $0.182^{+40.2\%}_{-26.6\%}$ |
| | | $\sigma_i^{(1)}/\sigma_{SM}$ | $0.370^{+0.7\%}_{-0.9\%}$ | $0.0631^{+1.6\%}_{-1.5\%}$ |
| | | $\sigma_{ii}^{(2)}/\sigma_i^{(1)}$ | $0.176^{+2.9\%}_{-2.1\%}$ | $0.0309^{+2.8\%}_{-2.2\%}$ |

Table 4.7: Cross sections (in fb) for $gg \to HZ$ production at the LHC at $\sqrt{s} = 8$ TeV and $\sqrt{s} = 13$ TeV for the SM and the dimension-six operators. Scale uncertainties are shown in percentages.

For this process, the factorisation and renormalisation scale is set to $m_H = 125$ GeV. Only LO results can be obtained as the NLO computation requires 2-loop multi-scale Feynman integrals which are currently not available. The results are shown in Table 4.7 for both the SM and the dimension-six operators cross sections, the corresponding scale uncertainties and the corresponding cross-section ratios for 8 and 13 TeV. The $O_{tW}$ and $O_{tB}$ operators do not contribute to this process, due to charge conjugation invariance. The $O_{\phi Q}^{(3)}$, $O_{\phi Q}^{(1)}$ and $O_{\phi t}$ give the same contributions (with a relative minus sign as determined by Eq. C.3) in the massless $b$-quark limit, as they affect in the same

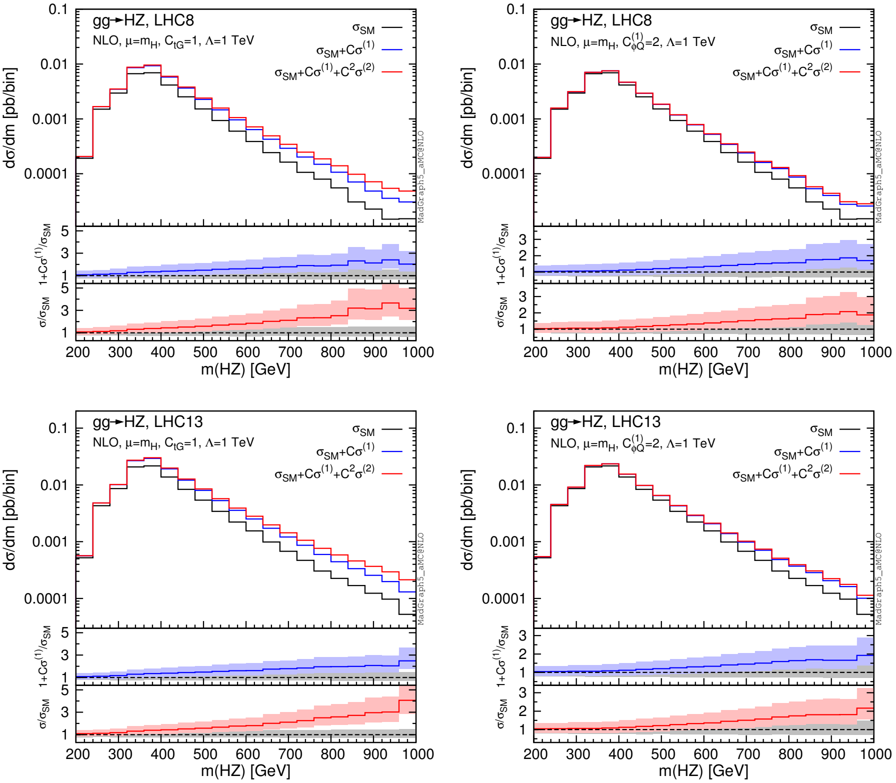

Figure 4.16: $HZ$ invariant mass distributions for $gg \to HZ$ at 8 and 13 TeV for the $O_{tG}$ and $O^{(1)}_{\phi Q}$ operators. Scale uncertainty bands are shown.

way the axial vector coupling of the top to the $Z$, which is the only component whose contribution is allowed by charge conjugation symmetry. If one wants to cancel the chiral anomaly in the triangle loop diagrams with the $Z$-boson in the $s$-channel, the $O_{\phi b}$ operator can be included with its Wilson coefficient set to $C_{\phi b} = 2C^{(1)}_{\phi Q} - C_{\phi t}$. By appropriately fixing the coefficient of $O_{\phi b}$, the axial-vector coupling of the bottom remains opposite to that of the top and the anomaly cancels. In practice this has a negligible numerical effect on the results.

The chromomagnetic operator gives a significant contribution reaching 35% of the SM cross section for $C_{tG} = 1$ and $\Lambda = 1$ TeV. The three current operators give contributions at the 6% level. In both cases, the contribution of the squared amplitudes are subdominant at the total cross section level. These results suffer from large scale uncertainties as it is often the case with gluon fusion processes at LO. The invariant mass distribution for the $HZ$ pair is shown in Fig. 4.16 for the SM and the dimension-six operators. For this process, we find that both the interference with the SM amplitude and the squared contribution are growing with energy.

## 4.5 Results for the ILC

The top-quark electroweak couplings can be accurately determined by future $e^+e^-$ colliders, using top-pair production, thanks to the clean background. Our approach can be applied to $e^+e^-$ colliders as well, providing more accurate predictions for deviations that will be measured in this process. In this section we present results obtained for the ILC at $\sqrt{s} = 500$ GeV for top pair production. For this process, the $O_{tG}$ operator contributes only at NLO, while the other operators contribute starting at LO. The results are presented in Table 4.8. In this case, we do not show the renormalisation scale uncertainties as these can be computed only at NLO and are at the 1-2% level.

| 500GeV | SM | $O_{tG}$ | $O_{\phi Q}^{(3)}$ | $O_{\phi Q}^{(1)}$ | $O_{\phi t}$ | $O_{tW}$ | $O_{tB}$ |
|---|---|---|---|---|---|---|---|
| $\sigma_{i,LO}^{(1)}$ | 566 | 0 | 15.3 | -15.3 | -1.3 | 272 | 191 |
| $\sigma_{i,NLO}^{(1)}$ | 647 | -6.22 | 18.0 | -18.0 | -1.0 | 307 | 216 |
| $K$-factor | 1.14 | N/A | 1.17 | 1.17 | 0.78 | 1.13 | 1.13 |
| $\sigma_{i,LO}^{(2)}$ | | 0 | 0.72 | 0.71 | 0.72 | 60.4 | 27.2 |
| $\sigma_{i,NLO}^{(2)}$ | | 0.037 | 0.83 | 0.82 | 0.82 | 68.8 | 31.0 |
| $\sigma_{i,LO}^{(1)}/\sigma_{SM,LO}$ | | 0 | 0.027 | -0.027 | -0.0022 | 0.48 | 0.34 |
| $\sigma_{i,NLO}^{(1)}/\sigma_{SM,NLO}$ | | -0.096 | 0.028 | -0.028 | -0.0015 | 0.47 | 0.33 |
| $\sigma_{i,LO}^{(2)}/\sigma_{i,LO}^{(1)}$ | | N/A | 0.047 | -0.047 | -0.57 | 0.22 | 0.14 |
| $\sigma_{i,NLO}^{(2)}/\sigma_{i,NLO}^{(1)}$ | | -0.006 | 0.046 | -0.046 | -0.82 | 0.22 | 0.14 |

Table 4.8: Cross sections (in fb) for $t\bar{t}$ production at the ILC at $\sqrt{s} = 500$ GeV. Renormalisation scale uncertainties are not shown. They are only present at NLO and remain at the 1% level.

Unlike the $t\bar{t}V$ processes, here we find significant contributions from the dipole operators $O_{tB}$ and $O_{tW}$, while the other operators are suppressed, with $O_{tG}$, $O_{\phi Q}^{(1)}$ and $O_{\phi Q}^{(3)}$ at the percent level, and $O_{\phi t}$ at the per mille level. This is mainly because the momenta of $Z$ and $\gamma$ are at least at the $t\bar{t}$ threshold, and so the same dipole structure, which suppresses $t\bar{t}V$ production at the LHC, enhances the $t\bar{t}$ production at the ILC. It follows that the ILC could provide useful information complementary to the LHC as discussed also in [175, 176].

We note here that the analysis of [175, 176] does not include the contribution from $O_{tG}$, although (following an anomalous coupling approach) it does include the contribution of the squares of the amplitudes with the top anomalous couplings and therefore also the CP-odd contributions.

## 4.6 Theoretical uncertainties

In this section we briefly discuss various theoretical uncertainties relevant to our results. In the SMEFT calculation there are two main types of theoretical uncertainties, those related to missing higher orders in the strong coupling and those from higher terms in the $1/\Lambda$ expansion. In the former class, we can list

- Uncertainties due to parton-distribution functions.

  This type of uncertainty is also present in the SM calculations and can be treated in the same way, i.e. by following the procedures associated with the corresponding PDF sets, as long as the scale of new physics is high enough and the EFT operators do not modify the DGLAP equations.

- Uncertainties due to missing higher orders in the $\alpha_s$ expansion as in the SM.

  This kind of uncertainty is typically estimated by varying the renormalisation and factorisation scales as done in SM calculations. All results presented in this chapter are provided along with uncertainties that are estimated by varying (9-point variation) these two scales independently.

- Uncertainties due to missing higher orders in the $\alpha_s$ expansion of the EFT operators.

  In the SMEFT an additional uncertainty, related to the scale at which the operators are defined, should be considered as well. It characterises the uncancelled logarithmic terms in the renormalisation group running and mixing of the operators. We did not evaluate these uncertainties explicitly even though it is possible in our framework. For the operators we have studied in this chapter, they are expected to be negligible compared to the first two scale uncertainties [174]. This is because the anomalous dimensions of the relevant operators happen to be smaller by roughly an order of magnitude compared to the beta function of $\alpha_s$ (see Ref. [174] for a discussion of the operator scale uncertainty in the single-top processes).

We now consider uncertainties due to missing $\mathcal{O}(\Lambda^{-4})$ contributions, also discussed in [196]. Up to this order, the cross section (or any other observable) can be written as:

$$\sigma = \sigma_{SM} + \sum_i \frac{C_i^{\text{dim6}}}{(\Lambda/1\text{TeV})^2}\sigma_i^{(1,\text{dim6})} + \sum_{i<j} \frac{C_i^{\text{dim6}}C_j^{\text{dim6}}}{(\Lambda/1\text{TeV})^4}\sigma_{ij}^{(2,\text{dim6})} + \\ + \sum_i \frac{C_i^{\text{dim8}}}{(\Lambda/1\text{TeV})^4}\sigma_i^{(1,\text{dim8})} \qquad (4.14)$$

The last two terms are formally $\mathcal{O}(\Lambda^{-4})$ contributions, and could in principle be neglected as they are expected to be suppressed for $\mathcal{O}(1)$ coefficients. One should then consider

- Impact of the squared contributions $\sigma_{ij}^{(2,\text{dim6})}$ coming from dimension-six operators.

  These contributions can be explicitly calculated with our approach, even though obtaining the complete results can be time consuming. In this chapter, we have always provided the results for $\sigma_{ii}^{(2)}$ for each operator $O_i$, for not only total cross sections but also for distributions. In fact, one could include these squared contributions in the central values as part of the theoretical predictions, if only one operator is taken to be non-zero at a time. As we have mentioned, this can be justified for cases where the expansion in $E^2/\Lambda^2$ is under control but the squared contribution may still be large, due to less constrained operator coefficients, i.e. if $C_i^2\frac{E^4}{\Lambda^4} > C_i\frac{E^2}{\Lambda^2} > 1 > \frac{E^2}{\Lambda^2}$ is satisfied. In any case, our results for the $\sigma_{ii}^{(2)}$ terms can provide useful information for the evaluation of the uncertainties, if the squared contributions are neglected or only partly included.

  As we have discussed already, the relative size of $\sigma_{ii}^{(2)}$ compared to $\sigma_i^{(1)}$ does not imply anything about the validity of the EFT and careful assessment should be done on a case-by-case basis.

- Validity of the EFT, i.e. contributions from missing higher-dimensional operators.

  The second contribution at $\mathcal{O}(\Lambda^{-4})$, $\sigma_i^{(1,\text{dim8})}$, comes from interference between SM and dimension-eight operators. These contributions cannot be computed in our approach, and will have to be neglected. A corresponding uncertainty should be taken into account. This can be easily done at the LO by calculating the interference contribution from typical dimension-eight operators. Alternatively, by simple power counting, these uncertainties may be estimated to be of order $C_i^{\text{dim6}}/(\Lambda/1\text{TeV})^2\sigma_i^{(1,\text{dim6})}s/\Lambda^2$. In this chapter, we do not assume a specific value of $\Lambda$, and so evaluating such uncertainties is not possible without additional assumptions. However, in a real analysis, for any given $\Lambda$, one can always apply a cut

$s_{\max}$ on the centre-of-mass energy of the process, so that this uncertainty remains under control.

## 4.7 Discussion

In this section we explore the sensitivity of the top processes discussed above to the various operators. Experimental results from [165, 168, 169, 197] are used. For the $t\bar{t}Z$ measurement by ATLAS [169] and the $t\bar{t}\gamma$ measurement by CMS [165], a direct comparison is difficult, because of the way in which the measured cross sections are defined (see app. C.2).

We thus define the "$R$" ratios in order to facilitate a direct comparison between the quoted experimental measurements and our theory predictions, as explained in appendix C.2. These ratios are always taken into account when experimental results on $t\bar{t}\mu^+\mu^-$ and $t\bar{t}\gamma$ are used. On the other hand, the other measurements can be directly compared with our predictions.

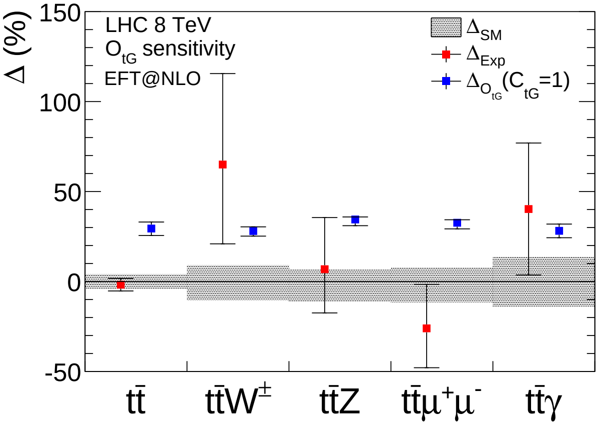

Figure 4.17: Sensitivity of various processes to the $O_{tG}$ operator. $\Delta$ denotes the percentage difference from the SM theoretical prediction for each process. Theory predictions for all $t\bar{t}V$ processes are at NLO in QCD while for $t\bar{t}$ the NNLO result of [58] is employed. Experimental measurements are also shown along with the corresponding experimental uncertainties taken from [197] for $t\bar{t}$, [168] for $t\bar{t}W$ and $t\bar{t}Z$, [169] for $t\bar{t}\mu^+\mu^-$ and [165] for $t\bar{t}\gamma$.

We first examine the $O_{tG}$ operator, which affects all production of top quark pairs with a vector boson, as well as $t\bar{t}$ production. The sensitivity of various processes to the $O_{tG}$ operator is demonstrated in Fig. 4.17. In the plot

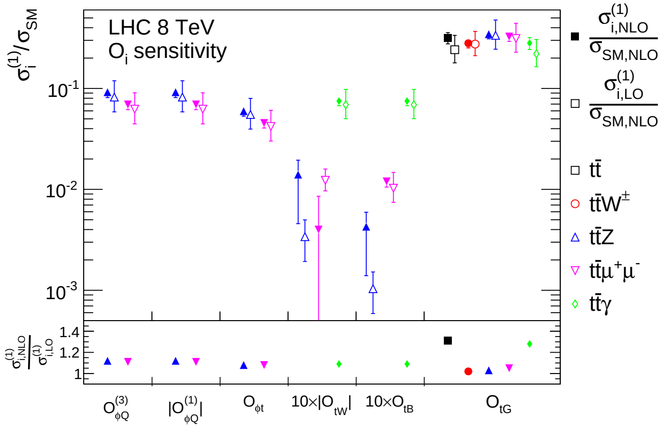

Figure 4.18: Sensitivity of various top quark processes to the various operators shown at LO and NLO at 8 TeV. $K$-factors are also shown for $\sigma_i^{(1)}$ as well as the scale uncertainties. We do not show the $K$-factors for the $O_{tB}$ and $O_{tW}$ operators in the $t\bar{t}Z$ and $t\bar{t}\mu^+\mu^-$ processes, as in this case accidental cancellations lead to large or even negative $K$-factors.

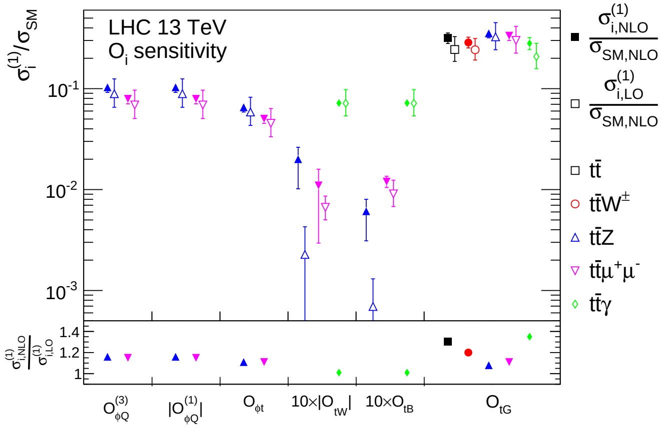

Figure 4.19: Sensitivity of various top quark processes to the various operators shown at LO and NLO at 13 TeV. Details as in Fig. 4.18.

we include the percentage deviation from the SM predictions for top pair production, and top pair production in association with a $W, Z$ boson or a photon, as well as the $t\bar{t}\mu^+\mu^-$ process for $C_{tG} = 1$ and $\Lambda = 1$ TeV. All SM predic-

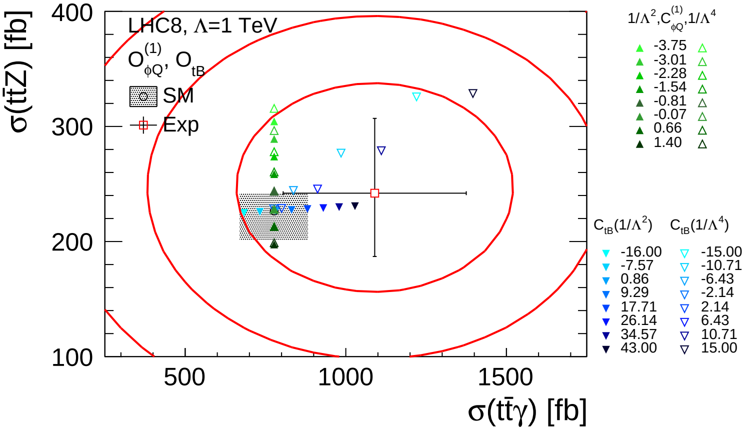

Figure 4.20: Sensitivity of the $t\bar{t}\gamma$ and $t\bar{t}Z$ processes to the $O^{(1)}_{\phi Q}$ and $O_{tB}$ operators. For each value of the coefficient we show the cross-section including i) only the interference term (filled triangles) and ii) both the interference and the squared contribution (unfilled triangles). The range for the Wilson coefficients is determined by the current constraints as discussed in Section 2. The experimental measurements used in this plot are taken from [165] and [168] for $t\bar{t}\gamma$ and $t\bar{t}Z$ respectively. The squared contribution of the $O_{tB}$ operator is very large, and therefore we employ a separate smaller interval to obtain cross sections within the boundaries of this plot.

tions and uncertainties are given at NLO, apart from the top pair production cross-section, which is given at NNLO+NNLL [58]. We also present the experimental measurements and the corresponding uncertainties (systematic and statistical uncertainties added in quadrature). Only the $\mathcal{O}(1/\Lambda^2)$ contribution is included. The $O_{tG}$ operator affects all processes considered here in a similar way, at the 30% level for $\Lambda = 1$ TeV and $C_{tG} = 1$[39]. At present, the most stringent direct constraints on this operator are obtained from the top pair production measurement, which is by far the most accurate one.

The relative sensitivity of the top processes to all operators can be summarised in Fig. 4.18, where the results for $C = 1$ are shown as a ratio over the SM NLO cross sections, for the 6 operators considered here both at LO and NLO, along with the corresponding $K$-factors in the lower panel. The reduc-

---

[39] Here, we choose a value for $C_{tG} = 1$ that is already excluded by the current constraints from $t\bar{t}$ process. The plot in figure 4.17 shows in general the strategy to be followed for a sensitivity study. Since this plot includes only the interference term, the results can be rescaled accordingly. In the plots of figures 4.20, 4.21 and 4.22 we use the actual current limits on the Wilson coefficients.

tion of the theoretical uncertainties at NLO is also evident in the plot. The corresponding sensitivity plot for 13 TeV is shown in Fig. 4.19, in which similar observations can be made.

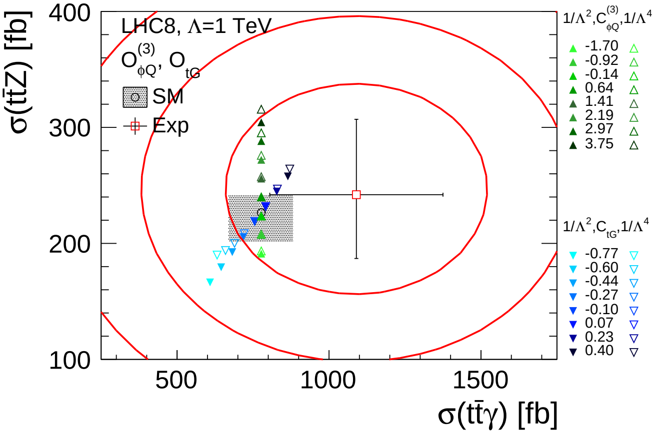

Figure 4.21: Sensitivity of the $t\bar{t}\gamma$ and $t\bar{t}Z$ processes to the $O^{(3)}_{\phi Q}$ and $O_{tG}$ operators. Details as in Fig. 4.20.

Using the experimental measurements, one can further explore the sensitivity of the $t\bar{t}\gamma$ and $t\bar{t}Z$ processes on the various operators as shown in Figs. 4.20, 4.21 and 4.22. In the contour plots we include the experimental results of [165] for $t\bar{t}\gamma$ and [168] for $t\bar{t}Z$ and the corresponding one and two sigma contour plots. In this case, we assume there is no correlation between the two measurements. The SM NLO predictions and the corresponding scale uncertainties are also shown in the plots. We plot the cross section obtained by varying the Wilson coefficients of the various operators. For clarity and to avoid overcrowding the contour plots, we present the operators in pairs. For the coefficients, we employ the current constraints to define our interval. Vertical lines in the plots indicate that the $t\bar{t}\gamma$ process is not affected by the specific operator, i.e. $O_{\phi t}, O^{(3)}_{\phi Q}$ and $O^{(1)}_{\phi Q}$. Cross sections with and without adding the $\mathcal{O}(1/\Lambda^4)$ contributions from the squared EFT amplitudes are compared. The $O_{tB}$ operator is very loosely constrained, and therefore including the squared term for the large allowed values of the Wilson coefficient has an enormous effect on the cross sections, as the $\mathcal{O}(1/\Lambda^4)$ contribution scales like $C^2_{tB}$. For the more constrained current operators $O^{(1)}_{\phi Q}$ and $O^{(3)}_{\phi Q}$, the squared contribution becomes important only at the edges of the allowed intervals. We also notice that for the $O_{\phi t}$ and $O_{tG}$ operators the $\mathcal{O}(1/\Lambda^4)$ contribution is important for a sizeable part of allowed interval, in the first case because the constraints are

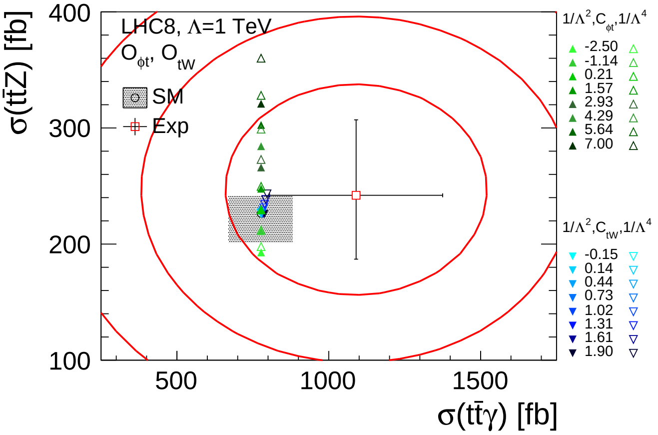

Figure 4.22: Sensitivity of the $t\bar{t}\gamma$ and $t\bar{t}Z$ processes to the $O_{\phi t}$ and $O_{tW}$ operators. Details as in Fig. 4.20.

rather loose and in the second case because $\sigma_{tG}^{(2)}$ is large. Finally, we note that the contour plots qualitatively demonstrate the size of the experimental uncertainties needed for these processes to have an impact on the allowed values of the coefficients. In that respect we observe for example that the $O_{tW}$ operator receives very stringent constraints from top decay, and it is not expected to be further constrained by $t\bar{t}V$ measurements even with a significant reduction of the experimental uncertainties.

## 4.8 Summary

We have presented the NLO QCD predictions in the SMEFT framework for the associated production of a top-quark pair and a neutral gauge boson at the LHC. In addition, we have considered top-pair production in $e^+e^-$ colliders and the top loop-induced process $gg \to HZ$ at the LHC. These processes are important because they directly probe the neutral gauge-boson couplings to the top quark, which are not well probed by other means. In our approach we have included the full set of dimension-six operators that parameterise these couplings.

We have studied the contribution of each relevant dimension-six operator, in both total cross sections and differential distributions. We have presented full results for $\mathcal{O}(\Lambda^{-2})$ contributions, along with the squared contribution of each operator at $\mathcal{O}(\Lambda^{-4})$. The latter contribution can be used to estimate uncertainties coming from higher order $\mathcal{O}(\Lambda^{-4})$ contributions. Scale uncertainties are provided in all cases, and their reduction at NLO reflects the increased precision of our predictions.

In $t\bar{t}\gamma$ and $t\bar{t}Z$, we find that the operator that contributes the most, given our choice of operator normalisation, is the chromomagnetic one. This observation is particularly important in the context of a global EFT fit, because it means that, when extracting information on operators modifying the top couplings with the weak gauge bosons, uncertainties due to a possible non-vanishing chromomagnetic operator should be carefully accounted for. We also find that the weak dipole operators give extremely suppressed contributions at $\mathcal{O}(1/\Lambda^2)$, due to a momentum suppression from the operator structure, and in $t\bar{t}Z$ an additional accidental cancellation between $gg$ and $q\bar{q}$ initial states.

A subset of the operators affects the associated production of the Higgs boson with a $Z$ boson in gluon fusion, and we have considered their effects on this process at the LHC. This might provide additional constraints on the operators once $ZH$ production is measured accurately at the LHC. Again, we find that the contribution of $O_{tG}$ is large, while all the current operators give the same contribution as they affect the axial vector of the Z in the same way. The weak dipole operators do not contribute due to charge conjugation parity. We have also found that, at the ILC, $t\bar{t}$ production is sensitive to weak dipole operators, and could provide information complementary to the LHC.

We have studied the sensitivity of the processes to the various operators in light of the current experimental measurements, as well as the constraints currently placed on the operators from other top measurements and electroweak precision observables. A discussion of the relevant uncertainties coming from missing higher orders in QCD and in the EFT has also been presented. The NLO results provide a solid basis for current and future measurements to be analysed in an EFT approach.

In summary, at NLO in QCD accuracy, deviations from the SM in the top sector can be extracted with improved accuracy and precision, keeping EFT uncertainties under control. As our calculation is based on the MG5_aMC framework, matching with the parton shower and top decays with spin correlations can be achieved in an automatic way. Therefore, the corresponding simulations can be directly used in experimental analyses in the future to provide reliable information on possible EFT signals. Furthermore, dedicated investigations of the features of deviations from the SM in these processes can be performed based on our results, with an expected improvement in sensitivity.

# 5 | Conclusions

In this 4-year research we have focused on top-quark precision physics within and beyond the SM. In the quest for precision we have studied the impact of EW corrections and photon-induced contributions on top-quark differential distributions at 8, 13 and 100 TeV. We compared predictions with two different PDF sets including the photon density and DGLAP evolution at NLO QCD + LO QED accuracy: the CT14QED and NNPDF2.3QED PDF sets. While contributions due to the photon PDF are negligible with CT14QED, this is not the case for NNPDF2.3QED, where such contributions at 13 TeV are sizeable and are affected by large PDF uncertainties. At high $p_T(t)$ and $m(t\bar{t})$, the photon-induced contributions can accidentally compensate the negative contributions of Sudakov logarithms or even change the sign of the EW corrections. Furthermore, we have shown that such a compensation strongly depends on the scale choice. In rapidity distributions, the impact of the $g\gamma$ initial state is sizeable in the peripheral region and much larger than NLO EW corrections, which do not receive large Sudakov enhancements in these kinematical configurations. Increasing the energy of the collider, photon-induced channels become less relevant for a fixed value of $p_T(t)$ or $m(t\bar{t})$, since smaller values of $x$ are probed and consequently the quark and gluon PDFs are much larger than the photon PDF. At 100 TeV, photon-induced channels are important only in the very boosted regime ($p_T(t) \gtrsim 5$ TeV or $m(t\bar{t}) \gtrsim 10$ TeV), where Sudakov logarithms are negative and above the 20% level. For the same reason, at the LHC photon-induced contributions are relatively larger at 8 TeV than at 13 TeV. We computed their size for the same differential (and normalised) distributions already analysed by ATLAS and CMS, taking into account both experimental errors and theory uncertainties. Having understood the behaviour of the EW corrections in $t\bar{t}$ distributions we proceeded towards more precision. The NNLO QCD predictions in $t\bar{t}$ production have reduced significantly the higher order uncertainties [101]. The automation of the EW corrections is used in order to include them using the newest available PDF sets *i.e.* the NNPDF3.0QED and PDF4LHC_LUXQED. In collaboration with the authors of [101], the combination of NNLO QCD and NLO EW calculations provides the most accurate predictions at differential level for the $t\bar{t}$ process at LHC, 13 TeV.

We have proceeded to the study at NLO QCD accuracy of $t\bar{t}V$, $t\bar{t}VV$ ($V = W^{\pm}, Z, \gamma$) and $t\bar{t}t\bar{t}$ processes as a background to $t\bar{t}H$ within the same computational framework (MadGraph5_aMC@NLO). Moreover, we have performed a complete analysis with realistic selection cuts on final states at NLO QCD accuracy including the matching to parton shower and decays, for both signal and background processes relevant for searches at the LHC for the $t\bar{t}H$ production. Specifically, we have considered the cases where the Higgs boson decays either into leptons, where $t\bar{t}V$ and $t\bar{t}VV$ processes and $t\bar{t}t\bar{t}$ production provide backgrounds, or into two photons giving the same signature as $t\bar{t}\gamma\gamma$ production. We have investigated the behaviour of fixed order NLO QCD corrections for several distributions and we have analysed their dependence on (the definition of) the renormalisation and factorisation scales. We have found that QCD corrections on key distributions cannot be described by overall $K$-factors. However, dynamical scales in general, even though not always, reduce the dependence of the corrections on kinematic variables and thus lead to flatter $K$-factors. For all the processes considered, NLO QCD corrections are in general necessary in order to provide precise and reliable predictions at the LHC. Notable examples discussed in the text are, e.g., the giant corrections in the tails of $p_T(t\bar{t})$ distributions for $t\bar{t}V$ processes and the large decrement of the top-quark central asymmetry for $t\bar{t}\gamma$ production. A special study for the central asymmetry in the $t\bar{t}W^{\pm}$ process is realised expanding also to the top-quark pair decay products. Some of the aforementioned calculations ($t\bar{t}W$, $t\bar{t}Z$) are compared with other codes and are included in the yellow report of Higgs cross section (YRHXS4), in the $t\bar{t}V$ section [12, section I.6.7]. Furthermore the fixed NLO QCD analysis in $t\bar{t}V$ was realised also for an 100 TeV future collider at both inclusive and differential level [11, chapter 13]. In the case of future (hadron) colliders inclusive cross sections receive sizeable corrections, which lead, e.g., to $K$-factors larger than two at 100 TeV for $t\bar{t}V$ and $t\bar{t}VV$ processes with a charged final state.

Having established the $t\bar{t}V$ behaviour at NLO QCD accuracy in the SM, we moved to NLO QCD predictions in the SMEFT framework for the associated production of a top-quark pair and a neutral gauge boson at the LHC. In this project, we also considered top-pair production in $e^+e^-$ colliders and the top loop-induced process $gg \to HZ$ at the LHC. These processes are important because they directly probe the neutral gauge-boson couplings to the top quark, which are not well probed by other means. In our approach we have included the full set of dimension-six operators that parameterise these couplings except the 4-Fermion operators. We studied the contribution of each relevant dimension-six operator, in both total cross sections and differential distributions, presenting full results for $\mathcal{O}(\Lambda^{-2})$ contributions, along with the squared contribution of each operator at $\mathcal{O}(\Lambda^{-4})$. Scale uncertainties were provided in all cases, and their reduction at NLO reflects the increased precision of our predictions. In $t\bar{t}\gamma$ and $t\bar{t}Z$, we found that the operator that contributes the most, given our choice of operator normalisation, is the chromomagnetic one. This observation is particularly important in the context of a global EFT fit, because it means that, when extracting information on operators modifying the top couplings with the weak gauge bosons, uncertainties due to a possible non-vanishing chromomagnetic operator should be carefully accounted for. We also found that the weak dipole operators give extremely suppressed contributions at $\mathcal{O}(\Lambda^{-2})$, due to a momentum suppression from the operator structure, and in $t\bar{t}Z$ an additional accidental cancellation between $gg$ and $q\bar{q}$ initial states.

# A | Appendix for chapter 2

## A.1 Notation for NNLO QCD + NLO EW combination

In this appendix we specify how EW corrections and NNLO QCD results are combined in the additive and multiplicative approaches. The notation matches the one introduced in [40]. The phenomenology of $t\bar{t}$ production within the additive approach is presented in sec. 2.5.1. The multiplicative approach is studied in sec. 2.5.2 where it is also compared to the additive one.

A generic observable $\Sigma^{t\bar{t}}$ in the process $pp \to t\bar{t}(+X)$ can be expanded simultaneously in the QCD and EW coupling constants as:

$$\Sigma^{t\bar{t}}(\alpha_s, \alpha) = \sum_{m+n\geq 2} \alpha_s^m \alpha^n \Sigma_{m+n,n} \,. \tag{A.1}$$

The LO ($m+n=2$), NLO ($m+n=3$) and NNLO ($m+n=4$) contributions read

$$\begin{aligned}
\Sigma^{t\bar{t}}_{\mathrm{LO}}(\alpha_s, \alpha) &= \alpha_s^2 \Sigma_{2,0} + \alpha_s \alpha \Sigma_{2,1} + \alpha^2 \Sigma_{2,2} \\
&\equiv \Sigma_{\mathrm{LO},1} + \Sigma_{\mathrm{LO},2} + \Sigma_{\mathrm{LO},3} \,, \\
\Sigma^{t\bar{t}}_{\mathrm{NLO}}(\alpha_s, \alpha) &= \alpha_s^3 \Sigma_{3,0} + \alpha_s^2 \alpha \Sigma_{3,1} + \alpha_s \alpha^2 \Sigma_{3,2} + \alpha^3 \Sigma_{3,3} \\
&\equiv \Sigma_{\mathrm{NLO},1} + \Sigma_{\mathrm{NLO},2} + \Sigma_{\mathrm{NLO},3} + \Sigma_{\mathrm{NLO},4} \,, \\
\Sigma^{t\bar{t}}_{\mathrm{NNLO}}(\alpha_s, \alpha) &= \alpha_s^4 \Sigma_{4,0} + \alpha_s^3 \alpha \Sigma_{4,1} + \alpha_s^2 \alpha^2 \Sigma_{4,2} + \alpha_s \alpha^3 \Sigma_{4,3} + \alpha^4 \Sigma_{4,4} \\
&\equiv \Sigma_{\mathrm{NNLO},1} + \Sigma_{\mathrm{NNLO},2} + \Sigma_{\mathrm{NNLO},3} + \Sigma_{\mathrm{NNLO},4} + \Sigma_{\mathrm{NNLO},5} \,.
\end{aligned} \tag{A.2}$$

In order to simplify the notation, we further define the following pure-QCD quantities

$$\Sigma_{\mathrm{LO\ QCD}} \equiv \Sigma_{\mathrm{LO},1} \,, \qquad \Sigma_{\mathrm{NLO\ QCD}} \equiv \Sigma_{\mathrm{NLO},1} \,, \tag{A.3}$$

$$\Sigma_{\mathrm{NNLO\ QCD}} \equiv \Sigma_{\mathrm{NNLO},1} \,, \qquad \Sigma_{\mathrm{QCD}} \equiv \Sigma_{\mathrm{LO\ QCD}} + \Sigma_{\mathrm{NLO\ QCD}} + \Sigma_{\mathrm{NNLO\ QCD}} \tag{A.4}$$

and those involving EW corrections

$$\Sigma_{\mathrm{LO\ EW}} \equiv \Sigma_{\mathrm{LO},2} \,, \qquad \Sigma_{\mathrm{res}} \equiv \Sigma_{\mathrm{LO},3} + \Sigma_{\mathrm{NLO},3} + \Sigma_{\mathrm{NLO},4} \,, \tag{A.5}$$

$$\Sigma_{\mathrm{NLO\ EW}} \equiv \Sigma_{\mathrm{NLO},2} \,, \qquad \Sigma_{\mathrm{EW}} \equiv \Sigma_{\mathrm{LO\ EW}} + \Sigma_{\mathrm{NLO\ EW}} + \Sigma_{\mathrm{res}} \,. \tag{A.6}$$

Throughout this work with the term “EW corrections” we refer to the quantity $\Sigma_{\mathrm{EW}}$, while the term “NLO EW corrections” will only refer to $\Sigma_{\mathrm{NLO\ EW}}$.

In the additive approach, which is presented in section 2.5.1, QCD and electroweak corrections are combined through the linear combination

$$\Sigma_{\rm QCD+EW} \equiv \Sigma_{\rm QCD} + \Sigma_{\rm EW}\,. \tag{A.7}$$

The so called "multiplicative approach", which has been discussed in sec. 2.5.1, is precisely defined in the following. The purpose of the multiplicative approach is to estimate the size of $\Sigma_{\rm NNLO,2}$, which for convenience we rename $\Sigma_{\rm mixed}$ and assuming complete factorisation of NLO QCD and NLO EW effects we estimate as

$$\Sigma_{\rm mixed} \equiv \Sigma_{\rm NNLO,2} \sim \Sigma_{\rm NLO\ QCD} \times \Sigma_{\rm NLO\ EW}\,. \tag{A.8}$$

In the regime where NLO QCD corrections are dominated by soft interactions and NLO EW by Sudakov logarithms, eq. (A.8) is a very good approximation, since the two effects factorise and are dominant. In other regimes $\Sigma_{\rm mixed}$ can be used as an estimate of the leading missing mixed QCD–EW higher orders. The advantage of the inclusion of $\Sigma_{\rm mixed}$ is the stabilisation of the scale dependence of the term $\Sigma_{\rm NLO\ EW}$, which in $t\bar{t}$ production has almost [40] the same functional form of of $\Sigma_{\rm LO\ QCD}$. To this end we define the multiplicative approach as

$$\begin{aligned}
\Sigma_{\rm QCD\times EW} &\equiv K^{\rm NLO}_{\rm EW}\ (\Sigma_{\rm LO\ QCD} + \Sigma_{\rm NLO\ QCD}) + \Sigma_{\rm LO\ EW} + \Sigma_{\rm NNLO\ QCD} + \Sigma_{\rm res} && \text{(A.9)}\\
&= K^{\rm NLO}_{\rm QCD}\ (\Sigma_{\rm LO\ QCD} + \Sigma_{\rm NLO\ EW}) + \Sigma_{\rm LO\ EW} + \Sigma_{\rm NNLO\ QCD} + \Sigma_{\rm res} && \text{(A.10)}\\
&= \Sigma_{\rm QCD} + K^{\rm NLO}_{\rm QCD}\ \Sigma_{\rm NLO\ EW} + \Sigma_{\rm LO\ EW} + \Sigma_{\rm res} && \text{(A.11)}\\
&= \Sigma_{\rm QCD+EW} + (K^{\rm NLO}_{\rm QCD} - 1) \times \Sigma_{\rm NLO\ EW} && \text{(A.12)}\\
&\sim \Sigma_{\rm QCD+EW} + \Sigma_{\rm mixed}\,, && \text{(A.13)}
\end{aligned}$$

where we used the standard $K$-factors

$$K^{\rm NLO}_{\rm QCD} \equiv \frac{\Sigma_{\rm LO\ QCD} + \Sigma_{\rm NLO\ QCD}}{\Sigma_{\rm LO\ QCD}}\,, \qquad K^{\rm NLO}_{\rm EW} \equiv \frac{\Sigma_{\rm LO\ QCD} + \Sigma_{\rm NLO\ EW}}{\Sigma_{\rm LO\ QCD}}\,. \tag{A.14}$$

In order to test the stability of the multiplicative approach under even higher mixed QCD-EW orders, we combine NNLO QCD corrections and NLO EW corrections in order to estimate, besides the $\Sigma_{\rm mixed}$ term, also NNNLO contributions of order $\alpha_s^4\alpha$. For this purpose we define the quantity

$$\Sigma_{\rm QCD^2\times EW} \equiv K^{\rm NLO}_{\rm EW}\ \Sigma_{\rm QCD} + \Sigma_{\rm LO\ EW} + \Sigma_{\rm res} \tag{A.15}$$

---

[40] We say "almost" because this order receives also QCD corrections to the $\Sigma_{\rm LO\ EW}$ contributions from the $g\gamma$ and $b\bar{b}$ initial states. Besides these effects $\Sigma_{\rm NLO\ EW}(\mu_2) = \Sigma_{\rm NLO\ EW}(\mu_1)\frac{\Sigma_{\rm LO\ QCD}(\mu_2)}{\Sigma_{\rm LO\ QCD}(\mu_1)}$.

$$= K^{\mathrm{NNLO}}_{\mathrm{QCD}} \left(\Sigma_{\mathrm{LO~QCD}} + \Sigma_{\mathrm{NLO~EW}}\right) + \Sigma_{\mathrm{LO~EW}} + \Sigma_{\mathrm{res}} \tag{A.16}$$

$$= \Sigma_{\mathrm{QCD}} + K^{\mathrm{NNLO}}_{\mathrm{QCD}}\, \Sigma_{\mathrm{NLO~EW}} + \Sigma_{\mathrm{LO~EW}} + \Sigma_{\mathrm{res}} \tag{A.17}$$

$$= \Sigma_{\mathrm{QCD+EW}} + (K^{\mathrm{NNLO}}_{\mathrm{QCD}} - 1) \times \Sigma_{\mathrm{NLO~EW}}\,, \tag{A.18}$$

where we introduced the $K$-factor

$$K^{\mathrm{NNLO}}_{\mathrm{QCD}} \equiv \frac{\Sigma_{\mathrm{QCD}}}{\Sigma_{\mathrm{LO~QCD}}}\,. \tag{A.19}$$

Finally, we briefly describe how the dependence on the photon PDF enters the different perturbative orders. At LO and NLO accuracy, all the contributions, with the exception of $\Sigma_{\mathrm{LO~QCD}}$ and the $\Sigma_{\mathrm{NLO~QCD}}$, depend on the photon PDF. The dominant photon-induced initial state is the $g\gamma \to t\bar{t}$ process, which contributes to $\Sigma_{\mathrm{LO~EW}}$ and, via QCD corrections to this order, to $\Sigma_{\mathrm{NLO~EW}}$. In addition, $\Sigma_{\mathrm{NLO~EW}}$, but also $\Sigma_{\mathrm{NLO},3}$ and $\Sigma_{\mathrm{NLO},4}$, receive contributions from the $q\gamma \to t\bar{t}q$ and $\bar{q}\gamma \to t\bar{t}\bar{q}$ processes. Moreover, in the case of $\Sigma_{\mathrm{LO},3}$ and $\Sigma_{\mathrm{NLO},4}$, also the $\gamma\gamma$ initial state contributes. As already discussed in ref. [9], almost all the photon-induced contribution arises form $\Sigma_{\mathrm{LO~EW}}$. In this work, at variance with ref. [9], we also include the term $\Sigma_{\mathrm{res}}$ in our calculation. However, since the size of $\Sigma_{\mathrm{res}}$ is in general small, the previous argument still applies. The numerical impact of $\Sigma_{\mathrm{res}}$ is discussed in sec. 2.5.2.

Given the structure of the photon-induced contributions described before, it is also important to note that, with LUXQED, the multiplicative approach is a better approximation of $\Sigma_{\mathrm{mixed}}$ than in the case of NNPDF3.0QED. Indeed, the order $\Sigma_{\mathrm{NLO~EW}}$ contains also terms that can be seen as "QCD corrections" to the $g\gamma$ contributions in $\Sigma_{\mathrm{LO},2}$ (negligible only with the LUXQED), but are not taken into account in the multiplicative approach.

# B | Appendix for chapter 3

## B.1 FxFx merging for the $t\bar{t}W^{\pm}$ process

In order to clarify the role of the FxFx merging for the $p_T(t\bar{t})$ distribution (fig. 3.6), we realise it for the $t\bar{t}W^{\pm}$ process. The FxFx merging is the extension of the MLM merging. The latter is used for merging LO samples of different multiplicities. The complexity in FxFx increases, because now the samples to be merged already include QCD corrections. For the case of $t\bar{t}W^{\pm}$, we want to merge the 0- and 1-jet multiplicity samples, both being at NLO in QCD. The MADGRAPH5_AMC@NLO command line for this is the following

```
import model loop_sm-no_b_mass
define w = w+ w-
generate p p > t t~ w [QCD] @0
add process p p > t t~ w j [QCD] @1
```

The FxFx merging is done for the Higgs as well as for the $t\bar{t}$ production in [157]. In this work the merging scale for the Higgs production is chosen to be $\mu_Q = 50$ GeV and for the $t\bar{t}$ production is set to $\mu_Q = 100$ GeV. Naturally one would expect that for the $t\bar{t}V$ processes, a scale of $\mu_Q \sim 150$ GeV would provide a smooth transition between the two multiplicities. This is indeed true for the $t\bar{t}H$ process. In figure B.1, we can see that both the differential jet rate plot and the $p_T$ of the leading jet are smooth for the merging scale $\mu_Q = 150$ GeV. In the insets of these plots we show the ratio of the merged sample between two different scales. In this inset we can see that a choice of $\mu_Q = 100$ GeV would lead to an unphysical 'kink' at the $p_T(j_1) = 100$ GeV region. For the $t\bar{t}W^{\pm}$ process the picture is quite different. We have verified that choosing

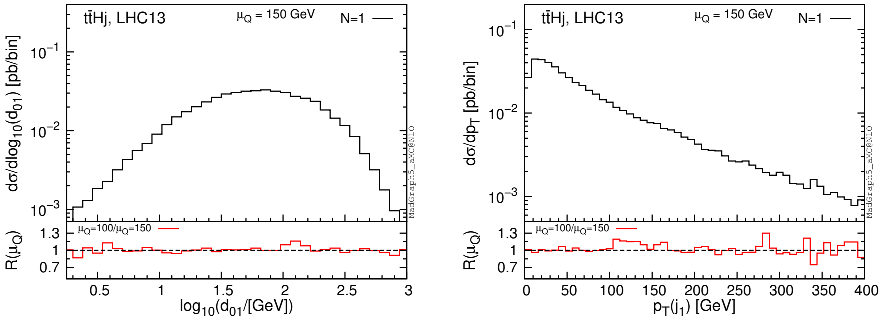

Figure B.1: Differential jet rate and $p_T(j_1)$ distributions for the $t\bar{t}H$ process merged at NLO in QCD up to 1-jet multiplicities (N=1).

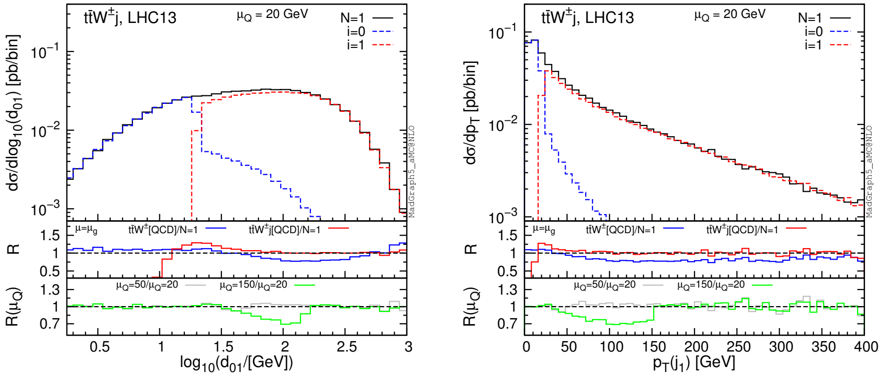

Figure B.2: Differential jet rate and $p_T(j_1)$ distributions for the $t\bar{t}W^{\pm}$ process merged at NLO in QCD up to 1-jet multiplicities (N=1).

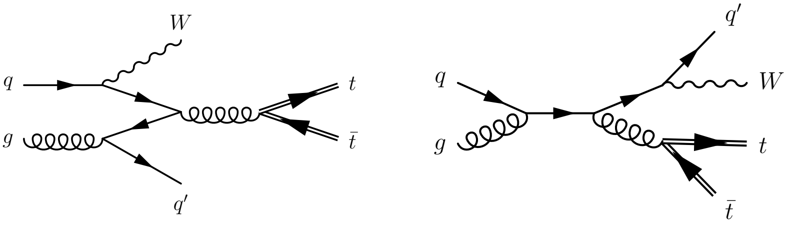

Figure B.3: Real emission NLO Feynman diagrams for $t\bar{t}W^{\pm}$. Left: the extra parton appears as ISR and it is not attached to the $W$ boson. Right: the extra parton appears as FSR to $t\bar{t}$ and it radiates the $W$ boson.

any scale between $100 < \mu_Q < 200$ GeV, the transition in the corresponding distributions is not smooth. In order to achieve smooth differential jet rate and $p_T(j_1)$ distributions for the $t\bar{t}W^{\pm}$ process, one has to chose a very low merging scale. This is shown if figure B.2. In this figure we show the same as in figure B.1 for $\mu_Q = 20$ GeV and we see that in this case the distributions are smooth. In the main panel we further disentangle the 0- and 1- jet multiplicities (dashed blue and dashed red respectively) following the recipe of [157]. In the first inset we compare the merged sample (N=1) with the pure independent samples of $t\bar{t}W$@NLO (solid blue) and $t\bar{t}Wj$@NLO (solid red), generated with the geometrical average factorisation and renormalisation scale. As expected, after the $\mu_Q$ value the merged (N=1) distribution of $p_T(j_1)$ is better described by the $t\bar{t}Wj$@NLO. In the second inset we show the ratio of the merged sample for different $\mu_Q$'s. We see that for $\mu_Q = 50$ GeV (gray) the results are similar, but for $\mu_Q = 150$ GeV (green) there is a large discontinuity appearing in both

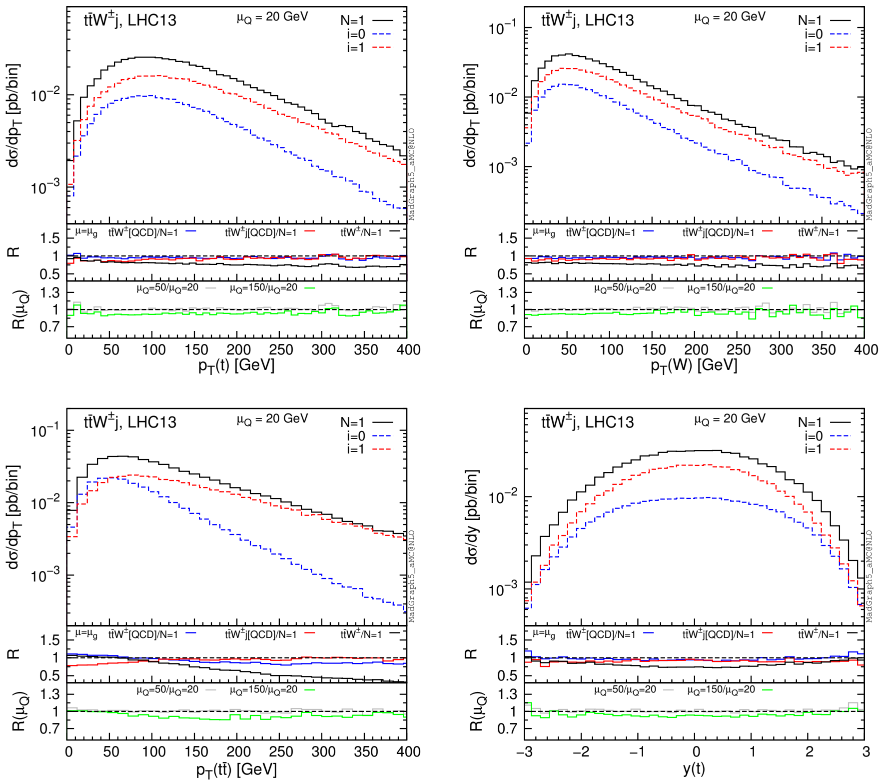

Figure B.4: Differential distributions of the FxFx merged $t\bar{t}W^{\pm}j$@NLO sample, in comparison with the pure $t\bar{t}W^{\pm}$@NLO, $t\bar{t}W^{\pm}j$@NLO and $t\bar{t}W^{\pm}$@LO ones.

distributions. This feature is related to the peculiarity of the $t\bar{t}W^{\pm}$ process itself. The absence of $gg$ channels up to NNLO in combination with the opening of the $qg$ channel at NLO (fig. B.3), forces these diagrams to have a significant contribution. In the merging procedure, these diagrams enter only above the merging scale and their contribution below the $\mu_Q$ is missed. Furthermore in diagrams of the form of the fig. B.3-left, the extra emission is attached to a QCD vertex (QCD jet). As a result, in the collinear limit, the extra emission can be factored out and described by a splitting function in the parton shower as $t\bar{t}Wq' \sim t\bar{t}W \times P_{q'g}$. However this kind of factorisation cannot be done in the diagrams of the form of fig. B.3-right, because the extra emission is attached to an EW vertex (EW jet) and on top of that it is always finite since it is regulated by the mass of the $W$ boson. These finite contributions are lost below the $\mu_Q$ value and that is why se see this deep reduction of the green line ($\mu_Q = 150$ GeV) in the second inset of the figure B.2-right. The only way to include these contributions throughout the whole phase space is to choose a low merging scale. In figure B.4, we show representative distributions for the process. The format is the same as for figure B.2, but in the first inset we further add the $t\bar{t}W$@LO line (solid black). From the first inset we see that the $pT(t), pT(W), y(t)$ distributions are already well described by the pure NLO samples. However with the FxFx merging the $pT(t\bar{t})$ distribution is described by the $t\bar{t}W^{\pm}j$@NLO for $pT(t\bar{t}) \gtrapprox m_W$ and by the $t\bar{t}W^{\pm}$@NLO for $pT(t\bar{t}) \lessapprox m_W$. Given that the $t\bar{t}W^{\pm}j$@NLO sample includes also the $gg$ channel for the first time, this prescription is the correct way to describe this observable correctly for the full phase space.

This feature of the EW jet is absent in the $t\bar{t}H$ process, since the Higgs can be emitted only from the top quarks. Furthermore for the $t\bar{t}H, t\bar{t}Z, t\bar{t}\gamma$ processes the $qg$ channel does also open up at NLO, but they all have the $gg$ channel already from the LO, therefore it is suppressed. However, the EW jet diagrams are present also in $t\bar{t}Z, t\bar{t}\gamma$ processes, so in principle a small error is expected also there if one choses a large merging scale for these processes. The global treatment of all $t\bar{t}V, t\bar{t}H$ processes with FxFx is to be realised within the near future, as an extension of what is shown here for the $t\bar{t}W^{\pm}$ process.

## B.2 $q_L\bar{q}_R \to t\bar{t}$ vs $q\bar{q} \to t\bar{t}W^{\pm}$

We first review the main features of polarised $q_L\bar{q}_R \to t\bar{t}$ scattering, on the same lines as $e^-_L e^+_R \to t\bar{t}$ is discussed in Ref. [198]. In the beam line basis, *i.e.*, when the polarization axis of the top is the light antiquark direction in the top rest frame, the polarised differential cross sections $d\sigma_{t\mathrm{pol},\bar{t}\mathrm{pol}}$ for an initial state $q_L\ \bar{q}_R$ pair read

$$\begin{aligned}
\frac{d\sigma_{\uparrow\uparrow}}{d\cos\theta^*} &= \frac{d\sigma_{\downarrow\downarrow}}{d\cos\theta^*} = \mathcal{N}(\beta)\frac{\beta^2(1-\beta^2)\sin^2\theta^*}{(1+\beta\cos\theta^*)^2}\,,\\
\frac{d\sigma_{\downarrow\uparrow}}{d\cos\theta^*} &= \mathcal{N}(\beta)\ \frac{\beta^4\sin^4\theta^*}{(1+\beta\cos\theta^*)^2}\,,\\
\frac{d\sigma_{\uparrow\downarrow}}{d\cos\theta^*} &= \mathcal{N}(\beta)\frac{[(1+\beta\cos\theta^*)^2+(1-\beta^2)]^2}{(1+\beta\cos\theta^*)^2}\,,
\end{aligned} \tag{B.1}$$

where $\mathcal{N}(\beta)$ is a normalization factor

$$\mathcal{N}(\beta) = \frac{\pi\alpha_S^2}{9s}\beta\,, \tag{B.2}$$

and $\cos\theta^*$ is the polar angle of the top quarks in parton-parton centre-of-mass frame. This basis is useful both at threshold, ($\beta \to 0$), where it is clear that only one amplitude, $q_L\bar{q}_R \to t_\uparrow\bar{t}_\downarrow$ is non-zero, meaning that the top quarks are completely polarised, and at high energy, ($\beta \to 1$), where it is manifest that the top anti-top polarizations are opposite,

$$\frac{d\sigma_{\uparrow\downarrow,\downarrow\uparrow}}{d\cos\theta^*} \overset{\beta\to 1}{=} \mathcal{N}(1)(1 \pm \cos\theta^*)^2\,, \tag{B.3}$$

a result which is also valid in the helicity basis [198]. Eq. B.3 predicts the total number of events with opposite top anti-top polarization to be the same far from threshold. The polarization information is transferred to the decay products angular distributions, and in particular to the leptons that are 100% correlated with the top-quark spins. One therefore expects the lepton polar distributions with respect to the beam axis to show a linear dependence in $\cos\theta_e$ at threshold that flattens out at high energies.

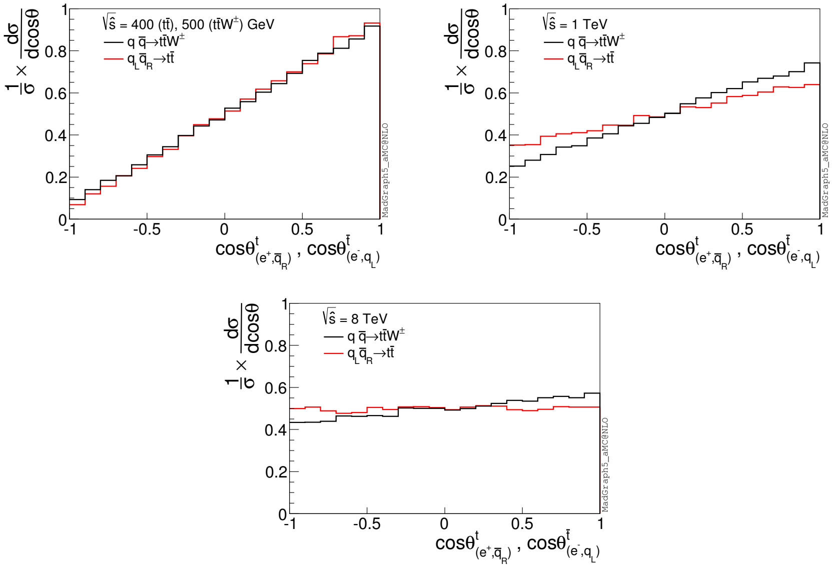

Figure B.5: Normalized $\cos\theta$ distributions for the leptons with respect to the spin axis for the $t, \bar{t}$ defined in the beam-axis as in Ref. [198] at different parton-parton energies (no PDF's). Close to threshold, *i.e.* 400 GeV for $t\bar{t}$ and 500 GeV for $t\bar{t}W^\pm$, the $t$ and $\bar{t}$ are fully polarised. As the energy increases the distribution flattens out up to a constant at very high energies in agreement with eq. B.3.

We have explicitly checked the expressions eq. B.1. Apart from more complicated analytic formulas the case of $q\bar{q} \to t\bar{t}W^\pm$ is totally analogous, as

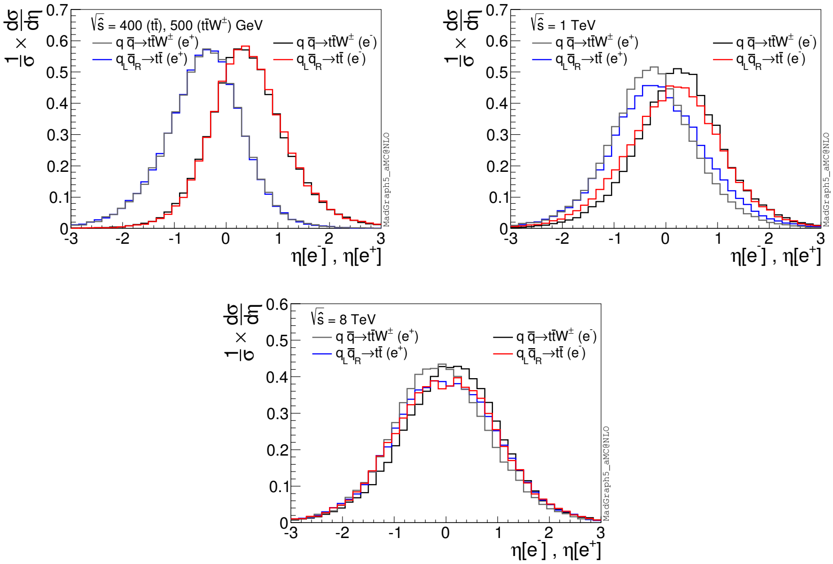

Figure B.6: Normalized pseudorapidity distributions in the $t\bar{t}$ center of mass frame. Close to threshold, *i.e.* 400 GeV for $t\bar{t}$ and 500 GeV for $t\bar{t}W^{\pm}$ full polarization of $t$ and $\bar{t}$ determines a sizable opposite asymmetry in the distributions of the $e^{+}$ and $e^{-}$. Far from threshold, the distribution becomes more and more symmetric.

the only non-trivial effect of the $W$-boson emission is that of selecting a $q_L\bar{q}_R$ in the initial state.

This is clearly shown in Figs. B.5 and B.6. In the first set of plots we show the lepton distributions from the top-quarks decay for both $q_L\bar{q}_R \to t\bar{t}$ and $q\bar{q} \to t\bar{t}W^{\pm}$ in the beam-axis frame at three values of $\sqrt{\hat{s}}$, one close to threshold (400 GeV for $t\bar{t}$ and 500 GeV for $t\bar{t}W^{\pm}$) and increasingly far from threshold (1 and 8 TeV). The two processes lead to very similar distributions. We have then considered the pseudorapidity distributions in the $t\bar{t}$ rest frame. We find that the $t$ and the $\bar{t}$ pseudorapidity distributions are equal and symmetric at LO and we do not show them. The lepton distributions, however, see Fig. B.6, display an opposite and equal forward-backward asymmetry whose shapes in the centre-of-mass frame of the $t\bar{t}$ pair are again extremely similar in $q_L\bar{q}_R \to t\bar{t}$ and $q\bar{q} \to t\bar{t}W^{\pm}$. The fact that the asymmetry is larger at threshold is a direct consequence of the fact that there the top quarks are fully polarised.

# C | Appendix for chapter 4

## C.1 Connection with "anomalous coupling" approach

In order to compare with other work in the literature, we present here the connection of the Wilson coefficients with the top quark anomalous couplings.

The anomalous coupling approach is followed in [175, 176] where the $t\bar{t}Z$ process is used to probe anomalous top couplings. Compared with the anomalous coupling parametrisation of the $\bar{t}tZ$ vertex,

$$\mathcal{L}_{ttZ} = e\bar{u}(p_t)\left[\gamma^\mu\left(C_{1,V}^Z + \gamma_5 C_{1,A}^Z\right) + \frac{i\sigma^{\mu\nu}q_\nu}{m_Z}\left(C_{2,V}^Z + i\gamma_5 C_{2,A}^Z\right)\right]v(p_{\bar{t}})Z_\mu \tag{C.1}$$

the relation between anomalous couplings and Wilson coefficients are:

$$C_{1,V}^Z = \frac{1}{2}\left(C_{\varphi Q}^{(3)} - C_{\varphi Q}^{(1)} - C_{\varphi t}\right)\frac{m_t^2}{\Lambda^2 s_W c_W} \tag{C.2}$$

$$C_{1,A}^Z = \frac{1}{2}\left(-C_{\varphi Q}^{(3)} + C_{\varphi Q}^{(1)} - C_{\varphi t}\right)\frac{m_t^2}{\Lambda^2 s_W c_W} \tag{C.3}$$

$$C_{2,V}^Z = \left(C_{tW}c_W^2 - C_{tB}s_W^2\right)\frac{2m_t m_Z}{\Lambda^2 s_W c_W} \tag{C.4}$$

$$C_{2,A}^Z = 0 \tag{C.5}$$

Similar relations for the top photon interactions are:

$$\mathcal{L}_{tt\gamma} = e\bar{u}(p_t)\left[Q_t\gamma^\mu + \frac{i\sigma^{\mu\nu}q_\nu}{m_Z}\left(C_{2,V}^\gamma + i\gamma_5 C_{2,A}^\gamma\right)\right]v(p_{\bar{t}})A_\mu \tag{C.6}$$

$$C_{2,V}^\gamma = \left(C_{tW} + C_{tB}\right)\frac{2m_t m_Z}{\Lambda^2} \tag{C.7}$$

$$C_{2,A}^\gamma = 0 \tag{C.8}$$

The CP-odd operators are zero simply because we have assumed $C_{tW}$ and $C_{tB}$ are real.

# C.2 Ratios for comparing with measurements

## C.2.1 ATLAS - $t\bar{t}Z$

The SM prediction employed by ATLAS for the $t\bar{t}Z$ process [169] also contains contribution of $t\bar{t}\gamma^*$ in the channel where the vector boson decays into two charged leptons ($t\bar{t}l^+l^-$). The total prediction, here called $\sigma^{SM}_{ATLAS}(t\bar{t}Z)$, can be written in terms of the $t\bar{t}Z$ and $t\bar{t}l^+l^-$ processes as follows:

$$\sigma^{SM}_{ATLAS}(t\bar{t}Z) = \sigma^{SM}(t\bar{t}\ell^+\ell^-, m(\ell\ell) > 5 \text{ GeV}) + \sigma^{SM}(t\bar{t}Z) \times [1 - BR(Z \to \ell^+\ell^-)]\,. \tag{C.9}$$

The $BR(Z \to \ell^+\ell^-)$ is taken from MadSpin [150]. The branching ratio and the NLO cross sections including the absolute scale uncertainties, using our parameter settings, are

$$\begin{aligned}
&\sigma^{SM}(t\bar{t}\mu^+\mu^-, m(\ell\ell) > 5 \text{ GeV}) = 11.63(1)^{+1.00}_{-1.38} \text{ fb}\\
&\sigma^{SM}(t\bar{t}\mu^+\mu^-, m(\ell\ell) > 10 \text{ GeV}) = 9.83(1)^{+0.75}_{-1.13} \text{ fb}\\
&\sigma^{SM}(t\bar{t}Z) = 226.5(6)^{+15.1}_{-25.3} \text{ fb}\\
&BR(Z \to \ell^+\ell^-) = 0.1029\,.
\end{aligned}$$

Applying these results to Eq. C.9, the corresponding prediction when using the same scales, PDF sets and generation procedure as in this paper is:

$$\sigma^{SM}_{ATLAS}(t\bar{t}Z) = 238.1(6)^{+16.6}_{-26.8} \text{ fb}\,.$$

In order to compare our $t\bar{t}\mu^+\mu^-$ results with the ATLAS measurement we apply to the experimental result the $R^{t\bar{t}Z}_{ATLAS}$, defined as

$$R^{t\bar{t}Z}_{ATLAS} = \frac{\sigma^{SM}(t\bar{t}\mu^+\mu^-, m(\ell\ell) > 10 \text{ GeV})}{\sigma^{SM}_{ATLAS}(t\bar{t}Z)} = 0.0413(1)^{+0.0003}_{-0.0001}\,.$$

The corresponding value for 13 TeV is

$$R^{t\bar{t}Z,13\text{TeV}}_{ATLAS} = 0.0408(1)^{+0.0003}_{-0.0002}\,.$$

## C.2.2 CMS - $t\bar{t}\gamma$

The measurement of $t\bar{t}\gamma$ described in Ref. [165] should be compared with the $W^+bW^-\bar{b}\gamma$ SM cross section calculated with $p_T(\gamma) > 20$ GeV and $\Delta R(\gamma, b/\bar{b}) >$

0.1. Our $t\bar{t}\gamma$ results are with $p_T(\gamma) > 20$ GeV, but they do not include photon radiation from the $t, \bar{t}$ decay products $(W^{\pm}, b, \bar{b})$. For this reason the $R^{t\bar{t}\gamma}_{CMS}$ value is applied to the experimental result, defined at LO as follows

$$R^{t\bar{t}\gamma}_{CMS} = \frac{\sigma^{SM}(t\bar{t}\gamma, p_T(\gamma) > 20 \text{ GeV})}{\sigma^{SM}(W^+bW^-\bar{b}\gamma, p_T(\gamma) > 20 \text{ GeV}, \Delta R(\gamma, b/\bar{b}) > 0.1)} = 0.4531(4)^{+0.0015}_{-0.0011}\,.$$

The LO cross sections are

$$\sigma^{SM}(t\bar{t}\gamma, p_T(\gamma) > 20 \text{ GeV}) = 604.0(3)^{+234.1}_{-154.8} \text{ fb}$$
$$\sigma^{SM}(W^+bW^-\bar{b}\gamma, p_T(\gamma) > 20 \text{ GeV}, \Delta R(\gamma, b/\bar{b}) > 0.1) = 1333.0(9)^{+520.9}_{-344.9} \text{ fb}\,.$$

The corresponding value for 13 TeV is

$$R^{t\bar{t}\gamma,13\text{TeV}}_{CMS} = 0.4453(5)^{+0.0008}_{-0.0003}\,.$$

# Bibliography

[1] LEP Working Group for Higgs boson searches, R. Barate et al., *Search for the standard model Higgs boson at LEP*, *Phys. Lett.* **B565** (2003) 61–75, [hep-ex/0306033].

[2] Tevatron New Physics Higgs Working Group, *Updated Combination of CDF and D0 Searches for Standard Model Higgs Boson Production with up to 10.0 $fb^{-1}$ of Data*, 2012. 1207.0449.

[3] CDF, D0 collaboration, T. Aaltonen et al., *Evidence for a particle produced in association with weak bosons and decaying to a bottom-antibottom quark pair in Higgs boson searches at the Tevatron*, *Phys. Rev. Lett.* **109** (2012) 071804, [1207.6436].

[4] ATLAS collaboration, *Observation of an excess of events in the search for the Standard Model Higgs boson in the gamma-gamma channel with the ATLAS detector*, ATLAS-CONF-2012-091 .

[5] CMS collaboration, S. Chatrchyan et al., *Observation of a new boson with mass near 125 GeV in pp collisions at $\sqrt{s} = 7$ and 8 TeV*, *JHEP* **06** (2013) 081, [1303.4571].

[6] F. Maltoni, M. Mangano, I. Tsinikos and M. Zaro, *Top-quark charge asymmetry and polarization in $t\bar{t}W^{\pm}$ production at the LHC*, *Phys.Lett.* **B736** (2014) 252–260, [1406.3262].

[7] F. Maltoni, D. Pagani and I. Tsinikos, *Associated production of a top-quark pair with vector bosons at NLO in QCD: impact on $t\bar{t}H$ searches at the LHC*, 1507.05640.

[8] O. Bessidskaia Bylund, F. Maltoni, I. Tsinikos, E. Vryonidou and C. Zhang, *Probing top quark neutral couplings in the Standard Model Effective Field Theory at NLO in QCD*, *JHEP* **05** (2016) 052, [1601.08193].

[9] D. Pagani, I. Tsinikos and M. Zaro, *The impact of the photon PDF and electroweak corrections on $t\bar{t}$ distributions*, *Eur. Phys. J.* **C76** (2016) 479, [1606.01915].

[10] M. Czakon, D. Heymes, A. Mitov, D. Pagani, I. Tsinikos and M. Zaro, *Top-pair production at the LHC through NNLO QCD and NLO EW*, 1705.04105.

[11] M. L. Mangano et al., *Physics at a 100 TeV pp collider: Standard Model processes*, 1607.01831.

[12] LHC Higgs Cross Section Working Group collaboration, D. de Florian et al., *Handbook of LHC Higgs Cross Sections: 4. Deciphering the Nature of the Higgs Sector*, 1610.07922.

[13] I. Tsinikos, *EW corrections to $t\bar{t}$ distributions: the photon PDF effect*, in *9th International Workshop on Top Quark Physics (TOP 2016) Olomouc, Czech Republic, September 19-23, 2016*, 2016. 1611.08234.

[14] M. E. Peskin and D. V. Schroeder, *An Introduction to quantum field theory.* 1995.

[15] M. D. Schwartz, *Quantum Field Theory and the Standard Model.* Cambridge University Press, 2014.

[16] E. Drexler, "Summary of interactions between particles described by the Standard Model." https://en.wikipedia.org/wiki/Standard_Model, 2014.

[17] P. W. Higgs, *Broken Symmetries and the Masses of Gauge Bosons*, *Phys. Rev. Lett.* **13** (1964) 508–509.

[18] T. Rias, "Cabibbo-Kobayashi-Maskawa matrix." https://en.wikipedia.org/wiki/Cabibbo-Kobayashi-Maskawa_matrix, 2008.

[19] S. Willenbrock, *The Standard model and the top quark*, *NATO Sci. Ser. II* **123** (2003) 1–41, [`hep-ph/0211067`].

[20] R. K. Ellis, W. J. Stirling and B. R. Webber, *QCD and collider physics*, *Camb. Monogr. Part. Phys. Nucl. Phys. Cosmol.* **8** (1996) 1–435.

[21] J. H. Kuhn and G. Rodrigo, *Charge asymmetry of heavy quarks at hadron colliders*, *Phys. Rev.* **D59** (1999) 054017, [`hep-ph/9807420`].

[22] CMS collaboration, V. Khachatryan et al., *Measurement of the inclusive 3-jet production differential cross section in proton?proton collisions at 7 TeV and determination of the strong coupling constant in the TeV range*, *Eur. Phys. J.* **C75** (2015) 186, [`1412.1633`].

[23] T. Kinoshita, *Mass singularities of Feynman amplitudes*, *J. Math. Phys.* **3** (1962) 650–677.

[24] T. D. Lee and M. Nauenberg, *Degenerate Systems and Mass Singularities*, *Phys. Rev.* **133** (1964) B1549–B1562.

[25] I. J. R. Aitchison and A. J. G. Hey, *Gauge theories in particle physics: A practical introduction. Vol. 2: Non-Abelian gauge theories: QCD and the electroweak theory.* 2004.

[26] S. Höche, *Introduction to parton-shower event generators*, in *Theoretical Advanced Study Institute in Elementary Particle Physics: Journeys Through the Precision Frontier: Amplitudes for Colliders (TASI 2014) Boulder, Colorado, June 2-27, 2014*, 2014. `1411.4085`.

[27] A. D. Martin, W. J. Stirling, R. S. Thorne and G. Watt, *Parton distributions for the LHC*, *Eur. Phys. J.* **C63** (2009) 189–285, [`0901.0002`].

[28] Y. L. Dokshitzer, *Calculation of the Structure Functions for Deep Inelastic Scattering and e+ e- Annihilation by Perturbation Theory in Quantum Chromodynamics.*, *Sov. Phys. JETP* **46** (1977) 641–653.

[29] V. N. Gribov and L. N. Lipatov, *Deep inelastic e p scattering in perturbation theory*, *Sov. J. Nucl. Phys.* **15** (1972) 438–450.

[30] G. Altarelli and G. Parisi, *Asymptotic Freedom in Parton Language*, *Nucl. Phys.* **B126** (1977) 298–318.

[31] R. J. Holt and C. D. Roberts, *Distribution Functions of the Nucleon and Pion in the Valence Region*, *Rev. Mod. Phys.* **82** (2010) 2991–3044, [`1002.4666`].

[32] J. Alwall, R. Frederix, S. Frixione, V. Hirschi, F. Maltoni, O. Mattelaer et al., *The automated computation of tree-level and next-to-leading order differential cross sections, and their matching to parton shower simulations*, *JHEP* **07** (2014) 079, [`1405.0301`].

[33] R. Frederix, S. Frixione, F. Maltoni and T. Stelzer, *Automation of next-to-leading order computations in QCD: The FKS subtraction*, *JHEP* **0910** (2009) 003, [`0908.4272`].

[34] G. Ossola, C. G. Papadopoulos and R. Pittau, *CutTools: A Program implementing the OPP reduction method to compute one-loop amplitudes*, *JHEP* **0803** (2008) 042, [`0711.3596`].

[35] V. Hirschi, R. Frederix, S. Frixione, M. V. Garzelli, F. Maltoni et al., *Automation of one-loop QCD corrections*, *JHEP* **1105** (2011) 044, [`1103.0621`].

[36] F. Cascioli, P. Maierhofer and S. Pozzorini, *Scattering Amplitudes with Open Loops*, *Phys.Rev.Lett.* **108** (2012) 111601, [`1111.5206`].

[37] C. Degrande, C. Duhr, B. Fuks, D. Grellscheid, O. Mattelaer and T. Reiter, *UFO - The Universal FeynRules Output*, *Comput. Phys. Commun.* **183** (2012) 1201–1214, [`1108.2040`].

[38] A. Alloul, N. D. Christensen, C. Degrande, C. Duhr and B. Fuks, *FeynRules 2.0 - A complete toolbox for tree-level phenomenology*, `1310.1921`.

[39] P. de Aquino, W. Link, F. Maltoni, O. Mattelaer and T. Stelzer, *ALOHA: Automatic Libraries Of Helicity Amplitudes for Feynman Diagram Computations*, *Comput.Phys.Commun.* **183** (2012) 2254–2263, [`1108.2041`].

[40] S. Frixione, V. Hirschi, D. Pagani, H. S. Shao and M. Zaro, *Weak corrections to Higgs hadroproduction in association with a top-quark pair*, *JHEP* **09** (2014) 065, [`1407.0823`].

[41] S. Frixione, V. Hirschi, D. Pagani, H. S. Shao and M. Zaro, *Electroweak and QCD corrections to top-pair hadroproduction in association with heavy bosons*, *JHEP* **06** (2015) 184, [`1504.03446`].

[42] C. Zhang, *Automating Predictions for Standard Model Effective Field Theory in MadGraph5_ aMC@NLO*, in *Proceedings, 12th International Symposium on Radiative Corrections (Radcor 2015) and LoopFest XIV (Radiative Corrections for the LHC and Future Colliders)*, 2016. `1601.03994`.

[43] S. Frixione and B. R. Webber, *Matching NLO QCD computations and parton shower simulations*, *JHEP* **0206** (2002) 029, [`hep-ph/0204244`].

[44] T. Sjostrand, S. Mrenna and P. Z. Skands, *PYTHIA 6.4 Physics and Manual*, *JHEP* **0605** (2006) 026, [`hep-ph/0603175`].

[45] T. Sjostrand, S. Mrenna and P. Z. Skands, *A Brief Introduction to PYTHIA 8.1*, *Comput.Phys.Commun.* **178** (2008) 852–867, [`0710.3820`].

[46] G. Corcella, I. Knowles, G. Marchesini, S. Moretti, K. Odagiri et al., *HERWIG 6: An Event generator for hadron emission reactions with interfering gluons (including supersymmetric processes)*, *JHEP* **0101** (2001) 010, [`hep-ph/0011363`].

[47] M. Bahr, S. Gieseke, M. Gigg, D. Grellscheid, K. Hamilton et al., *Herwig++ Physics and Manual*, *Eur.Phys.J.* **C58** (2008) 639–707, [`0803.0883`].

[48] ATLAS, CDF, CMS, D0 collaboration, *First combination of Tevatron and LHC measurements of the top-quark mass*, `1403.4427`.

[49] M. Kobayashi and T. Maskawa, *CP Violation in the Renormalizable Theory of Weak Interaction*, *Prog. Theor. Phys.* **49** (1973) 652–657.

[50] CDF collaboration, F. Abe et al., *Observation of top quark production in $\bar{p}p$ collisions*, *Phys. Rev. Lett.* **74** (1995) 2626–2631, [`hep-ex/9503002`].

[51] D0 collaboration, S. Abachi et al., *Search for high mass top quark production in $p\bar{p}$ collisions at $\sqrt{s} = 1.8$ TeV*, *Phys. Rev. Lett.* **74** (1995) 2422–2426, [`hep-ex/9411001`].

[52] W. Bernreuther, *Top quark physics at the LHC*, *J. Phys.* **G35** (2008) 083001, [`0805.1333`].

[53] A. Quadt, *Top quark physics at hadron colliders*, *Eur. Phys. J.* **C48** (2006) 835–1000.

[54] Particle Data Group collaboration, K. A. Olive et al., *Review of Particle Physics*, *Chin. Phys.* **C38** (2014) 090001.

[55] CDF collaboration, T. A. Aaltonen et al., *Direct Measurement of the Total Decay Width of the Top Quark*, *Phys. Rev. Lett.* **111** (2013) 202001, [`1308.4050`].

[56] H. S. Do, S. Groote, J. G. Korner and M. C. Mauser, *Electroweak and finite width corrections to top quark decays into transverse and longitudinal W bosons*, *Phys. Rev.* **D67** (2003) 091501, [`hep-ph/0209185`].

[57] J. Alwall, R. Frederix, J. M. Gerard, A. Giammanco, M. Herquet, S. Kalinin et al., *Is $V(_{tb}) \simeq 1$?*, *Eur. Phys. J.* **C49** (2007) 791–801, [`hep-ph/0607115`].

[58] M. Czakon, P. Fiedler and A. Mitov, *Total Top-Quark Pair-Production Cross Section at Hadron Colliders Through $O(\alpha_S^4)$*, *Phys. Rev. Lett.* **110** (2013) 252004, [`1303.6254`].

[59] R. Bonciani, S. Catani, M. L. Mangano and P. Nason, *NLL resummation of the heavy quark hadroproduction cross-section*, *Nucl. Phys.* **B529** (1998) 424–450, [`hep-ph/9801375`].

[60] A. B. Galtieri, F. Margaroli and I. Volobouev, *Precision measurements of the top quark mass from the Tevatron in the pre-LHC era*, *Rept. Prog. Phys.* **75** (2012) 056201, [`1109.2163`].

[61] CMS collaboration, M. Dünser, *Measurements of the top-quark mass and properties at CMS*, *J. Phys. Conf. Ser.* **623** (2015) 012011.

[62] A. V. Manohar, *Effective field theories*, *Lect. Notes Phys.* **479** (1997) 311–362, [`hep-ph/9606222`].

[63] A. Pich, *Effective field theory: Course*, in *Probing the standard model of particle interactions. Proceedings, Summer School in Theoretical Physics, NATO Advanced Study Institute, 68th session, Les Houches, France, July 28-September 5, 1997. Pt. 1, 2*, pp. 949–1049, 1998. `hep-ph/9806303`.

[64] W. Skiba, *Effective Field Theory and Precision Electroweak Measurements*, in *Physics of the large and the small, TASI 09, proceedings of the Theoretical Advanced Study Institute in Elementary Particle Physics, Boulder, Colorado, USA, 1-26 June 2009*, pp. 5–70, 2011. `1006.2142`. .

[65] W. Buchmuller and D. Wyler, *Effective Lagrangian Analysis of New Interactions and Flavor Conservation*, *Nucl. Phys.* **B268** (1986) 621–653.

[66] B. Grzadkowski, M. Iskrzynski, M. Misiak and J. Rosiek, *Dimension-Six Terms in the Standard Model Lagrangian*, *JHEP* **10** (2010) 085, [`1008.4884`].

[67] C. Englert and M. Spannowsky, *Effective Theories and Measurements at Colliders*, *Phys. Lett.* **B740** (2015) 8–15, [`1408.5147`].

[68] M. Czakon, D. Heymes and A. Mitov, *High-precision differential predictions for top-quark pairs at the LHC*, *Phys. Rev. Lett.* **116** (2016) 082003, [`1511.00549`].

[69] S. Moch and P. Uwer, *Theoretical status and prospects for top-quark pair production at hadron colliders*, *Phys. Rev.* **D78** (2008) 034003, [`0804.1476`].

[70] N. Kidonakis, *Two-loop soft anomalous dimensions and NNLL resummation for heavy quark production*, *Phys. Rev. Lett.* **102** (2009) 232003, [`0903.2561`].

[71] M. Czakon, A. Mitov and G. F. Sterman, *Threshold Resummation for Top-Pair Hadroproduction to Next-to-Next-to-Leading Log*, *Phys. Rev.* **D80** (2009) 074017, [`0907.1790`].

[72] V. Ahrens, A. Ferroglia, M. Neubert, B. D. Pecjak and L. L. Yang, *Renormalization-Group Improved Predictions for Top-Quark Pair Production at Hadron Colliders*, *JHEP* **09** (2010) 097, [`1003.5827`].

[73] M. Beneke, P. Falgari and C. Schwinn, *Threshold resummation for pair production of coloured heavy (s)particles at hadron colliders*, *Nucl. Phys.* **B842** (2011) 414–474, [`1007.5414`].

[74] N. Kidonakis, *Next-to-next-to-leading soft-gluon corrections for the top quark cross section and transverse momentum distribution*, *Phys. Rev.* **D82** (2010) 114030, [`1009.4935`].

[75] V. Ahrens, A. Ferroglia, M. Neubert, B. D. Pecjak and L.-L. Yang, *RG-improved single-particle inclusive cross sections and forward-backward asymmetry in $t\bar{t}$ production at hadron colliders*, *JHEP* **09** (2011) 070, [`1103.0550`].

[76] V. Ahrens, A. Ferroglia, M. Neubert, B. D. Pecjak and L. L. Yang, *Precision predictions for the t+t(bar) production cross section at hadron colliders*, *Phys. Lett.* **B703** (2011) 135–141, [`1105.5824`].

[77] M. Beneke, P. Falgari, S. Klein and C. Schwinn, *Hadronic top-quark pair production with NNLL threshold resummation*, *Nucl. Phys.* **B855** (2012) 695–741, [`1109.1536`].

[78] M. Cacciari, M. Czakon, M. Mangano, A. Mitov and P. Nason, *Top-pair production at hadron colliders with next-to-next-to-leading logarithmic soft-gluon resummation*, *Phys. Lett.* **B710** (2012) 612–622, [`1111.5869`].

[79] M. Czakon, M. L. Mangano, A. Mitov and J. Rojo, *Constraints on the gluon PDF from top quark pair production at hadron colliders*, *JHEP* **07** (2013) 167, [`1303.7215`].

[80] B. D. Pecjak, D. J. Scott, X. Wang and L. L. Yang, *Resummed differential cross sections for top-quark pairs at the LHC*, *Phys. Rev. Lett.* **116** (2016) 202001, [`1601.07020`].

[81] W. Beenakker, A. Denner, W. Hollik, R. Mertig, T. Sack and D. Wackeroth, *Electroweak one loop contributions to top pair production in hadron colliders*, *Nucl. Phys.* **B411** (1994) 343–380.

[82] J. H. Kuhn, A. Scharf and P. Uwer, *Electroweak corrections to top-quark pair production in quark-antiquark annihilation*, *Eur. Phys. J.* **C45** (2006) 139–150, [`hep-ph/0508092`].

[83] W. Bernreuther, M. Fuecker and Z. G. Si, *Mixed QCD and weak corrections to top quark pair production at hadron colliders*, *Phys. Lett.* **B633** (2006) 54–60, [`hep-ph/0508091`].

[84] J. H. Kuhn, A. Scharf and P. Uwer, *Electroweak effects in top-quark pair production at hadron colliders*, *Eur. Phys. J.* **C51** (2007) 37–53, [`hep-ph/0610335`].

[85] W. Bernreuther, M. Fuecker and Z.-G. Si, *Weak interaction corrections to hadronic top quark pair production*, *Phys. Rev.* **D74** (2006) 113005, [`hep-ph/0610334`].

[86] W. Bernreuther, M. Fucker and Z.-G. Si, *Weak interaction corrections to hadronic top quark pair production: Contributions from quark-gluon and b anti-b induced reactions*, *Phys. Rev.* **D78** (2008) 017503, [`0804.1237`].

[87] A. V. Manohar and M. Trott, *Electroweak Sudakov Corrections and the Top Quark Forward-Backward Asymmetry*, *Phys. Lett.* **B711** (2012) 313–316, [`1201.3926`].

[88] J. H. Kühn, A. Scharf and P. Uwer, *Weak Interactions in Top-Quark Pair Production at Hadron Colliders: An Update*, *Phys. Rev.* **D91** (2015) 014020, [`1305.5773`].

[89] J. M. Campbell, D. Wackeroth and J. Zhou, *Electroweak Corrections at the LHC with MCFM*, *PoS* **DIS2015** (2015) 130, [`1508.06247`].

[90] W. Hollik and M. Kollar, *NLO QED contributions to top-pair production at hadron collider*, *Phys. Rev.* **D77** (2008) 014008, [`0708.1697`].

[91] W. Bernreuther and Z.-G. Si, *Distributions and correlations for top quark pair production and decay at the Tevatron and LHC.*, *Nucl. Phys.* **B837** (2010) 90–121, [`1003.3926`].

[92] W. Hollik and D. Pagani, *The electroweak contribution to the top quark forward-backward asymmetry at the Tevatron*, *Phys. Rev.* **D84** (2011) 093003, [`1107.2606`].

[93] J. H. Kuhn and G. Rodrigo, *Charge asymmetries of top quarks at hadron colliders revisited*, *JHEP* **01** (2012) 063, [`1109.6830`].

[94] W. Bernreuther and Z.-G. Si, *Top quark and leptonic charge asymmetries for the Tevatron and LHC*, *Phys. Rev.* **D86** (2012) 034026, [`1205.6580`].

[95] A. D. Martin, R. G. Roberts, W. J. Stirling and R. S. Thorne, *Parton distributions incorporating QED contributions*, *Eur. Phys. J.* **C39** (2005) 155–161, [`hep-ph/0411040`].

[96] NNPDF collaboration, R. D. Ball, V. Bertone, S. Carrazza, L. Del Debbio, S. Forte, A. Guffanti et al., *Parton distributions with QED corrections*, *Nucl. Phys.* **B877** (2013) 290–320, [`1308.0598`].

[97] C. Schmidt, J. Pumplin, D. Stump and C. P. Yuan, *CT14QED PDFs from Isolated Photon Production in Deep Inelastic Scattering*, `1509.02905`.

[98] A. Manohar, P. Nason, G. P. Salam and G. Zanderighi, *How bright is the proton? A precise determination of the photon PDF*, `1607.04266`.

[99] L. A. Harland-Lang, V. A. Khoze and M. G. Ryskin, *Photon-initiated processes at high mass*, `1607.04635`.

[100] CMS collaboration, *Comparisons of Theory Predictions for the* $t\bar{t}$ *Process with Data from pp Collisions at* $\sqrt{s}$= *8 TeV*, .

[101] M. Czakon, D. Heymes and A. Mitov, *Dynamical scales for multi-TeV top-pair production at the LHC*, `1606.03350`.

[102] NNPDF collaboration, R. D. Ball et al., *Parton distributions for the LHC Run II*, *JHEP* **04** (2015) 040, [`1410.8849`].

[103] D. de Florian, G. F. R. Sborlini and G. Rodrigo, *QED corrections to the Altarelli–Parisi splitting functions*, *Eur. Phys. J.* **C76** (2016) 282, [`1512.00612`].

[104] D. de Florian, G. F. R. Sborlini and G. Rodrigo, *Two-loop QED corrections to the Altarelli-Parisi splitting functions*, `1606.02887`.

[105] J. R. Andersen et al., *Les Houches 2015: Physics at TeV Colliders Standard Model Working Group Report*, 2016. `1605.04692`.

[106] M. Cacciari, M. Greco and P. Nason, *The P(T) spectrum in heavy flavor hadroproduction*, *JHEP* **05** (1998) 007, [`hep-ph/9803400`].

[107] A. D. Martin, R. G. Roberts, W. J. Stirling and R. S. Thorne, *Physical gluons and high E(T) jets*, *Phys. Lett.* **B604** (2004) 61–68, [`hep-ph/0410230`].

[108] S. Dulat, T.-J. Hou, J. Gao, M. Guzzi, J. Huston, P. Nadolsky et al., *New parton distribution functions from a global analysis of quantum chromodynamics*, *Phys. Rev.* **D93** (2016) 033006, [`1506.07443`].

[109] ZEUS collaboration, S. Chekanov et al., *Measurement of isolated photon production in deep inelastic ep scattering*, *Phys. Lett.* **B687** (2010) 16–25, [`0909.4223`].

[110] V. Bertone, S. Carrazza and J. Rojo, *APFEL: A PDF Evolution Library with QED corrections*, *Comput. Phys. Commun.* **185** (2014) 1647–1668, [`1310.1394`].

[111] V. Bertone, S. Carrazza, D. Pagani and M. Zaro, *On the Impact of Lepton PDFs*, *JHEP* **11** (2015) 194, [`1508.07002`].

[112] V. Bertone and S. Carrazza, *Combining NNPDF3.0 and NNPDF2.3QED through the APFEL evolution code*, `1606.07130`.

[113] J. Baglio, L. D. Ninh and M. M. Weber, *Massive gauge boson pair production at the LHC: a next-to-leading order story*, *Phys. Rev.* **D88** (2013) 113005, [`1307.4331`].

[114] D. Pagani, *Top quark forward-backward asymmetry at the Tevatron: the electroweak contribution*, *PoS* **CORFU2011** (2011) 027, [`1205.6182`].

[115] CMS collaboration, V. Khachatryan et al., *Measurement of the differential cross section for top quark pair production in pp collisions at* $\sqrt{s} = 8$ *TeV*, *Eur. Phys. J.* **C75** (2015) 542, [`1505.04480`].

[116] ATLAS collaboration, G. Aad et al., *Measurement of the differential cross-section of highly boosted top quarks as a function of their transverse momentum in* $\sqrt{s} = 8$ *TeV proton-proton collisions using the ATLAS detector*, *Phys. Rev.* **D93** (2016) 032009, [`1510.03818`].

[117] ATLAS collaboration, G. Aad et al., *Measurements of top-quark pair differential cross-sections in the lepton+jets channel in pp collisions at* $\sqrt{s} = 8$ *TeV using the ATLAS detector*, `1511.04716`.

[118] M. Aliev, H. Lacker, U. Langenfeld, S. Moch, P. Uwer and M. Wiedermann, *HATHOR: HAdronic Top and Heavy quarks crOss section calculatoR*, *Comput. Phys. Commun.* **182** (2011) 1034–1046, [`1007.1327`].

[119] L. A. Harland-Lang, A. D. Martin, P. Motylinski and R. S. Thorne, *Parton distributions in the LHC era: MMHT 2014 PDFs*, *Eur. Phys. J.* **C75** (2015) 204, [`1412.3989`].

[120] CMS Collaboration, *Measurement of the inclusive and differential tt production cross sections in lepton + jets final states at 13 TeV*, Tech. Rep. CMS-PAS-TOP-16-008, CERN, Geneva, 2016.

[121] CMS Collaboration, *Measurement of the differential cross section for* $\mathrm{t\bar{t}}$ *production in the dilepton final state at* $\sqrt{s} = 13$ TeV, Tech. Rep. CMS-PAS-TOP-16-011, CERN, Geneva, 2016.

[122] C. W. Bauer, N. Ferland and B. R. Webber, *Standard Model Parton Distributions at Very High Energies*, `1703.08562`.

[123] J. Butterworth et al., *PDF4LHC recommendations for LHC Run II*, *J. Phys.* **G43** (2016) 023001, [`1510.03865`].

[124] ATLAS Collaboration collaboration, G. Aad et al., *Observation of a new particle in the search for the Standard Model Higgs boson with the ATLAS detector at the LHC*, *Phys.Lett.* **B716** (2012) 1–29, [`1207.7214`].

[125] CMS Collaboration collaboration, S. Chatrchyan et al., *Observation of a new boson at a mass of 125 GeV with the CMS experiment at the LHC*, *Phys.Lett.* **B716** (2012) 30–61, [`1207.7235`].

[126] P. Torrielli, *Rare Standard Model processes for present and future hadronic colliders*, `1407.1623`.

[127] W. Beenakker, S. Dittmaier, M. Kramer, B. Plumper, M. Spira et al., *Higgs radiation off top quarks at the Tevatron and the LHC*, *Phys.Rev.Lett.* **87** (2001) 201805, [`hep-ph/0107081`].

[128] W. Beenakker, S. Dittmaier, M. Kramer, B. Plumper, M. Spira et al., *NLO QCD corrections to t anti-t H production in hadron collisions*, *Nucl.Phys.* **B653** (2003) 151–203, [`hep-ph/0211352`].

[129] S. Dawson, L. Orr, L. Reina and D. Wackeroth, *Associated top quark Higgs boson production at the LHC*, *Phys.Rev.* **D67** (2003) 071503, [`hep-ph/0211438`].

[130] S. Dawson, C. Jackson, L. Orr, L. Reina and D. Wackeroth, *Associated Higgs production with top quarks at the large hadron collider: NLO QCD corrections*, *Phys.Rev.* **D68** (2003) 034022, [`hep-ph/0305087`].

[131] K. Melnikov, M. Schulze and A. Scharf, *QCD corrections to top quark pair production in association with a photon at hadron colliders*, *Phys.Rev.* **D83** (2011) 074013, [`1102.1967`].

[132] A. Lazopoulos, T. McElmurry, K. Melnikov and F. Petriello, *Next-to-leading order QCD corrections to $t\bar{t}Z$ production at the LHC*, *Phys.Lett.* **B666** (2008) 62–65, [`0804.2220`].

[133] M. Garzelli, A. Kardos, C. Papadopoulos and Z. Trocsanyi, *Z - boson production in association with a top anti-top pair at NLO accuracy with parton shower effects*, *Phys.Rev.* **D85** (2012) 074022, [`1111.1444`].

[134] A. Kardos, Z. Trocsanyi and C. Papadopoulos, *Top quark pair production in association with a Z-boson at NLO accuracy*, *Phys.Rev.* **D85** (2012) 054015, [`1111.0610`].

[135] M. Garzelli, A. Kardos, C. Papadopoulos and Z. Trocsanyi, *$t\,\bar{t}\,W^{\pm}$ and $t\,\bar{t}\,Z$ Hadroproduction at NLO accuracy in QCD with Parton Shower and Hadronization effects*, *JHEP* **1211** (2012) 056, [`1208.2665`].

[136] J. M. Campbell and R. K. Ellis, *$t\bar{t}W^{\pm}$ production and decay at NLO*, *JHEP* **1207** (2012) 052, [`1204.5678`].

[137] G. Bevilacqua and M. Worek, *Constraining BSM Physics at the LHC: Four top final states with NLO accuracy in perturbative QCD*, *JHEP* **1207** (2012) 111, [`1206.3064`].

[138] Y. Zhang, W.-G. Ma, R.-Y. Zhang, C. Chen and L. Guo, *QCD NLO and EW NLO corrections to $t\bar{t}H$ production with top quark decays at hadron collider*, *Phys.Lett.* **B738** (2014) 1–5, [`1407.1110`].

[139] R. Frederix, S. Frixione, V. Hirschi, F. Maltoni, R. Pittau and P. Torielli, *Scalar and pseudoscalar Higgs production in association with a top-antitop pair*, *Phys.Lett.* **B701** (2011) 427–433, [`1104.5613`].

[140] M. Garzelli, A. Kardos, C. Papadopoulos and Z. Trocsanyi, *Standard Model Higgs boson production in association with a top anti-top pair at NLO with parton showering*, *Europhys.Lett.* **96** (2011) 11001, [`1108.0387`].

[141] A. Denner and R. Feger, *NLO QCD corrections to off-shell top-antitop production with leptonic decays in association with a Higgs boson at the LHC*, `1506.07448`.

[142] A. Kardos and Z. Trócsányi, *Hadroproduction of $t\bar{t}$ pair in association with an isolated photon at NLO accuracy matched with parton shower*, *JHEP* **05** (2015) 090, [`1406.2324`].

[143] A. Kardos and Z. Trócsányi, *Hadroproduction of $t\bar{t}$ pair with two isolated photons with PowHel*, `1408.0278`.

[144] H. van Deurzen, R. Frederix, V. Hirschi, G. Luisoni, P. Mastrolia and G. Ossola, *Spin Polarisation of $t\bar{t}\gamma\gamma$ production at NLO+PS with GoSam interfaced to MadGraph5_ aMC@NLO*, *Eur. Phys. J.* **C76** (2016) 221, [`1509.02077`].

[145] CMS Collaboration, V. Khachatryan et al., *Search for the associated production of the Higgs boson with a top-quark pair*, *JHEP* **1409** (2014) 087, [`1408.1682`].

[146] ATLAS collaboration, *Search for $H \to \gamma\gamma$ produced in association with top quarks and constraints on the top quark-Higgs boson Yukawa coupling using data taken at 7 TeV and 8 TeV with the ATLAS detector*, .

[147] ATLAS collaboration, G. Aad et al., *Search for the associated production of the Higgs boson with a top quark pair in multilepton final states with the ATLAS detector*, `1506.05988`.

[148] N. Craig, M. Park and J. Shelton, *Multi-Lepton Signals of Top-Higgs Associated Production*, `1308.0845`.

[149] S. Catani, F. Krauss, R. Kuhn and B. Webber, *QCD matrix elements + parton showers*, *JHEP* **0111** (2001) 063, [`hep-ph/0109231`].

[150] P. Artoisenet, R. Frederix, O. Mattelaer and R. Rietkerk, *Automatic spin-entangled decays of heavy resonances in Monte Carlo simulations*, *JHEP* **1303** (2013) 015, [`1212.3460`].

[151] S. Frixione, E. Laenen, P. Motylinski and B. R. Webber, *Angular correlations of lepton pairs from vector boson and top quark decays in Monte Carlo simulations*, *JHEP* **0704** (2007) 081, [`hep-ph/0702198`].

[152] S. Frixione, *Isolated photons in perturbative QCD*, *Phys.Lett.* **B429** (1998) 369–374, [`hep-ph/9801442`].

[153] A. Denner, *Techniques for calculation of electroweak radiative corrections at the one loop level and results for W physics at LEP-200*, *Fortsch.Phys.* **41** (1993) 307–420, [`0709.1075`].

[154] R. Frederix, S. Frixione, V. Hirschi, F. Maltoni, R. Pittau et al., *Four-lepton production at hadron colliders: aMC@NLO predictions with theoretical uncertainties*, *JHEP* **1202** (2012) 099, [`1110.4738`].

[155] S. Frixione, P. Nason and G. Ridolfi, *Strong corrections to W Z production at hadron colliders*, *Nucl.Phys.* **B383** (1992) 3–44.

[156] S. Frixione, *A Next-to-leading order calculation of the cross-section for the production of W+ W- pairs in hadronic collisions*, *Nucl.Phys.* **B410** (1993) 280–324.

[157] R. Frederix and S. Frixione, *Merging meets matching in MC@NLO*, *JHEP* **1212** (2012) 061, [`1209.6215`].

[158] J. H. Kuhn and G. Rodrigo, *Charge asymmetry in hadroproduction of heavy quarks*, *Phys.Rev.Lett.* **81** (1998) 49–52, [`hep-ph/9802268`].

[159] J. Aguilar-Saavedra, E. !'lvarez, A. Juste and F. Rubbo, *Shedding light on the $t\bar{t}$ asymmetry: the photon handle*, *JHEP* **1404** (2014) 188, [`1402.3598`].

[160] ATLAS collaboration, G. Aad et al., *Measurement of the charge asymmetry in top-quark pair production in the lepton-plus-jets final state in pp collision data at $\sqrt{s} = 8\,\mathrm{TeV}$ with the ATLAS detector*, *Eur. Phys. J.* **C76** (2016) 87, [`1509.02358`].

[161] M. Cacciari, G. P. Salam and G. Soyez, *The Anti-$k_t$ jet clustering algorithm*, *JHEP* **0804** (2008) 063, [`0802.1189`].

[162] M. Cacciari, G. P. Salam and G. Soyez, *FastJet User Manual*, *Eur.Phys.J.* **C72** (2012) 1896, [`1111.6097`].

[163] *https://twiki.cern.ch/twiki/bin/view/lhcphysics/cernyellowreportpagebr3*, *SM Higgs Branching Ratios and Partial-Decay Widths (CERN Report 3, 2013 update)* .

[164] CDF collaboration, T. Aaltonen et al., *Evidence for $t\bar{t}\gamma$ Production and Measurement of $\sigma_{t\bar{t}\gamma}/\sigma_{t\bar{t}}$*, *Phys. Rev.* **D84** (2011) 031104, [`1106.3970`].

[165] CMS collaboration, *Measurement of the inclusive top-quark pair + photon production cross section in the muon + jets channel in pp collisions at 8 TeV*, 2014, `CMS-PAS-TOP-13-011`.

[166] ATLAS collaboration, G. Aad et al., *Observation of top-quark pair production in association with a photon and measurement of the $t\bar{t}\gamma$ production cross section in pp collisions at $\sqrt{s} = 7$ TeV using the ATLAS detector*, *Phys. Rev.* **D91** (2015) 072007, [`1502.00586`].

[167] CMS collaboration, V. Khachatryan et al., *Measurement of top quark-antiquark pair production in association with a W or Z boson in pp collisions at $\sqrt{s} = 8\,TeV$*, *Eur. Phys. J.* **C74** (2014) 3060, [`1406.7830`].

[168] CMS collaboration, V. Khachatryan et al., *Observation of top quark pairs produced in association with a vector boson in pp collisions at $\sqrt{s} = 8$ TeV*, `1510.01131`.

[169] ATLAS collaboration, G. Aad et al., *Measurement of the $t\bar{t}W$ and $t\bar{t}Z$ production cross sections in pp collisions at $\sqrt{s} = 8\,TeV$ with the ATLAS detector*, `1509.05276`.

[170] C. Zhang and F. Maltoni, *Top-quark decay into Higgs boson and a light quark at next-to-leading order in QCD*, *Phys.Rev.* **D88** (2013) 054005, [`1305.7386`].

[171] C. Zhang, *Effective field theory approach to top-quark decay at next-to-leading order in QCD*, *Phys. Rev.* **D90** (2014) 014008, [`1404.1264`].

[172] C. Degrande, F. Maltoni, J. Wang and C. Zhang, *Automatic computations at next-to-leading order in QCD for top-quark flavor-changing neutral processes*, *Phys. Rev.* **D91** (2015) 034024, [`1412.5594`].

[173] D. Buarque Franzosi and C. Zhang, *Probing the top-quark chromomagnetic dipole moment at next-to-leading order in QCD*, *Phys. Rev.* **D91** (2015) 114010, [`1503.08841`].

[174] C. Zhang, *Single top production at next-to-leading order in the Standard Model effective field theory*, `1601.06163`.

[175] R. Röntsch and M. Schulze, *Constraining couplings of top quarks to the Z boson in $t\bar{t}$ + Z production at the LHC*, *JHEP* **07** (2014) 091, [`1404.1005`].

[176] R. Röntsch and M. Schulze, *Probing top-Z dipole moments at the LHC and ILC*, *JHEP* **08** (2015) 044, [`1501.05939`].

[177] J. A. Aguilar-Saavedra, *A Minimal set of top anomalous couplings*, *Nucl. Phys.* **B812** (2009) 181–204, [`0811.3842`].

[178] C. Zhang and S. Willenbrock, *Effective-Field-Theory Approach to Top-Quark Production and Decay*, *Phys. Rev.* **D83** (2011) 034006, [`1008.3869`].

[179] C. Degrande, J.-M. Gerard, C. Grojean, F. Maltoni and G. Servant, *Non-resonant New Physics in Top Pair Production at Hadron Colliders*, *JHEP* **03** (2011) 125, [`1010.6304`].

[180] J. A. Aguilar-Saavedra, B. Fuks and M. L. Mangano, *Pinning down top dipole moments with ultra-boosted tops*, *Phys.Rev.* **D91** (2015) 094021, [`1412.6654`].

[181] A. Tonero and R. Rosenfeld, *Dipole-induced anomalous top quark couplings at the LHC*, *Phys.Rev.* **D90** (2014) 017701, [`1404.2581`].

[182] C. Zhang, N. Greiner and S. Willenbrock, *Constraints on Non-standard Top Quark Couplings*, *Phys. Rev.* **D86** (2012) 014024, [`1201.6670`].

[183] N. Greiner, S. Willenbrock and C. Zhang, *Effective Field Theory for Nonstandard Top Quark Couplings*, *Phys. Lett.* **B704** (2011) 218–222, [`1104.3122`].

[184] A. Buckley, C. Englert, J. Ferrando, D. J. Miller, L. Moore, M. Russell et al., *Global fit of top quark effective theory to data*, *Phys. Rev.* **D92** (2015) 091501, [`1506.08845`].

[185] A. Buckley, C. Englert, J. Ferrando, D. J. Miller, L. Moore, M. Russell et al., *Constraining top quark effective theory in the LHC Run II era*, `1512.03360`.

[186] J. de Blas, M. Chala and J. Santiago, *Renormalization Group Constraints on New Top Interactions from Electroweak Precision Data*, *JHEP* **09** (2015) 189, [`1507.00757`].

[187] C. Degrande, *Automatic evaluation of UV and R2 terms for beyond the Standard Model Lagrangians: a proof-of-principle*, *Comput. Phys. Commun.* **197** (2015) 239–262, [`1406.3030`].

[188] V. Hirschi and O. Mattelaer, *Automated event generation for loop-induced processes*, *JHEP* **10** (2015) 146, [`1507.00020`].

[189] E. E. Jenkins, A. V. Manohar and M. Trott, *Renormalization Group Evolution of the Standard Model Dimension Six Operators I: Formalism and lambda Dependence*, *JHEP* **10** (2013) 087, [`1308.2627`].

[190] E. E. Jenkins, A. V. Manohar and M. Trott, *Renormalization Group Evolution of the Standard Model Dimension Six Operators II: Yukawa Dependence*, *JHEP* **01** (2014) 035, [`1310.4838`].

[191] R. Alonso, E. E. Jenkins, A. V. Manohar and M. Trott, *Renormalization Group Evolution of the Standard Model Dimension Six Operators III: Gauge Coupling Dependence and Phenomenology*, *JHEP* **04** (2014) 159, [`1312.2014`].

[192] J. Preskill, *Gauge anomalies in an effective field theory*, *Annals Phys.* **210** (1991) 323–379.

[193] O. Domenech, A. Pomarol and J. Serra, *Probing the SM with Dijets at the LHC*, *Phys. Rev.* **D85** (2012) 074030, [`1201.6510`].

[194] A. Biekötter, A. Knochel, M. Krämer, D. Liu and F. Riva, *Vices and virtues of Higgs effective field theories at large energy*, *Phys. Rev.* **D91** (2015) 055029, [`1406.7320`].

[195] B. Hespel, F. Maltoni and E. Vryonidou, *Higgs and Z boson associated production via gluon fusion in the SM and the 2HDM*, *JHEP* **06** (2015) 065, [`1503.01656`].

[196] L. Berthier and M. Trott, *Consistent constraints on the Standard Model Effective Field Theory*, *JHEP* **02** (2016) 069, [`1508.05060`].

[197] CMS collaboration, *Combination of ATLAS and CMS top quark pair cross section measurements in the eμ final state using proton-proton collisions at 8 TeV*, 2014, `ATLAS-CONF-2014-054`.

[198] S. J. Parke and Y. Shadmi, *Spin correlations in top quark pair production at $e^+e^-$ colliders*, *Phys. Lett.* **B387** (1996) 199–206, [`hep-ph/9606419`].